A Long Baseline Search for Neutrino Flavor Oscillations

by

Lee Harold Lueking

A dissertation submitted to The Johns Hopkins University
in conformity with the requirements for the degree of
Doctor of Philosophy

Baltimore, Maryland
1987

Abstract

A measurement of the electron neutrino to muon neutrino mixing probability has been conducted in a newly designed narrow band neutrino beam at BNL. The detector employed was 225 metric tons of target and absorber material instrumented with proportional wire chambers located 1 km from the neutrino source. The beamline provided muon neutrinos to the detector at a calculated rate of 1.5×10^4 per m^2 per 10^{12} protons on target with a relative electron neutrino background at the level of 8.3×10^{-3}. Analysis of data from 3×10^{19} protons on target taken at two energies, 1.27 GeV and 1.46 GeV, shows that the ν_μ event energy distribution and rate were consistent with that calculated for the beamline but that the ν_e event rate was higher than expected.

Acknowledgements

Dozens of people from the three collaborating universities as well as from Brookhaven National Laboratory contributed great portions of their lives to the design, construction, trouble-shooting, and operation of the neutrino beam-line and detector. I couldn't possibly thank all of the engineers and technicians from BNL, Nevis, and the University of Illinois without excluding someone. However, from Johns Hopkins I would like to give special thanks to Jack Spangler, Mark Warns, Vivian Leventon, Vivian Lewis and Tim Cook who were not only hard working but also special friends. Also my thanks to Estella Hankin and Nancy Skoczynski for keeping my business together while I was at Brookhaven.

My gratitude is given to Dr. Barry Blumenfeld for his guidance as my advisor throughout most of my graduate school career. He has assisted me through the many trying times of the experiment and has given much physics direction to my work. I would also like to thank Bruce Barnett, Leon Madansky, Aihud Pevsner and C.Y. Chien for their help and advice concerning the experiment and High Energy Physics in general.

I have had the privilege of working closely with many talented physicists who were involved with the experiment. Among them are Lisa Chichura, John Krizmanic , Eric Lincke, Bill Lyle, Ed O'Brien, Brad Rubin, Chris Stoughton, Dr. W.Y. Lee, Dr. Tom O'Halloran, Dr. George Tzanakos, and Dr. Maged Atiya. I thank them for their numerous contributions and for the many painstaking hours of dedicated work which each of them contributed. Special thanks to C.Y. Chi, Kevin Reardon, Nik Kondakis and Dr. Richard Seto, who were especially helpful throughout the experiment and during the analysis. I would also like to thank Mike Murtaugh for the many enlightening discussions concerning neutrino physics and the bubble chamber data which he provided and helped me use.

This work is dedicated to my parents Harold and Guelah Lueking, only with their encouragement and support has it been possible. I would especially like to thank my wife, Jean, for waiting and proof reading the manuscript. Also, I want to express my appreciation to Dr. T. James for his inspiration.

LHL

March 1987

Table of Contents

List of Figures

List of Tables

Chapter 1.
Neutrino Oscillations and Their Measurement

1.1. Historical Aspects and Theory

Neutrino oscillations were first introduced by Pontecorvo[1] in the form of a $\bar{\nu}_e \leftrightarrow \nu_e$ transition. This mixing was explored by him around 1955 in an effort to explain an apparent contradiction in experimental results between Reines[2] and Davis.[3] The Reines experiment had confirmed the existence of the inverse β reaction $\bar{\nu}p \rightarrow e^+n$. The Davis experiment was studying the reaction $\bar{\nu}n \rightarrow e^-p$ and a positive indication was misreported to Pontecorvo. This form of the transition was in fact not only ruled out by the experimental evidence, but later found to be suppressed by the fact that $\bar{\nu}_e$ and ν_e have opposite helicities. About ten years later, however, the formalism was adopted for the case of ν flavor oscillations.[4]

There is a rich background of literature describing flavor oscillations.[5] The general description which follows parallels that of Flaminio.[6] If the weak interaction eigenstates $(\nu_e, \nu_\mu, \nu_\tau)$ are not identical to the mass eigenstates (ν_1, ν_2, ν_3) then a unitary matrix U can be established which relates the two sets,

$$\begin{pmatrix} \nu_e \\ \nu_\mu \\ \nu_\tau \end{pmatrix} = U \begin{pmatrix} \nu_1 \\ \nu_2 \\ \nu_3 \end{pmatrix}. \tag{1.1}$$

This can be written in the more general form

$$\nu_\alpha = \sum_i U_{\alpha i} \nu_i \tag{1.2a}$$

$$\nu_j = \sum_\beta U^\dagger_{j\beta} \nu_\beta, \tag{1.2b}$$

with $\alpha, \beta = e, \mu, \tau$.

A neutrino with a particular flavor at $t = 0$, will be a linear combination of mass eigenstates expressed as eq. 1.2a. Each of these mass eigenstates is described by the plane wave

$$\nu_i(t) = \nu_i(0) \exp i(P_i x - E_i t)$$

with P_i being the momentum, and E_i the energy. The momentum is the same for all of the mass eigenstates and thus $P_i = P$. Hence the factor $\exp(iPx)$, being common to all terms, can then be neglected. The time development of the original flavor eigenstate can now be expressed as

$$\nu_\alpha(t) = \sum_i U_{\alpha i} \exp(-iE_i t)\nu_i(0).$$

A measurement of the flavor of the state at time t will yield the probability amplitude for the flavor β with the form

$$A(\alpha \to \beta) = < \nu_\beta(0)|\nu_\alpha(t) > = \sum_i U_{\alpha i} \exp(-iE_i t) < \nu_\beta|\nu_i(0) > .$$

With eq. 1.2a this becomes

$$A(\alpha \to \beta) = \sum_i U^\dagger_{i\beta} \exp(-iE_i t). \tag{1.3}$$

The probability of finding flavor β after time t beginning with flavor α is given by

$$\begin{aligned} P_{\alpha\beta}(t) &= |\sum_i U_{\alpha i} U^\dagger_{i\beta} \exp(iE_i)\, t|^2 \\ &= \sum_i |U_{\alpha i} U^\dagger_{i\beta}|^2 + 2\mathrm{Re} \sum_{i>j} U_{\alpha i} U^\dagger_{i\beta} U_{\beta j} U^\dagger_{j\alpha} \exp[i(E_j - E_i)\, t]. \end{aligned} \tag{1.4}$$

The first term can be rewritten as

$$\begin{aligned} \sum_i |U_{\alpha i} U^\dagger_{i\beta}|^2 &= \sum_i |U_{\alpha i} U^\dagger_{i\beta}|^2 - 2\mathrm{Re} \sum_{i>j} U_{\alpha i} U^\dagger_{i\beta} U_{\beta j} U^\dagger_{j\alpha} \\ &= \delta_{\alpha\beta} - 2\mathrm{Re} \sum_{i>j} |U_{\alpha i} U^\dagger_{i\beta} U_{\beta j} U^\dagger_{j\alpha}| \exp(i\phi_{\alpha\beta ij}), \end{aligned}$$

where ϕ represents the phase of the product $U_{\alpha i} U^\dagger_{i\beta} U_{\beta j} U^\dagger_{j\alpha}$. The probability is then

$$\begin{aligned} P_{\alpha\beta}(t) = \delta_{\alpha\beta} &+ 2\mathrm{Re} \sum_{i>j} |U_{\alpha i} U^\dagger_{i\beta} U_{\beta j} U^\dagger_{j\alpha}| \exp[i[\phi_{\alpha\beta ij} + (E_j - E_i)\, t]] \\ &- 2\mathrm{Re} \sum_{i>j} |U_{\alpha i} U^\dagger_{i\beta} U_{\beta j} U^\dagger_{j\alpha}| \exp(i\phi_{\alpha\beta ij}), \end{aligned}$$

which is written equivalently as

$$P_{\alpha\beta}(t) = \delta_{\alpha\beta} + 2\mathrm{Re} \sum_{i>j} |U_{\alpha i} U^\dagger_{i\beta} U_{\beta j} U^\dagger_{j\alpha}| \,[\cos[(E_i - E_j)\, t - \phi_{\alpha\beta ij}] - \cos\phi_{\alpha\beta ij}]. \tag{1.5}$$

If U is real, CP is conserved, and this can be further reduced to eq. 1.6.

$$P_{\alpha\beta}(t) = \delta_{\alpha\beta} - 4\sum_{i>j} |U_{\alpha i} U^T_{i\beta} U_{\beta j} U^T_{j\alpha}| \sin^2\left[(E_i - E_j)\, t/2\right] \tag{1.6}$$

For the case where m_i and $m_j \ll P \cong E$ then $E_i(P) = (P^2 + m_i^2)^{1/2} \cong P + (m_i^2/2P)$. The energy dependant term then can be simplified as

$$(E_i - E_j)\, t/2 = \left(m_i^2 - m_j^2\right) t/4E$$

Including the appropriate constants, this is generally written in the form

$$\left(m_i^2 - m_j^2\right) t/4E = 1.267 \delta m^2(\text{eV}) L(\text{m})/E(\text{MeV}) \tag{1.7}$$

1.2. Two Neutrino Case

In order to simplify the study and because no evidence for neutrino oscillation has been found to this point, a two neutrino case is generally adopted. This system facilitates the comparison of parameters as measured by various experiments. Also, in the event that one of the mass differences dominates, the three neutrino treatment reduces to the two neutrino case. In this situation, the unitary matrix reduces to a simple rotation through an angle θ, and eq. 1.1 becomes

$$\begin{pmatrix} \nu_e \\ \nu_\mu \end{pmatrix} = \begin{pmatrix} \cos\theta & \sin\theta \\ -\sin\theta & \cos\theta \end{pmatrix} \begin{pmatrix} \nu_1 \\ \nu_2 \end{pmatrix}. \tag{1.8}$$

With this simplification, eq. 1.6 is reduced to the form

$$P(\nu_e \leftrightarrow \nu_\mu) = \sin^2 2\theta \sin^2\left(1.267 \delta m^2 L/E\right). \tag{1.9}$$

A general quantity employed to characterize the sensitivity of various oscillation experiments is L/E. The larger the value of this quantity, the higher the sensitivity to small δm^2.

In the ideal measurement of the mixing parameters the quantities attained are simply the 'signal' or the number of ν_e events, N_{ν_e}, and the 'normalization' or the number of ν_μ events, N_{ν_μ}. Due to the fact that the neutrino beam has an energy distribution and the cross sections for interaction vary over the extent of this distribution, the mixing parameters are calculated with an integration over energy and cross section

$$\frac{N_{\nu_e}}{N_{\nu_\mu}} = \frac{\int dE \Phi(E)\, \sigma(E)\, P(\nu_\mu \rightarrow \nu_e)}{\int dE \Phi(E)\, \sigma(E) \left[1 - P(\nu_\mu \rightarrow \nu_e)\right]}, \tag{1.10}$$

where $\Phi(E)$ is the beam flux, $\sigma(E)$ is the cross section of the reaction in the detector.

1.3. Data Acquisition and Analysis

The detector of this experiment was located at 1 km from the source as shown in Figure 1.1 and dedicated to the measurement of a ν_e component in a narrow band ν_μ beam. In the two principle sets of data the primary component of the beam was centered at 1.27 and 1.46 GeV and was $\pm 16\%$ in width. Thus the L/E for the experiment was .8 and .7 m/MeV for the two sets of data. The actual analysis of the data is somewhat more complicated than eq. 1.6 suggests in that the acceptance of the detector and the number of background events must be determined for both the signal and the normalization. The actual measurement is more like

$$\frac{N_{\nu_e}}{N_{\nu_\mu}} = \frac{\sum_{n=1}^{\#\ e\ Chan.} \int dE \Phi(E)\, \sigma_n(E)\, A_n(E)\, P(\nu_\mu \to \nu_e) + \sum_{m=1}^{\#\ e\ bg} \int dE B_m(E)}{\sum_{n=1}^{\#\ \mu\ Chan.} \int dE \Phi(E)\, \sigma_n(E)\, A_n(E)\, [1 - P(\nu_\mu \to \nu_e)] + \sum_{m=1}^{\#\ \mu\ bg} \int dE B_m(E)}. \tag{1.11}$$

This equation includes acceptance terms for each production channel $A_n(E)$, and an estimation of the background which comes from several sources $B_m(E)$. The number of events representing the signal and background here represents the total number of candidates for each.

An extensive amount of work has been done to calculate the beam flux, $\Phi(E)$, generated by the neutrino source. The source was a two horn magnetic lens system which was designed to focus π^+ and K^+ secondaries from a copper target. These secondaries were momentum selected by collimators and allowed to decay in a 90 meter decay tunnel. A Monte Carlo was developed to trace particles through this system and generate the neutrino beam flux function.

There were many interaction channels with significant cross sections available in the energy region which the experiment explored. The four principle charged current channels for ν_μ and ν_e were:

1.	$\nu_\mu n \to \mu^- p$	$\nu_e n \to e^- p$
2.	$\nu_\mu p \to \mu^- p \pi^+$	$\nu_e p \to e^- p \pi^+$
3.	$\nu_\mu n \to \mu^- p \pi^0$	$\nu_e n \to e^- p \pi^0$
4.	$\nu_\mu n \to \mu^- n \pi^+$	$\nu_e n \to e^- n \pi^+$

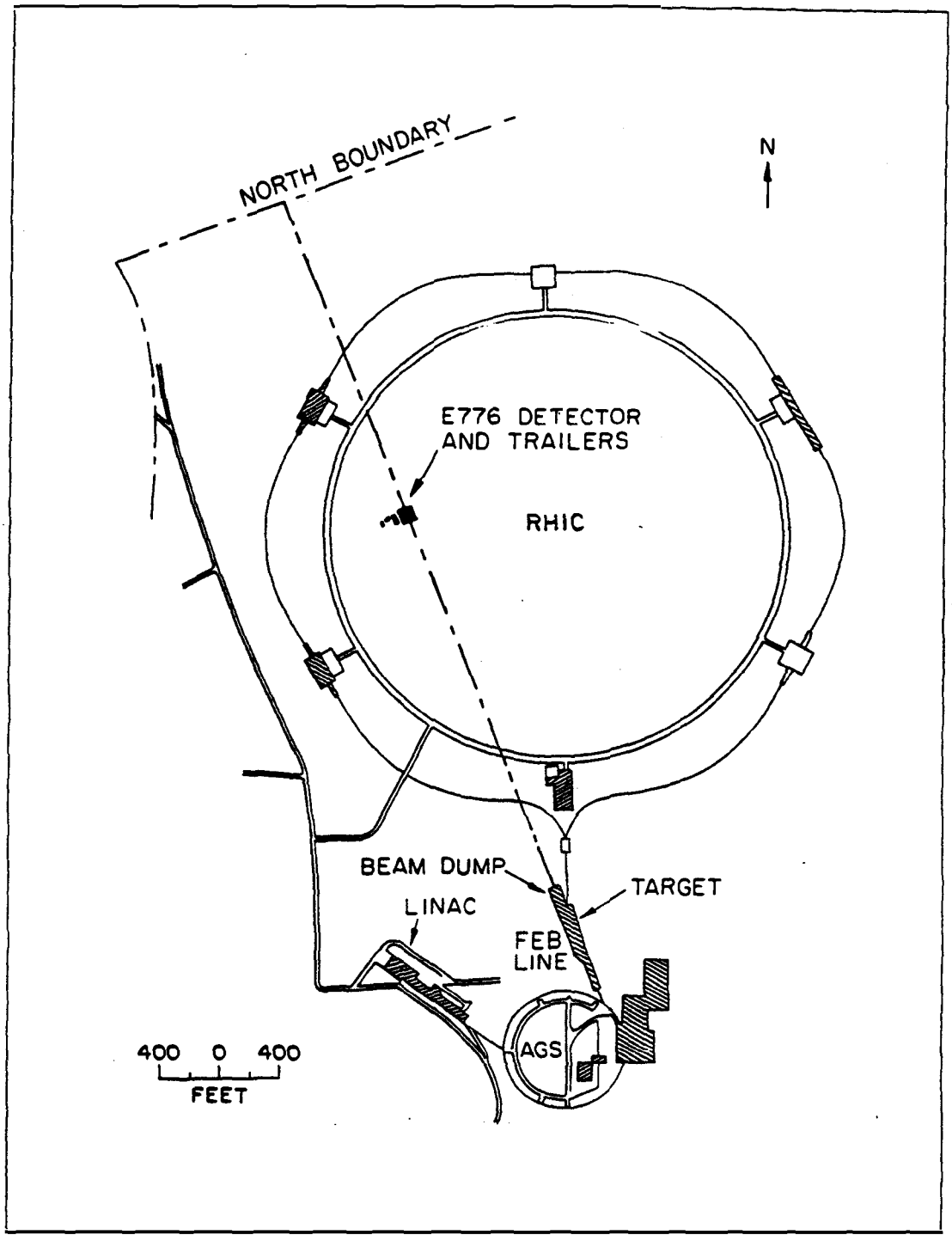

Figure 1.1: Detector location relative to the AGS and neutrino beamline.

The six principle neutral current channels available for ν_μ and ν_e were:

5.	$\nu_\mu n \rightarrow \nu_\mu n$	$\nu_e n \rightarrow \nu_e n$
6.	$\nu_\mu p \rightarrow \nu_\mu p$	$\nu_e p \rightarrow \nu_e p$
7.	$\nu_\mu n \rightarrow \nu_\mu p \pi^-$	$\nu_e n \rightarrow \nu_e p \pi^-$
8.	$\nu_\mu p \rightarrow \nu_\mu p \pi^0$	$\nu_e p \rightarrow \nu_e p \pi^0$
9.	$\nu_\mu p \rightarrow \nu_\mu n \pi^+$	$\nu_e p \rightarrow \nu_e n \pi^+$
10.	$\nu_\mu n \rightarrow \nu_\mu n \pi^0$	$\nu_e n \rightarrow \nu_e n \pi^0$

These represent the most simple topologies available. In addition there were multi-pion events in cases where the incident neutrino energy was sufficiently high.

Values for the acceptance parameters, $A_n(E)$, for the signal and normalization were determined utilizing the event Monte Carlo. Events were generated with the appropriate dynamics, then stepped through the detector accounting for ionization energy loss, scattering and nuclear interaction. These events were then reconstructed and the percentage of events passing all of the data cuts became the acceptance. This procedure has been performed for all of the event types with an energy distribution which matches that of the data as calculated with the beam Monte Carlo.

In calculating the backgrounds there were many sources which were considered for the signal and the normalization. For the signal, the background can be broken into five categories:

1. ν_e background calculated with the beam Monte Carlo.
2. misidentified shower events from charged current single pion ν_μ interactions.
3. misidentified shower events from neutral current single pion ν_μ interactions.
4. Multi-pion and other exotic shower events.
5. Cosmic ray induced events.

For the normalization, the background comes primarily from four sources:

1. misidentified charged current events.
2. misidentified neutral current events.
3. misidentified multi-pion events.
4. Cosmic ray induced background.

1.4. Report Organization

This report discusses the principle elements of this project including design, testing, data taking and analysis. The detector is discussed in Chapter 2 with details of its construction, gas system, electronics, data readout and triggers. The setup in the BNL A2 test beam used to measure characteristics of the detector performance are also given in Chapter 2. Calculation of the flux produced by the dichromatic beam, including the ν_e background, is presented in chapter 3. Chapter 4 explains the Event Monte Carlo which was used in the acceptance and background calculations. Chapters 5 and 6 deal with the muon normalization and electron signal analysis of the data. Some preliminary results and concluding remarks are included in Chapter 7.

Chapter 2.
The Detector

The E776 Neutrino detector was comprised of 2 major components: the electron shower detector and the muon spectrometer. The upstream portion of the apparatus was made of elements providing target material for ν_μ and ν_e interactions, and designed to measure electromagnetic shower energies, particle trajectories and event timing . At the downstream end magnetized steel plates in the muon spectrometer provided enough material to stop low momentum muons and allowed momentum analysis in the toroidal field for those which penetrated all of the steel. Figure 2.1 provides an overview of the apparatus and shows details of its construction. Not shown in the figure are a 5 cm thick lead wall installed immediately in front of the detector, and a ~1.5 m thick concrete shielding wall located about 5 m upstream from the detector. The purpose of the lead wall was to convert beam related high energy gamma rays into electromagnetic showers before they entered the detector. The Concrete provided shielding against neutrons and muons from the beam source area.

2.1. Electron Shower Detector

Component	Material	Z Average	A Average	Density $\left(g/cm^3\right)$	Mass per plane (k gram)	Number of planes
Absorber	Concrete	10.7	21.5	2.31	1775	81
Drift cell	Aluminum	13	26.98	2.7	692	90
Scintillator enclosure	Aluminum	13	26.98	2.7	1145	10
Scintillator	Acrylic	6	12	1.17	814	10
Total detector mass					225.626 metric tons	

Table 2.1: Breakdown of the detector mass and composition.

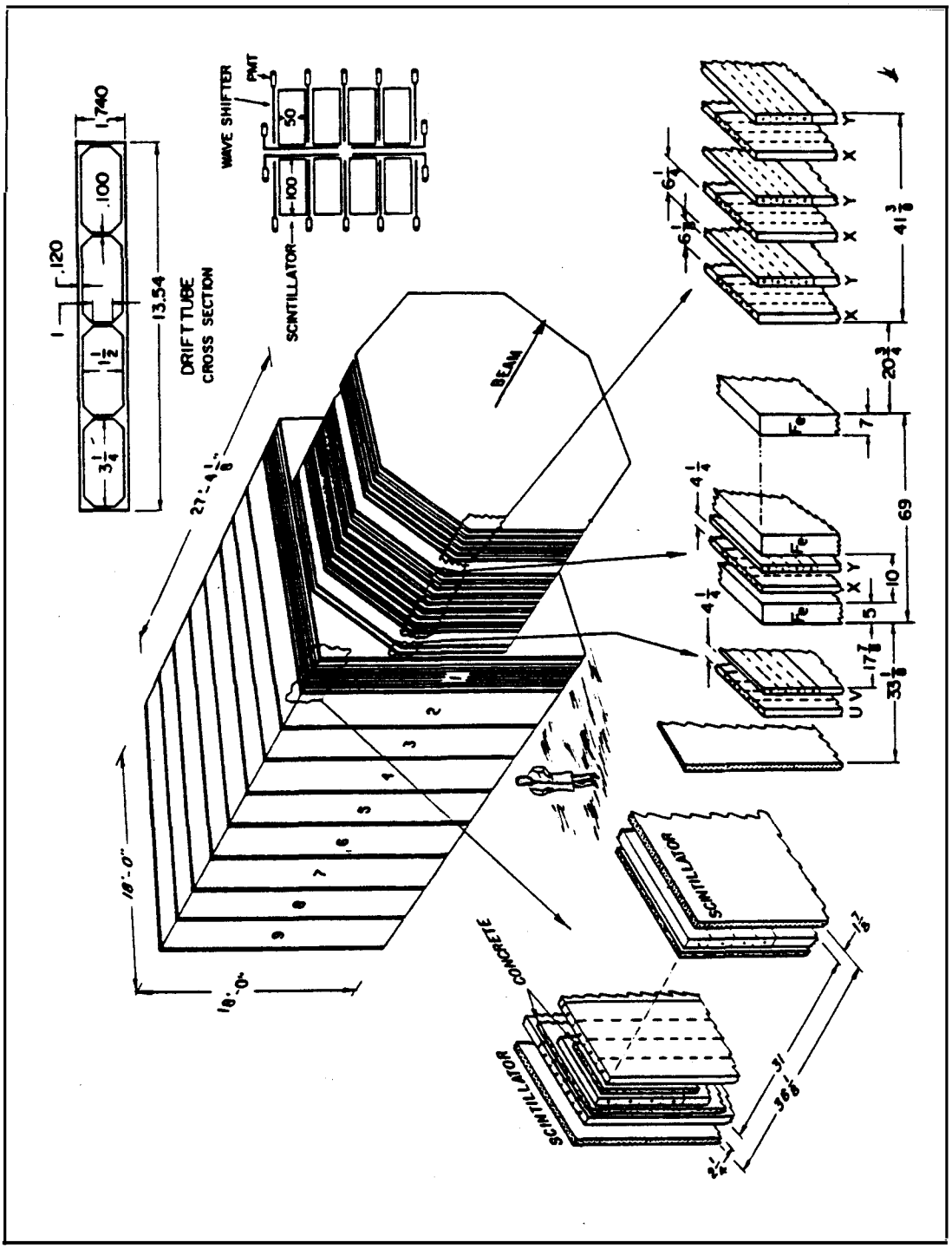

Figure 2.1: An overview of the detector construction and dimensions.

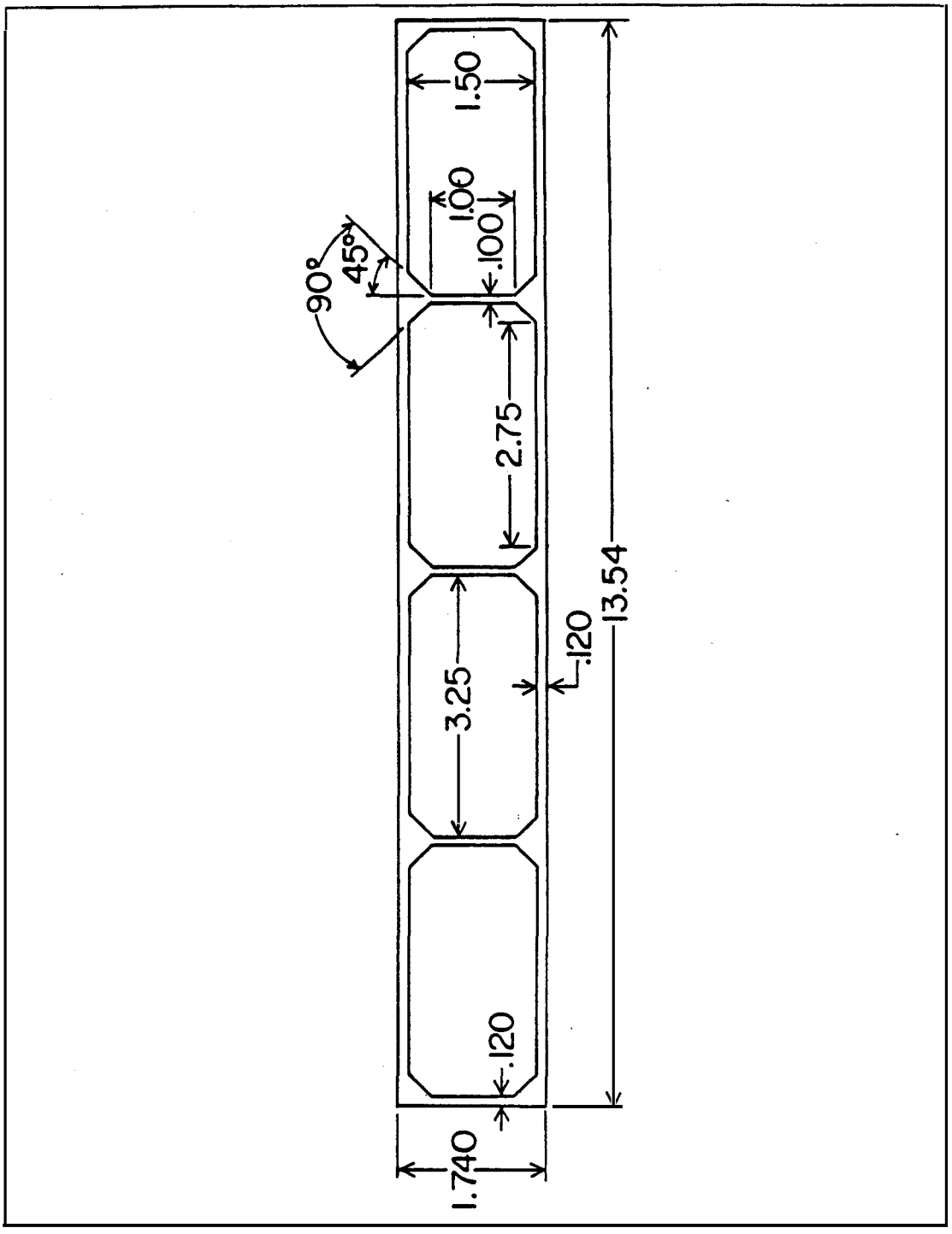

Figure 2.2: The cross sectional view of the proportional drift chambers employed in the both the shower detector and toroid elements.

Ninety planes of proportional drift chambers and concrete absorber material provided the bulk of the electron detector with a total mass of 225 metric tons. Ten planes of 2.5 cm acrylic scintillator gave timing information. The dimensions of the proportional drift tubes (PDTs) shown in Figure 2.2 were 4.3 cm x 8.6 cm with a 50 μm wire extending through the axial center across their 550 cm length. Formed in extruded aluminum modules of four tubes each, a complete plane contained 16 modules for a total of 64 wires. Strapped to each PDT module was a slab of 2.54 cm concrete. Every 10^{th} PDT plane the concrete absorber was replaced by a plane of acrylic scintillator to provide timing. Therefore the total arrangement of the PDTs, absorber and scintillator was a front scintillator plane followed by nine sections of PDT, concrete, and scintillator. Each of these sections was composed of 8 planes of alternating X and Y drift tubes with concrete strapped to them, followed by an X PDT plane with concrete, a Y PDT plane with no concrete and a scintillator plane. As compiled in Table 2.1 each PDT plane represents nearly 2.5 metric tons of material and .33 radiation lengths. The total mass of the electron detector was therefore 225 metric tons which represented 30 radiation lengths of absorber.

The PDTs were assembled from extruded aluminum modules. An end plate and mounting bracket were welded at each end of the 550 cm module and 50μm gold plated tungsten wire was strung with a tension of 250 g through the length of each cell. The wires were mounted at the center of the rectangular cross section using Delrin plugs and tapered gold plated brass pins. There was some initial concern that force down on horizontal wires might cause the wire to sag over such a large span and this effect was investigated. The sag for various tensions on a horizontal wire over the 550 cm span is shown in Figure 2.3 as it was measured and calculated. The effect was not a major problem for the wire tension used.

Because the drift cells were operated in the proportional drift mode, determination of both drift time and gas gain were important. A field and drift time map of the chamber is shown in Figure 2.4a and Figure 2.4b for voltage of 2.25 kV. The gas gain for the cells can be approximated using the parameterization of Wolf [7]

$$\ln A = \frac{V}{\ln(b/a)} \frac{\ln 2}{\Delta V} \left[\ln \left(\frac{V}{pa \ln(b/a)} \right) - \ln K \right], \tag{2.1}$$

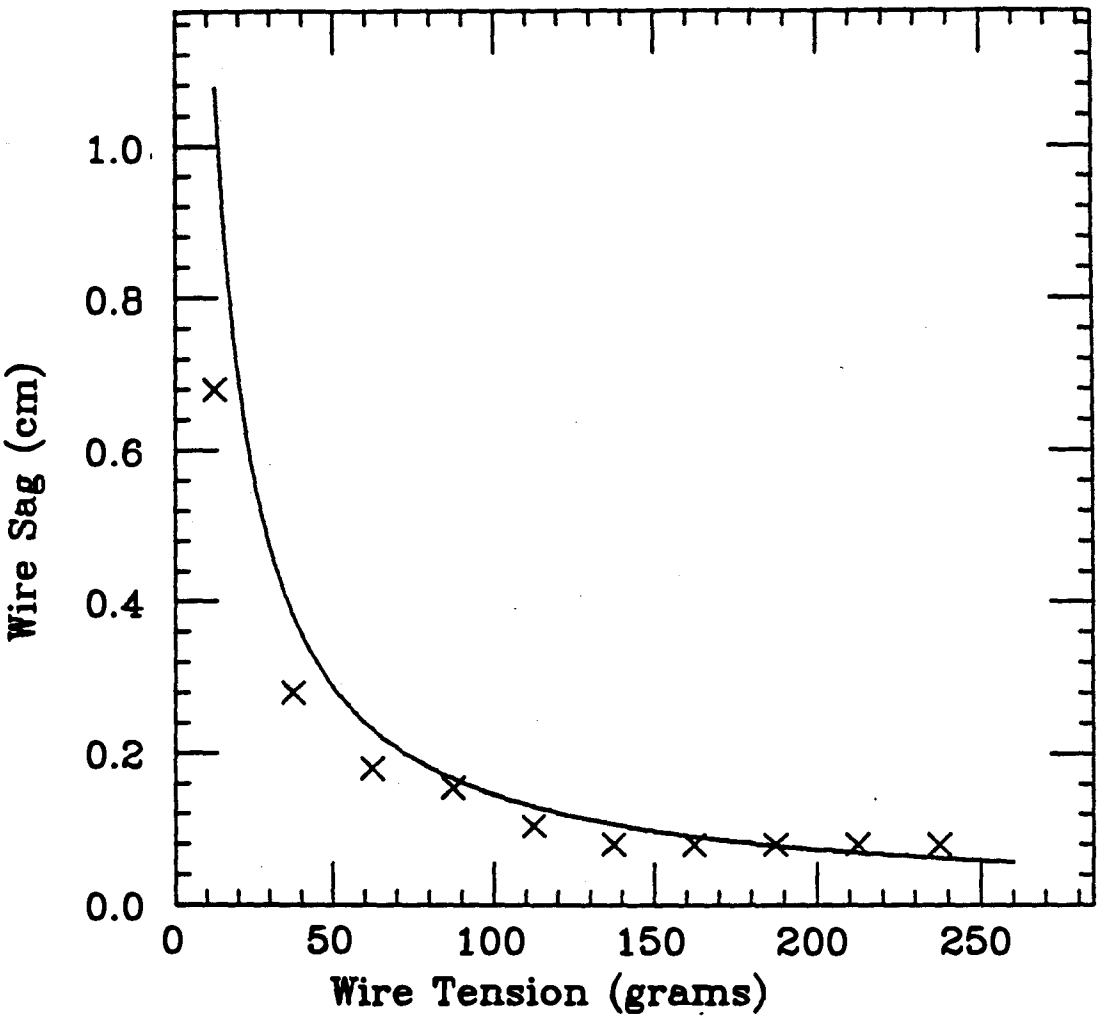

Figure 2.3: The measured and calculated wire sagging effect in the center of the 550 cm length of an horizontal drift tube.

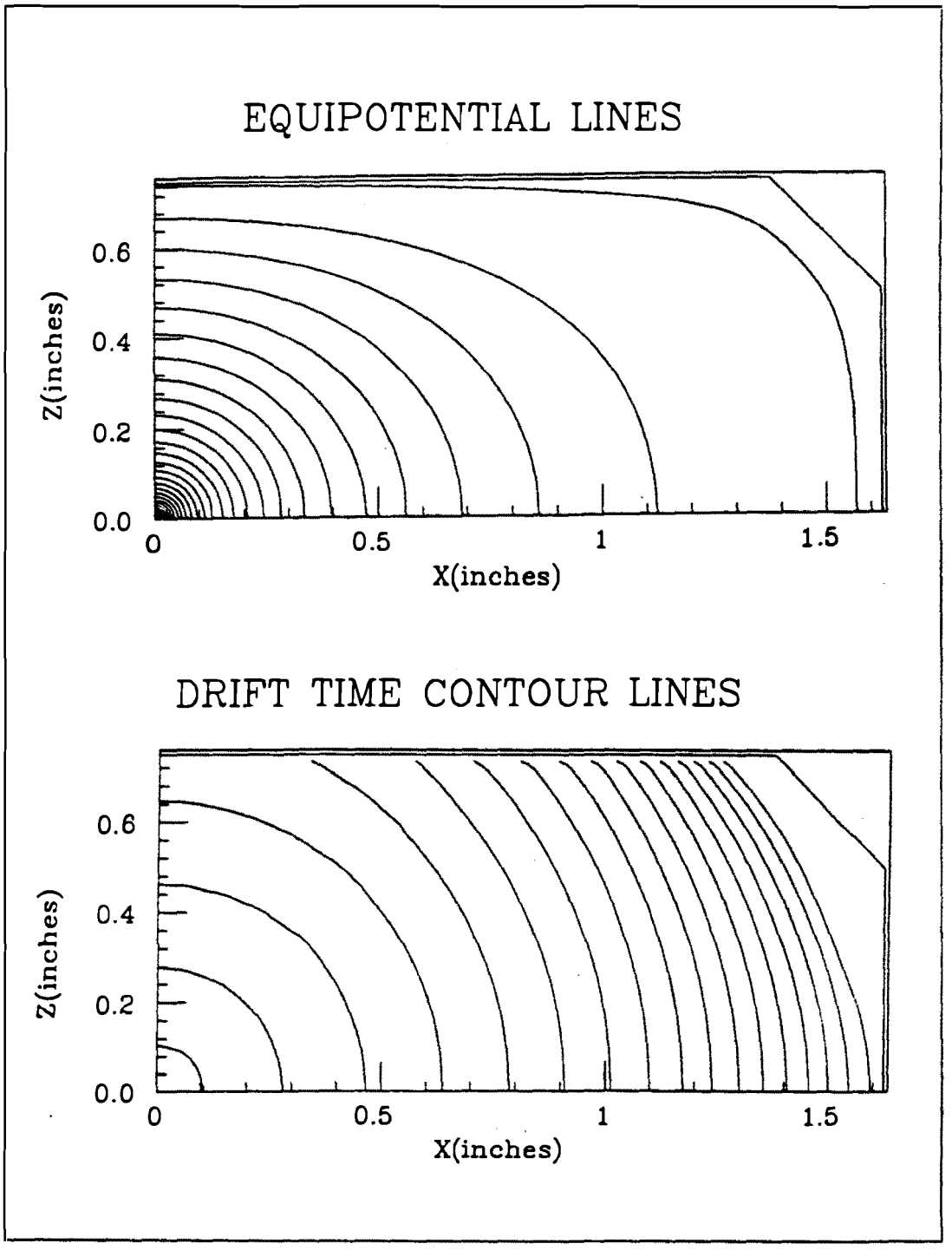

Figure 2.4: The drift cells at the 2.25 kV operating potential. Shown are the equipotential lines calculated for the drift cell using the relaxation method and the drift time contours calculated using those equipotentials and mobility of electrons in the gas. The time contours represent 100 ns intervals.

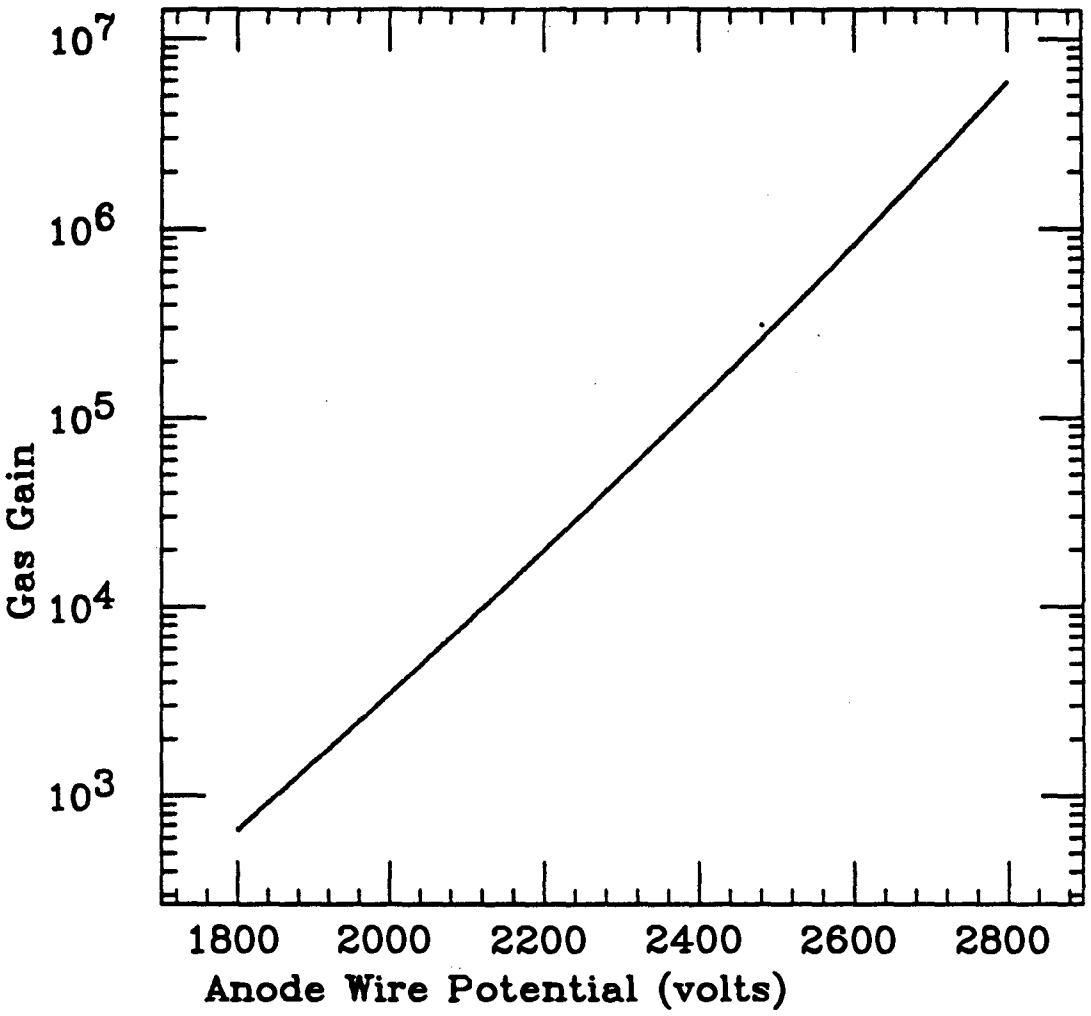

Figure 2.5: Gas gain as a function of operating voltage for the drift cells using the Ward parameterization.

where a and b are the anode and cathode radii respectively, V is the operating voltage of the anode and p is the pressure. The parameters K and ΔV are dependant only on the gas and are valid over a broad range of operating conditions with constants $K = 5.64 \times 10^4$ V/cm atm and $\Delta V = 40.3$ V. Employing parameters for the drift cells, wire radius $r = 25 \times 10^{-4}$cm, and assuming b to be the radius of an inscribed cylinder in the rectangular chamber cathode $b = 1.905$ cm, the gas gain can be calculated. Gas gain as a function of operating voltage is plotted in Figure 2.5. The nominal operating voltage of 2.25 kV therefore provides a gas gain of about 2×10^4.

A rough estimate of the signal parameters expected from the drift chamber and electronics system can be calculated for a minimum ionizing particle. Assuming the energy loss of 1.3 KeV/cm for Argon[8] at S.T.P. and the fact that the ionization energy for Argon is 26.4 eV[9] about 50 ion pairs per centimeter are produced. Thus, for a particle traversing the 3.8 cm thickness of the cell, 190 ion pairs are produced. Using the known and calculated gains of the system (gas gain (GG) $=2 \times 10^4$, preamp gain (PG)$=2 \times 10^2$ across 100 Ω, flash shaper gain (SG)=5, and flasher input of 2 Volts full scale for 63 flash encoder counts) the signal peak area response was calculated. This response, PA, was typically

$$PA = \frac{190 \text{ pairs } 1.6 \times 10^{-19} \text{ Coulomb/pair } 2 \times 10^4 \text{ (GG) } 2 \times 10^4 \text{ (PG) } 5 \text{ (SG)}}{22.4 \text{ nsec/flash tick } 2/63 \text{ Volts/flash count}}$$

$$= 85 \text{ flash units.}$$

This agrees well with the pulse areas measured for minimum ionizing muons.

2.2. Concrete Absorber and Target

The concrete absorber was chosen for many reasons among them were its composition of medium Z materials, the strength when molded in thin slabs, and its low cost. Shown in Table 2.2 is the composition of the concrete absorber, the average Z is about 10, with CaO being the largest component, and the average density is 2.3 g/cm^3. This atomic number was chosen to provide a reasonable radiation length to mass ratio. The radiation length is approximated to about 1% by[10]

$$\frac{1}{L_{rad}} = \frac{4N_A Z^2 r_e}{137A}\left(ln\frac{183}{Z^{1/3}}\right), \tag{2.4}$$

with N_A the Avagadro number, and r_e the classical electron radius. The radiation length per target mass goes approximately like $1/Z^2$. Hence, the Z chosen, while

Compound	%	Z Average	A Average	Density g/cm^3
CaO	36.5	14.0	28.03	3.3
SiO_2	13.8	10.0	20.03	2.6
MgO	6.3	10.0	20.16	3.6
CO_2	27.1	7.3	14.67	1.6
other	16.3	10.0	20.0	2.3
Average concrete values		10.73	21.5	2.31

Table 2.2: Principle components of the concrete absorber.

providing only a moderate number of nucleon targets, is a compromise which allows good shower development and electron energy resolution. Slabs of the concrete were strapped to the drift tubes as they were installed in the detector providing an efficient means of mounting.

2.3. Scintillation Counter Planes

Component	λ_{max} absorptance	λ_{max} emission	Attenuation	Refractive index	Pulse width	Rise time	Decay time
PS10 Scintillator	–	415 nm	100-200 cm (geometry dependant)	1.49	7.0 ns	1.1 ns	3.9 ns
Poly WLS Wavelength Shifter (BBQ)	400 nm	490 nm	300 cm	1.49	–	–	20 ns

Table 2.3: Characteristics for Polycast acrylic plastic scintillator and BBQ waveshifter.

Scintillator plates were installed every 10 planes of drift tubes to provide track timing. Each scintillator plane was constructed of two halves each containing four sections of acrylic plastic 254 cm x 127 cm x 2.54 cm thick with highly polished edges, and specifications shown in Table 2.3. BBQ wave shifter bars, specifications

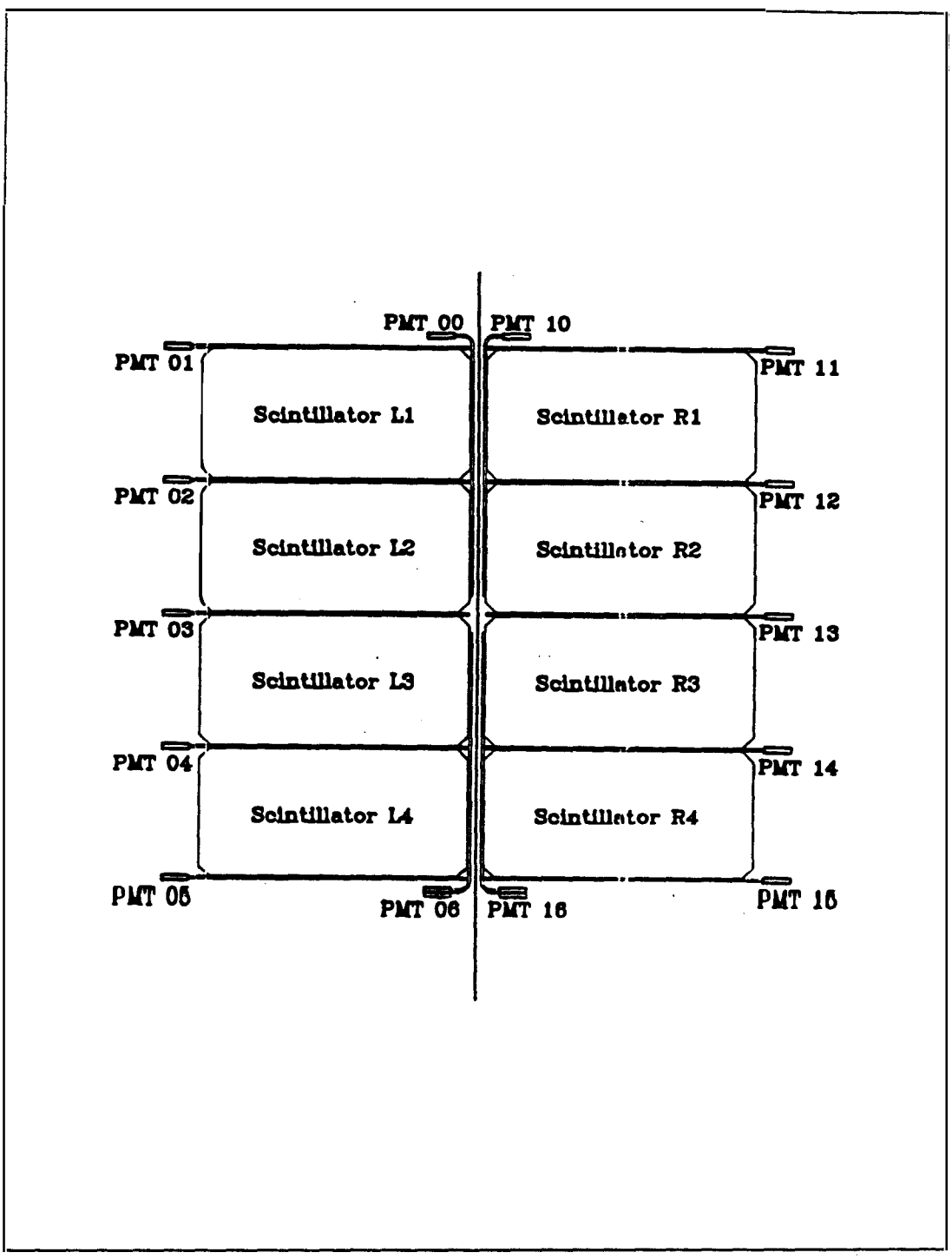

Figure 2.6: Details of the construction of the scintillation counter planes.

also shown in Table 2.3, surrounded each section of acrylic on three sides directing light to seven phototubes for each half plane. Details of the construction are shown in Figure 2.6. The complete acrylic-waveshifter package was wrapped in light tight plastic sheeting and assembled in an aluminum housing sealed at each joint with a light tight caulking compound. The thickness of the aluminum housing was chosen such that it, with the scintillator inside, represented the same amount of material per plane as one plane of concrete absorber which it replaced.

Each scintillator plane was tested for efficiency and light leaks before its installation. The efficiency tests were done with cosmic rays and demonstrated that the wave shifter bars on the long sides of the scintillator channel collect an average of about seven photo-electrons for each minimum ionizing particle which passed through the plate. For the short side wave shifter bar about four photo-electrons were observed. Timing resolution of 12 ns was measured. The efficiencies for the scintillator planes were measured to be 98% for good phototubes with optimum settings of high voltage and threshold. Each half plane was installed in the detector, hanging it from the steel support structure, and light leaks were detected and sealed.

2.4. Toroid Muon Spectrometer

The downstream end of the detector consisted of a toroidal magnetic spectrometer. In this section there were five planes of magnetized steel, the first three 12.7 cm thick and the last two 17.8 cm thick. Between each of these steel slabs one set of X and Y PDT planes were installed for position tracking. At the upstream beginning of the toroids, one UV PDT plane pair was installed for precise, unambiguous measurement of the toroid entry parameters for tracks leaving the electron detector. Three additional XY plane pairs were positioned at the downstream end of the toroids for measuring tracks penetrating all 5 planes of steel and exiting the back. These provided a large lever arm as they were placed 53 cm behind the downstream steel plate. The same extruded aluminum modules employed in the electron shower detector were used in the toroids with the lengths adjusted to fit the toroid shape and accommodate the hole, where necessary, in the center through which the current windings passed.

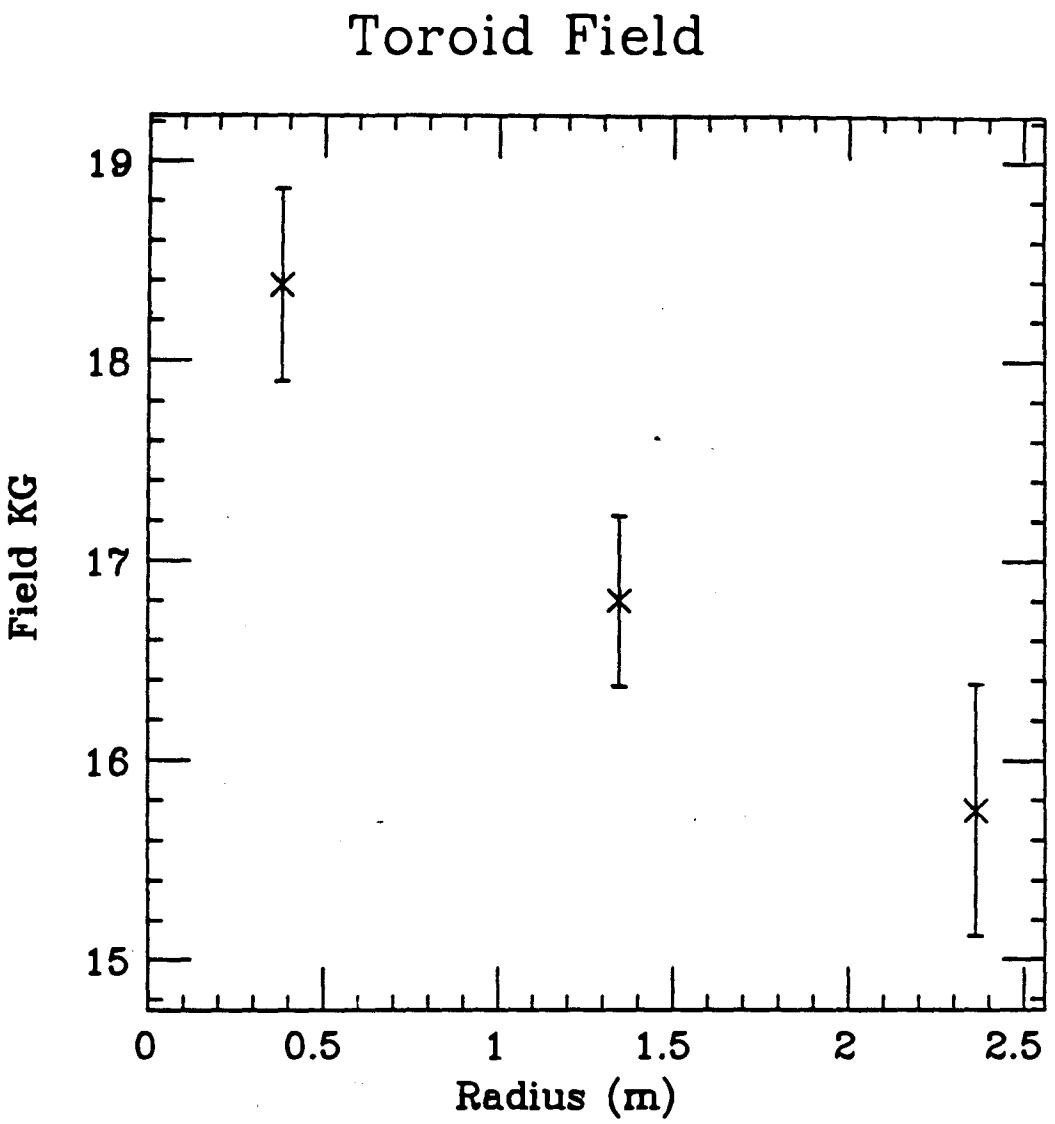

Figure 2.7: Average values and measurement errors for the toroidal magnetic field.

The 20 and 30 ton octagonal steel slabs were magnetized with four 15 kA current windings providing a total field strength of about 18 kG. This field was measured at radial positions of 38 cm, 134.6 cm and 236.2 cm by integrating the voltages produced by test coils wound through holes in the toroid steel. As the current in the toroid winding was increased the dV/dt was integrated and the field calculated. Details of the measurement are discussed in Appendix C. Average values for field measurements are shown in Figure 2.7.

2.5. Gas and Gas Distribution System

Gas flowed through the PDTs utilizing the system shown schematically in Figure 2.8. Each section of the detector was provided with a separate distribution and the flow was daisy-chained through each X-Y plane pair entering at plane-X wire-0 and exiting at plane-Y wire-0. Flow rates through each plane were monitored with flow meters and maintained at 60-100 cc/minute. This flow rate represented a complete detector volume change approximately every 4 days. With the leak-tight construction of the detector this provided more than adequate protection against gas contamination which might have caused low chamber efficiencies.

The gas mixture, 80% Ar and 20% C_2H_6, was purchased in 300 cubic foot bottles and each was tested before being entered into the system. The test consisted of collecting charge distributions from an Fe^{55} source at positions 1 cm and 4 cm from the sense wire of a small test chamber with the same cross section as that of the detector PDTs. When the charge accumulated at the 4 cm position was less than 75% that accumulated at the 1 cm position the gas was considered contaminated and not used. Tests indicated that this level of contamination was greater than 400 ppm of O_2.

2.6. Electronic Readout System

Signals were readout and digitized from 3 major detector sources: (1) electron detector PDTs, (2) toroid PDTs, and (3) scintillator PMTs. Electron detector signals passed from the PDT wire through current amplifying preamps and were then sent push-pull to flash encoding ADCs (FADCs). Toroid detector signals passed from the PDT wire through current amplifying preamps with fast time response, then were sent push-pull to TDCs. Responses from the scintillation counter phototube

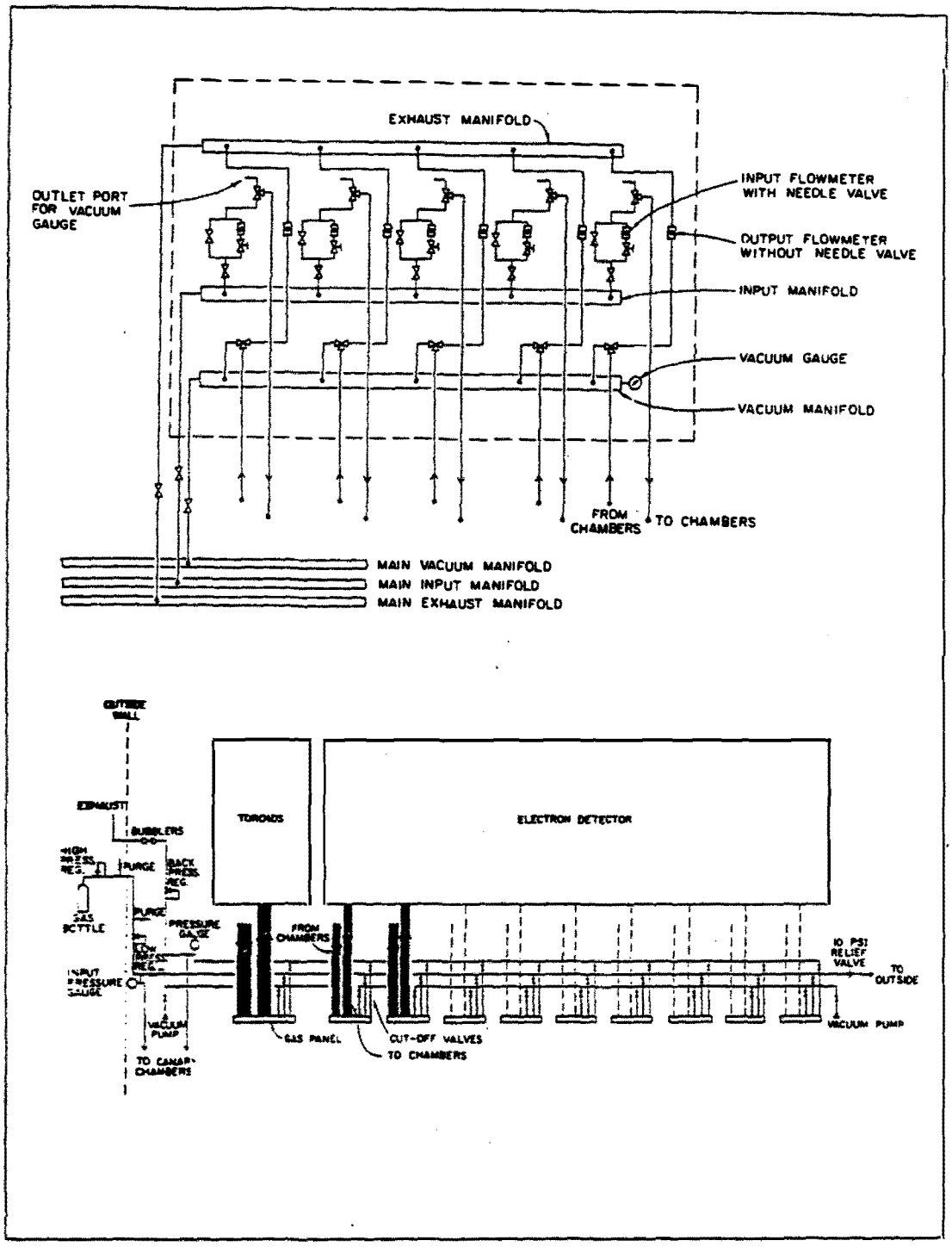

Figure 2.8: Details of the gas distribution system.

bases were directed to signal shapers where stretched/amplified pulses and timing pulses were generated. The stretched signals were sent push-pull to FADCs and the timing pulses were transported to 5.6 ns TDCs.

2.6.1. Signal Transport and Digitization

An overview of the electron detector signal transport and digitization is represented in Figure 2.9. The signal passed through a 750 pf DC blocking capacitor to the preamp. The preamp was a current amplifier, with gain 2×10^2, input impedance of 300Ω, and 100Ω differential output. Twisted pair ribbon cables transmitted this output to a receiver/shaper where the differential signals were recombined and further amplified by a factor of 5. The output from the shaper entered 6 bit FADCs where an A to D conversion was performed on the signal every 22.4 ns and the result stepped into static memory 256 words deep by a 44.64 MHz write clock. The data was 'frozen' in the memory by suspending the write clock at a time subsequent to the trigger. The delay between receiving the trigger and stopping of the write clock was adjusted so that the trigger occurred in channel 128 of the memory (i.e. 128 channels or $128 \times 22.4\text{nsec} = 2.88\mu\text{sec}$ after the trigger, the write clock stopped and the data was stored). The write clock was generated by the 'Trigger Source', and this clock was fanned out to all of the FADC and TDC modules. Details of the timing are shown in the diagram of Figure 2.7.

As in the electron detector the signals from the toroid detector wires passed through a 750pf DC blocking capacitor to the preamp. The preamp used on the toroid PDT chambers was that employed in the electron detector with the exception of a slight modification in the value of the coupling capacitors between the first and last stages of the amplifier; this caused the response to be faster. The differential signals were transmitted via twisted pair ribbon cables to receivers where they were recombined and discriminated against a threshold voltage of 40 mV. From the resulting logic state, a single bit was generated and clocked into the 256 bit deep static memory. The same write clock employed for the FADCs was used by these TDCs and the data was 'frozen' in the memory in the same fashion.

Scintillation counter signals from the phototube bases were transported to a special receiver through a back terminated 50 Ω coaxial cable. In the special receiver,

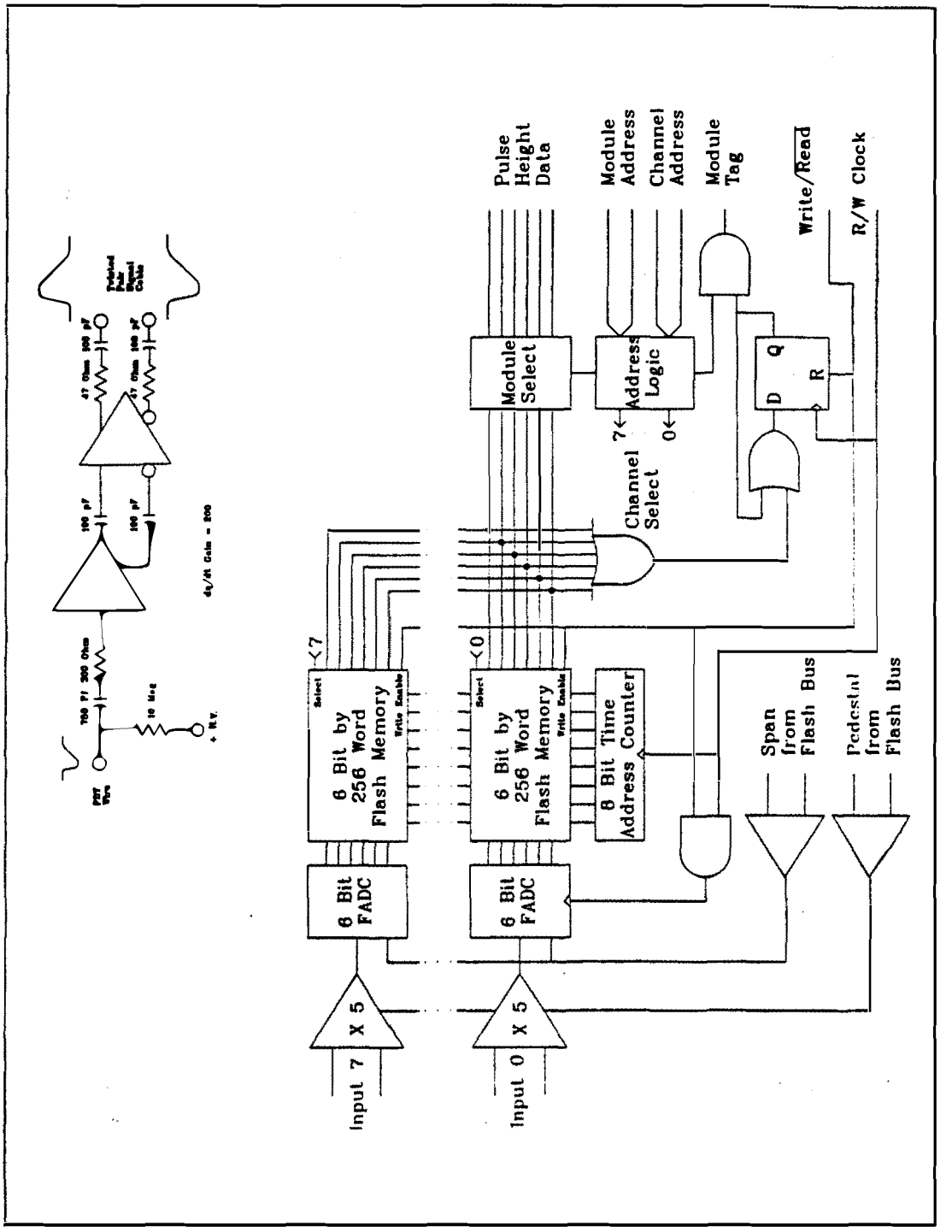

Figure 2.9: Electron detector preamp and flash ADC (FADC) electronics.

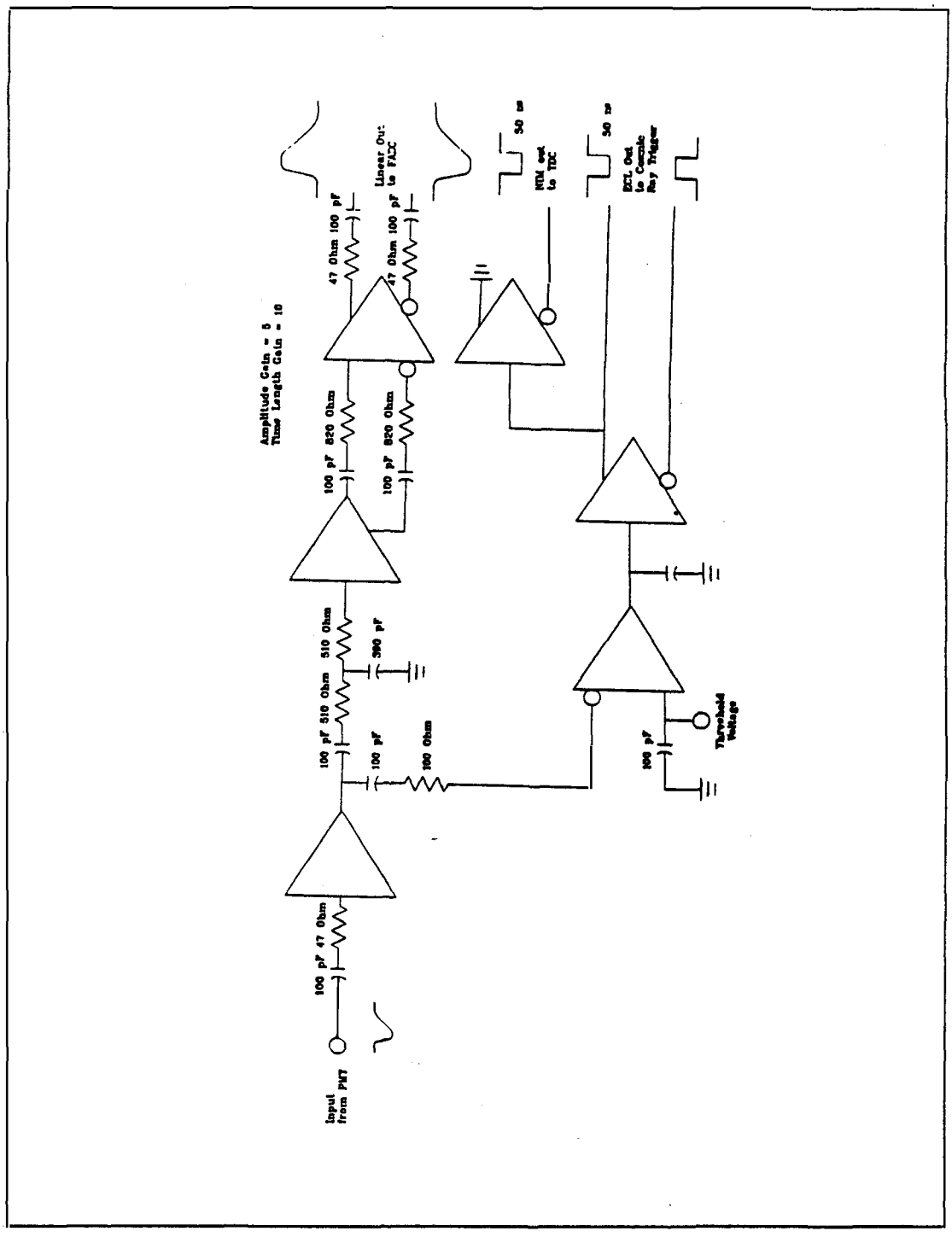

Figure 2.10: The PMT stretcher provided both prompt time and stretched/amplified signals.

two types of signals were produced. First, a shaped differential version which had been stretched in time by a factor of 10 and amplified by 5 was produced and transmitted via twisted pair ribbon cable to the flash encoders employed for the electron detector; this provided pulse shape and area. Second, a NIM timing pulse discriminated at 6 mV was generated. This NIM signal was utilized in the cosmic ray trigger, to be discussed later, and also sent to specially designed TDCs. At these TDCs the prompt NIM pulse was discriminated and stepped with 2 11.2 ns clocks 180° out of phase into two sets of static memories each 256 bits deep, thus providing 5.6 ns accuracy. Details of the PMT stretcher are shown in Figure 2.10.

The data for the PMT TDCs was stepped into their memories and stored with a technique similar to that used in the FADC and TDC channels discussed above with two important differences. First, the clock frequency which was used for these TDC channels was doubled generating a 11.2 nsec period. Second, because of the shorter period of the clock, the 256 bit memory represented only half of the 5.73 μsec duration of the FADC and toroid TDC gate length. Of these special TDCs, one card (16 channels) was devoted to the timing signals which were received from the three Cerenkov detectors located in the pion decay tunnel (discussed in Chapter 3). Because these signals arrived in the last half of the FADC gate, the clock was derived from the regular FADC clock. For the TDCs used to record the PMT times a special clock was required which stopped immediately when the trigger was received, there by capturing the first half of the flash gate. It was necessary to delay the stop by 100 nsec to include all 12 buckets of the 2.5 μsec beam spill (see Figure 2.13).

2.6.2. Data Readout

Each FADC or TDC card was plugged into a FADC or TDC bus (crate) which was terminated on one end by a 'control link' and on the other end by a 'data link'. The purpose of the control link in the FADC crates was to control the state of the crate (e.g. on/off, test), set up particular test addresses in the crate which could be read out, and to establish the levels for the span and pedestal of the FADC cards in that crate (see Figure 2.11). The special control cards for the TDC crates controlled the state of the crate, set up test addresses, and established a threshold for the crate. All of the control links were daisy chained together and each of the

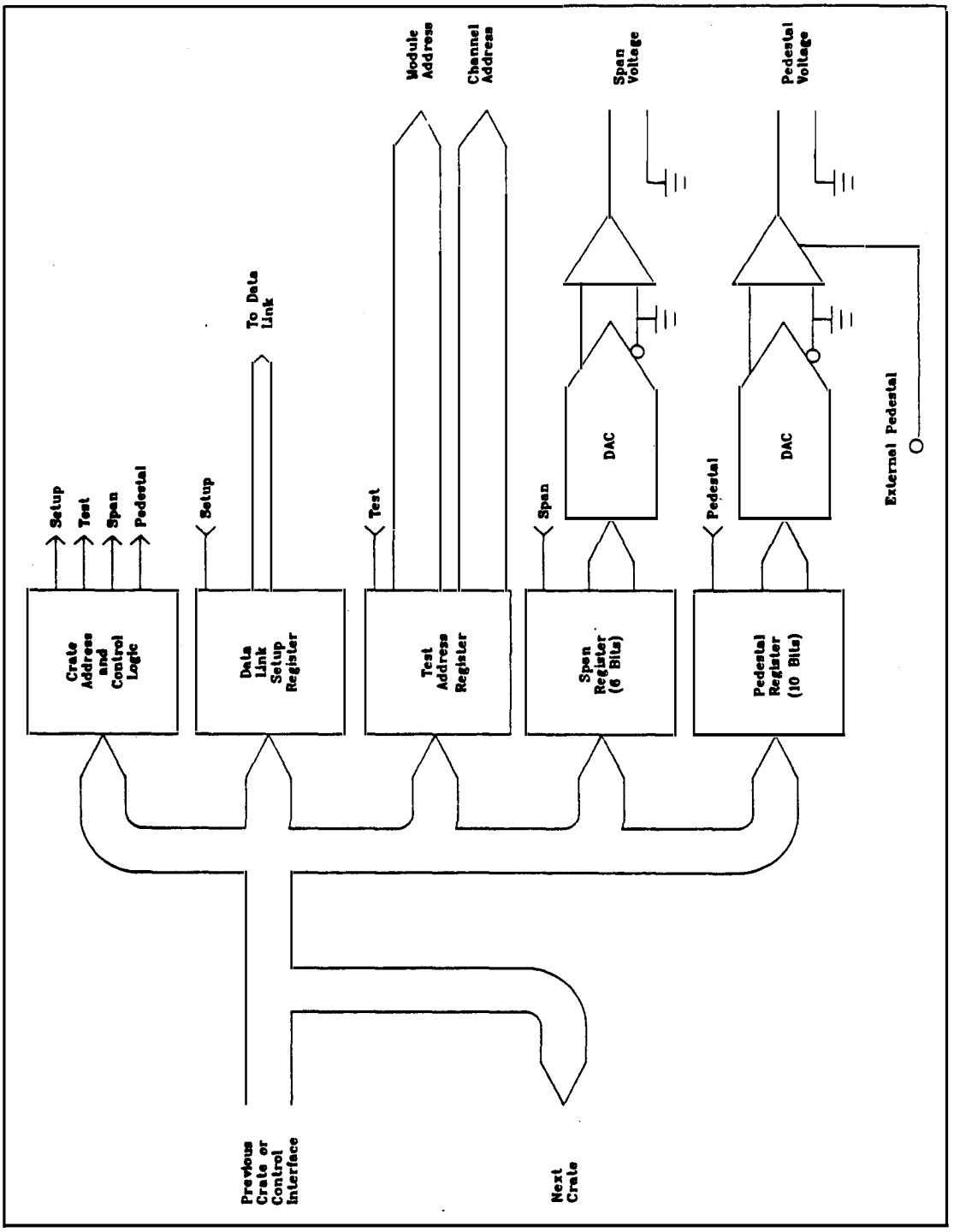

Figure 2.11: Flow diagram of the flash control link.

23 flash and 2 TDC crates could be setup in a particular configuration by properly addressing the control information sent through the chain.

The data links retrieved the information which had been stored in the FADC and TDC memories during the open gate period. All of the FADC data links(Figure 2.12) were chained together and the readout began when the write clock was stopped. Each data link performed several functions. First, each word in each flash card in the crate was checked, and a flag was set if the card had data. This simple procedure was done for all of the cards in the crate in parallel and avoided wasting time reading out empty flash cards. Then for each card with the data flag set, all of the channels were stepped through and each of the 256 words was read onto the bus. Finally, the data link compared each word to a switch selected minimum (always set to zero for the data runs), encoded it with the time and address, and shipped it through the chain to the acquisition computer interface. Data links for the TDCs were also daisy chained together and functioned similar to the flash data links but the words were only one bit, and only the first and last times for each series of high states was encoded and sent to the acquisition processor. Thus, from this information, a pulse length as well as a beginning time were recorded in the TDC data.

These control and data links were interfaced through a Nevis design system to an LSI11/03 computer. This online computer established the setup configurations of the control links and performed the online data aquisition from the flash and TDC data links. The data from the flash and TDC crates was also routed to an on-line PDP11/70 where several online monitoring functions were performed. A block diagram of the entire online system is shown in Figure 2.14. In addition to the data readout system discussed above, the online computer was interfaced to a standard CAMAC system. This interface fulfilled a number of control and monitoring functions as well as data acquisition requirements. The control and monitoring functions included PDT high voltage setup and monitoring in both electron and toroid detectors, Phototube high voltage setup and monitoring in the scintillators, detector temperature and pressure, and preamp power supply monitoring. The data acquired by the CAMAC included information from the pion monitor chambers, peak horn current from the horn power supply, AGS pulse number, beam intensity and AGS

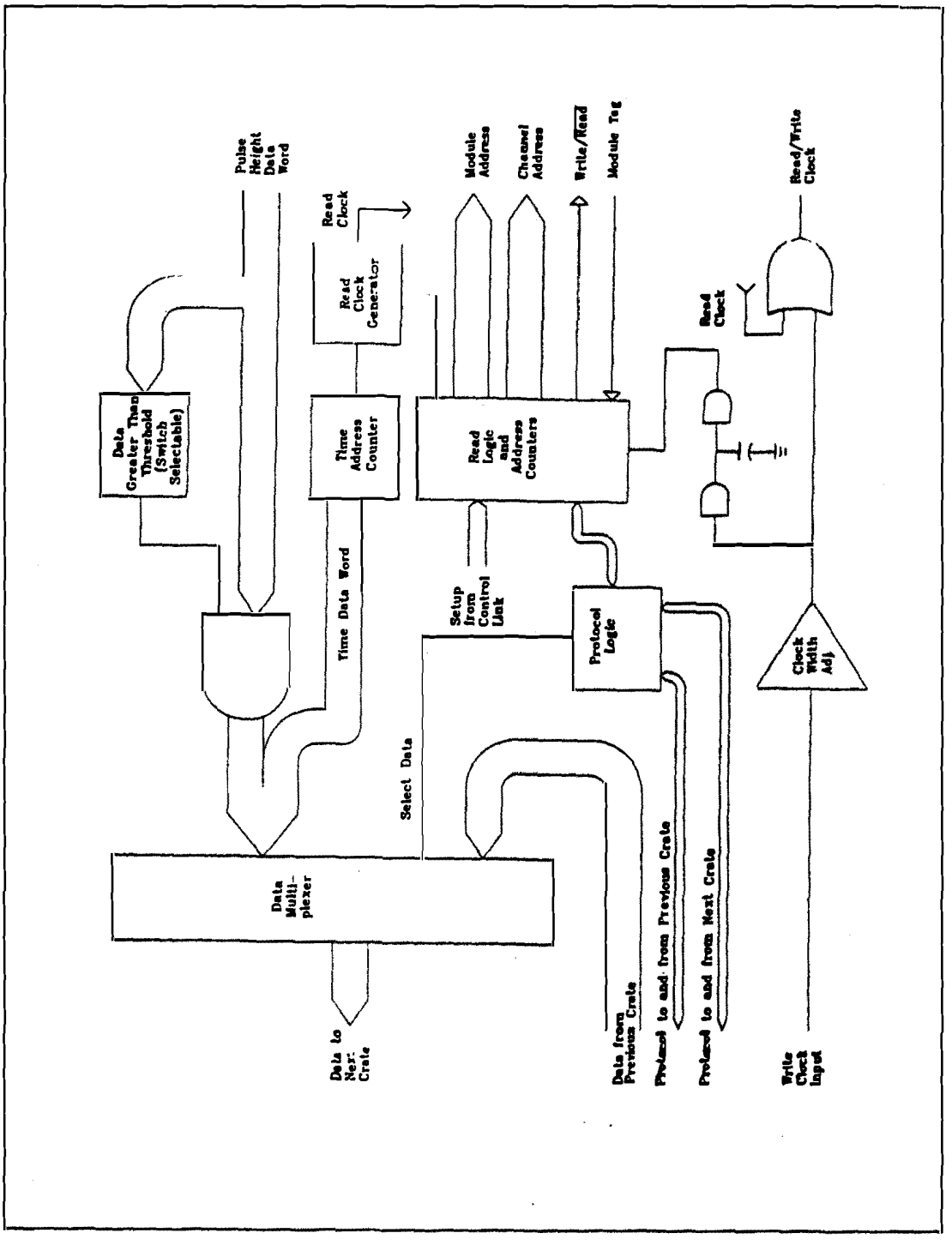

Figure 2.12: Flow diagram of the flash data link.

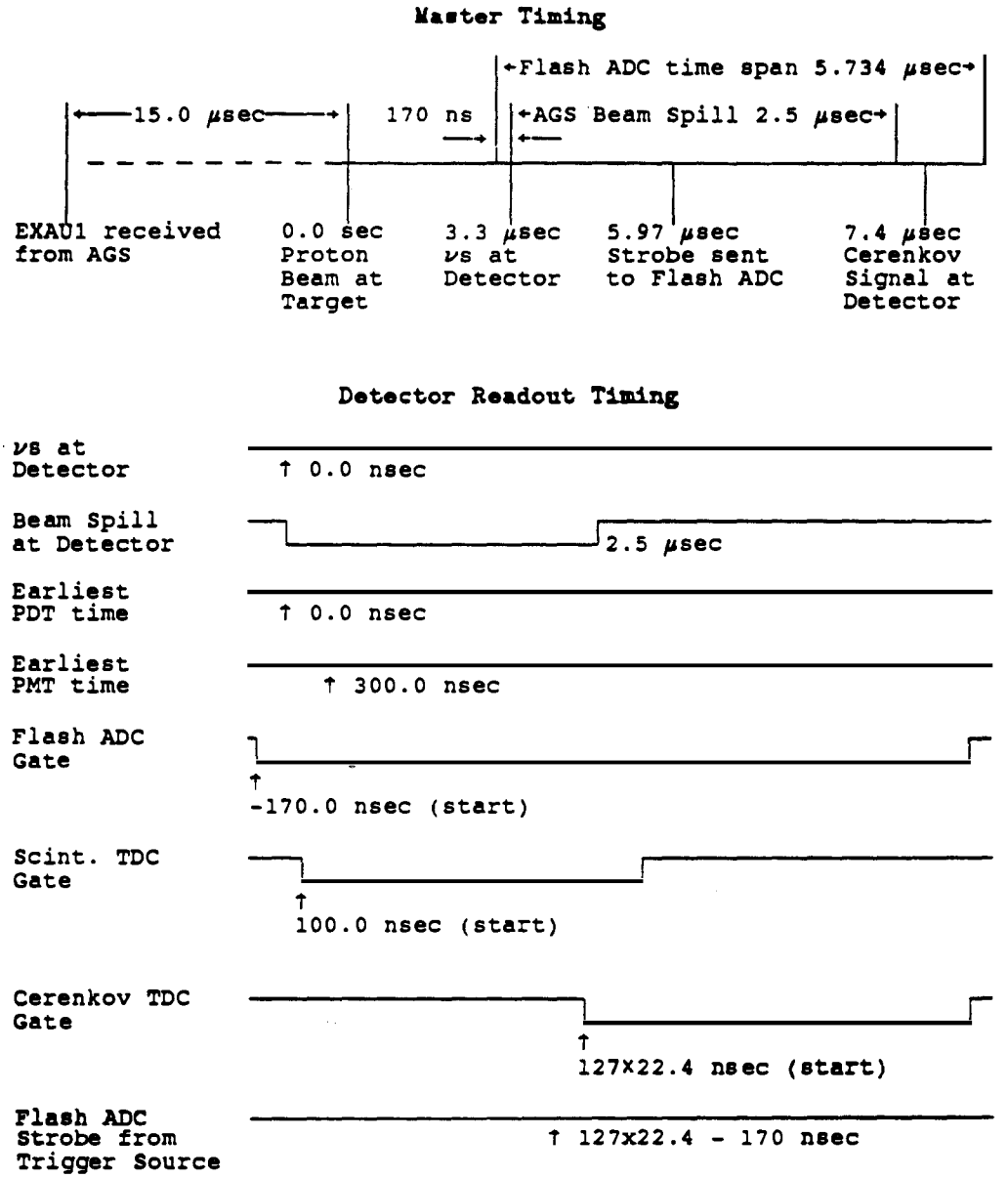

Figure 2.13: Timing diagram showing beam spill, trigger, Flash and TDC electronics timing.

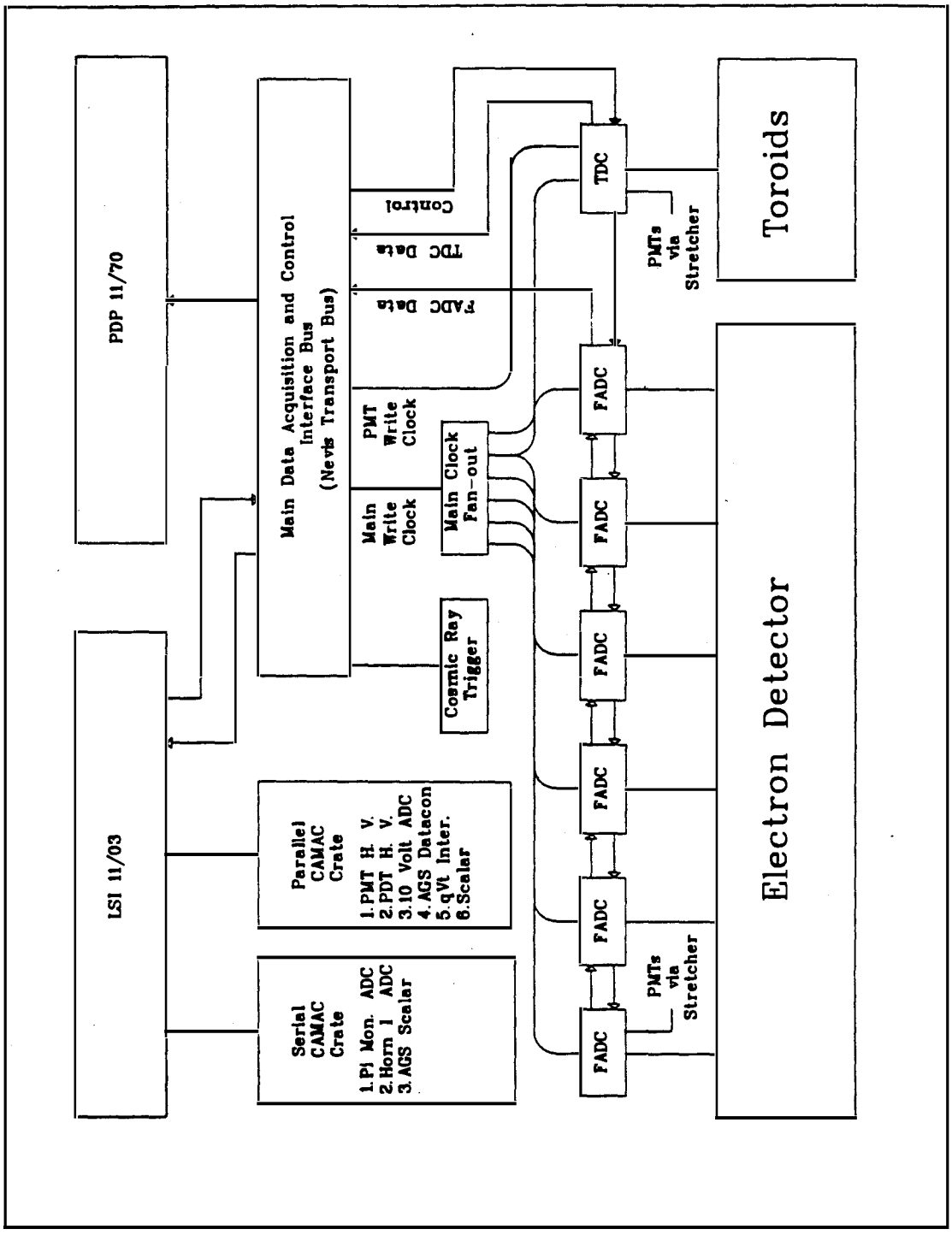

Figure 2.14: Schematic summary of the data acquisition system.

computer information over the Datacon.* The various Datacon information words which were collected in these runs are included in Appendix E.

2.7. Data Acquisition and Detector Monitoring Software

Control of the online data acquisition and some simple monitoring was performed by an online routine on the LSI11/03. The main purpose of this routine was the initial setup and data retrieval from the flash and TDC buses. This routine also read out the pion monitor, horn current, and Datacon information through CAMAC. In addition, this routine setup and monitored both PMT and PDT high voltages, monitored ±10 Volt preamp power, and constantly read in temperature and pressure conditions. It also conducted a simple check for missing planes over several events in an effort to quickly find major detector problems. A flow chart of this online program is given in Figure 2.15.

Area monitored	Description of parameters monitored
Detector noise distributions	Histogram of number of PDT hits in the first one-third of the detector for several beam pulses.
	Histogram of number of PDT hits in the middle one-third of the detector for several beam pulses.
	Histogram of number of PDT hits in the last one-third of the detector for several beam pulses.
	Histogram of number of PMT hits in the detector for several beam pulses.
Atmospheric conditions	Tempurature readings from several thermal sensors located on the detector and with the Flash electronics.
	Barometric pressure measured with an electronic transducer.

Table 2.4: Detector and detector related beam parameters monitored on-line.

An online monitor program was run on the PDP11/70. This routine had two principle elements: (1) the event display, and (2) online beam monitoring. The event display produced a picture of hits which were read out from the detector

* The Datacon is a serial dataway employed by the AGS for information transfer to and from their main computer.

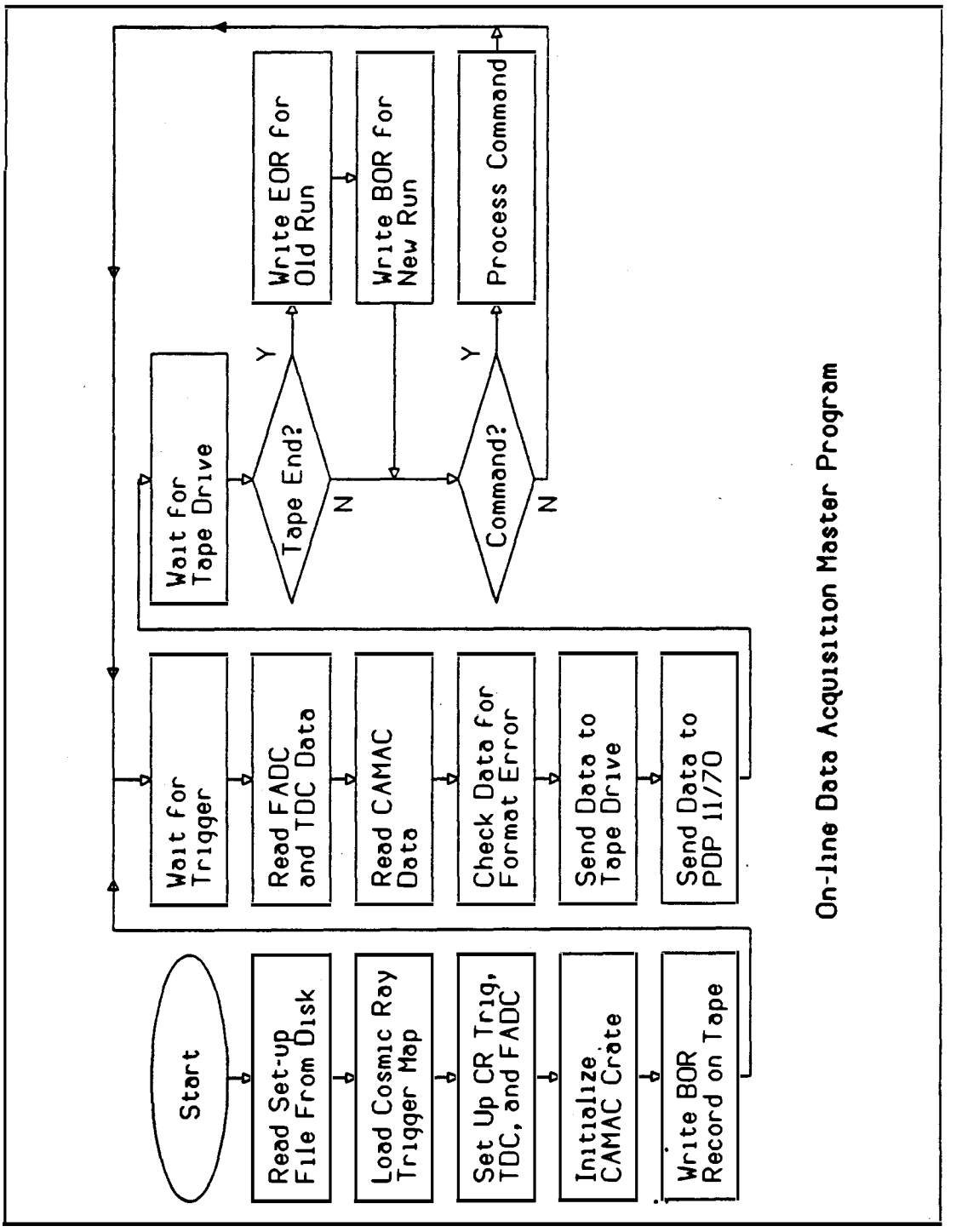

Figure 2.15: Flowchart of the online LSI11/03 data acquisition and monitoring routine.

Area monitored	Description of parameters monitored
Horn power supply	Histogram of the total horn current(all 20 capacitor modules) for several triggers.
	Histogram of charge time for horn power supply capacitor banks.
	Horn current provided by each of the 20 capacitor modules updated with each pulse.
Pion monitor	Pad 5 of pion monitor 1 normalized to beam intensity from U-716 current transformer (see Chapter 3 for details).
	Pad 6 of pion monitor 1 normalized to beam intensity from U-716 current transformer (see Chapter 3 for details).
	Profile of all pads of each pion monitor updated with each beam pulse.
U-line instrumentation	Target telescope to monitor beam targeting.
	Target temperature measured with a thermocouple.
	Beam intensity from U-716 current transformer.
	Radiation levels along U-line from U-line radiation monitors.
Cerenkov timing	Histogram for Cerenkov 1 time for several beam pulses.
	Histogram for Cerenkov 2 time for several beam pulses.
	Histogram for Cerenkov 3 time for several beam pulses.
	Histogram of the Difference between Cerenkov 1 and Cerenkov 2 times.
	Histogram of the Difference between Cerenkov 1 and Cerenkov 3 times.

Table 2.5: Beam parameters monitored on-line. Several of the items will be futher discussed in Chapter 3.

every few events. It was possible to watch either beam events and/or cosmic rays, with the latter providing useful immediate information concerning the performance of the detector. The online beam monitor provided useful information concerning AGS and U-line beam transport, horn power supply operation, beam targeting, beam timing, pion monitor profiles and noise hit distributions in the detector. A complete list of monitored parameters is given in Table 2.4 and Table 2.5. All of this

information was useful in determining if the beam quality and timing were within satisfactory limits.

The offline detector monitoring software was developed to trouble shoot and maintain the detector performance. Cosmic ray events were extracted from each data tape (approximately 2 hours of running) and various histograms were produced. The number of hits, average pulse height, average area and the standard deviation for each quantity were histogrammed for each wire in the electron detector and PMT FADC channel. For the toroids and PMT TDCs, the number of hits and the pulse duration were monitored. By examining these histograms for one or two runs each day, failures and irregularities were easily spotted and corrected.

2.8. Triggers

2.8.1. Beam and Free Triggers

In order to retain every possible event from each AGS pulse, the trigger was derived from an autodet signal sent to us from the AGS which was synchronized with the beam extraction. This pulse was delayed by the appropriate amount to position the 2.4 μsec beam spill in the first half of the 5.5 μsec gate and allow 2.5 μsec drift time for the PDTs. An additional free trigger was also taken 100 ms after each beam trigger to supply a sample of events from which the cosmic ray background could be calculated. The complete timing chart for these triggers is shown in Figure 2.16.

2.8.2. Cosmic Ray Trigger

Because we depended heavily on cosmic ray tracks for the calibration of our drift tubes, a track selection cosmic ray trigger selector was developed. In this selector the hit pattern requirements for each quadrant of each scintillator plane were loaded into a map. A loose trigger requirement was established by OR-ing all 14 phototubes in each plane and requiring that two or more planes occur in coincidence. The phototube hit pattern for the trigger was then compared with the allowed hit patterns in the cosmic ray map to determine if the correct plane and track criteria had been met. If the requirements were satisfied, the trigger was accepted and the detector read out. If the requirements were not met, the event

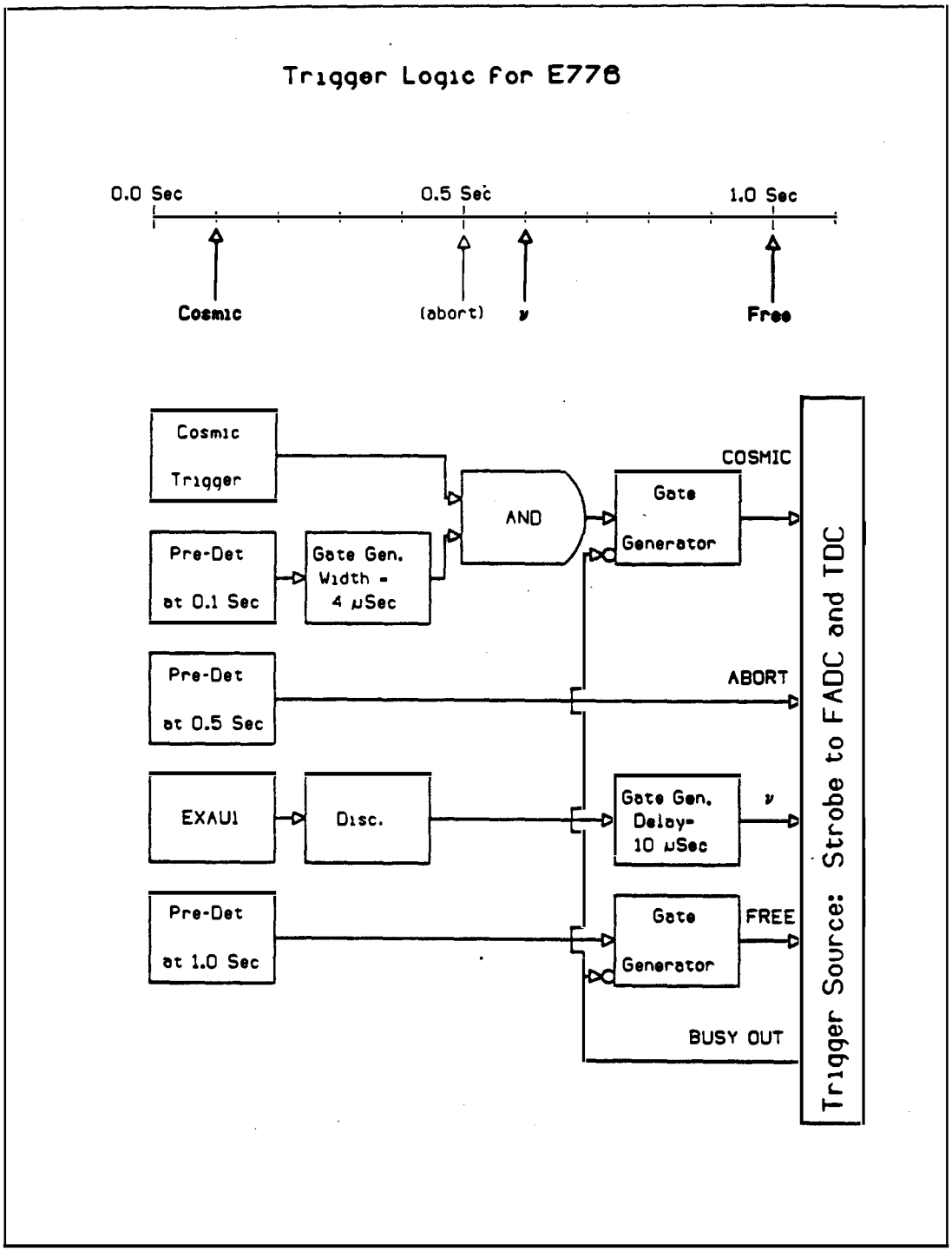

Figure 2.16: Timing diagram for beam spill and triggers.

was rejected. This trigger arrangement was capable of testing events at rates of up to 20 kHz and allowed events with special angular distributions to be saved. However, because of the coarse segmentation of the scintillator planes, especially in the horizontal direction, very select triggers with small angle distributions were not possible.

2.9. Test Detector Setup

In order to test and calibrate detector response to different particles incident at various angles, a small version of the E776 detector was built and tested in the AGS A2 test beam. This detector consisted of 40 PDT planes with concrete absorber, and 4 scintillator planes constructed with the same materials and with the same specifications as the main detector. Two pieces of 20 planes each allowed us to stagger the detector in such a manner that the 16 wire x 16 wire cross sectional dimension could be used to take test data at angles up to nearly 30 degrees with respect to the beam axis. The techniques regarding the gas and power distribution were nearly identical for the test detector and the main detector. The readout electronics for the two detectors was exactly the same for the PDT and PMT readouts. This detector is represented in Figure 2.17.

In addition to PDT and PMT information, several other beam and trigger parameters were procured with the FADCs, TDCs or CAMAC and included in the readout scheme. This information consisted of signals from two Time-Of-Flight scintillation counters, two atmospheric nitrogen Cerenkov counters, and a set of 4 veto scintillation counters. The complete configuration of these counters in the beam line is shown in Figure 2.18.

Particle identification was accomplished by using the information from the time-of-flight and Cerenkov counters. The TOF counters provided 100 ps timing resolution which enabled us to distinguish between pions and protons at the 10^{-2} level. The Cerenkov counter signals in coincidence provided a contamination to the electron sample of less than 10^{-4}. The electron beam was studied using a Pb glass block. More complete results of particular aspects of the test run are discussed in Chapter 4 where they are compared with the event Monte Carlo.

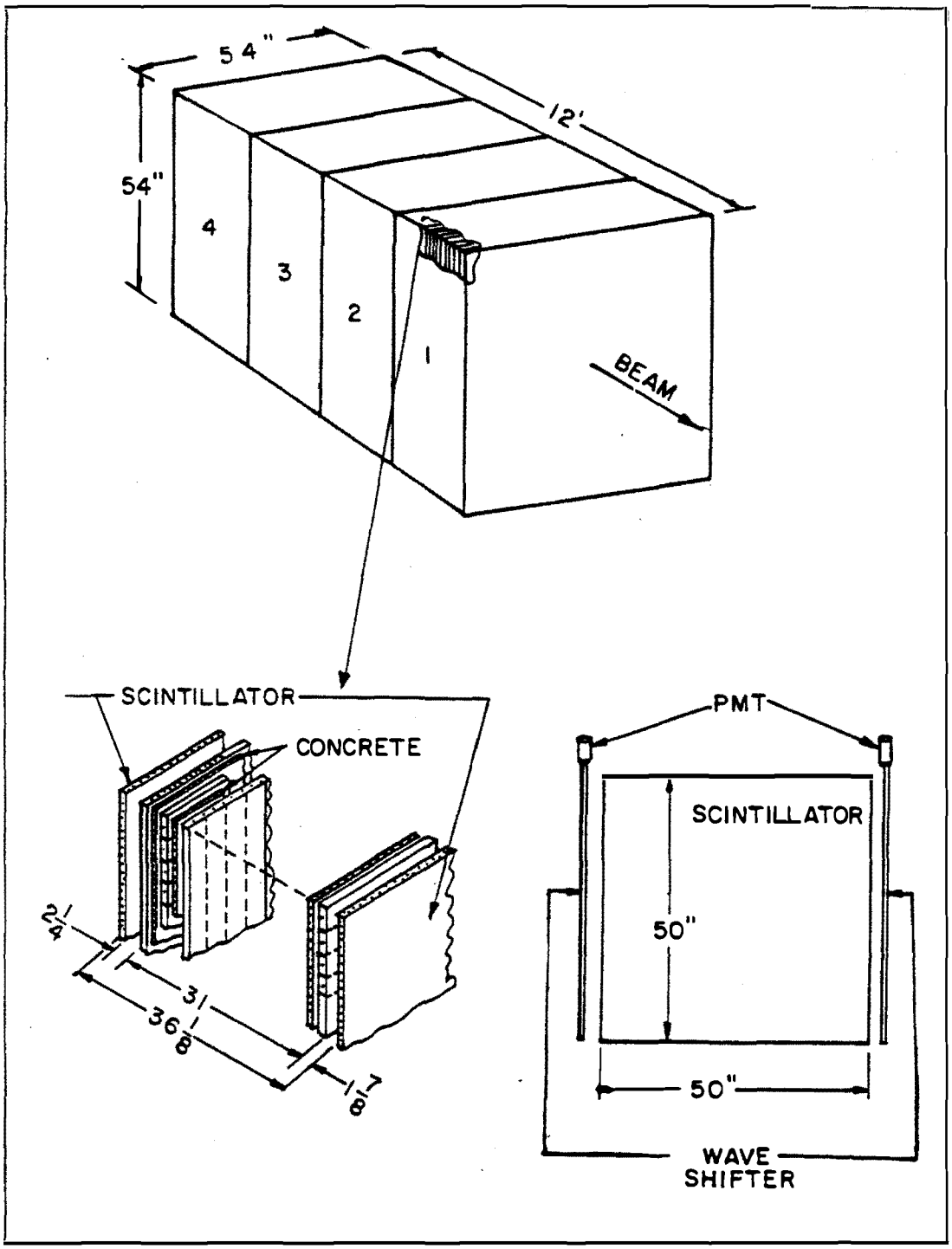

Figure 2.17: Specifications for the construction of the detector used in the BNL A2 test beam.

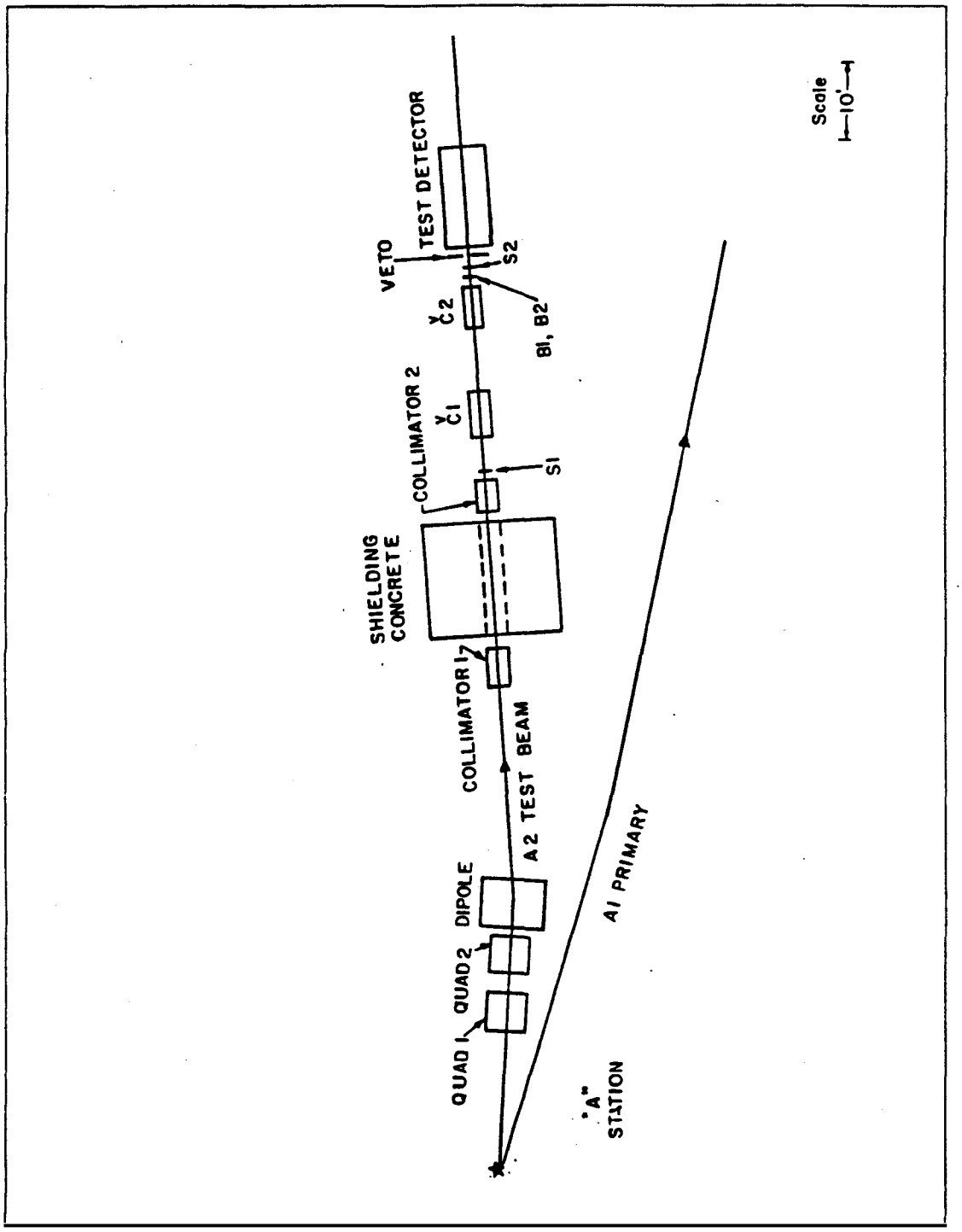

Figure 2.18: A2 test beam line elements and instrumentation.

Chapter 3.
The Neutrino Beam and Beamline

The narrow band ν_μ beam employed for the oscillation search was produced with secondary charged particles from a copper target. Protons accelerated to 28 GeV constituted the primary beam which was focused onto the copper target. Secondary particles, mostly pions and kaons, were produced in the target and entered a two horn focusing system where their momenta were selected with collimators. After exiting the horns the particles were allowed to decay in a 90 m tunnel. Muons from these decays were absorbed in iron shielding at the end of the decay tunnel to reduce the ν_e contamination.

3.1. Principle Elements

Protons were provided by the Brookhaven AGS at 28 GeV in 2.7 μs spills. Twelve approximately equal bunches of protons, 35 ns in length and separated by 224 ns, were injected into the AGS at 200 MeV. They were accelerated to 28 GeV, then extracted in a single revolution around the accelerator and transported through the neutrino line (U-line) to the target. Each spill contained from 10 to 15 $\times 10^{12}$ protons. The AGS RF structure observed in our data is shown in Figure 3.1.

The proton target was a 5 mm diameter copper cylinder 13 cm in length. Copper was used because of its absorption length, thermal conductivity, and proven durability. The nuclear absorption length of Cu is 16 cm so about 60% of the protons incident on the target interacted. The high thermal conductivity allowed the heat from the proton beam energy to be removed efficiently. Copper is known to be less susceptible to fragmentation in high intensity proton beams than other materials and this was a major motivation for its use. The target diameter was chosen to be 5 mm to match the observed horizontal stability of the proton beam, though the beam size was measured to be less than 2mm.

Particles from the target were focused with a two horn lens system. Several considerations were taken into account when designing the horn focusing system. The angular acceptance of secondary particles from the target was desired to be from 20 mr to 140 mr. A momentum of 3 GeV/c was desired with a momentum

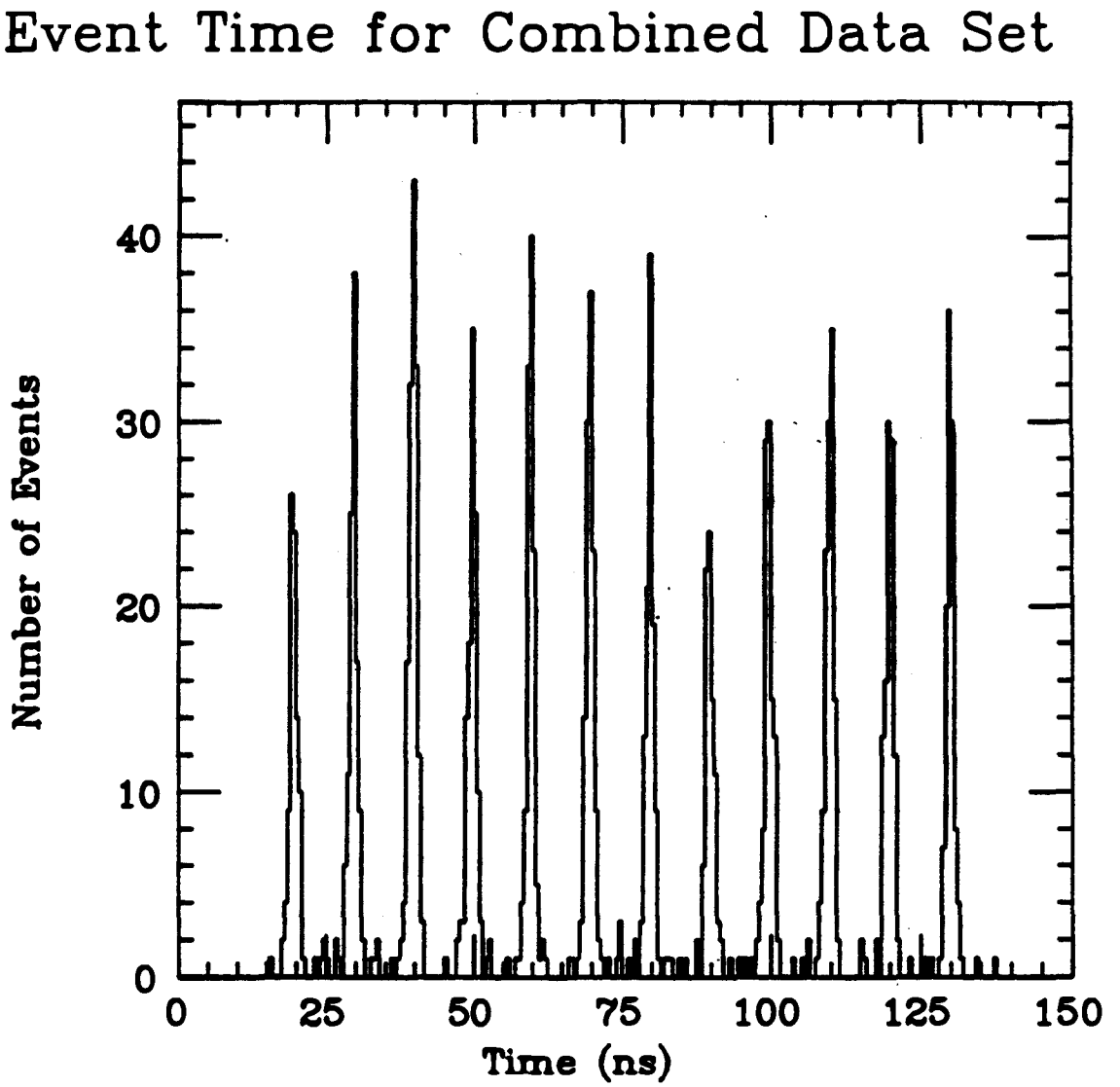

Figure 3.1: The AGS RF timing structure observed in the data.

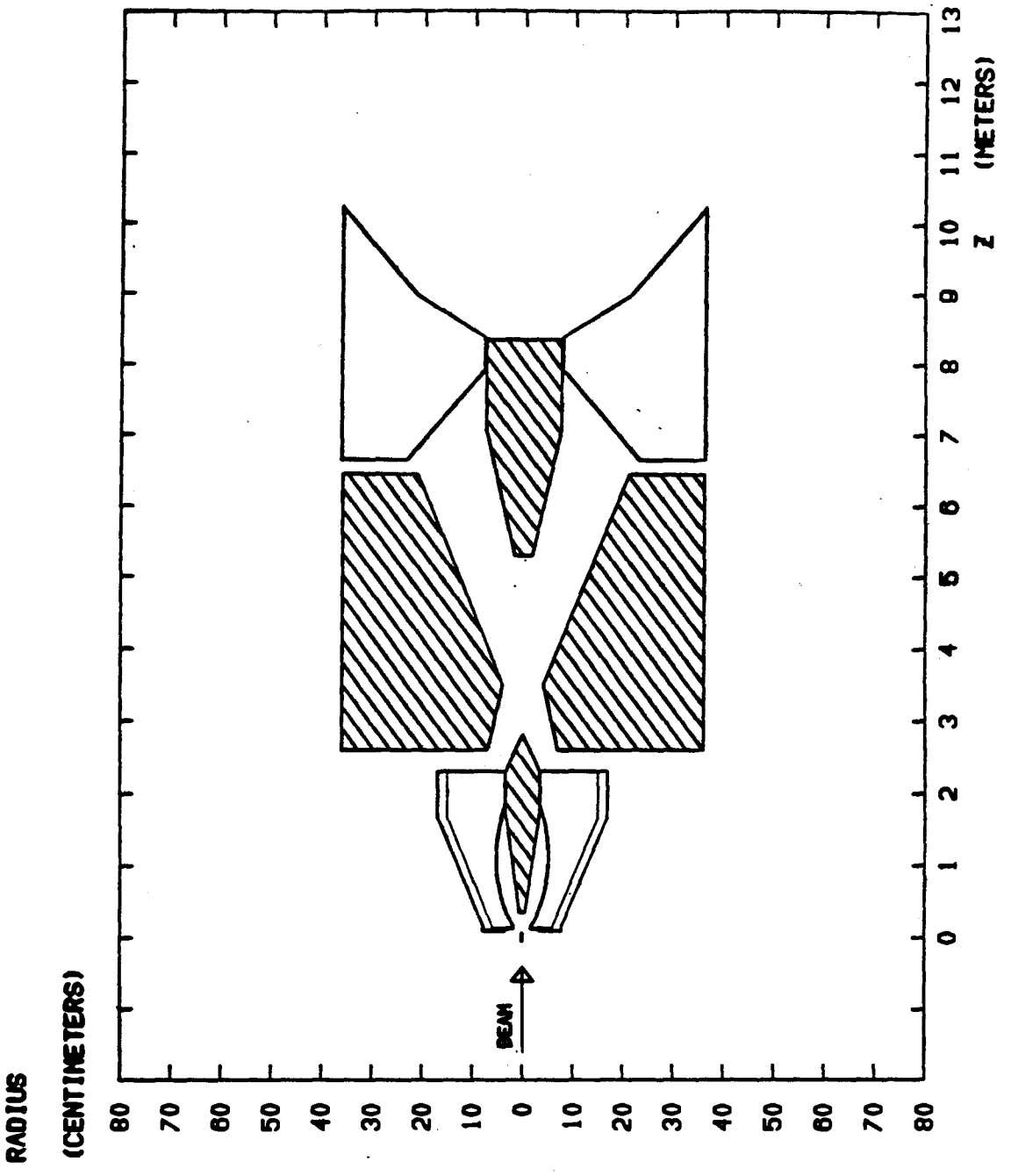

Figure 3.2: The conductors and collimators of the two horn focusing system used to produce the ν_μ beam.

bite of 10%. The angular divergence of the pion beam was required to be less than 2 mrad. With these in mind the horn system shown in Figure 3.2 was designed to operate with a current of 240 kA. This design was accomplished by calculating the magnetic surfaces and collimators required to satisfy the acceptance, momentum, and angular divergence requirements.

The decay of the πs and Ks focused by the horns was allowed in a tunnel extending to 90m from the target. This decay length provided for the decay of 50% of the π s and 95% of the Ks. The first 40m of the decay path immediately downstream from the horn was in a cylindrical helium bag which reduced beam scattering and interaction with the air. Without the helium, the pion multiple scattering would have been 1.8 mrad. Following the decay region was a 32 m filter constructed of steel and earth which removed most of the undecayed hadrons and the majority of muons. Shown in Figure 3.3 is the complete neutrino source area.

3.2. Neutrino Beam Calculation

The characteristics of the neutrino beam were studied with Monte Carlo calculation. Production of πs and Ks in the target was modeled after several parameterization models and the differences evaluated. Charged and neutral particles were tracked from the target, through the horn and collimators with multiple Coulomb scattering. The particles were then allowed to decay in the decay tunnel with appropriate dynamics. From these calculations the relative rates and energy distributions for the ν_μ and ν_e components of the beam were determined for our detector location and size. Also, the radial distribution of πs and Ks in the decay tunnel was studied.

3.2.1. Target Production

Particle production parameters for the target can be determined from empirical formulations and tables. The two sources which were used and compared are the Sanford and Wang emperical formulation[11] and the Grote, Hagedorn and Ranft tables.[12] Target production of π^+ and K^+ as a function of particle momentum for various angles is shown in Figure 3.4 for the Sanford and Wang parameterization. In order to compare the two distributions, the production for each was integrated

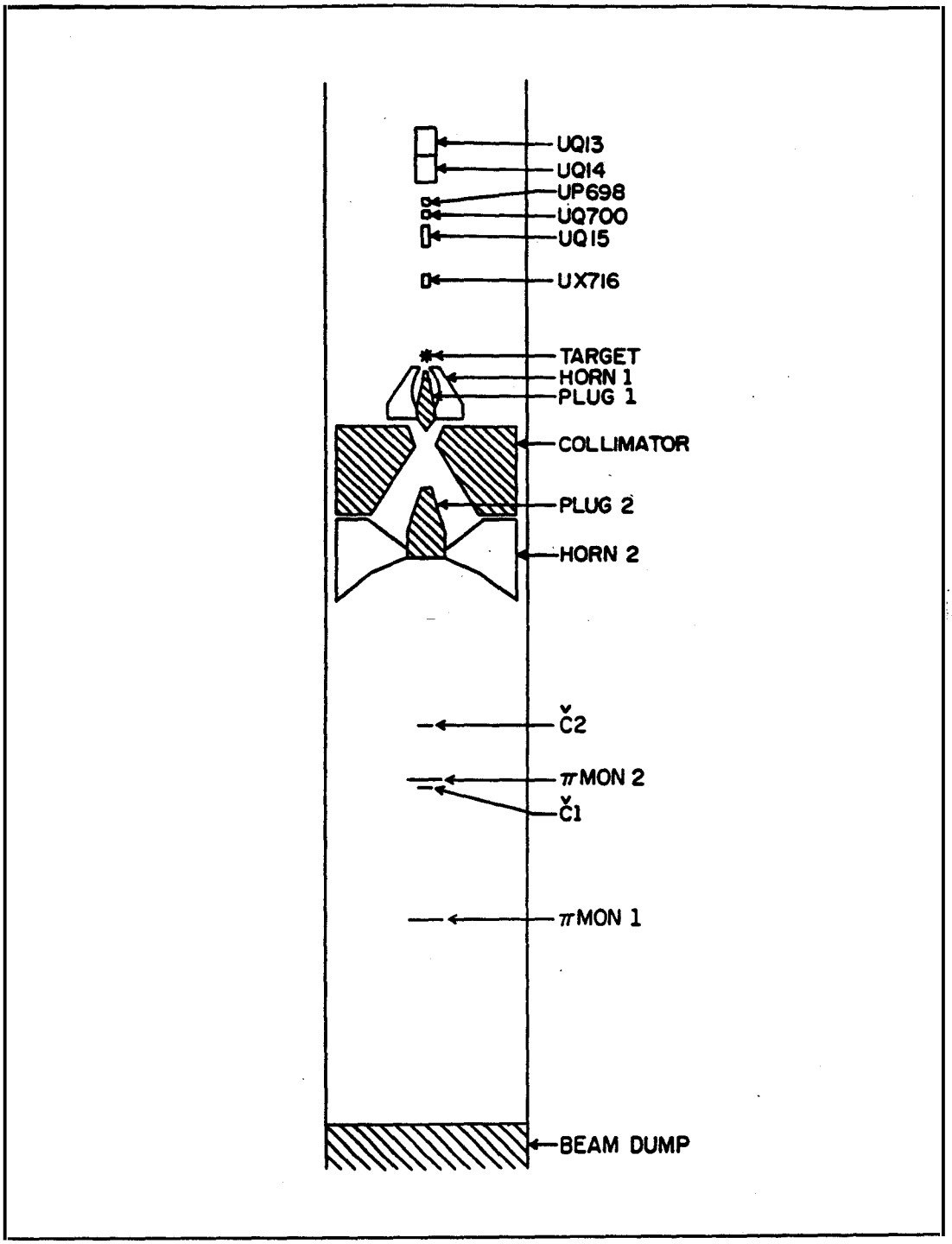

Figure 3.3: The neutrino source area including the target, dual horn system, decay tunnel and instrumentation.

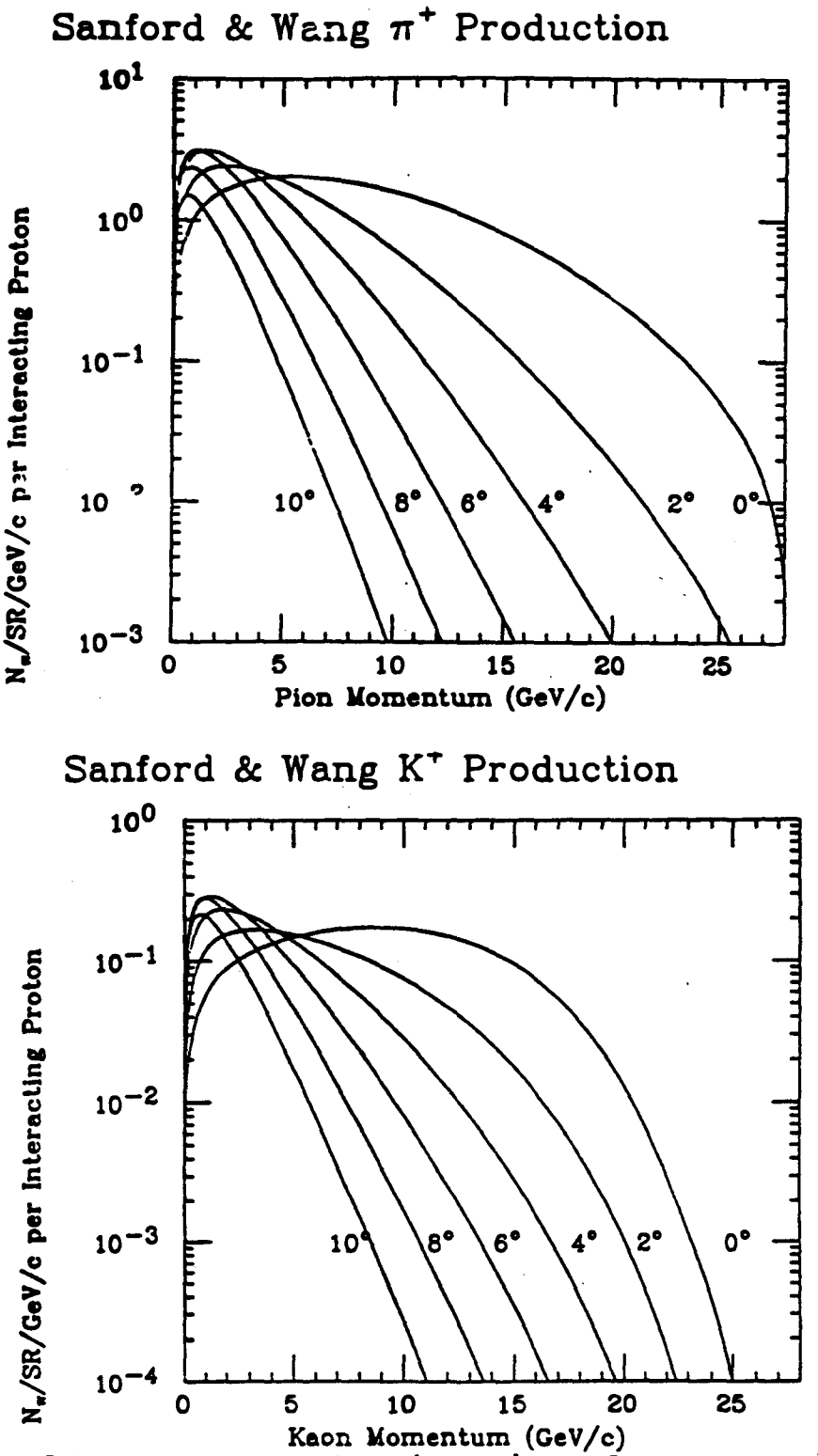

Figure 3.4: Target production for various angles as a function of secondary particle momentum for Pions and Kaons, using the Sanford and Wang formulation. The curves are parameterizations fit to data from protons on a Beryllium target.

Production	Sanford & Wang	Grote Hagedorn & Ranft
π^+	.619	.571
π^-	.473	.433
K^+	.068	.054
K^-	.020	.023
K^+/π^+	.12	.10

Table 3.1: Integrated pion and kaon production for Sanford-Wang and Grote-Hagedorn-Ranft formulas.

as in eq. 3.1.

$$\frac{N_{\pi,K}}{N_{int.p}} = \int_1^{8(GeV/c)} dp \int_{20}^{200(mrad)} 2\pi \sin\theta d\theta \frac{d^2N}{dpd\Omega}. \tag{3.1}$$

The reason for the wide limits on the momentum and angular integrations is to include the region of the production responsible for the broadband ν_μ and ν_e components of the beam. The result of this integration is shown in Table 3.1 for the π^+, π^-, K^+ and, K^- distributions. These values differ by nearly 10% for Sanford and Wang and Grote,Hagedorn and Ranft, which indicates an uncertainty in the absolute flux calculation. The values for N_{K^+}/N_{π^+} are also shown in Table 3.1 and they are observed to depend slightly on the choice of parameterization as well.

The particles produced in the target were tracked through the beamline elements. Charged particles were either focused or defocused (depending on their charge) in the magnetic field of the horn and the momenta of those focused are selected by the collimators. These two cases are demonstrated in Figure 3.5. Neutral particles are followed through the paths allowed by the physical placements of beam elements and tunnel dimensions.

3.2.2. The ν_μ and ν_e Beam Components

Particles are allowed to decay in flight with the appropriate branching ratios and dynamics. The products from these decays form the components of the ν beam. A list of the decay modes considered and their branching ratios is given in Table 3.2. Reactions 1 and 4 are the primary sources for ν_μ and give the beam its dichromatic

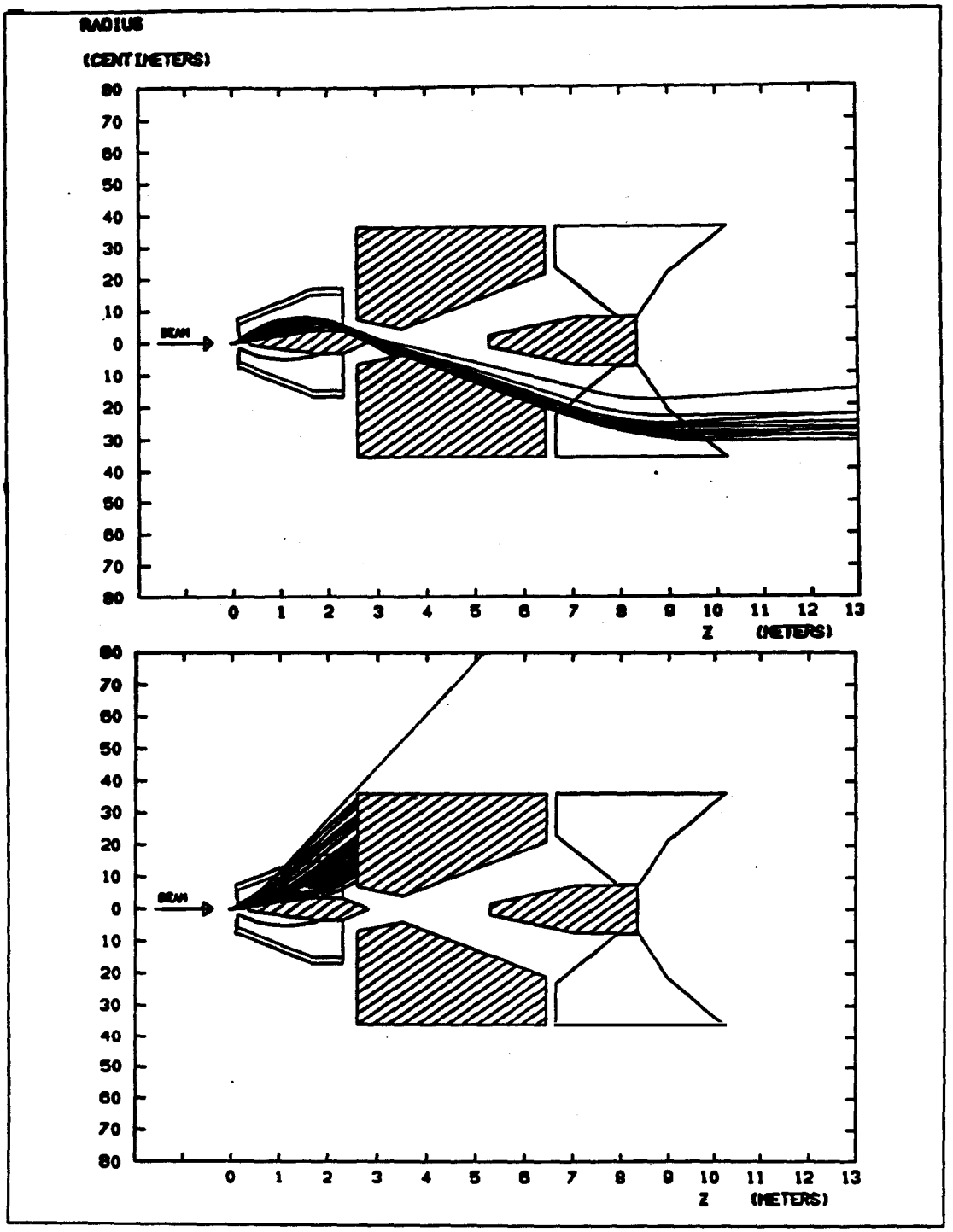

Figure 3.5: Charged particles as they are traced through the horn system are either focused (positive particles) or defocused (negative particles).

Reaction number	Decay reaction	Product	Branching ratio
1	$\pi^+ \to \mu^+\nu_\mu$	ν_μ	1.0
	$\mu^+ \to e^+\bar{\nu}_\mu\nu_e$	$\bar{\nu}_\mu, \nu_e$	1.0
2	$\pi^+ \to e^+\nu_e$	ν_e	1.2×10^{-4}
3	$K^+ \to \mu^+\nu_\mu$	ν_μ	.635
	$\mu^+ \to e^+\bar{\nu}_\mu\nu_e$	$\bar{\nu}_\mu, \nu_e$	.635
4	$K^+ \to \pi^0\mu^+\nu_\mu$	ν_μ	.03
5	$K^+ \to \pi^0 e^+\nu_e$	ν_e	.048
6	$\pi^- \to \mu^-\bar{\nu}_\mu$	$\bar{\nu}_\mu$	1.0
	$\mu^- \to e^-\nu_\mu\bar{\nu}_e$	$\nu_\mu, \bar{\nu}_e$	1.0
7	$\pi^- \to e^-\bar{\nu}_e$	$\bar{\nu}_e$	1.2×10^{-4}
8	$K^- \to \mu^-\bar{\nu}_\mu$	$\bar{\nu}_\mu$	.635
	$\mu^- \to e^-\nu_\mu\bar{\nu}_e$	$\nu_\mu, \bar{\nu}_e$	.635
9	$K^- \to \pi^0 e^-\bar{\nu}_e$	$\bar{\nu}_e$	.048
10	$K^0 \to \pi^- e^+\nu_e$	ν_e	.0968
11	$K^0 \to \pi^+ e^-\bar{\nu}_e$	$\bar{\nu}_e$	.0968

Table 3.2: Decay reactions considered in the beam Monte Carlo calculation. The K^0 decay branching ratios assume 50% K_S and 50% K_L; $\bar{K}^0$s were not considered.

character. The energy of a neutrino produced by π^+ or K^+ decay is given by eq. 3.2 as a function of angle in the laboratory frame.[13]

$$E_\nu = E_{\pi,K}\left(1 - M_\mu^2/M_{\pi,K}^2\right)/\left(1+\gamma^2\theta^2\right) \tag{3.2}$$

The result of the calculation for the ν_μ component of the beam due to πs and Ks is shown in Figure 3.6 and Figure 3.7 for the two horn currents of interest. These plots include the wideband ν_μ component also.

Most of the ν_e background in the beam was produced by reactions 1, 2, 5 and 10 of Table 3.2. The major source arises with the decay of muons which originate from decaying πs and Ks. The most naive calculation gives this at the 2×10^{-3} level. However, by including the helicity of the muon an additional multiplicative term of $(1+\cos\theta_\nu)$ increases this level to about .5%. The tracking and decay of K^0, source

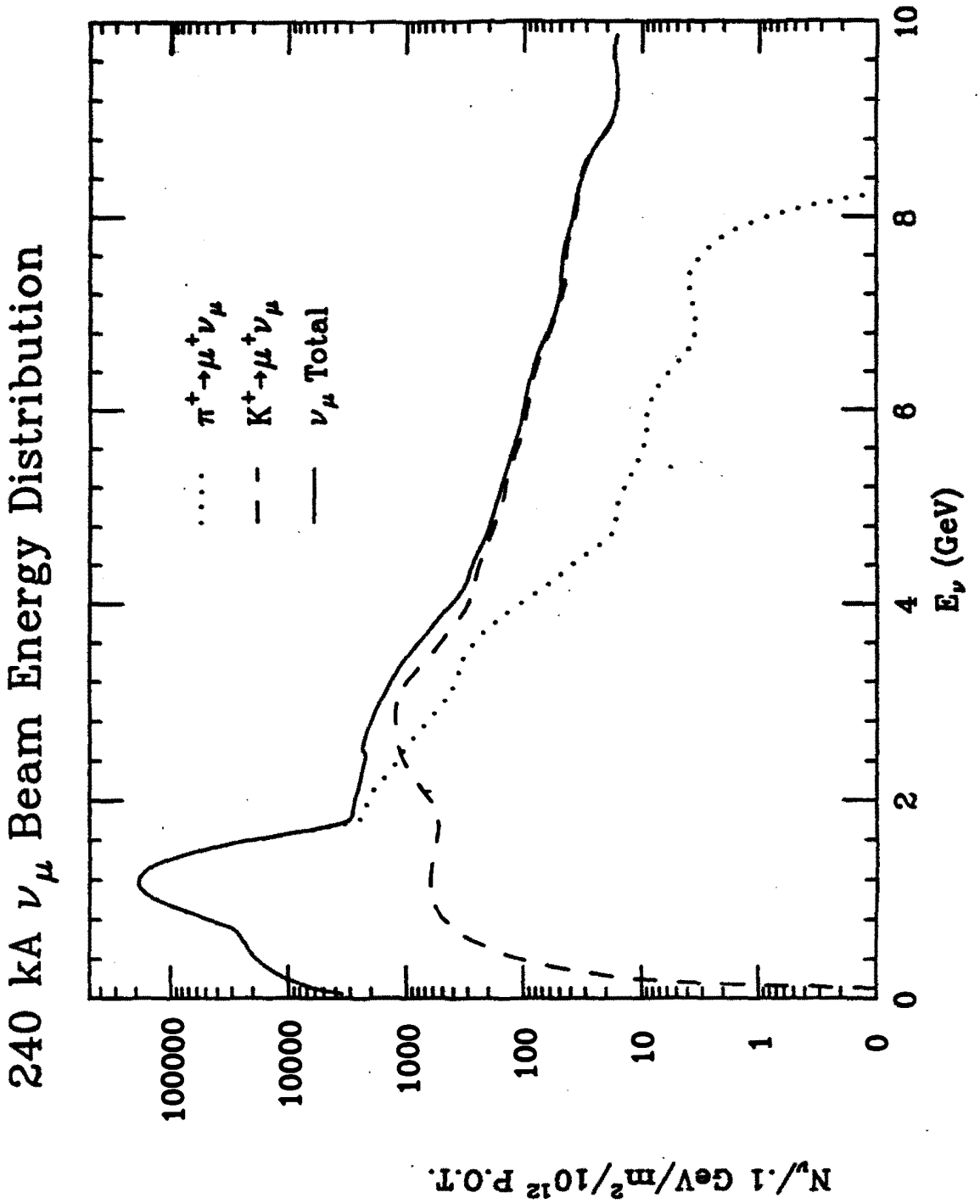

Figure 3.6: Energy distribution of ν_μ beam components generated by π^+ and K^+ decays for 240 kA horn current.

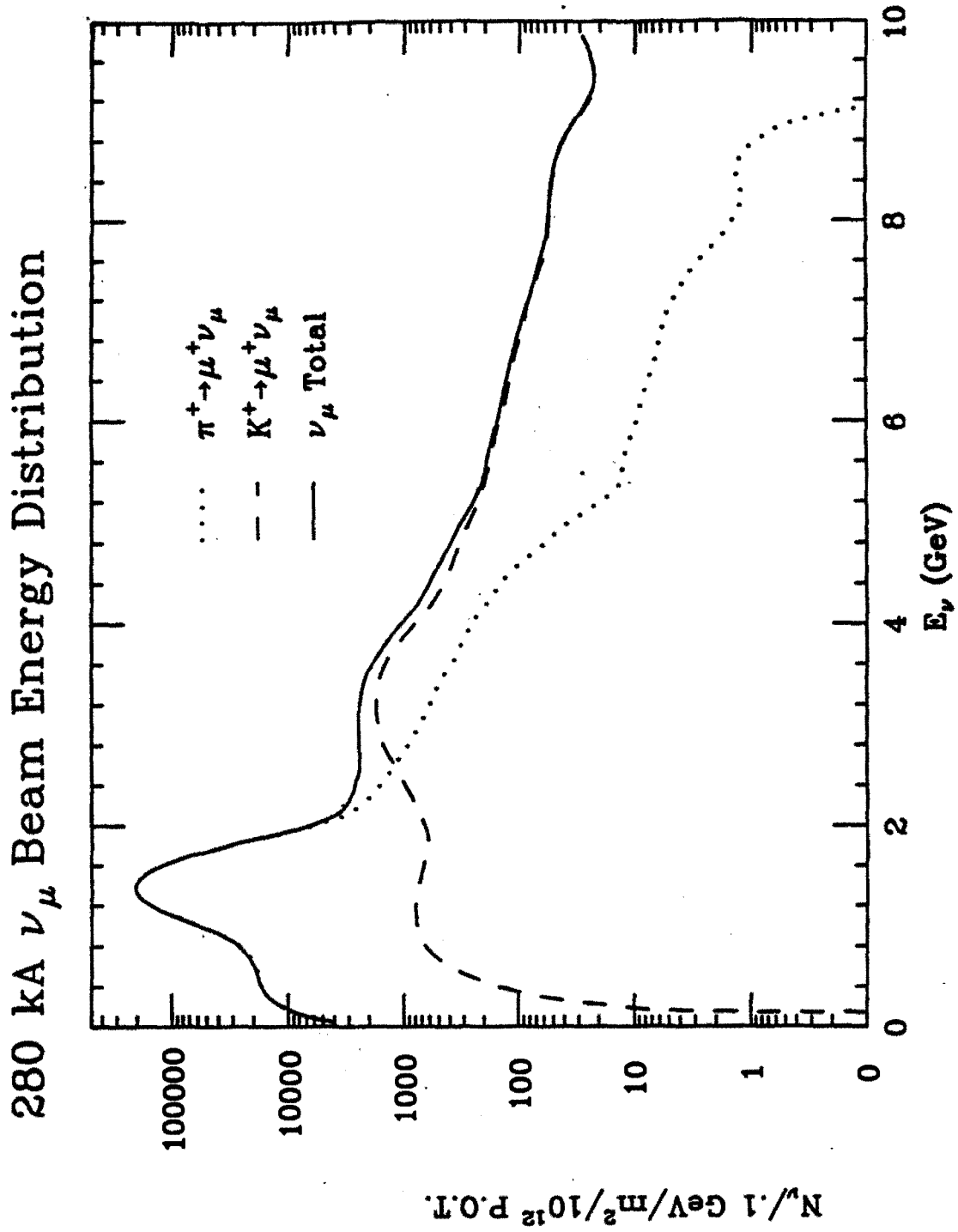

Figure 3.7: Energy distribution ν_μ beam components generated by π^+ and K^+ decays for 280 kA horn current.

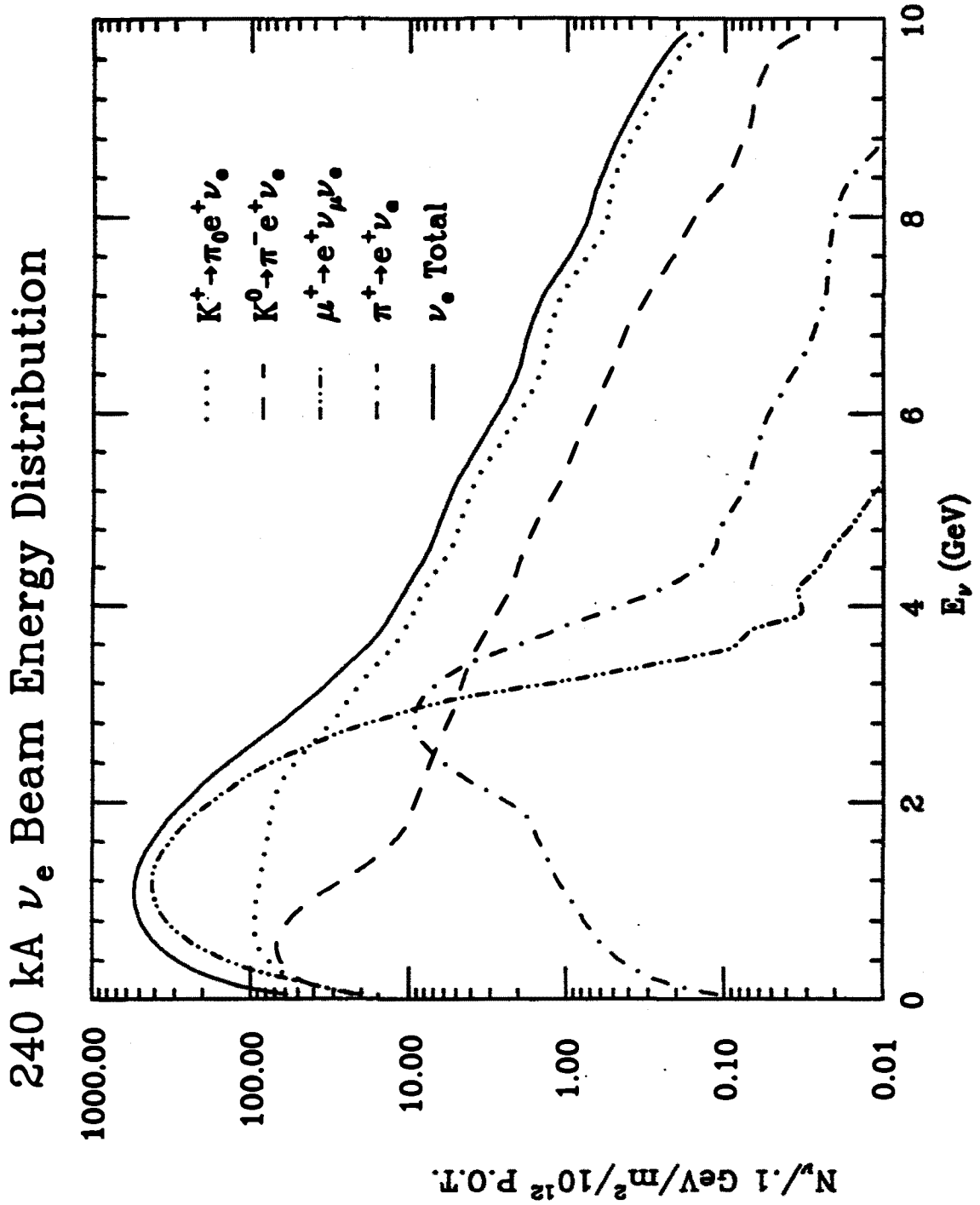

Figure 3.8: Beam ν_e background from $\mu^+ \to e^+ \bar{\nu}_\mu \nu_e$, $K^0 \to \pi^- e^+ \nu_e$, $K^+ \to \pi^+ e^+ \nu_e$, $\pi^+ \to e^+ \nu_e$ for 240 kA horn current.

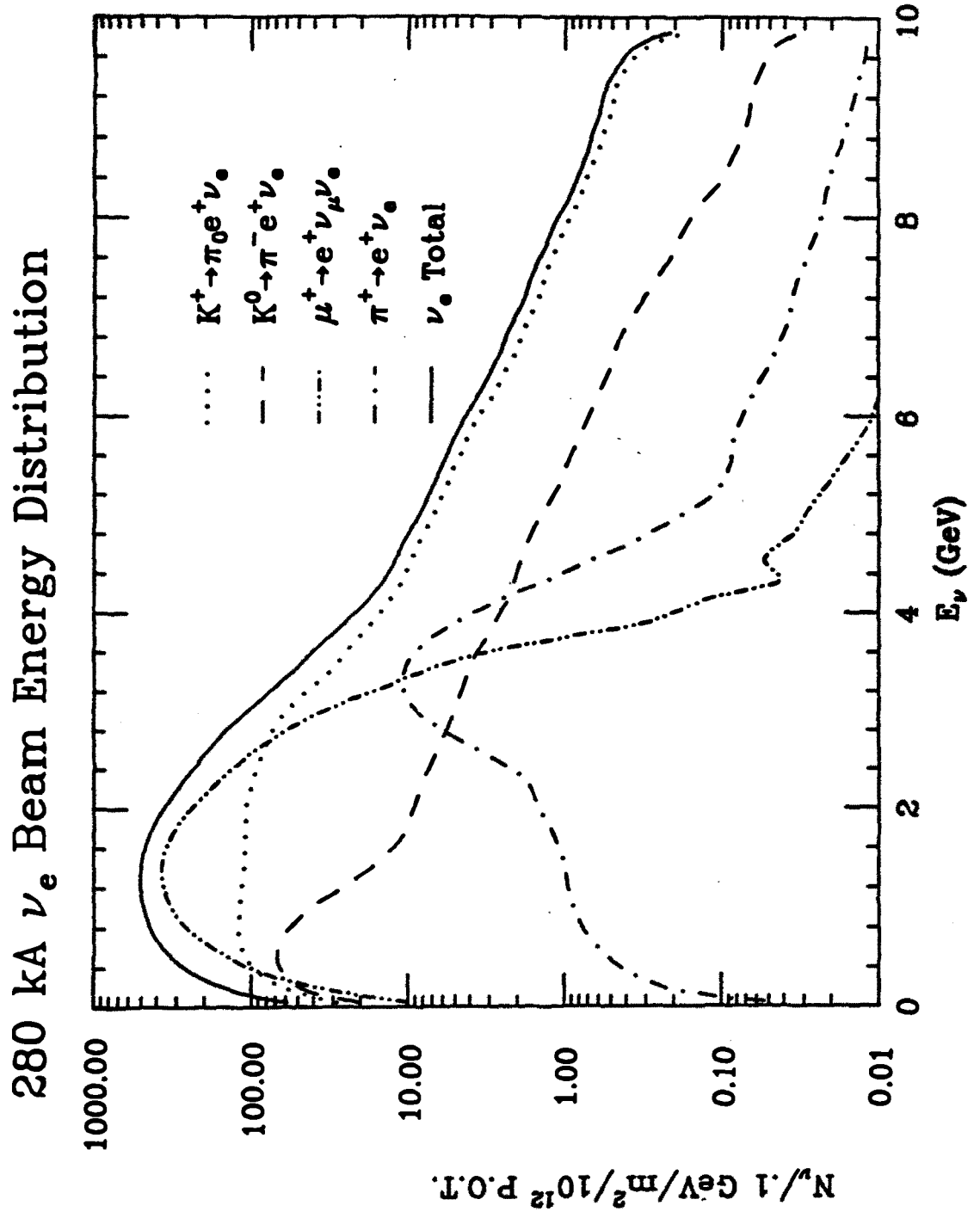

Figure 3.9: Beam ν_e background from $\mu^+ \to e^+ \bar{\nu}_\mu \nu_e$, $K^0 \to \pi^- e^+ \nu_e$, $K^+ \to \pi^+ e^+ \nu_e$, $\pi^+ \to e^+ \nu_e$ for 280 kA horn current.

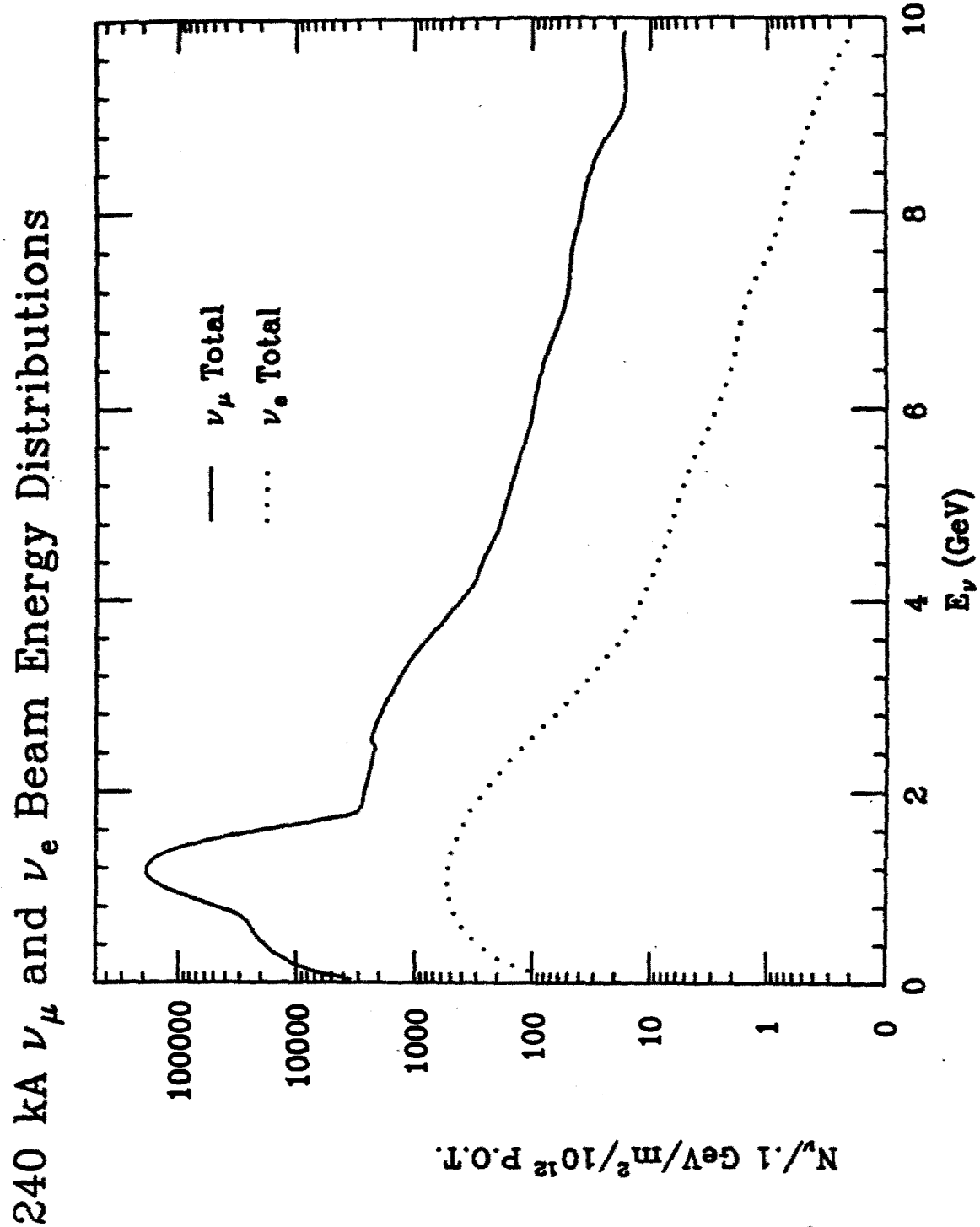

Figure 3.10: The neutrino beam energy distributions for the ν_μ beam and ν_e backgrounds.

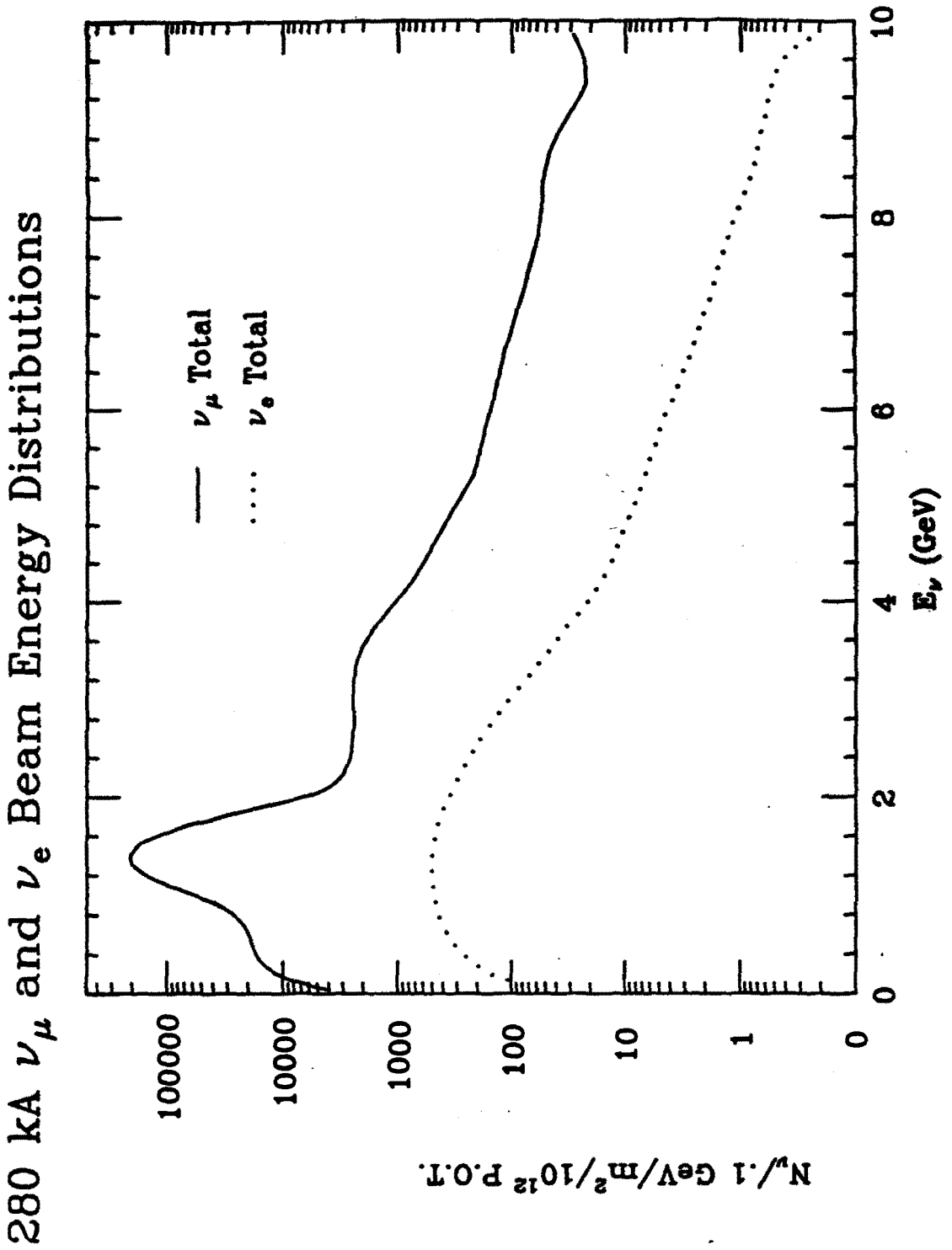

Figure 3.11: The neutrino beam energy distributions for the ν_μ beam and ν_e backgrounds.

10, includes many geometries which are not well understood, for example tunnel shielding, horn support hardware, etc. The calculation shows that this background is at the level of .1%. Reactions 5 and 2 contribute to the background at the levels of .2% and .01% respectively. Distributions for each of these sources of background are given in Figure 3.8 and Figure 3.9 for horn currents of 240 kA and 280 kA respectively. Integrating these sources of ν_e gives a background at the level of 8.3×10^{-3}. The Energy distributions for the ν_μ and ν_e components are shown in Figure 3.10 and Figure 3.11.

Beam component	Decay reaction	Neutrinos in the detector fiducial ($5.16 \times 5.16 m^2$) per interacting proton	
		240 kA	280 kA
ν_μ	$\pi^+ \rightarrow \mu^+ \nu_\mu$	4.485×10^{-5}	5.267×10^{-5}
ν_μ	$K^+ \rightarrow \mu^+ \nu_\mu$	1.248×10^{-6}	1.858×10^{-6}
ν_μ	total	4.610×10^{-5}	5.453×10^{-5}
ν_e	$\pi^+ \rightarrow e^+ \nu_e$	5.107×10^{-9}	6.191×10^{-9}
ν_e	$\mu^+ \rightarrow e^+ \bar{\nu}_\mu \nu_e$	2.423×10^{-7}	2.460×10^{-7}
ν_e	$K^+ \rightarrow \pi^0 e^+ \nu_e$	9.271×10^{-8}	1.384×10^{-7}
ν_e	$K_L^0 \rightarrow \pi^- e^+ \nu_e$	3.597×10^{-8}	3.597×10^{-8}
ν_e	total	3.761×10^{-7}	4.266×10^{-7}
ν_e/ν_μ		8.3×10^{-3}	7.8×10^{-3}

Table 3.3: Summary of neutrino beam Monte Carlo calculation for 240 kA and 280 kA horn currents.

Summaries of the results of the 240KA and 280 KA calculations are given in Table 3.3. In these calculations a detector area of 516 cm by 516 cm was used as the fiducial. The two sets of calculations show no remarkable differences except for the appropriate shift in the principle beam energy. The ν_e to ν_μ background decreases by about 6% in the 280 kA case compared to the 240 kA calculation.

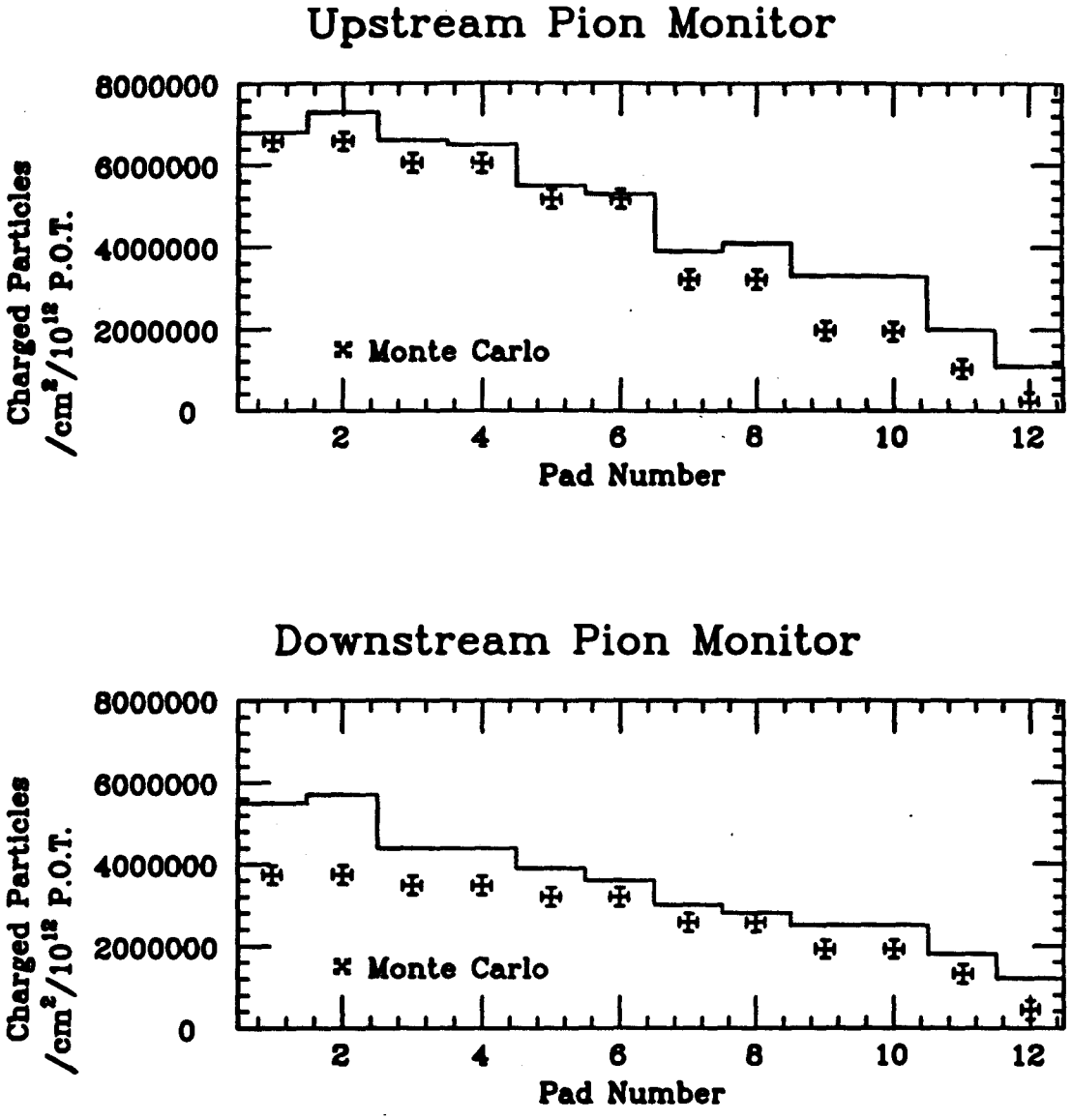

Figure 3.12: Radial distribution of pions, kaons, and protons as calculated and measured for 40 m and 60 m downstream of the second horn.

3.2.3. Radial Distributions of the Charged Particle Beam

In addition to the rate calculations for horn currents of 240 and 280 kA discussed above, another important feature which was studied was the radial distribution of charged particles in the decay tunnel. The charged particles considered in the Monte Carlo were pions, kaons and protons. These distributions, Figure 3.12, were produced for locations 40 m and 60 m downstream of the horn in order to compare them with data collected by monitors to be discussed later (section 3.3.1). The comparison is absolute and suggests that the Monte Carlo particle production was lower than that measured in the monitors by 10% for the upstream measurement and 25% for the downstream measurement. However, the radial distributions agree quite well qualitatively.

3.3. Beam Instrumentation and the Horn Power Supply

Beam instrumentation included intensity and profile measurements, timing Cerenkov counters and monitoring of the horn current. Two pion/kaon monitors provided pulse by pulse data on the intensity of the pion flux at locations 40 m and 60 m downstream from the last horn. Beam timing with respect to the AGS signal used for the trigger was monitored with 3 lucite Cerenkov counters. The current from each of the 20 capacitor modules of the horn power supply was monitored and recorded with each trigger. The logic and timing employed in this monitoring is shown in Figure 3.13.

3.3.1. Pion Monitors

The pion monitors were ionization chambers with the anode segmented in a bull's-eye pattern cut diagonally as shown in Figure 3.14. Two additional pads were included to measure the tail of the radial distribution for a total of 12 pads. Anode and cathode of the chambers were separated by a .5 cm drift space and the continuous plane of the cathode was maintained at -300 volts. The drift volume was filled with helium which was continuously flowed at a rate of 1 cubic foot per hour and kept at a pressure of 2 inches of water above atmospheric. Details of the construction of the chambers are also shown in Figure 3.14. Signals from each of the 12 pads for each of the 2 monitors were carried via 50 Ω coaxial cable to a

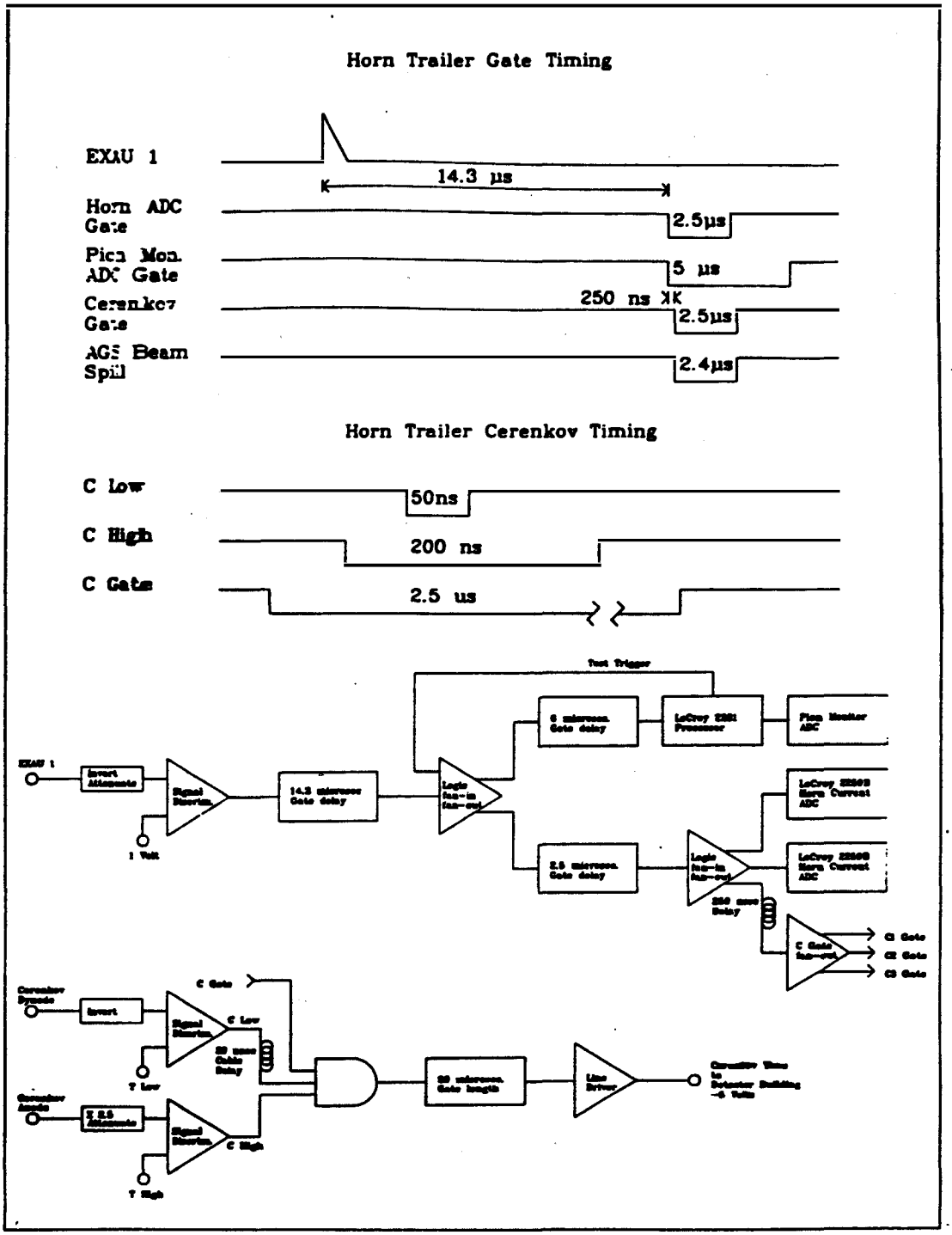

Figure 3.13: Logic and timing for the beamline instrumentation.

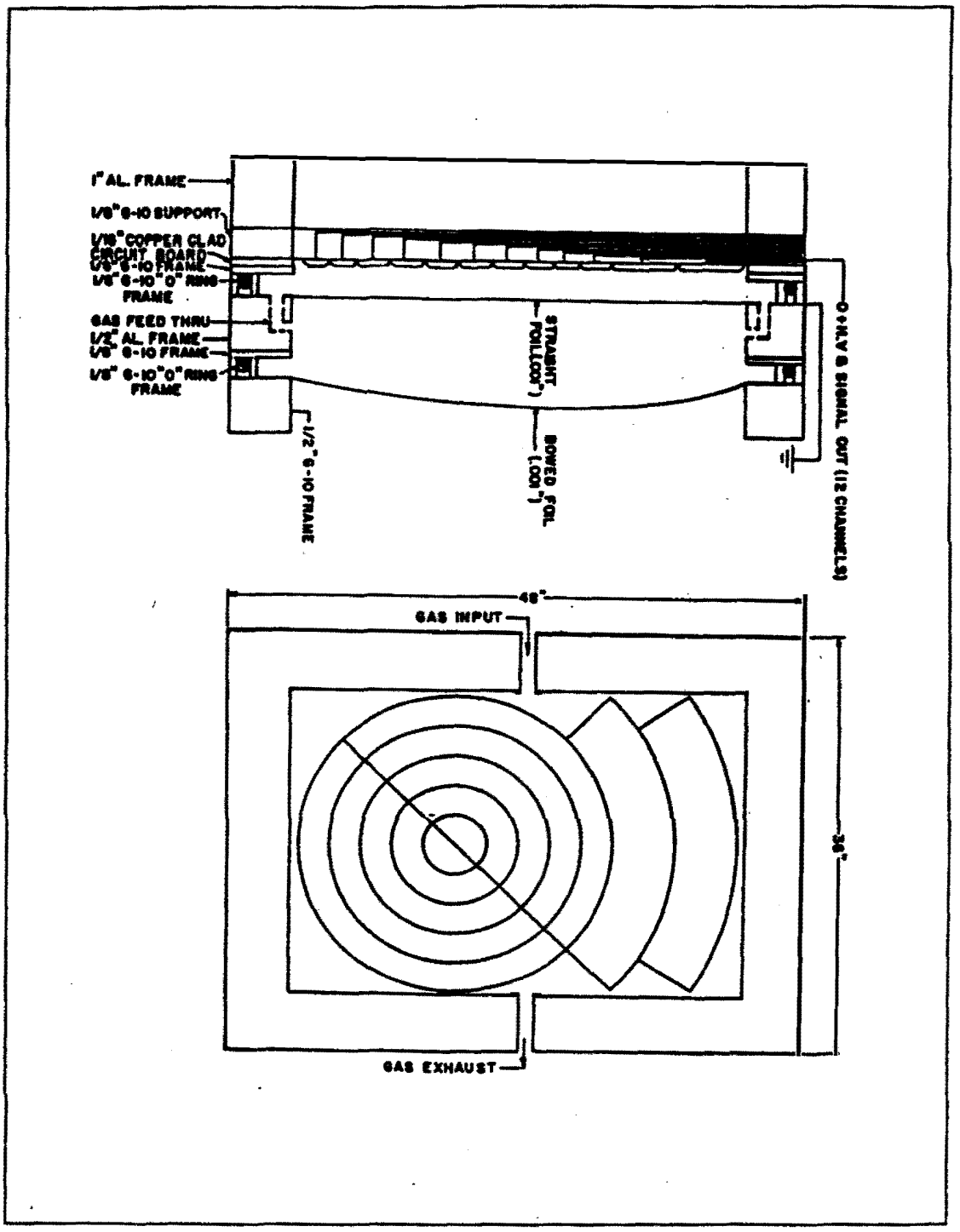

Figure 3.14: Bull's-eye pattern of the pion monitors and details of their construction and operation.

resistive splitter where they were divided by 30. This divided signal was digitized with a LeCROY 2281 charge ADC system and the data was recorded with each beam pulse.

Pion monitor response was studied with respect to a number of beam parameters. Linearity of the device was studied by comparing the response for differing proton beam intensities ranging from 3 to 15 $\times 10^{12}$ protons on target. Figure 3.15 shows the linear response. Monitor response as a function of horn current is shown in Figure 3.16 demonstrating the target production to be linear with momentum. The profile of the beam at each of the two monitor positions is shown in Figure 3.12 which compare moderately well with the beam calculations discussed above.

3.3.2. Cerenkov Counters

Three lucite counters were included in the decay tunnel and their times were used to eliminate jitter due to the uncertainty of AGS extraction timing. All three counters were mounted near the upstream pion monitor. They were made of a small cylinder of lucite, which produced Cerenkov light with the incidence of beam particles, glued to a phototube. Both dynode and anode from each phototube base were used with high-low discrimination to eliminate timing jitter. This timing pulse was gated with the beam trigger and sent to the detector facility through 93 Ω cable. The times for each of the counters was digitized with TDCs used for the detector scintillators and recorded with the other beam event data. Timing resolution with this technique was a few nanoseconds.

3.3.3. Horn Power Supply and Horn Current Monitoring

The current for the horn was provided by 20 banks of capacitors which were discharged quickly through the dual horn system. The horn power supply is represented schematically by Figure 3.17. All of the capacitor banks were charged to the required voltage with two 5 amp constant current supplies. The banks were then discharged through ignitrons prior to the beam by one-quarter of the period ($\sim 63 \mu sec$) of the horn circuit. This LRC horn circuit consisted of the power supply, coaxial current transmission lines, and two horn system.

The current provided by each of these modules was measured using an associated current transformer. The output from the current transformers was monitored

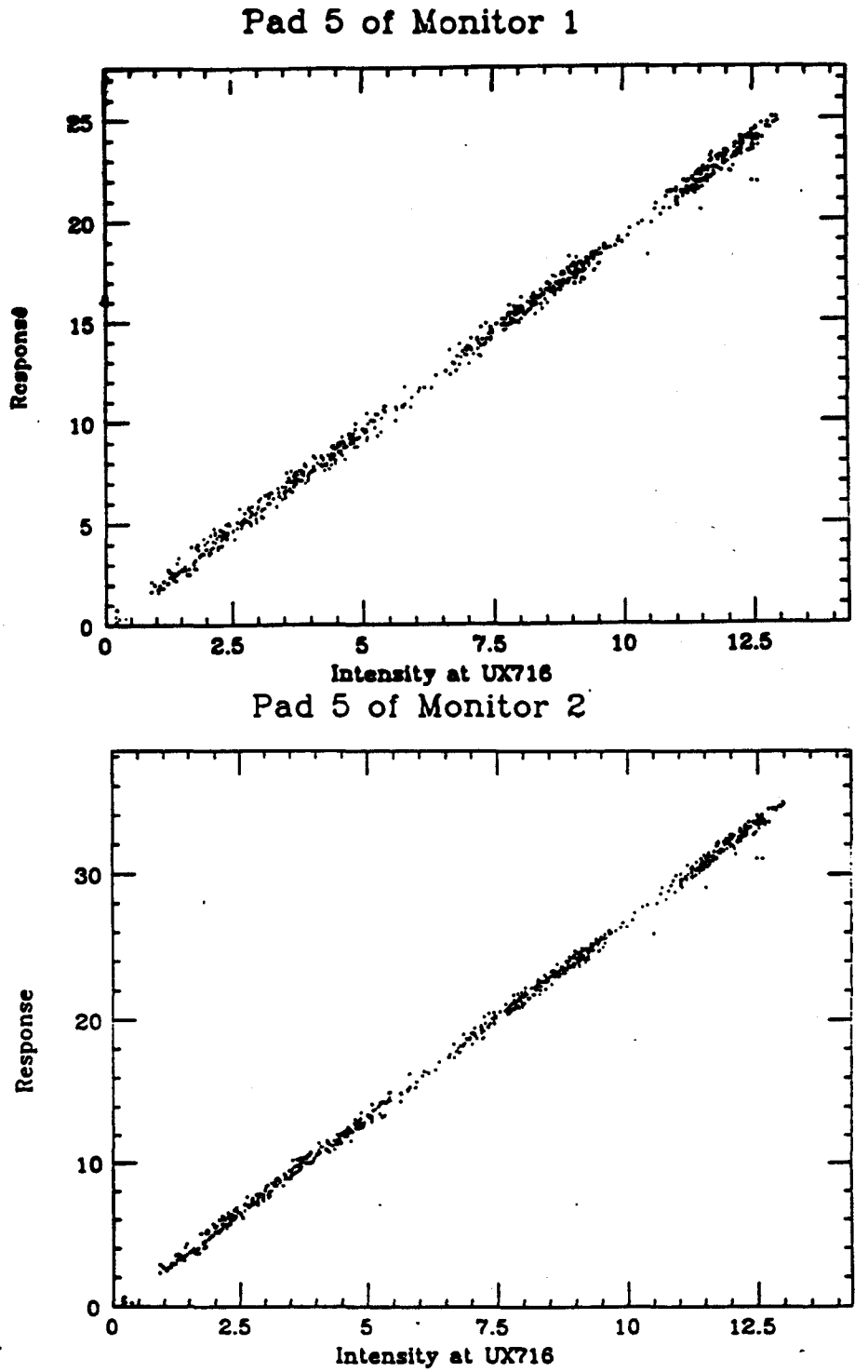

Figure 3.15: Linearity of the pion monitor response with beam intensity.

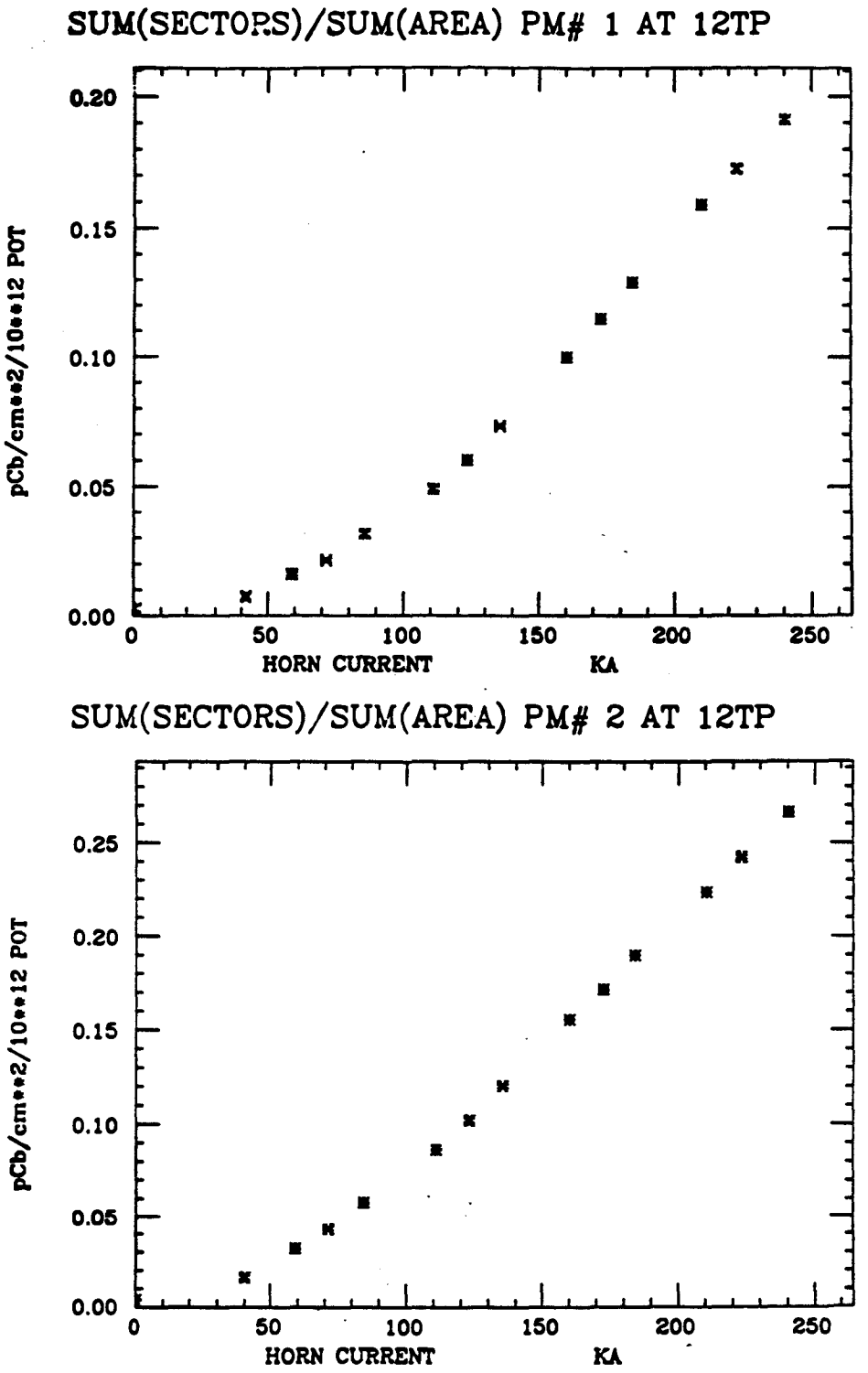

Figure 3.16: Response of the pion monitor as a function of horn current.

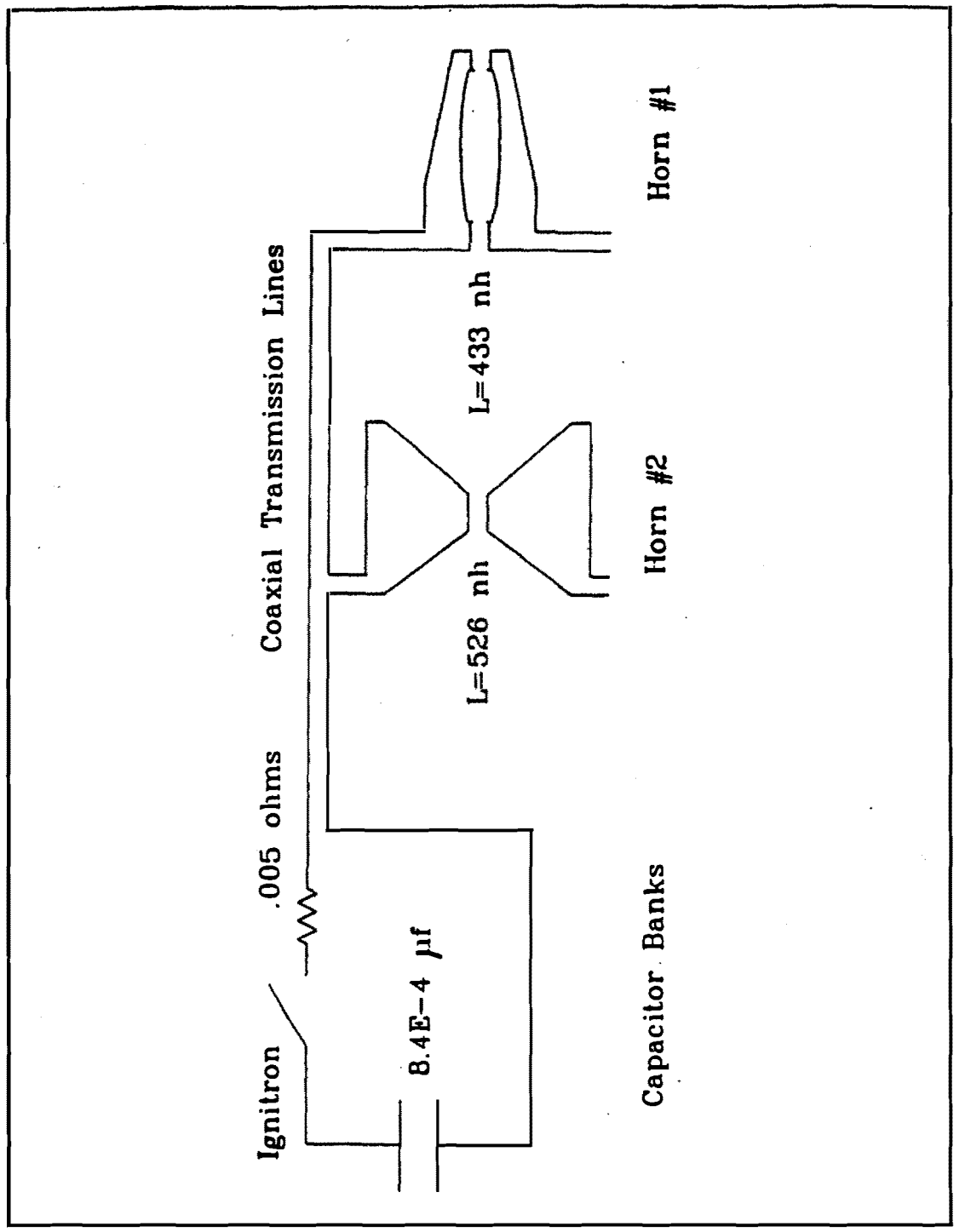

Figure 3.17: The horn power supply and horn circuit.

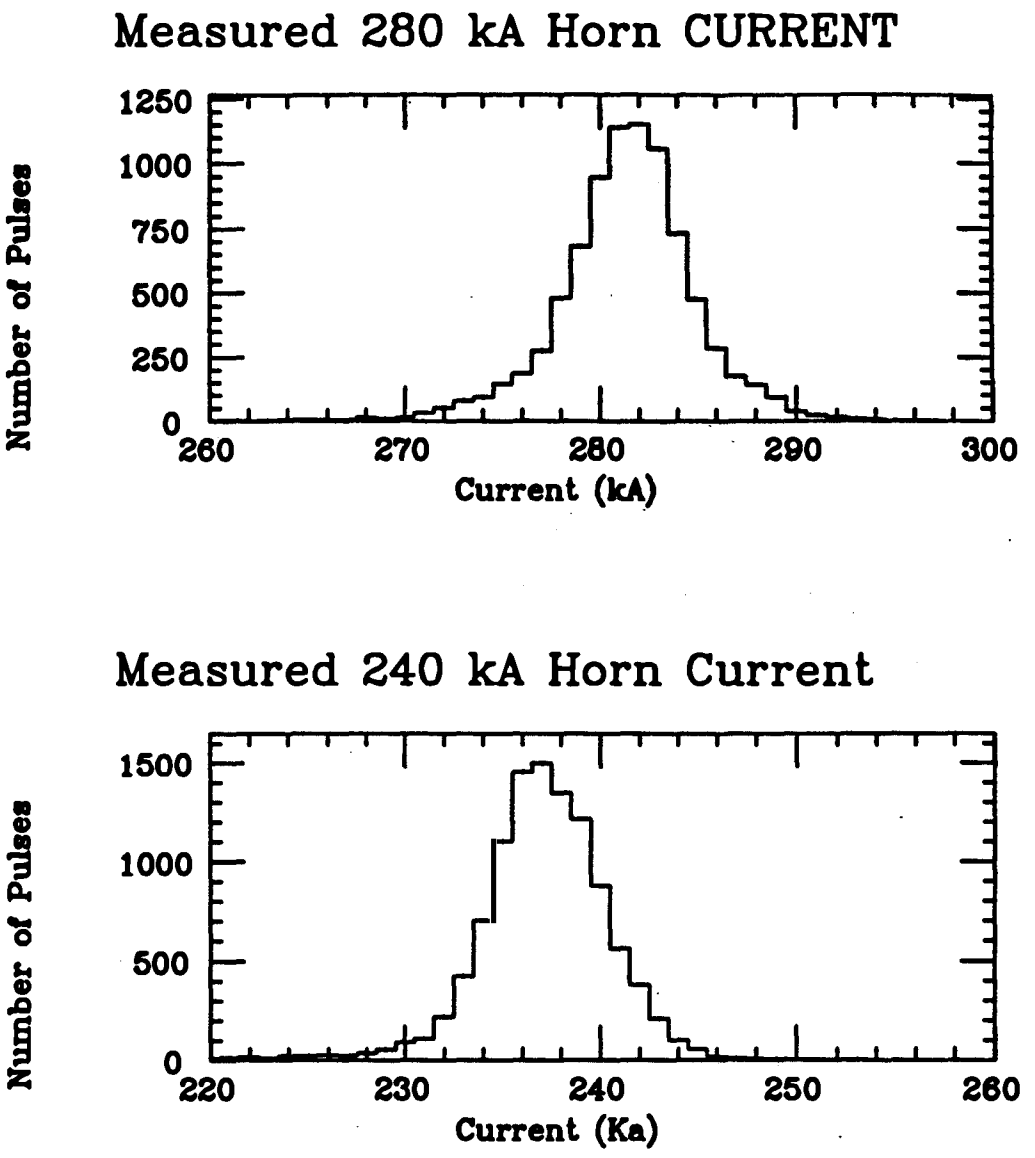

Figure 3.18: Horn current distribution for several pulses.

online and recorded with the data from each beam pulse. Measurements taken from 240 kA and 280 kA runs are shown in Figure 3.18 and demonstrate that the horn current was stable to the 1% level. These measurements indicate that the current was ~1% below the 240 kA value and ~1% above the 280 kA value during the runs.

Chapter 4.
Event Monte Carlo

Analysis of the data relied heavily on the accuracy of the event Monte Carlo. In the energy regime around 1 GeV many interaction cross sections played significant rolls and events with multiparticle vertices began to dominate the topologies. These complexities were confused further by the hadronic interactions which the products of the reactions underwent before they emerged from the complex nucleus in which they occurred. In addition, the coarseness of the detector tended to hide many of the intricate features of these events. Particle identification was difficult, even for those tracks which clearly emerged form the target material and the Monte Carlo was essential in determining the number of correct and incorrect assignments which were made to tracks in the analysis. These features determined the validity of the detector acceptance and background calculations which were utilized in the data analysis.

Although the major part of the flux in the dichromatic neutrino beam was below 2 GeV , around 10% was above and events from these higher energy neutrinos represented a major concern. At 800 MeV, simple event topologies of the quasi-elastics dominate, by 2 GeV the cross sections for nucleon resonances with single pions become the major component. Around 3 GeV multi-pion and deep inelastic multi-hadron cross sections become significant. One of the principle features studied with the Monte Carlo was the manner in which these high energy events appear as background for the lower energy muon and electron signals.

4.1. Event Generation

Interactions were first generated in the target material. The energy was chosen according to the calculated beam energy distribution and an event type was selected weighted by its interaction channel cross section relative to the total cross section at that energy. Fermi motion of the target nucleus was chosen and the interaction four-momentum parameters were calculated in the center of mass system. A Q^2 and azimuthal orientation were then selected for the event. Four-momentum vectors in

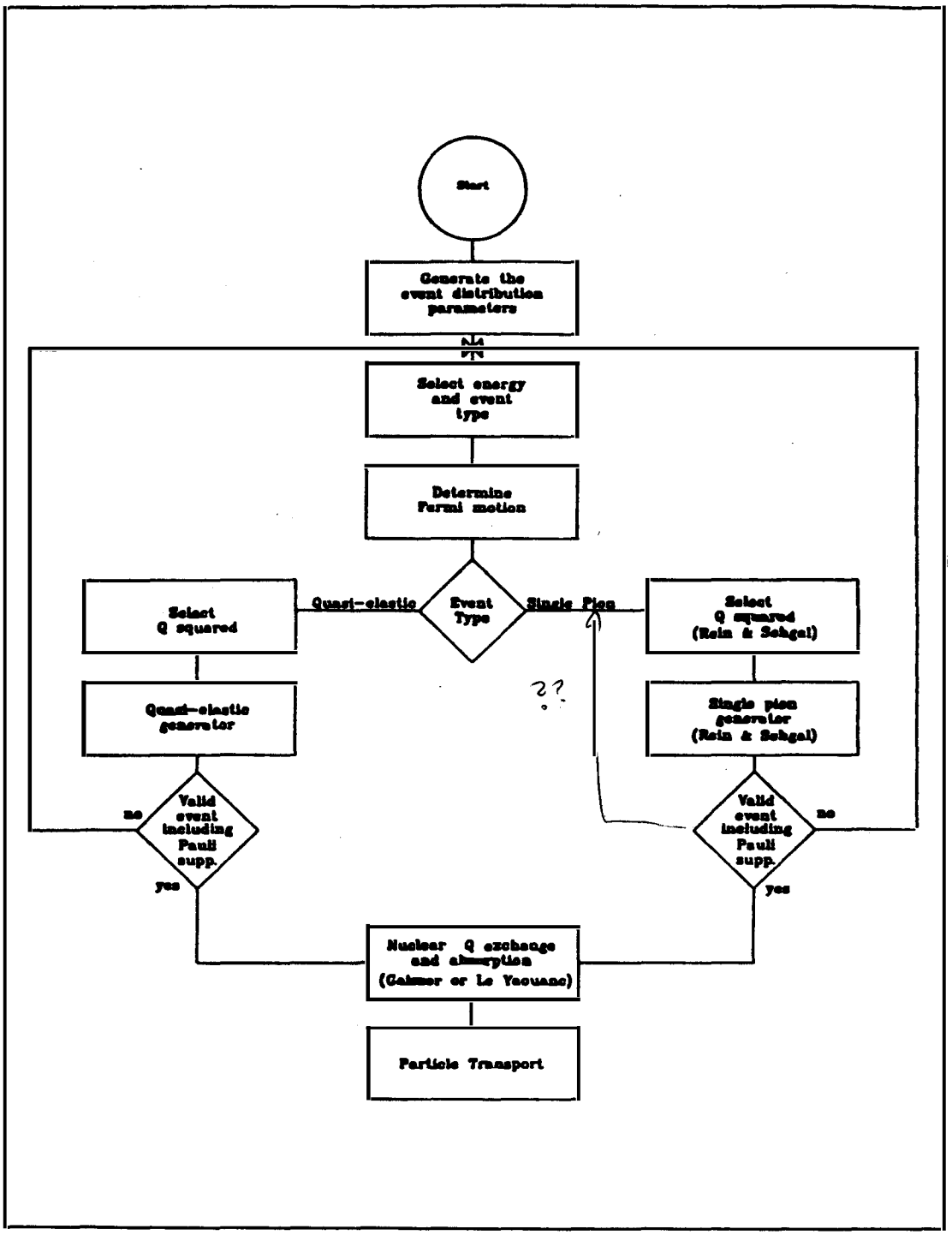

Figure 4.1: The Monte Carlo event generator flow chart.

the laboratory frame were calculated for each secondary particle from the interaction. The Pauli exclusion principle was then imposed to determine if the event was energetically allowed. Finally, pions and nucleons underwent charge exchange and/or absorption in the target nucleus. The flow chart of Figure 4.1 demonstrates the major components of event generation by the Monte Carlo.

Initially, the event energy and type were chosen. Events were thrown with energy distributions based on those calculated with the beam Monte Carlo discussed in Chapter 3. The four beam energy distributions which were available were the ν_μ beam spectra for 240 kA and 280 kA and the ν_e background spectra for 240 kA and 280 kA. In addition it was possible to throw single energies and block spectra which were useful in studying acceptances, resolutions and other energy dependant parameters. The event types were chosen based on the relative cross section of each reaction channel with respect to the total cross section at the energy of the event. The cross sections for the principal charged and neutral current interaction channels considered in the Monte Carlo are presented in Figure 4.2 and Figure 4.3.

Because the target nucleon was part of a larger nucleus, the relative number of protons to neutrons and its Fermi motion were considered. The concrete absorber was composed largely of CaO with fractions of SiO_2, MgO, CO_2 and other medium Z materials(see section 2.2) all of which contain nearly equal numbers of protons and neutrons. The aluminum in the PDT chambers which represents 33% of the detector mass has a very slight excess of neutrons. The total excess of neutrons to protons in the detector is roughly 2%; this was ignored in the Monte Carlo event generation and a one-to-one ratio was used. The Fermi momentum for each event was selected from a sphere in momentum space with radius

$$P_{Fermi}\,(MeV/c) = (.19733/1.3 \times 9/4\pi\,(A-Z)\,/A)^{1/3}\,. \qquad (4.1)$$

With the target and Fermi momentum selected, a Q^2 for the event was chosen and the Pauli exclusion model was used to suppress certain low Q^2 events. The probability of the event occurring depends on $d\sigma/dQ^2$ for quasi-elastic events and this was produced using a widely accepted model.[14] For nucleon resonances the chance of an event occurring depended upon $d\sigma/dQ^2dW$, where W was the mass

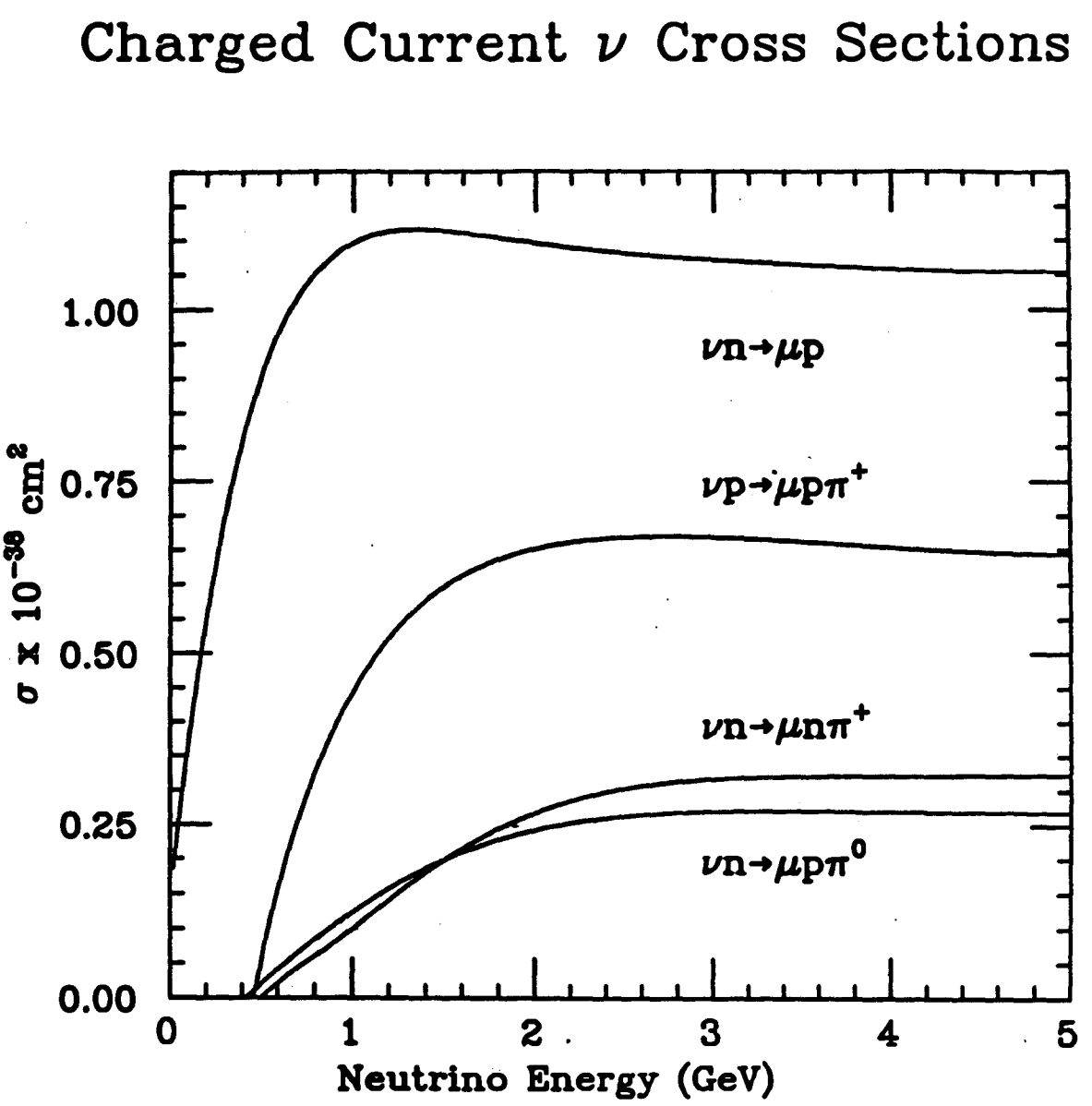

Figure 4.2: Neutrino charged current cross sections as a function of neutrino energy for $\nu_\mu n \rightarrow \mu^- p$ quasi-elastic, $\nu_\mu p \rightarrow \mu^- p\pi^+$ single pion, $\nu_\mu n \rightarrow \mu^- p\pi^0$ single pion, $\nu_\mu n \rightarrow \mu^- n\pi^+$ single pion.

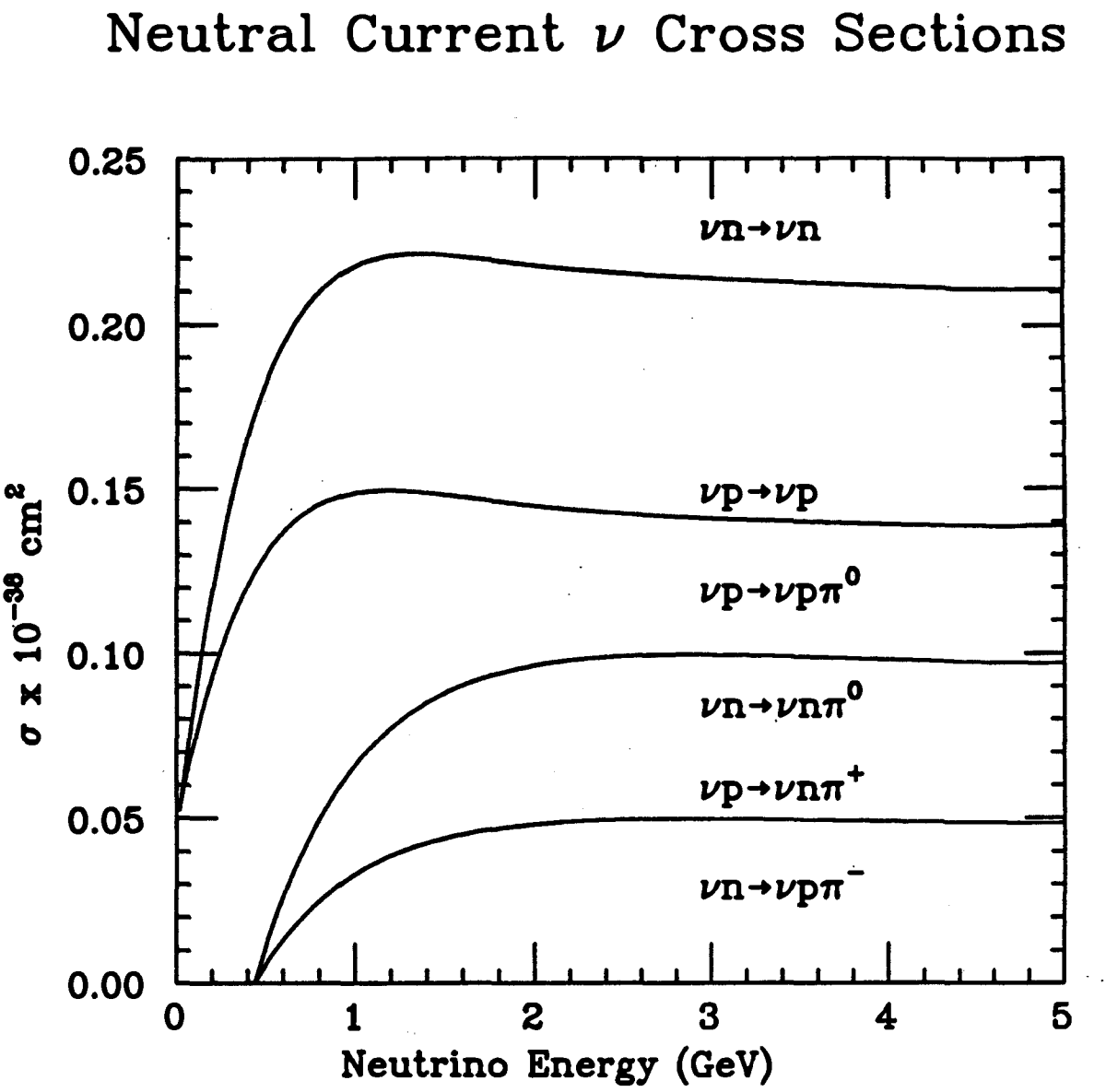

Figure 4.3: Neutrino neutral current cross sections as a function of neutrino energy for $\nu_\mu n \to \nu n$, $\nu_\mu p \to \nu p$, $\nu_\mu p \to \nu n \pi^+$, $\nu_\mu p \to \nu p \pi^0$, $\nu_\mu n \to \nu - p\pi^-$, $\nu_\mu n \to \nu - n\pi^0$.

of the resonance state; the values for this were based on a model and the corresponding FORTRAN code by Rein and Sehgal. [15] The Pauli exclusion principle was included to further suppress certain events. The principle requires that any reaction is forbidden if any of the final state particles produced are in a quantum state already fully occupied. Although in a shell model calculation the suppression factor depends weakly on which shell target nucleon is located, an averaged model was used. Above $Q^2 \sim 0.1 GeV^2$ the suppression has no effect.

	Resonance name	Resonance symbol $L_{2i,2j}$	Central mass (MeV)	Total width Γ_0(MeV)	Single π branching Ratio	Charged current cross section ($\times 10^{-40} cm^2$) 2 GeV	20 GeV
*	$\Delta(1234)$	P_{33}	1234	124	1	80.0	82.58
*	$N^*(1440)$	P_{11}	1450	370	.65	3.9	10.93
*	$N^*(1520)$	D_{13}	1525	125	.56	9.57	18.12
*	$N^*(1535)$	S_{11}	1540	270	.45	9.88	14.28
	$\Delta(1620)$	S_{31}	1620	140	.25	0.20	0.57
	$N^*(1650)$	S_{11}	1640	140	.60	0.48	0.89
	$\Delta(1640)$	P_{33}	1640	370	.20	0.88	4.54
	$N^*(1675)$	D_{15}	1680	180	.35	1.15	2.04
*	$N^*(1680)$	F_{15}	1680	120	.62	1.52	3.73
	$N^*(1670)$	D_{13}	1670	180	.10	4.16	10.96
	$N^*(1730)$	P_{11}	1710	100	.19	0.86	5.65
	$\Delta(1730)$	D_{33}	1730	300	.12	1.24	2.57
	$N^*(1740)$	P_{13}	1740	210	.19	3.89	15.06
	$\Delta(1920)$	S_{31}	1920	300	.19	0.13	1.28
	$\Delta(1920)$	F_{33}	1920	340	.15	0.64	2.20
	$\Delta(1950)$	F_{37}	1950	340	.40	0.67	4.33
	$\Delta(1960)$	P_{33}	1960	300	.17	0.24	2.22
	$N^*(1970)$	F_{17}	1970	325	.06	0.26	1.55

Table 4.1: Nucleon resonances contributing to single pion production. Those employed in the Monte Carlo event generator are indicated by an * on the left.

The Monte Carlo used for the analysis of this paper included only two general event type generators: quasi-elastic and exclusive single pion. The quasi elastic generator produced $\nu_\mu n \rightarrow \mu^- p$ and $\nu_e n \rightarrow e^- p$ events. The single pion generator was adapted from Rein and Sehgal and included several, not all, of the charged and neutral current nuclear resonance single pion interaction channels. A list of well established N^* and Δ resonances and their single pion branching ratios is given in Table 4.1, with those included in the Monte Carlo indicated by asterisks[16]. From this it is observed that approximately 97% of the charged current single pion cross section has been taken into account for 2 GeV neutrinos. The table also shows that at 2 GeV about 78% of the total resonance cross section is accounted for by the single pion channels considered. It is also noted that the version employed for the analysis of this report employed only resonance masses below 2 GeV.

After the events were produced, and the direction of the component particles determined, the pions and nucleons were allowed to charge exchange and/or be absorbed by the nucleus. The charge exchange and absorption model which was employed was that of Gaisser et al.[17] In this model pions were allowed to scatter forward and backward through the nucleus until they emerged. In the process they could be absorbed, charge exchange or, emerge with their direction reversed. Nucleons were allowed similar processes, excluding the scattering, based on the calculation made by Le Yaouanc.[18]

4.2. Particle Transport

The second phase of the Monte Carlo transported particles produced by the generator from the target nucleus through the material of the detector. The detector was represented as a series of plates of concrete, aluminum, scintillator plastic, and toroid iron. The electrons, muons, pions, and nucleons were stepped through these plates and allowed to interact according to the particle type.

Electrons underwent electromagnetic interactions and showers were developed in the detector. Neutral pions, π^0s, decayed isotropically into two γs, which developed into electromagnetic showers. Electromagnetic showers were transported through the detector with a standard version of EGS4.[19] The energy cutoff for particles in the shower was set at 50 keV. For each wire position through which the track or

tracks passed, a drift time and pulse area were calculated and this information was written into the data format.

Muons, pions and nucleons were stepped through the detector and allowed to either decay, interact or exit. A flow diagram for the transport of these particles is included in Figure 4.4. Muons and pions decayed in the detector according to their travel distance and the appropriate decay length. Pions and nucleons which emerged from the nucleus underwent hadronic interactions as they were stepped through the detector.The charged particles underwent multiple Coulomb scattering [20] and lost energy due to ionisation.[21] If the track was within the toroid iron it was given a curvature calculated from the value of the magnetic field and the momentum of the particle at that position. Particles were considered to have stopped in the detector if either their kinetic energy was less than 1 MeV or the ionisation energy loss per step was greater than the kinetic energy of the particle. At each step it was verified that the position of the track was within the boundaries of the detector. As in the shower case a drift time and pulse area were determined for each track and written into the data format.

Hadronic interactions for pions and nucleons were allowed to occur based on the nuclear interaction length, λ, which was calculated using a model largely from Grant. [22] Employing cross section data from proton on Al, Fe and Cu an extrapolation was made by scaling λ_{total} by $A^{2/3}$ i.e. σ_{total} by $A^{1/3}$ ($\lambda = A/N_A\sigma$). For pions, this interaction length was increased by an additional factor of 1.07. Initially, the number of interaction lengths the particle would travel was chosen. The particle was determined to have interacted hadronically if it had gone more than this predetermined length through the detector. If this had occurred the pion or nucleon was allowed interact with a nucleus either elastically or inelastically according to the relative values of $\sigma_{elastic}$ and σ_{total}. The elastic scattering was performed as described by Ranft. [22] An inelastic interaction was allowed to proceed through one of several channels including nuclear absorption, nuclear excitation and decay, nuclear charge exchange, and for particles with more than 400 MeV kinetic energy nuclear cascades were produced. Each particle which was produced in the interaction was in turn stepped through the detector with either the EGS or hadron logic.

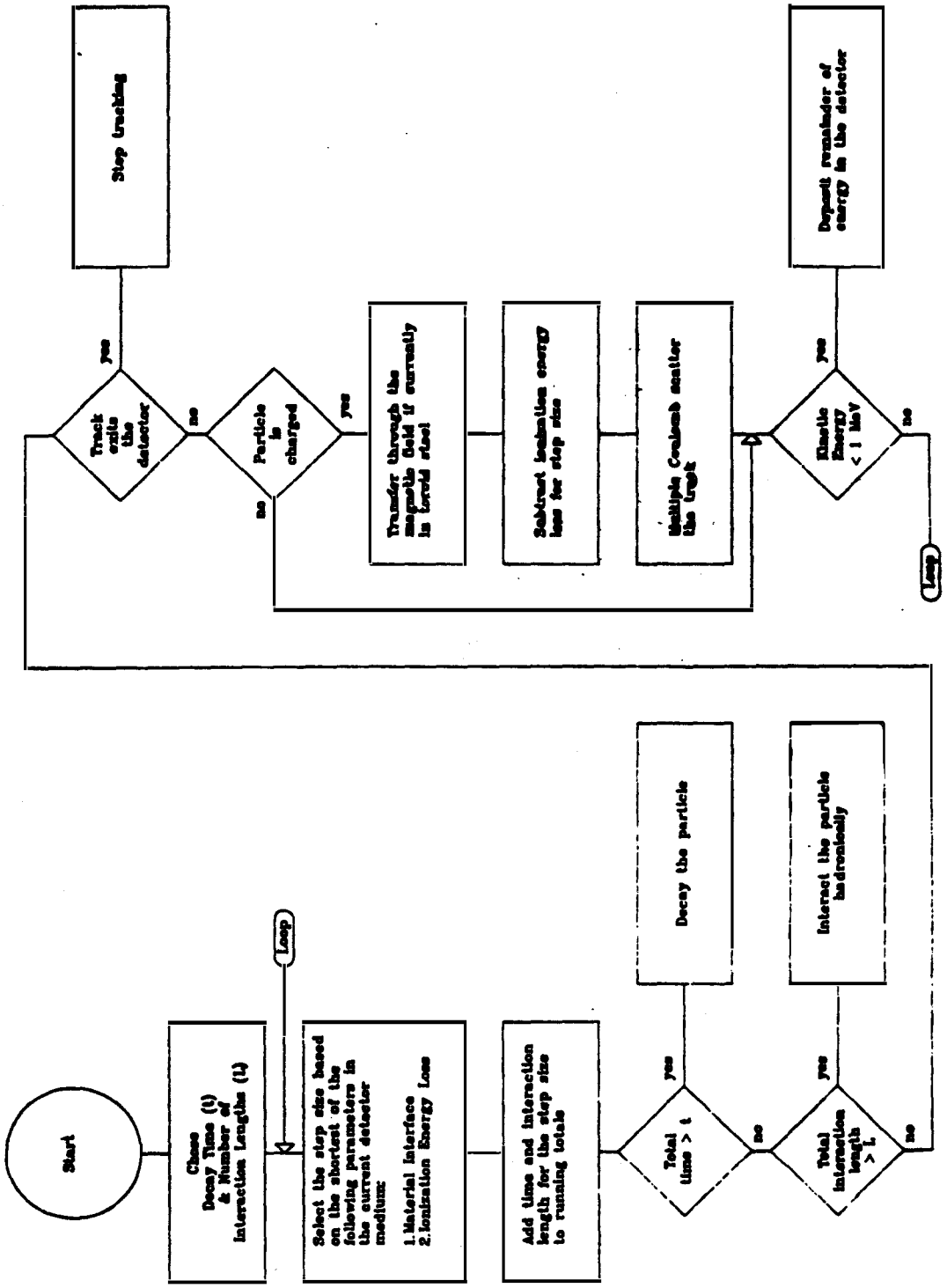

Figure 4.4: Flow chart of the event Monte Carlo particle transport.

4.3. Monte Carlo Verification

To verify that the event generators and the particle transport sections of the Monte Carlo were functioning correctly, they were compared with data. The event generators were checked against BNL 7 foot deuterium bubble chamber data. It was impossible to test the neutral current and Deep inelastic event types in this way and there was some ambiguity in part of the charged current data, however good agreement existed for the well understood bubble chamber data. The transport section of the Monte Carlo was checked against particle data gathered in the BNL A2 test beam for electrons, π^+s and protons.This portion of the Monte Carlo agreed moderately well with the data. The Monte Carlo was compared with ~5000 deuterium bubble chamber events from the 7 foot BNL bubble chamber. The four principle charged current ν_μ interaction channels were considered. In both the Monte Carlo and bubble chamber cases, ten energy slices were selected ranging from .4 to 4. GeV with widths of $\pm$ 200 MeV. The Monte Carlo data was thrown with a Fermi motion of 47 MeV to simulate that of the deuterium target of the bubble chamber and 10000 events were produced at each energy. Selection of events from the bubble chamber data was performed in accordance with those criteria established by Kitagaki et al. [24] All fits require that the probability, as calculated from the χ^2, be greater than 1%. For μp and $\mu p\pi^+$ events, only 3 constraint fits were used. The largest ambiguity existed in the $\mu p\pi^0$ and $\mu n\pi^+$ data as these events were based on 0 constraint fits due to the missing neutral. In these cases only 2 prong events were used to avoid confusion introduced by the spectator particles. In approximately 15% of the cases, the $\mu n\pi^+$ and $\mu p\pi^0$ channels were ambiguous and the type was selected based on the calculated χ^2. Corrections considered by the bubble chamber group have not been included as they were small.

The comparison included studies of the behavior of Q^2, and the angular and kinetic energy distributions for the muon, proton, and pion. The average values are compared in Figure 4.5 through Figure 4.7 with statistical error bars. The number of bubble chamber events decreased quickly at higher energies and thus the quality of these plots is suspect above about 3 GeV. Larger disagreements existed in the $\mu n\pi^+$ and $\mu p\pi^0$ comparisons. These disagreements were caused by the ambiguity,

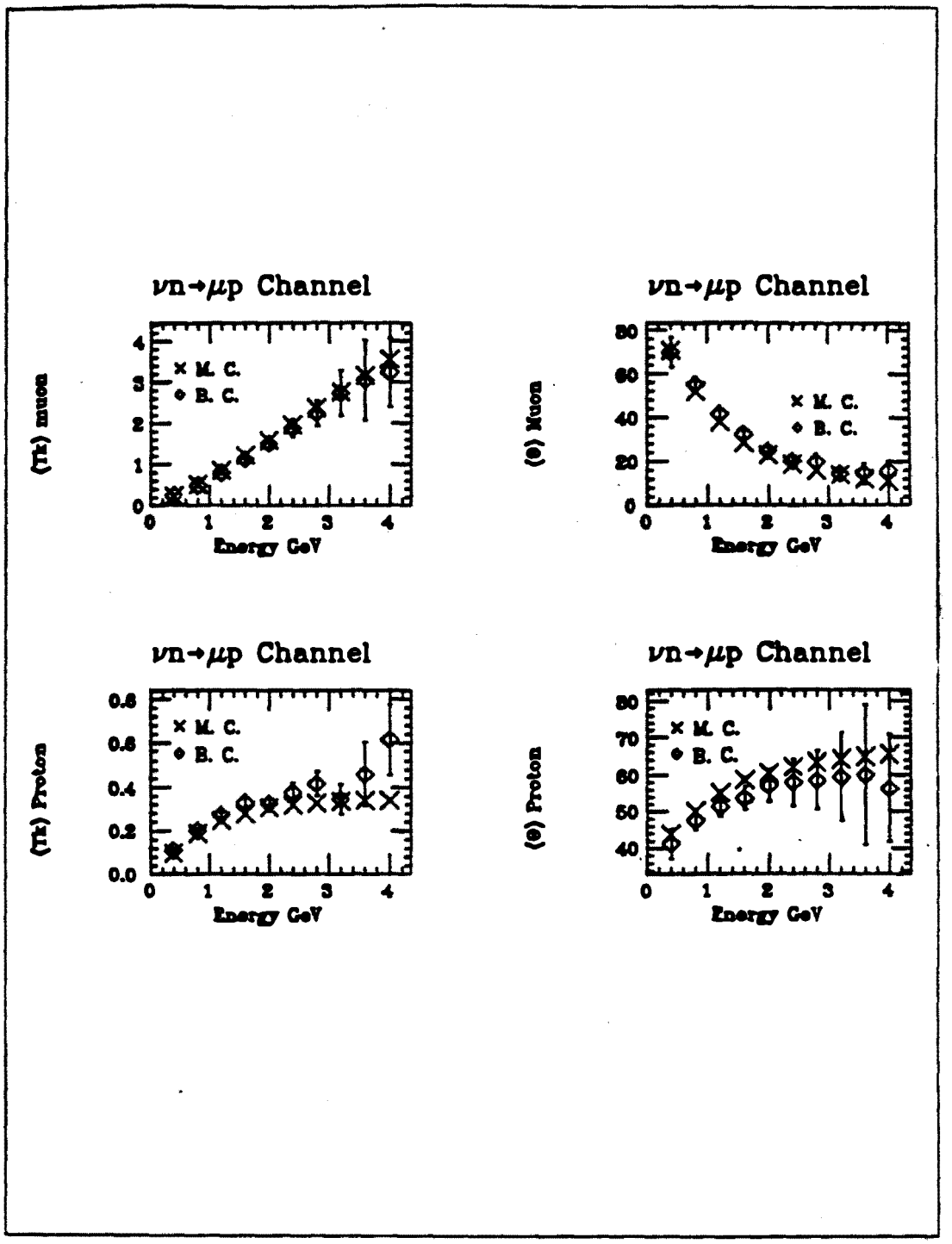

Figure 4.5: Comparison of Monte Carlo event generator with BNL 7 foot bubble chamber results for $\nu_\mu n \rightarrow \mu^- p$. The horizontal axis represents event energy as reconstructed for the bubble chamber data and as thrown for the Monte Carlo.

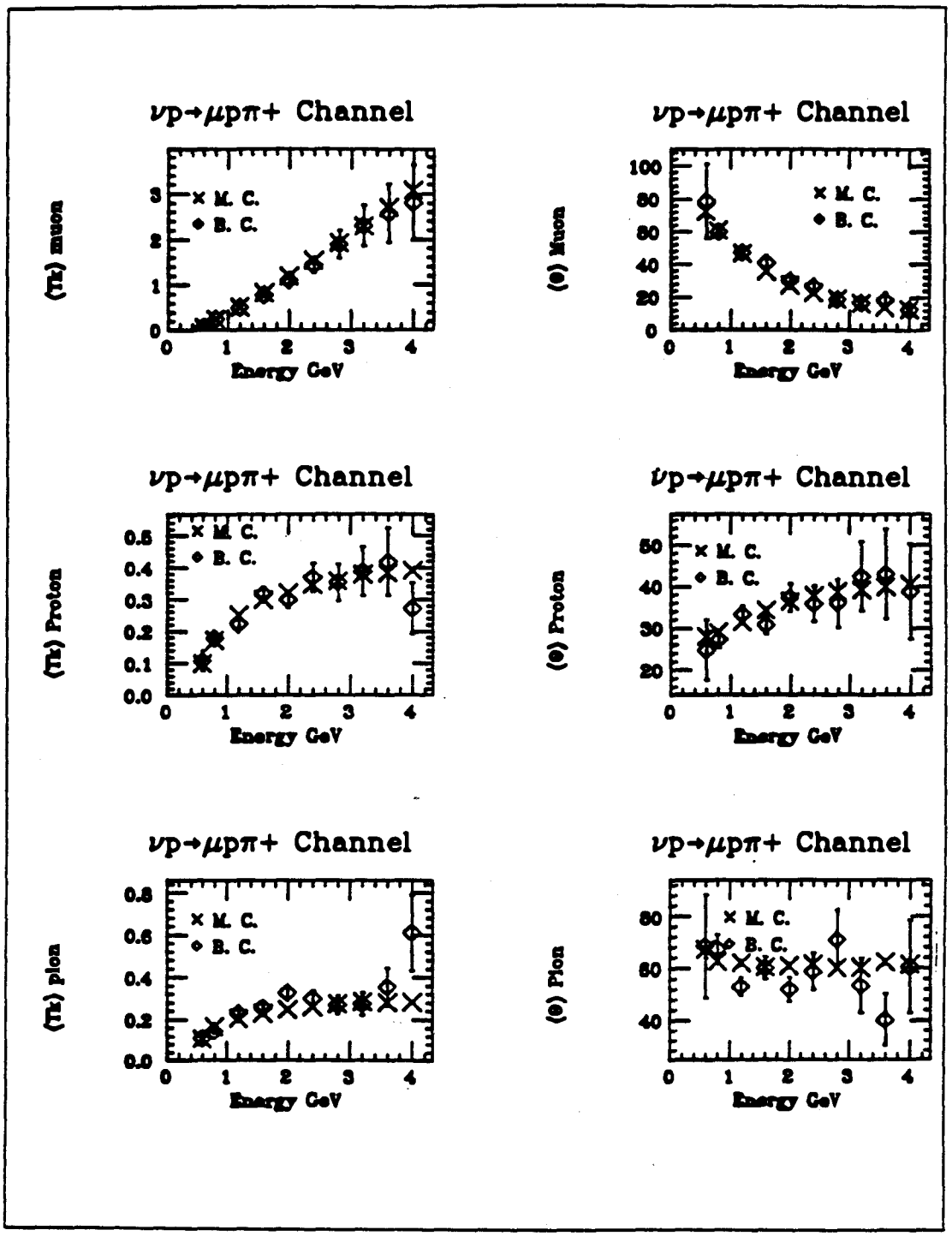

Figure 4.6: Comparison of Monte Carlo event generator with BNL 7 foot bubble chamber results for $\nu_\mu p \rightarrow \mu^- p \pi^+$. The horizontal axis represents event energy as reconstructed for the bubble chamber data and as thrown for the Monte Carlo.

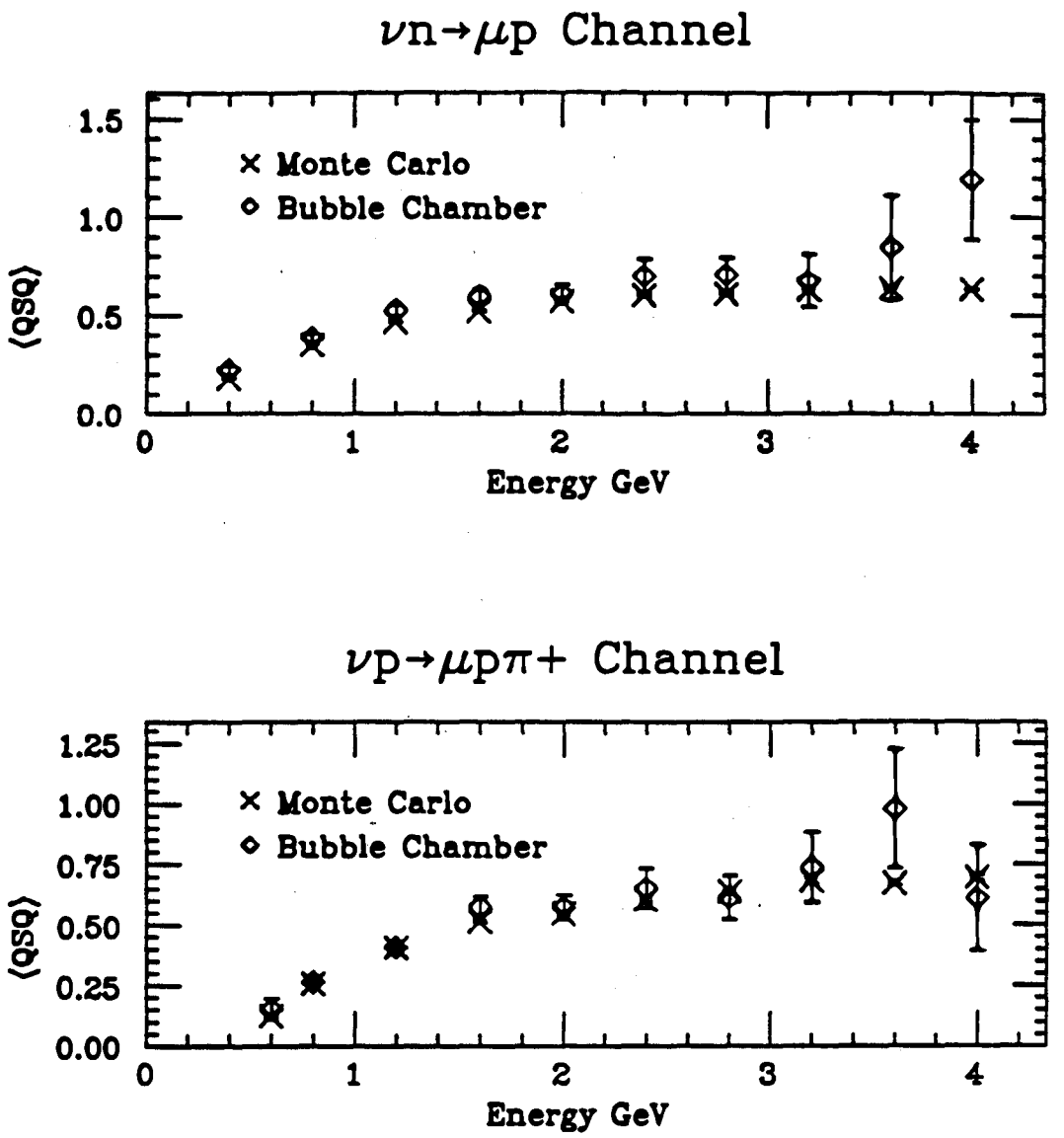

Figure 4.7: Comparison of Monte Carlo event generator with BNL 7 foot bubble chamber Q^2 distributions. The horizontal axis represents event energy as reconstructed for the bubble chamber data and as thrown for the Monte Carlo.

due to the missing neutral particle, inherent in the identification of these event types in the bubble chamber analysis. The results for the quasi-elastic and $\mu p\pi^+$ cases indicate that the Monte Carlo is correct at the kinematic level.

Details of the acquisition of the A2 test beam data have been discussed in chapter 2. Several aspects of the electron data were compared with Monte Carlo generated electrons. A comparison of the two is presented in Figure 4.8 through Figure 4.11 for 1 GeV showers showing length, number of hits, transverse energy distribution or radius, and the number of skipped planes. Length of the shower was defined as the number of planes from the most upstream hit in the pattern to the point in the shower where not more than six consecutive empty planes were detected. The transverse extension of the shower used for the length determination was ± 2 wires from the center of the pattern. The transverse energy distribution was simply the total pulse area measured for all cells ± 1 wire from the transverse center of the shower divided by the pulse area for all cells ± 2 wires from the transverse center of the shower. The number of skipped planes refers to the number of planes within the longitudinal and transverse limits of the shower in which no energy was deposited. This number was significant as it demonstrated the random nature of electromagnetic showers which was an important feature utilized in their identification. The differences in the distributions for length, number of hits, and radius are due largely to noise hits in the A2 data. The agreement in the number of skipped planes between the data and Monte Carlo is better because this parameter is less sensitive to extraneous hits unrelated to the shower.

A comparison for 1.2 GeV proton and .6 GeV pion data with Monte Carlo is presented in Figure 4.12. The track length distribution for protons generated with the Monte Carlo agreed well with that measured in the test beam. The agreement for pion track lengths was not very satisfactory. However, because the length of Monte Carlo tracks was greater than that of the data tracks, the chance of selecting a pion as a muon was less for the real data than for the simulation. The signifigance of this to the muon analysis will be futher discussed in Chapter 5 (section 5.6) where the muon neutrino backgrounds are discussed. The effect of this disagreement on the electron neutrino background is not known.

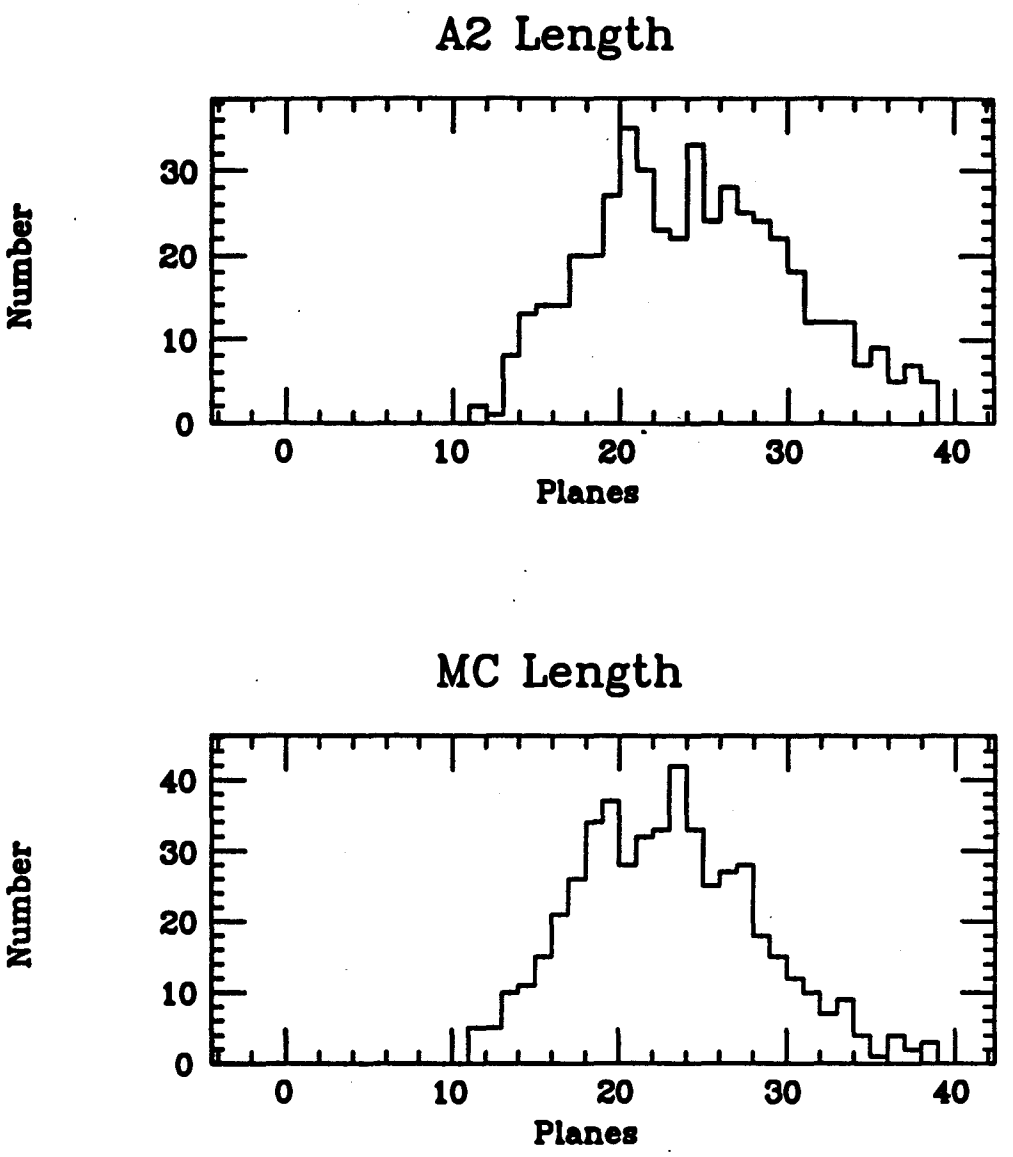

Figure 4.8: Electron shower length for 1 GeV electron for A2 test beam and Monte Carlo.

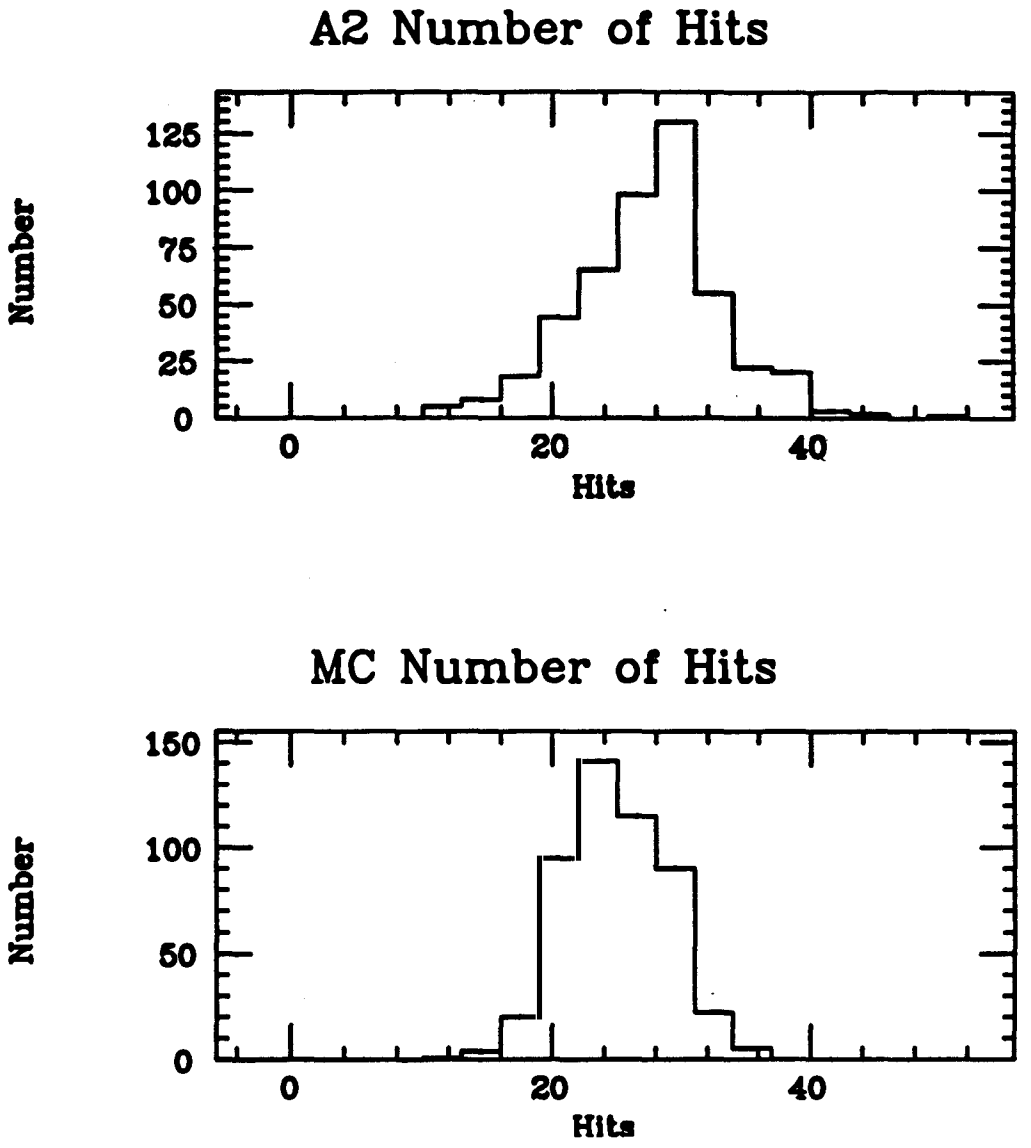

Figure 4.9: Number of hits in 1 GeV electron showers for A2 test beam data and Monte Carlo.

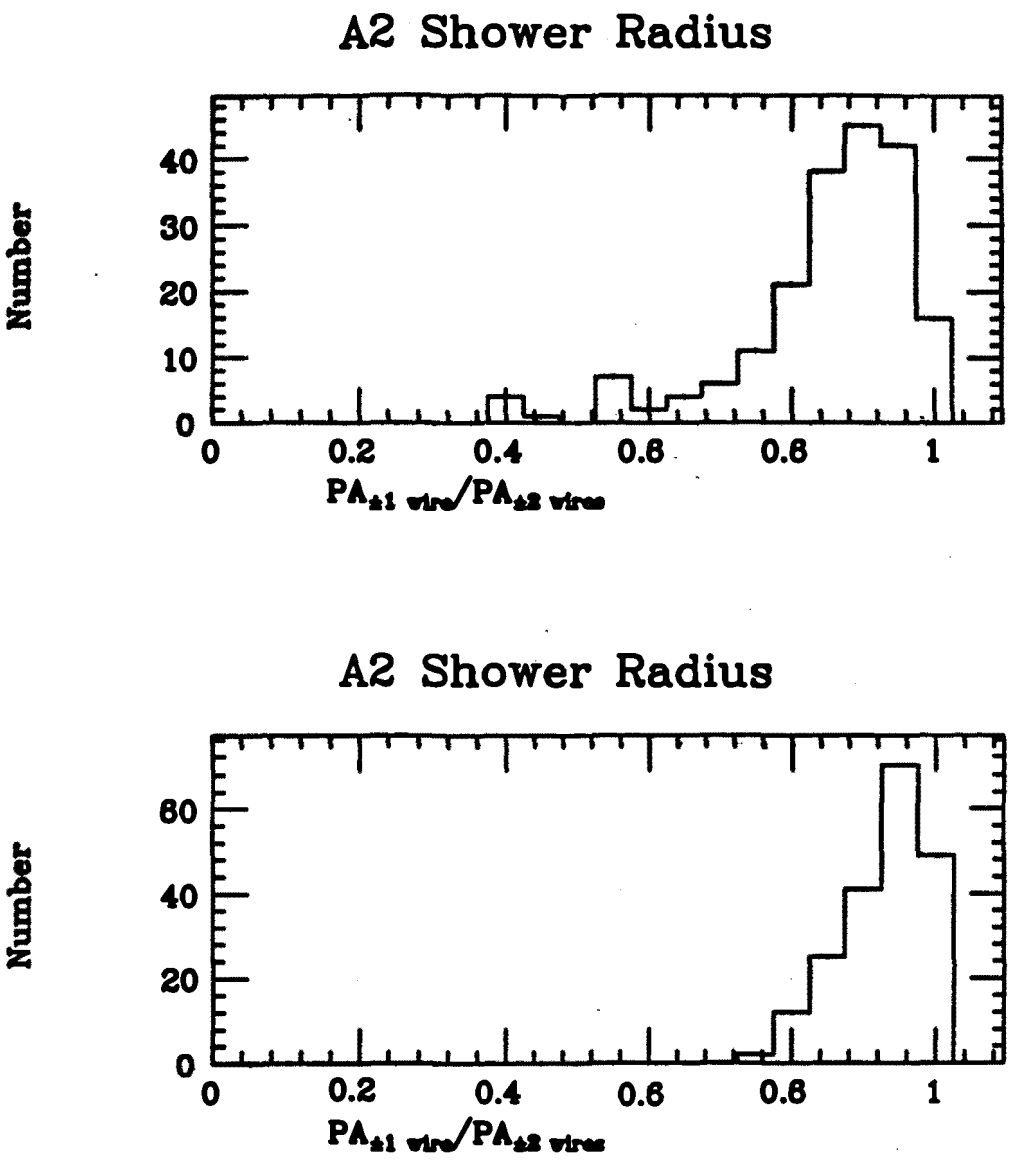

Figure 4.10: Transvers energy distribution in 1 GeV electron showers for A2 test beam data and Monte Carlo.

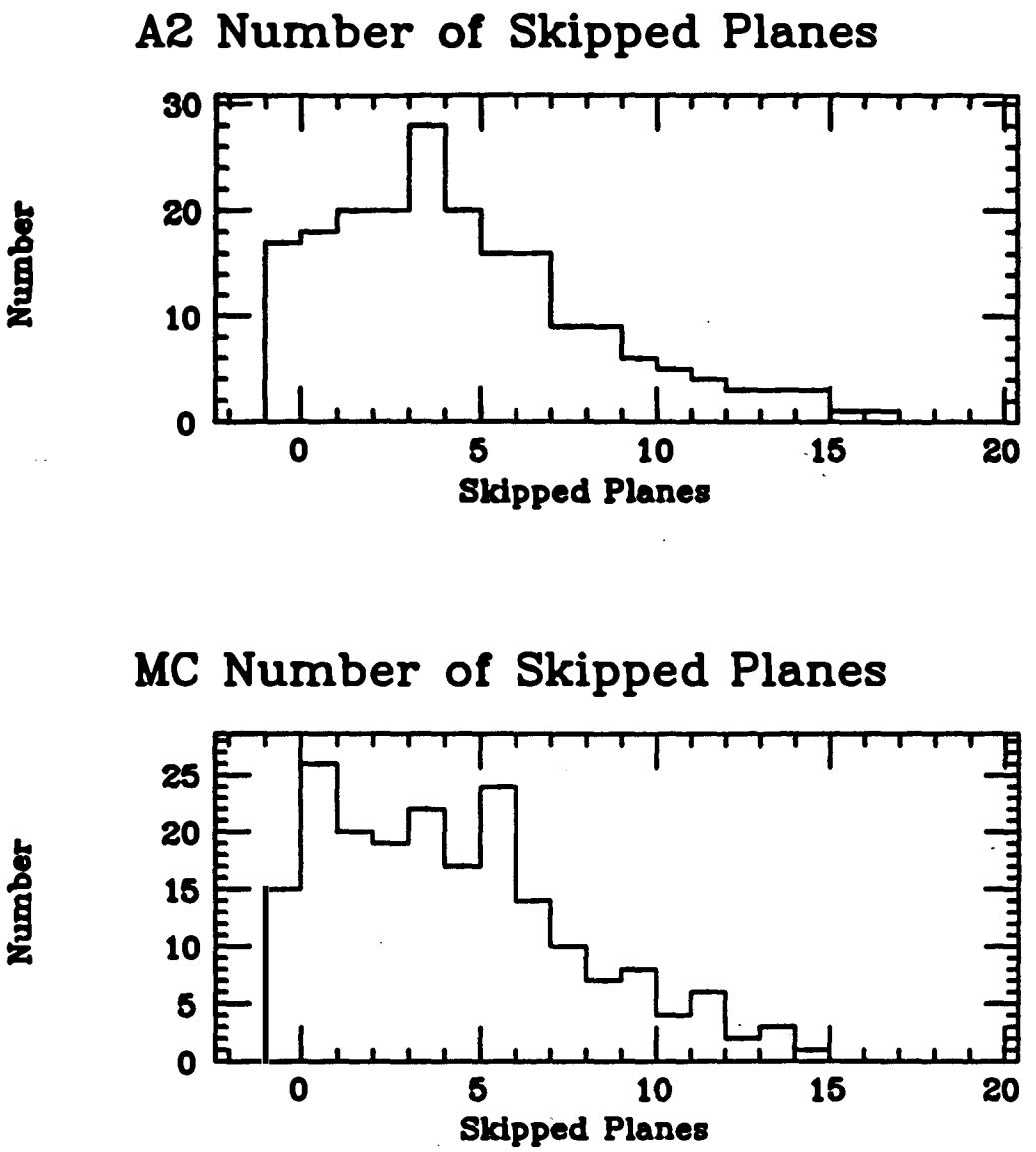

Figure 4.11: Number of skipped planes in 1 GeV electron showers for A2 test beam data and Monte Carlo.

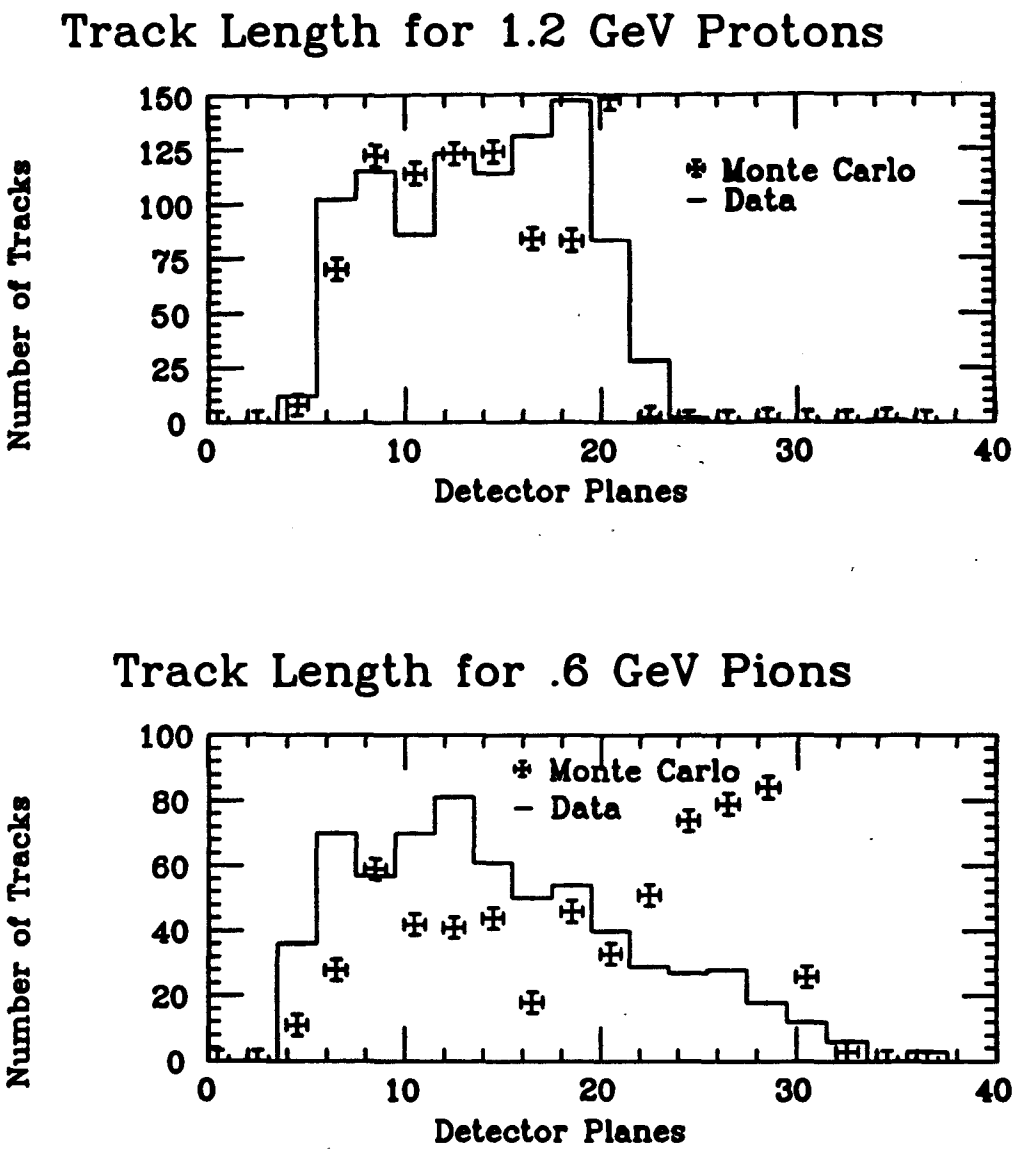

Figure 4.12: Comparison of Monte Carlo proton and pion track length with data from the A2 test beam.

Chapter 5.
Muon Analysis

5.1. Data Screening

The trigger, as described in Chapter 2, provided information for every beam spill. Most of the triggers, however, were completely empty or contained only random noise hits in the detector. An initial series of edits was established to eliminate these empty events. In the muon analysis there were a total of four edits. The first two, Edit 1 and Edit 3, were to reduce junk events; the third, Edit 6, selected 'contained' track and shower events; and the last, Edit 7, selected contained tracks with length greater than 23 planes. The first two edits were carefully checked by manual scans on random samples of the data and the final two were checked with manual scans of the entire edited samples. These edits are discussed in Appendix D. The effect of each of these edits on the reduction of the data sample is shown in Table 5.1 on page 114.

5.2. Muon Reconstruction

The muon event reconstruction proceeded upon the edited data with several steps. First, a pattern recognition algorithm was employed which found track-like hit patterns, matched them in the X and Y views, and selected a vertex position. Second, the calculated trajectories of these tracks were used to determine which scintillator phototubes to use in the timing, and a time was extracted from the event. Third, the track momentum was calculated from range if the track stopped in the electron absorber or toroid steel, and from bending in the toroid magnetic field if the track penetrated the back of the toroids. Next, the vertex angles of the tracks were determined using approximately the first half of each track. Each event was then classified based upon vertex hit patterns and finally the energy of the incident neutrino was calculated from the kinematics of the particular event classification.

5.2.1. Pattern Recognition

The pattern recognition algorithm for hits in the main detector, though similar to that used in the final edits, requires higher quality tracks than that of the edits. A typical example of a muon track is contained in Figure 5.1. Initially, track-like groups of hits were searched for and associated into tracks allowing up to 10 skipped planes within the pattern. Then the end points of these tracks were matched in the X and Y views with a difference of 5 planes allowed at either end. After this matching, vertex points were determined which agreed with track orientation and location in the detector. The track and vertex associations for each event were examined visually to assure correctness, and incorrectly fit events were entered manually. These incorrectly fit events included those in which obvious cosmic rays had been included in the event patten. Of the total muon candidate sample, approximately 10% required manual intervention.

For tracks which entered the toroids, a pattern recognition algorithm loosely selected hits which were then more carefully screened and bad ones rejected. Initial pattern recognition in the toroids was accomplished by choosing hits within the multiple scattering limits of the track entering the toroids. Then these hits were fit to a parabola and additional hits selected which were within 4 wires of the track. The second screening more carefully determined the positions of hits in the toroids to be used in the subsequent momentum range or fit determination.

In planes where multiple hits occurred in adjacent wires averaged positions were used. In planes where multiple hits were not in adjacent wires within the plane a decision was made regarding which point to use. This selection was based upon straight line segments which were constructed using the positions of unambiguous hits in other planes. The end point of the track was defined as two or more missing planes in the trajectory. Toroid hits chosen were examined visually to avoid improper toroid patterns.

5.2.2. Event Timing

Once the trajectory of the tracks in each event was determined, the track fit parameters for the leading (longest) track were employed to extract the event time from the scintillation counters. This was performed by calculating the position where

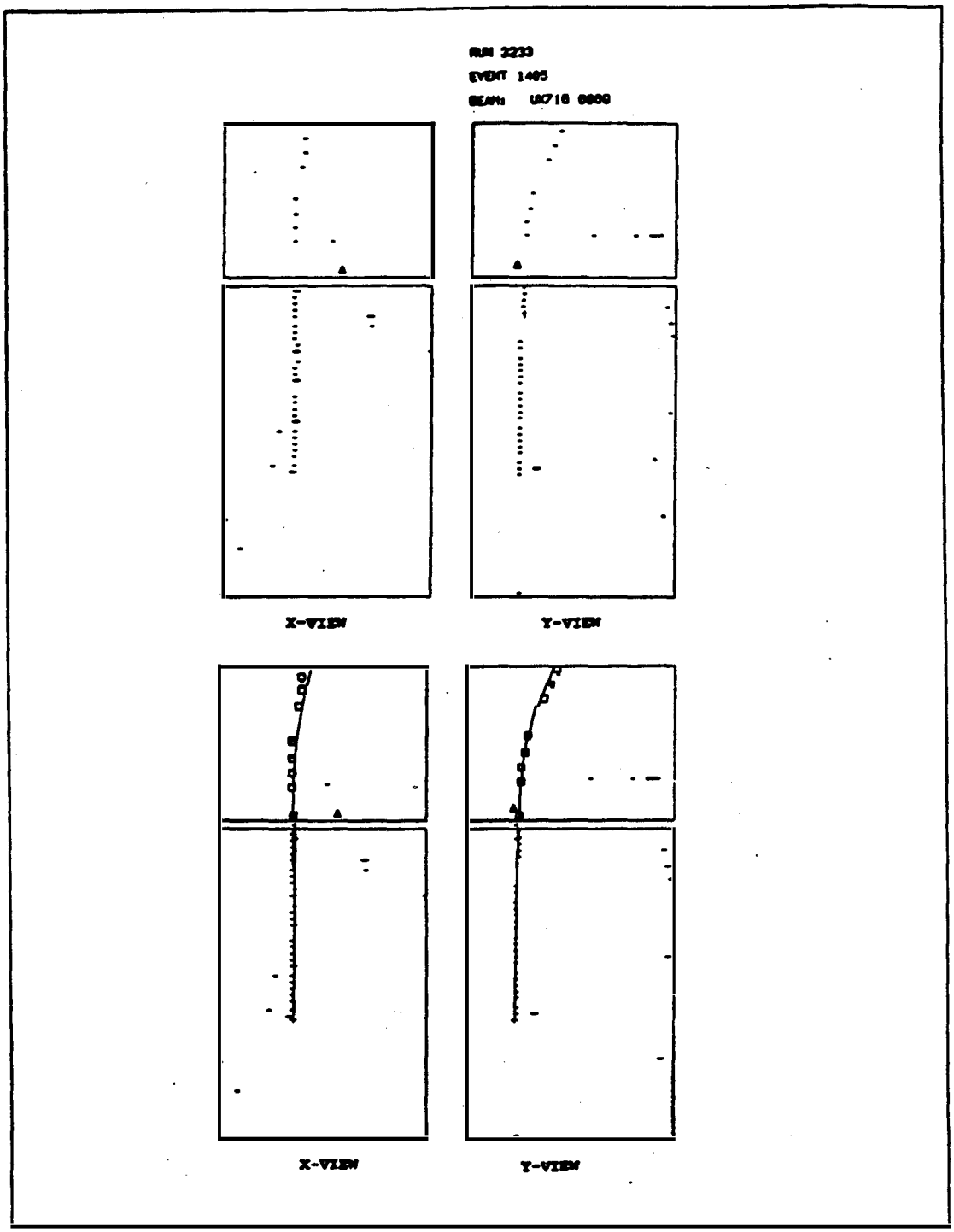

Figure 5.1: A typical example of a muon neutrino event with the muon penetrating the toroids. Also shown is the muon fit for the event.

the track passed through each scintillator plane, translating this position into plate location in the plane, and finally decoding which phototubes to use in the time. The time from each of these phototubes was extracted from the TDCs in conjunction with the pulse areas recorded in the corresponding FADC channel. These times were then corrected for time of flight to the upstream plane of the detector and the average value of all of the times was calculated. Then, the times were scanned again and those outside of one σ from the mean were eliminated and a new mean and σ calculated. This technique eliminated the danger, in the rare but possible case, of spurious phototube times causing gross timing errors. These event times were further corrected by subtracting a constant which was calculated from times recorded with the Cerenkov counters located in the pion decay tunnel. This was done to eliminate jitter due to extraction timing variations.

5.2.3. Vertex Angle

The points selected by the pattern recognition routine were re-evaluated using the scintillator time as the PDT start time and the drift distances for each hit in the track were calculated. Vertex angles were determined using approximately the first half of the track to optimize angular resolution and avoid multiple scattering effects which increase as the track loses momentum. For a few tracks special rules were required. For example in very short tracks no less than 4 hits per view were used and in long tracks only the first 15 hits per view were used. For this section of the track right–left ambiguities (due to drift chamber geometry) were resolved using the drift distances and a simple χ^2 minimization technique. The angular resolution achieved using the technique discussed above is shown in Figure 5.2. It was measured using single muon tracks and events generated with the Monte Carlo. The angular resolution for the reconstruction was less than 1 degree for single tracks. However, as seen in the lower plot of Figure 5.2, the resolution for muons measured in events the angular resolution was worse (2 degrees) due to the uncertainty in hit selection near the vertex.

5.2.4. Particle Energy from Track Range

Track energy for particles which stop in the main detector or toroid steel was determined from range. Beginning with their most downstream hit and an assumed

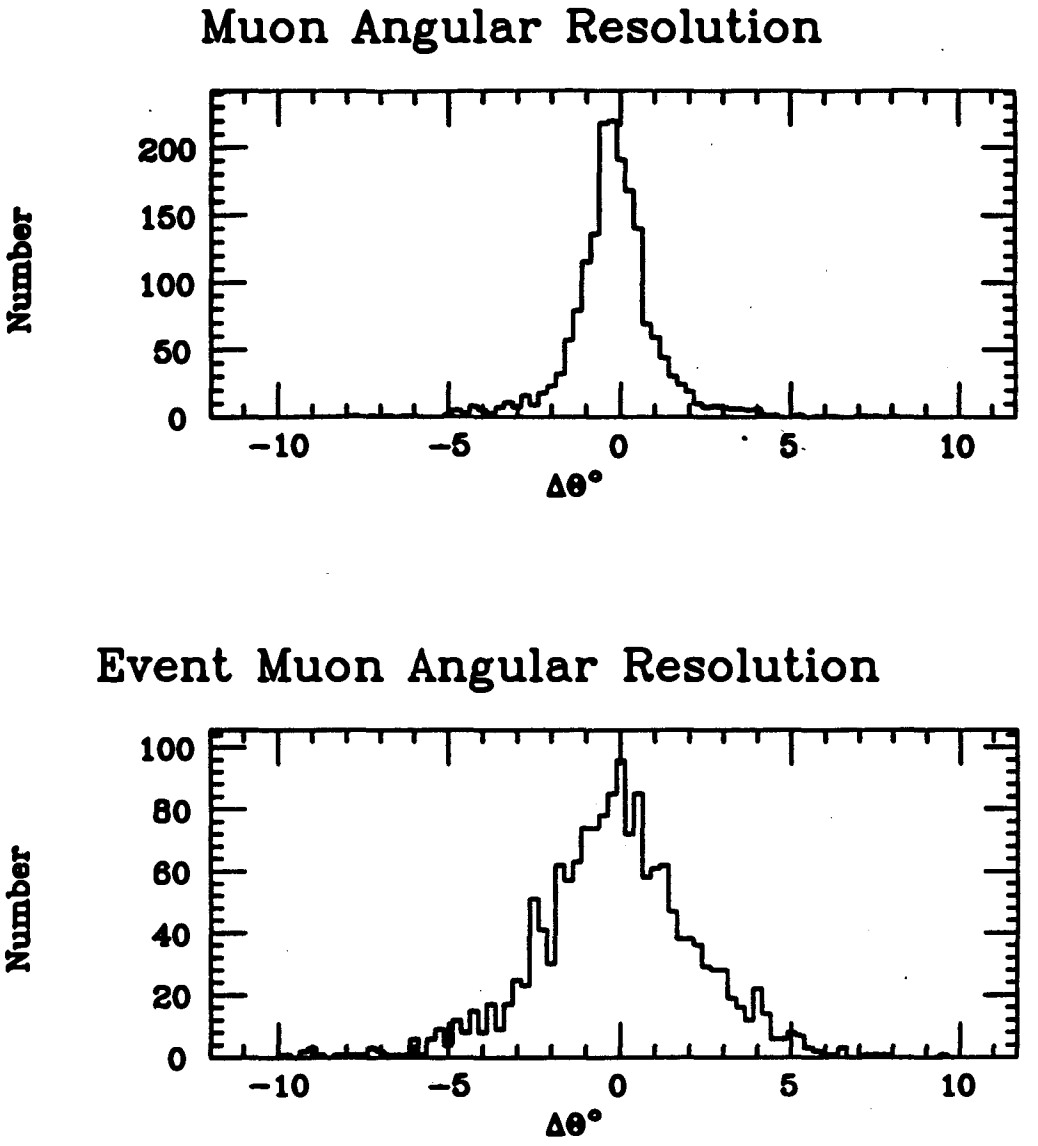

Figure 5.2: Angular resolution of muon reconstruction as evaluated with Monte Carlo single muons and Monte Carlo events.

initial energy at that location, the track was stepped through the detector backwards adding amounts of energy at each plane based upon the calculated dE/dx using the model of Sternheimer et. al.[25] for ionization energy loss. The assumed initial kinetic energy was approximately 12 MeV in the concrete and aluminum absorber and 100 MeV in the toroids. Empirically, the range energy relationship is given by

$$R = const.T^{1.75}. \tag{5.1}$$

This is valid for medium Z elements with $.1 < \beta < .7$. With this, the energy resolution for a particle using its range is

$$dT/T = \frac{1}{1.75} dR/R. \tag{5.2}$$

Therefore, for a track which ranges out after 80 planes in the main detector, if its length is determined to ±4 planes, has a kinetic energy of approximately 1 Gev and a kinetic energy resolution of about 3%. If a 1 Gev track ranges out in the toroids where the uncertainty in the range is approximately half the thickness of the next plane of steel, then the energy resolution will be 6% for the 12.7 cm plates and 8% for the 17.8 cm steel plates.

In the calculation of the range, corrections were required for the angle at which the track passed through the material of the detector. In the main detector, the correction was simply $1/\cos\theta$, where θ is the angle of the trajectory with respect to the beam axis. This represented an approximation since multiple scattering tended to change the direction of the particle as it went through the material; studies indicate that in most cases this correction is small in the main detector. In the toroids, the direction of the track changed rapidly due to the magnetic field and the large degree of multiple scattering in the iron. Therefore, the range calculation was based upon the hit to hit distance as the particle traveled from one measurement plane to the next.

Only muons were considered to have entered the toroids and for tracks which stopped in the steel plates the energy was determined via range. Tracks entering the toroids were required to travel at least 20 planes in the electron detector (1.5 nuclear interaction lengths) and through the first steel toroid (.75 nuclear interaction lengths), thus they were most likely muons. The energy was determined by assigning

an initial momentum of 100 MeV/c to the track and stepping through the steel with the dE/dx energy loss appropriate for the track momentum. The distance through each steel plane was corrected by the angle through the steel at that plane as calculated from the hit positions. This procedure was performed for the condition where the track stopped at the point indicated by the hits, as well as for the case where it penetrated an additional iron plate. After these two conditions for the track were also appropriately stepped through the electron detector, a minimum and maximum momentum were determined. The average of P_{min} and P_{max} was used for the track's momentum, and the uncertainty established as $\pm (P_{max} - P_{min})/2$.

Due to this uncertainty of where the track actually stopped in the toroids, the momentum resolution was much poorer there than in the electron detector. A simple calculation indicates that a 1 GeV normally incident muon has an energy loss of 150 MeV per 12.7 cm plane, and 210 MeV per 17.8 cm plane. This limits the resolution of muons in the energy region of 1 GeV to 7.5% for those stopping in the first three planes and 10% for those stopping in the last 2 planes.

Work performed with the event Monte Carlo provided the resolutions indicated in Figure 5.3. These plots are from reconstruction of 1700 single muon Monte Carlo tracks which were thrown with a continuous momentum distribution between .5 and 6 GeV/c at angles between 0 and 45 degrees and originating near the center of the detector. Of these, 200 were determined to have stopped in the electron detector, 400 stopped in the toroids the remainder penetrated all 5 planes of the toroids. Gaussian fits to the distributions give $-.07 \pm .027$ for the energy offset and resolution of stopping tracks in the electron detector and $-.043 \pm .084$ for toroid stopping tracks. The small peaks outside of the main distributions in both plots were caused by high energy tracks in which the hit pattern in the toroids was not properly identified. Due to this incorrect identification the track was determined to have stopped in the toroids and its momentum underestimated. Although this appears as a major problem, in fact the area contained within these small peaks represents only 4% of the tracks entering the toroids. Furthermore, because the number of events in the real data with energy high enough to penetrate all 5 planes

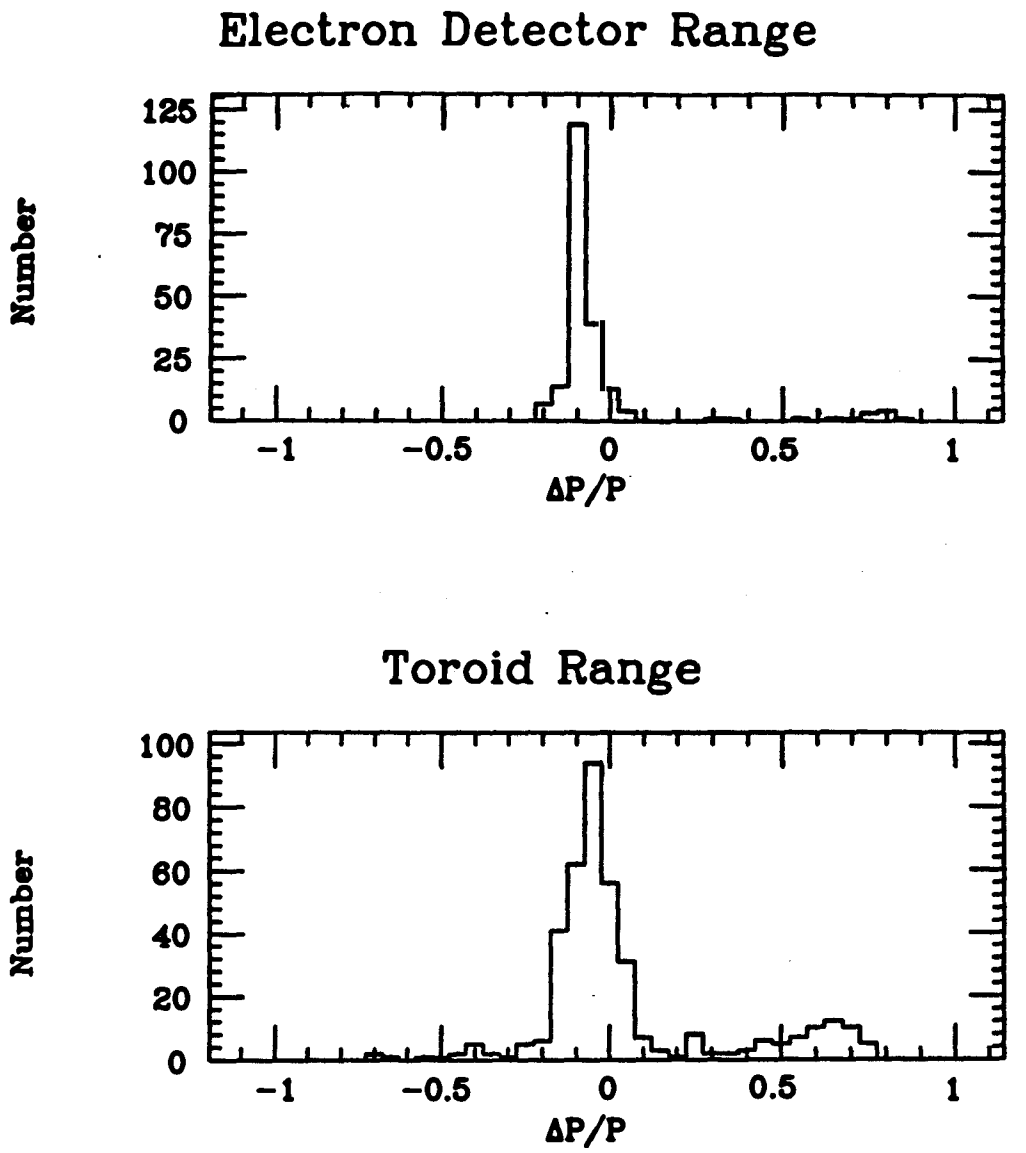

Figure 5.3: Muon range momentum resolution as determined with the event Monte Carlo. Distributions are for $(P_{M.C.} - P_{fit})/P_{M.C.}$.

of the toroids was less than 30% of the total, this misidentification should have occurred in only about 1% of the data fits.

5.2.5. Track Momentum from Bending in Toroids

In cases where the track penetrated all 5 steel toroid planes a more sophisticated momentum analysis was required. First the trajectory of the track as it left the electron detector was determined using the final 20 planes of measurement and their drift distance to eliminate the right–left ambiguity. With this, the momentum of the track was determined by stepping through a series of momenta and calculating the trajectory of the track through the toroids. For each momentum, a scattering matrix was calculated and inverted, as discussed in Appendix B. Using this correlation matrix, a χ^2 was calculated for the fit as it related to the actual hit positions. The momentum with the minimum χ^2 was then selected and uncertainties chosen based on χ^2 variation of 1 unit over the minimum. Details of the trajectory calculation can be found in Appendix A and a discussion of the measurement of the toroid field in Appendix C. A plot of the measured field and the function used to approximate it is represented by Figure 5.4.

The resolution of the momentum measurement in the toroids was determined in several ways. A rough calculation was made assuming values for the magnitude of multiple scattering and the expected radius of curvature due to the magnetic field. Cosmic ray tracks entering the back of the toroids and ranging out in the electron detector were collected and measured. The momentum uncertainty based upon the characteristics of the χ^2 from the momentum fit gives an indication of the resolution. Finally, using Monte Carlo events and comparing the reconstructed momentum to the values thrown, the resolution can be examined.

A rough estimate of the momentum resolution shows that ideally it is independent of the particle momentum. The multiple scattering is given by the Fermi approximation as

$$\Delta\theta = \frac{.015\,(GeV/c)}{p\beta}\sqrt{\frac{l}{l_{rad}}}. \tag{5.3}$$

The bending angle due to the magnetic field is given by

$$\theta = \frac{3 \times 10^{-4} B(\mathrm{kG}) l(\mathrm{cm})}{p(\mathrm{GeV/c})}. \tag{5.4}$$

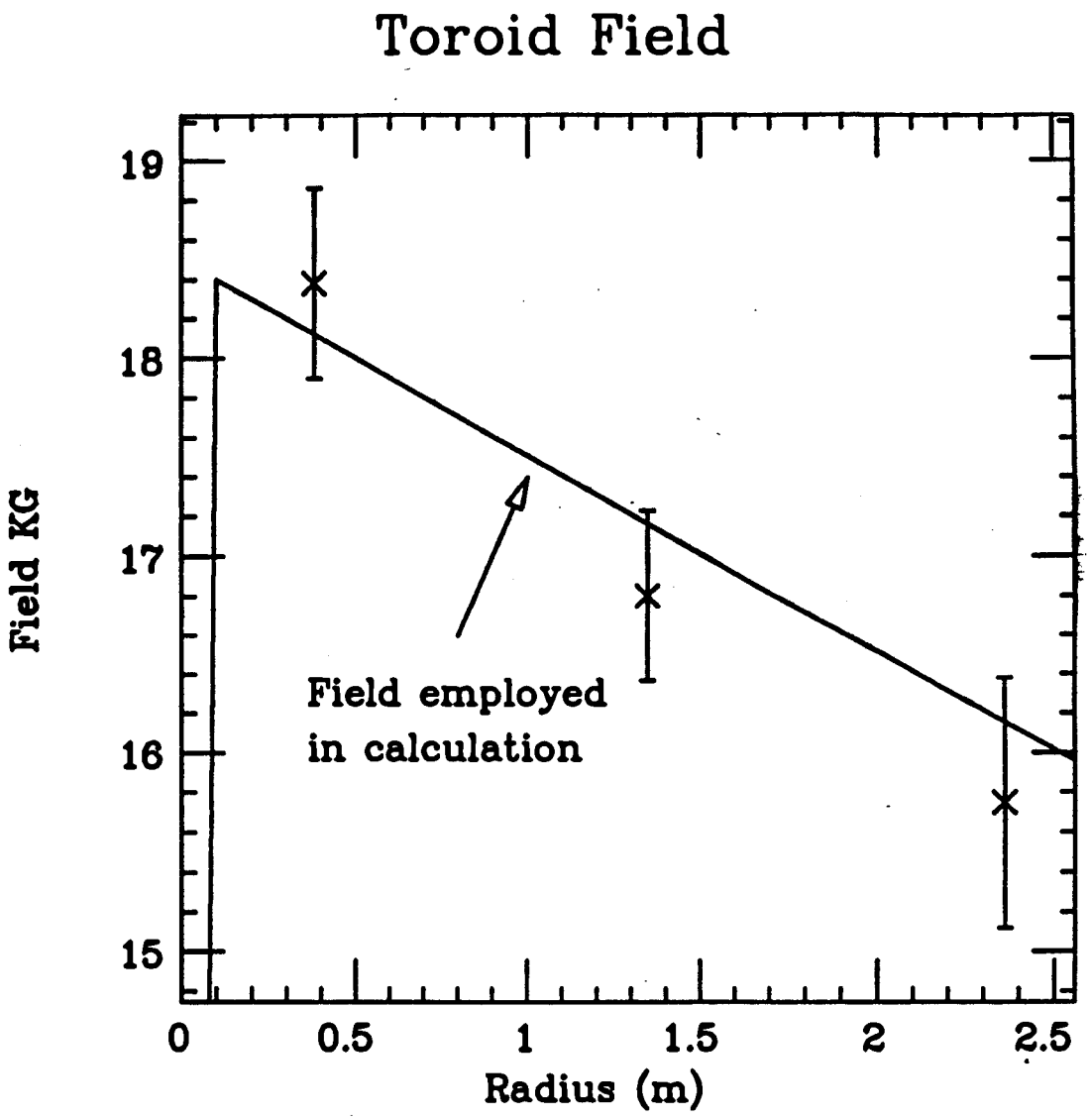

Figure 5.4: The toroid field measured and that used in the reconstruction program.

Thus the resolution is

$$\frac{\Delta p}{p} = \frac{\Delta \theta}{\theta} \simeq \frac{.015\,(GeV)}{3 \times 10^{-4} B\sqrt{l l_{rad}}}. \tag{5.5}$$

Therefore, for our magnetic field $B \sim 18$ kG, the total thickness of steel $l = 73.7$ cm, and the radiation length of iron $l_{rad} = 1.76$ cm, the resolution is approximately 23%.

The initial test of the toroid track fitter and measurement of the resolution was performed with cosmic ray muons entering the rear of the detector. With the procedure for fitting tracks in the toroids, the momentum was measured for a select group of cosmic rays which entered the back of the toroids, were bent by the magnetic field, then entered and ranged out in the electron detector. By comparing the range momentum to that calculated from their bending an estimate of the resolution was achieved and is shown in Figure 5.5. The statistics were limited with only about 80 events, but in principle it could be done much better. It has the severe limitation that the momentum of the tracks collected were within a narrow range from about 2 to 3 GeV/c constrained by the size and geometry of the detector.

The resolutions based on the χ^2 function have also been determined. By definition the momentum was one sigma away from its most probable value when the χ^2 was 1 unit greater then the minimum χ^2. A typical χ^2 curve for an event is shown in Figure 5.6, the 1 sigma points calculated for the momentum are indicated by the arrows. The positive and negative uncertainties ascertained with this technique are shown in Figure 5.7 as a function of track momentum for Monte Carlo and data events.

Using tracks generated by the Monte Carlo, the toroid momentum resolution as a function of track momentum and angle was calculated. The results for the angular calculation are shown in Figure 5.8 and Figure 5.9 shows the angular resolution in 15 degree slices. The momentum resolution as a function of momentum are given in Figure 5.10 and Figure 5.11. The resolution tends to get worse as the momentum increases due to position measurement errors. In itself, this would not be very satisfying because the same magnetic field which was used in the Monte Carlo was used in the track reconstruction algorithm; however, both the Monte Carlo and the reconstruction were tested in this way.

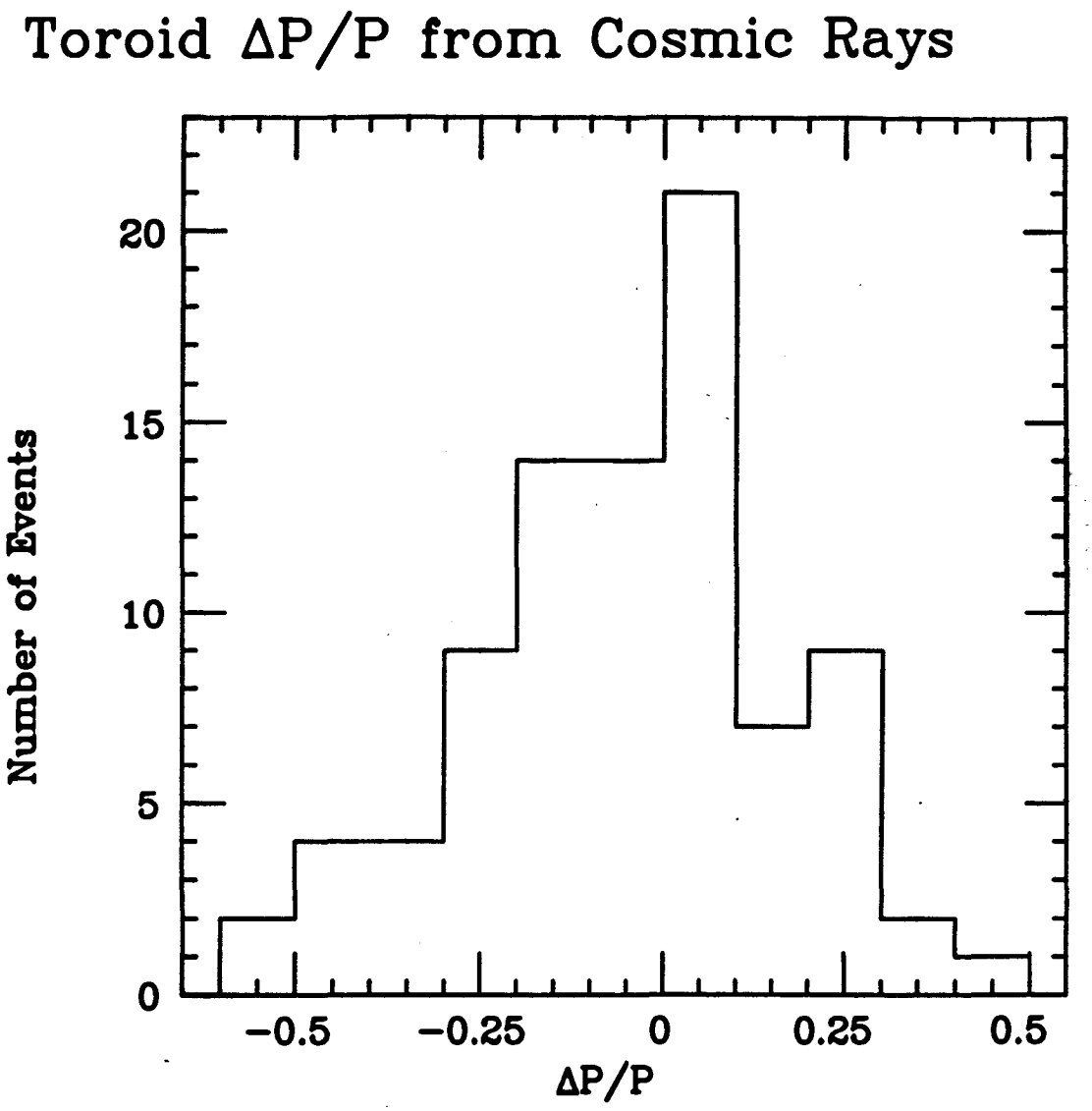

Figure 5.5: Toroid momentum resolution as measured with cosmic rays entering the rear of the detector. The width of the distribution is ±20%.

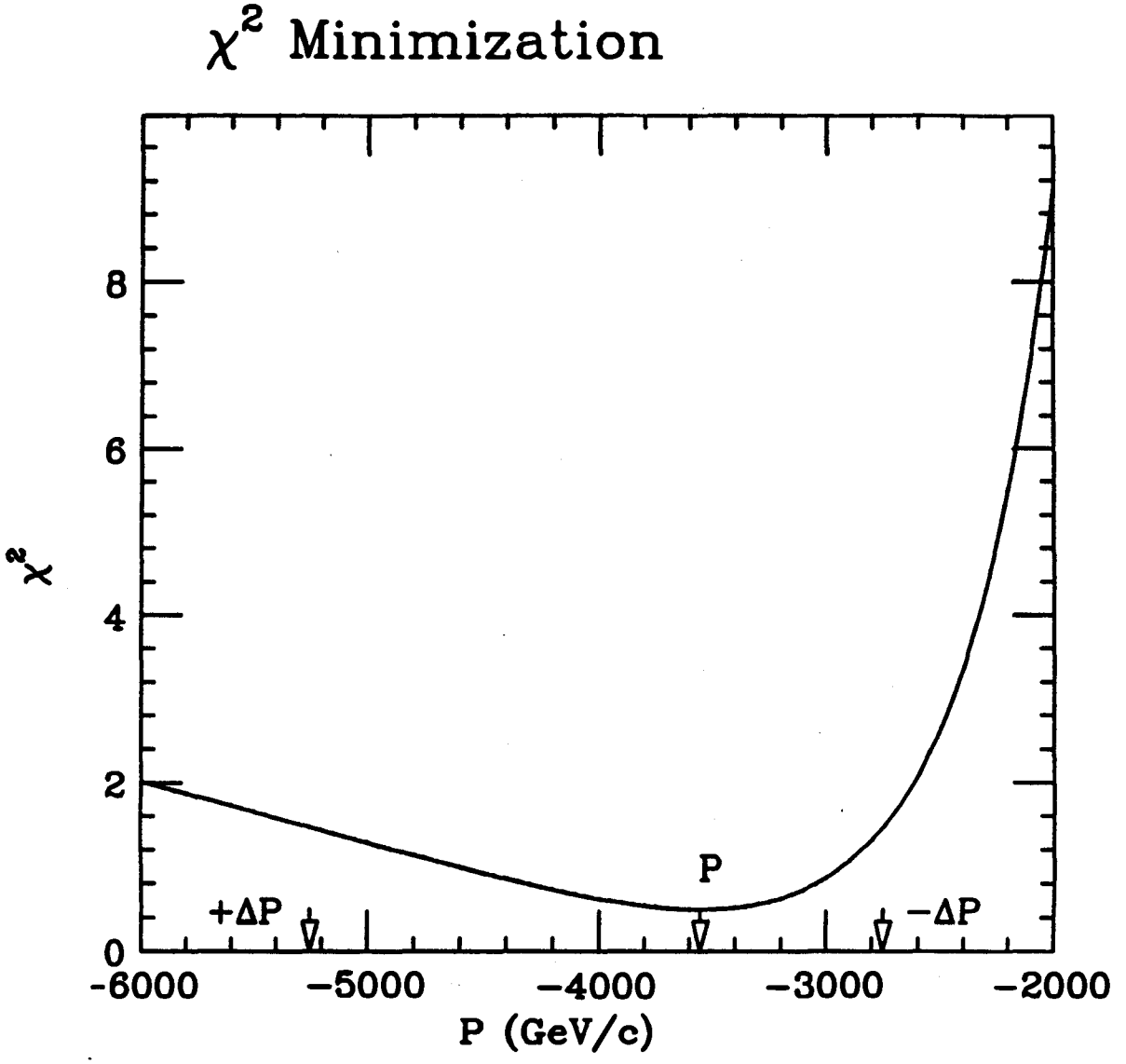

Figure 5.6: A typical χ^2 minimization curve used to determine the track momentum in the toroids. The arrows indicate the location of the selected momentum and the one sigma errors for the measurement and the negative momentum scale indicates a negative charge.

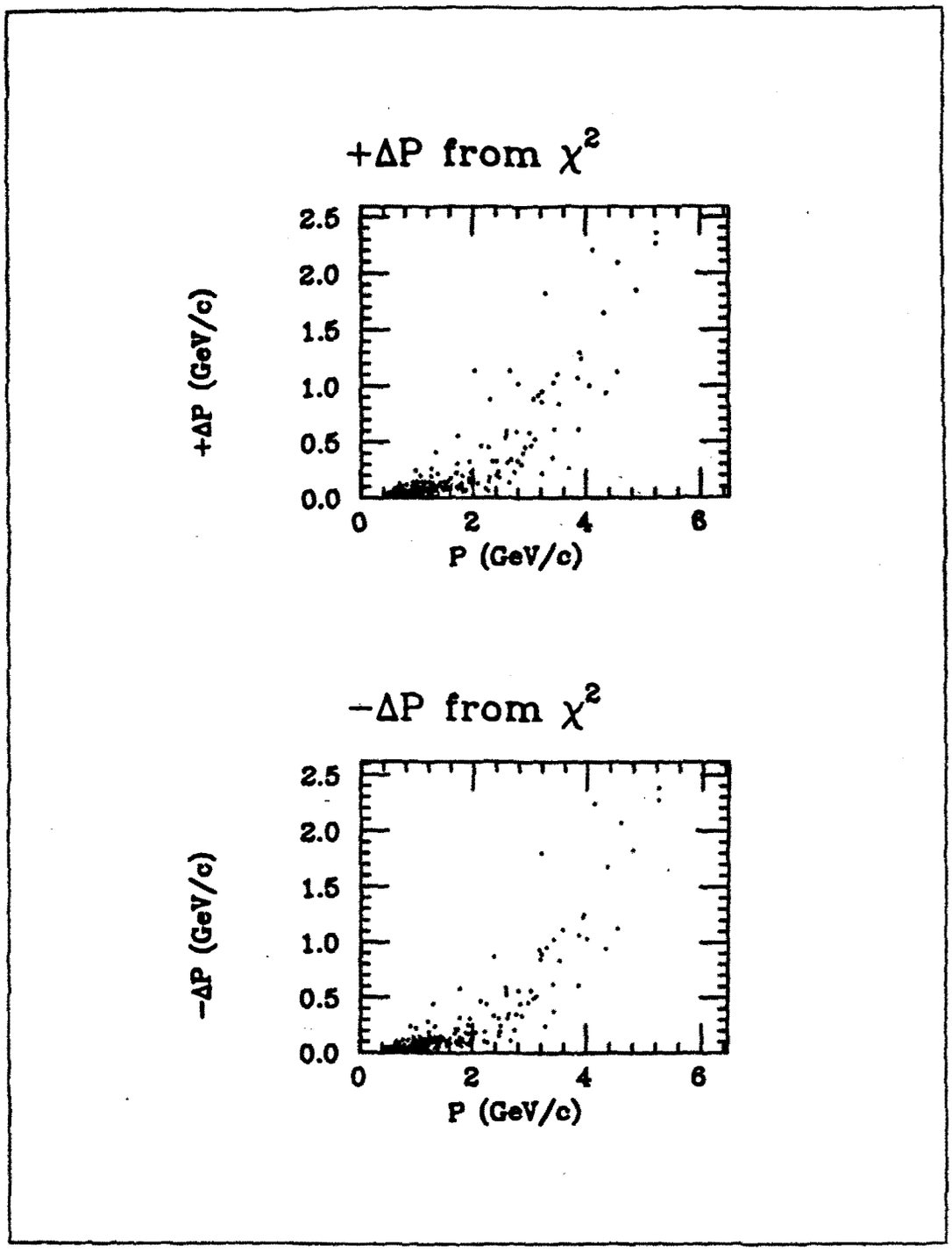

Figure 5.7: Momentum uncertainties as calculated with the χ^2 variation by one unit from the minimum for data and Monte Carlo.

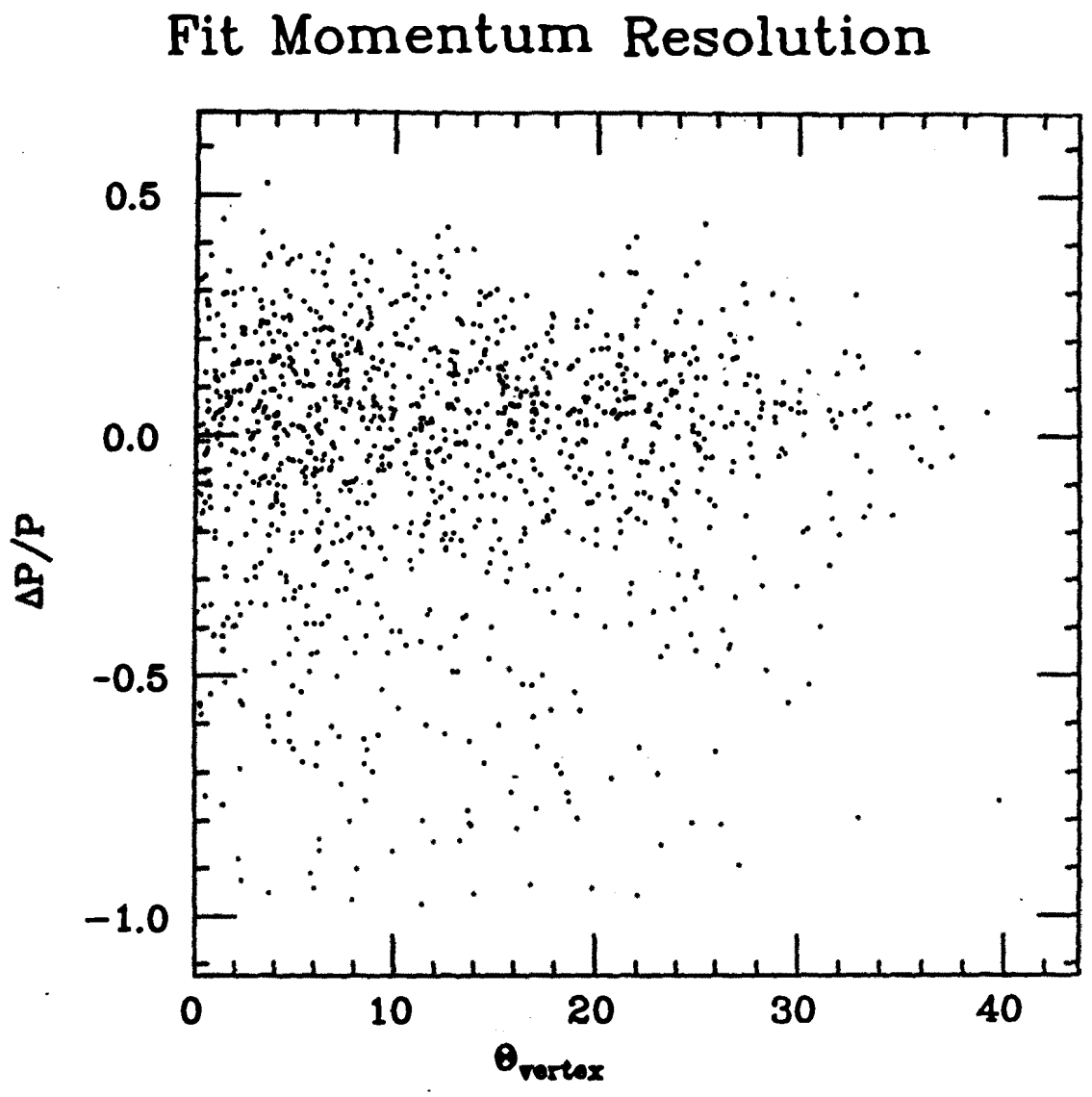

Figure 5.8: Toroid momentum resolution as a function of vertex angle in degrees. Distributions are for $(P_{M.C.} - P_{fit})/P_{M.C.}$.

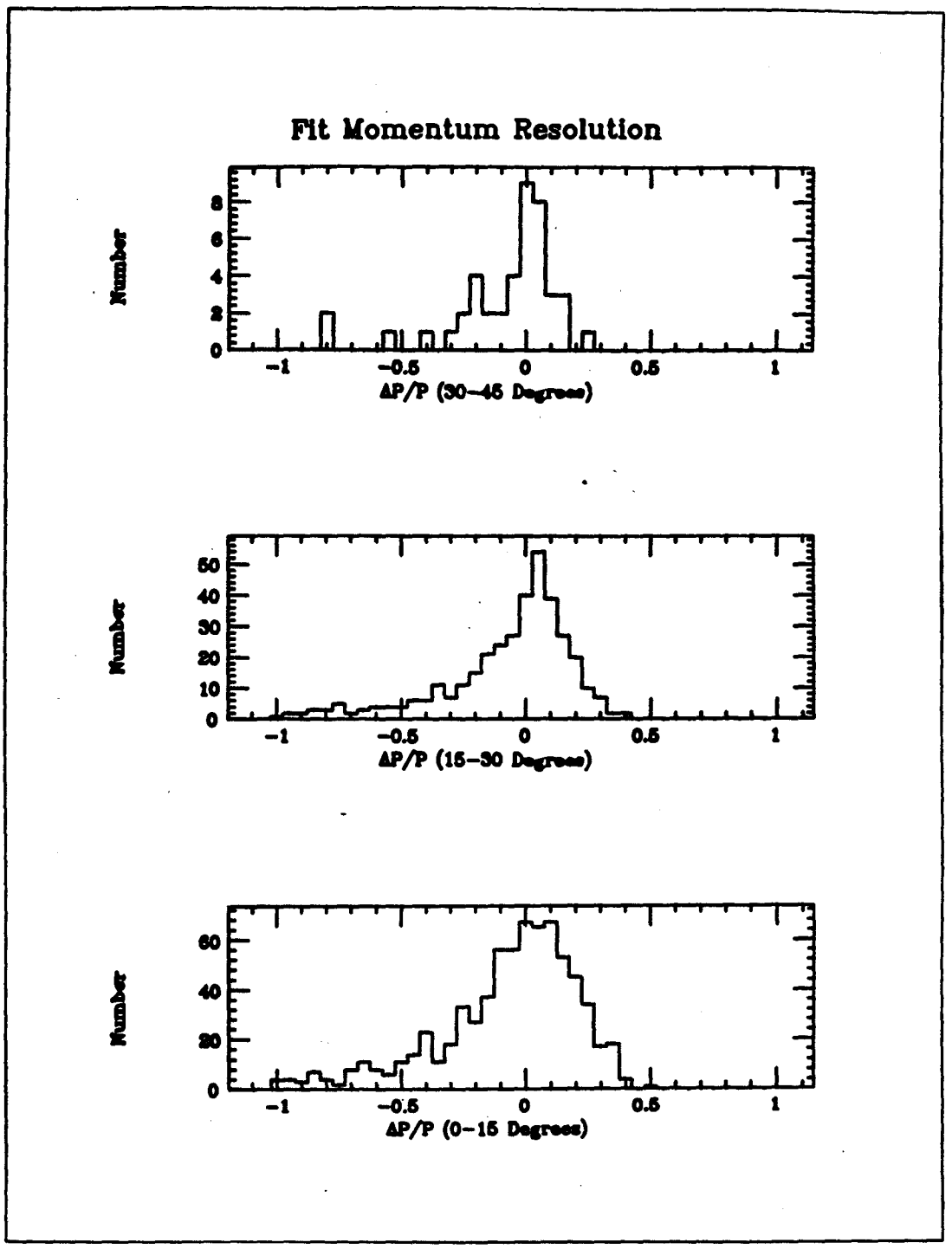

Figure 5.9: Toroid momentum resolution as a function of vertex angle in 15 degree slices. Distributions are for $(P_{M.C.} - P_{fit})/P_{M.C.}$.

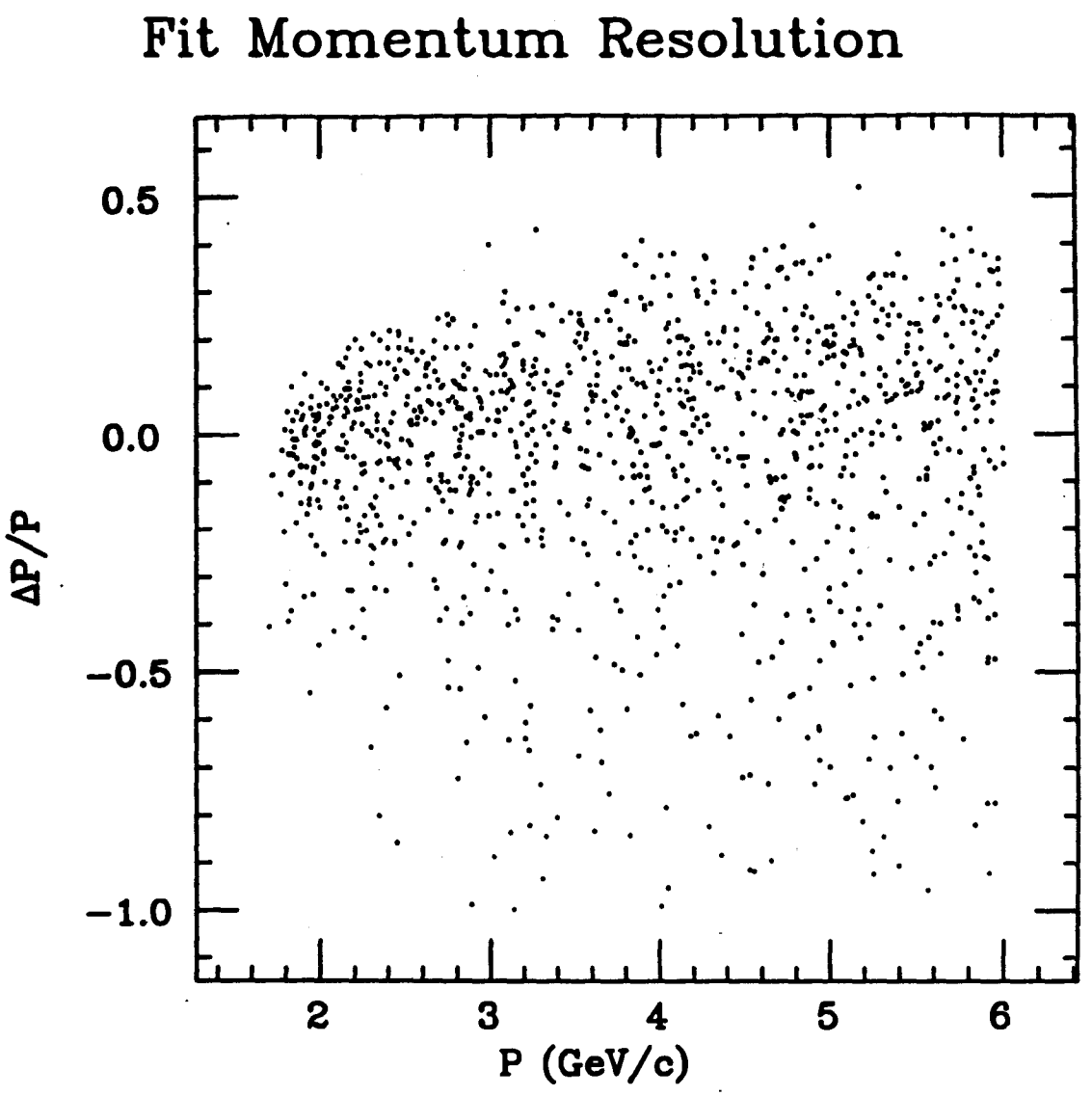

Figure 5.10: Toroid momentum resolution as a function of track momentum. Distributions are for $(P_{M.C.} - P_{fit})/P_{M.C.}$.

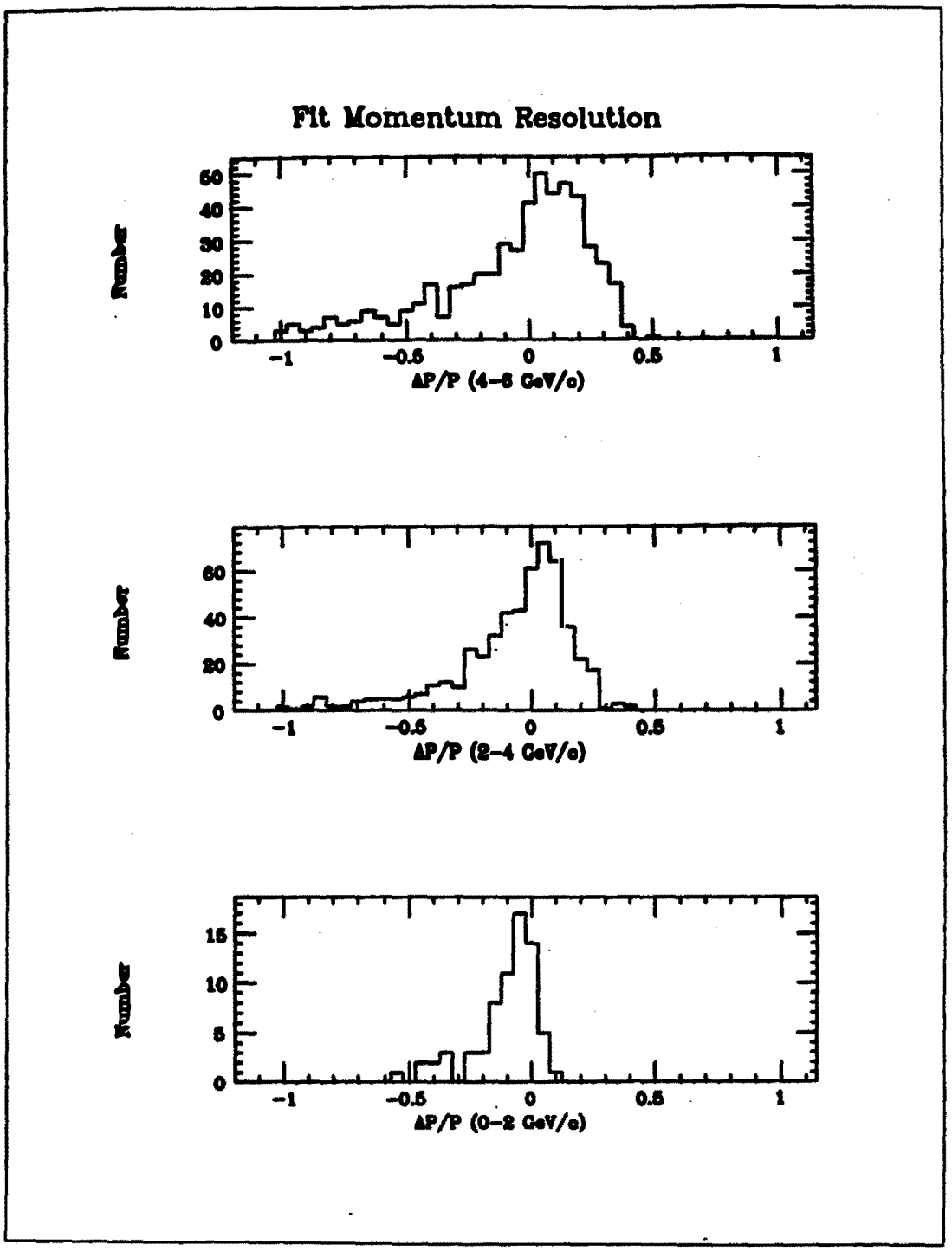

Figure 5.11: Toroid momentum resolution as a function of track momentum in 2 GeV/c slices. Distributions are for $(P_{M.C.} - P_{fit})/P_{M.C.}$.

5.3. Contained Muon Tracks

In order to produce an energy spectrum, tracks which were determined to have entered or left the detector were eliminated. In the electron detector, this was accomplished by projecting the fitted beginning or end of the track onto the next plane in the same view, i.e. two planes away, and checking that it be at least two wires (~ 16cm.) from the edge. The vertex was required to be greater than four wires from the edge and at least 4 planes from the upstream end of the detector. The track was not allowed to begin in the final 20 planes of the electron detector. The following rules were required for a track which exited the electron detector and entered the toroids.

1. Its projection from the electron detector onto the first XY drift tube pair, which was after the first 12.7 cm steel plate, was within a region bordered by a 30 cm band around the edge of the toroids. (note: the reason that the cut on the first toroid planes was more stringent than the remaining planes was due to the fact that this steel plate was approximately 10 cm smaller than the others).
2. Any hit downstream of the first steel plate must have fallen within a region bordered by a 20cm band around the edge of the toroids.
3. A projection of the track, using the final two measurements in a 'connect the dot' fashion, must have been within a 10 cm border in the following plane for tracks which were defined to have stopped in the toroids.
4. If a track was determined to have stopped in the toroids it was required to have no hits in the 6 downstream tracking planes.
5. The track must not have entered the toroids nor at any plane within the toroid steel have pass within a 60 cm square at the radial center of the detector. This rejection was required to eliminate tracks entering the hole through which the copper windings of the toroids were inserted. The large size of this dead region was defined by the construction of the drift tubes in the toroids. All of these criteria combined insured that all of the leading track energy was contained for events, and that cosmic rays entering the detector were not misidentifyed as neutrino events.

In addition to the containment criteria, an additional track length cut and an angular cut were imposed on the data. The minimum track length required was 23 planes in the electron detector and 20 planes for tracks entering the toroids. This represented a longitudinal or z-component energy cut on the muon of 500 MeV. The length cut also reduced the misidentification of pions or protons as muons because 23 planes of detector represents nearly 2 nuclear interaction lengths of material. The angular cut imposed on the tracks was 50 degrees.

5.4. Vertex Classification

In order to sort out the various topologies of events, an attempt was made to classify vertices. The scheme allowed the encoding of each vertex into a combination of (1) leading tracks, (2) all other tracks, (3) remote showers and (4) stubs. The leading track was always defined as that one which had the longest range in the electron detector or that one which penetrated into the toroids. In other words, it is the most likely candidate for the muon. The designation 'other' was used for additional tracks which had enough hits to be measured; this generally meant at least 5 hits in both views. Remote showers were defined as 2 or more correlated hits within 3 radiation lengths of the vertex. Finally, stubs were short hit patterns which were adjacent to the vertex but did not contain enough information to measure a range or an angle. To be included in any of the above categories, the hit was required to have been in time with the event. To be 'in time', the times for the hits were not earlier than the t_0 determined from the scintillation counters and not later than $t_0 + 1.5$ μsec of drift time.

The event classifications were not as obviously related to interaction type as they might appear. Due to intranuclear scattering, charge exchange and absorption occured for pions and protons. Because of the coarseness of the detector, low energy particles simply did not appear, especially when they were produced at wide angles. The charge exchange and absorption have been discussed in Chapter 4. The Monte Carlo indicated that the quasi-elastic channel appeared about half of the time with no additional hits near the vertex. This type of event in the data was classified as a 'clean vertex' event. The Monte Carlo also showed that although this particular category of events includes predominately quasi-elastics, it is contaminated at

about the 35% level by single pion events for the energy spectra which we were investigating.

5.5. Neutrino Energy Calculation and Resolution

At this point, the events were defined well enough that the energy of the incident neutrino could be determined. This was accomplished using the kinematical expression

$$E_\nu = \frac{2E_\mu M_{target} + M_w^2 - M_{target}^2 - M_\mu^2}{2\left(P_\mu \cos\theta + M_{target} - E_\mu\right)}, \tag{5.6}$$

where M_w is the mass of the secondary nucleon or nucleon resonance which was produced in the interaction. Due to our inability to determine the event type precisely, all events were reconstructed using the proton as the target mass. This caused the reconstructed neutrino energy to be shifted significantly from its real value when the event was in fact from a nuclear resonance. This shifting effect is even more severe for high mass resonances which were not contained in the event Monte Carlo and therefore could not be studied in detail, however their production is not large. The reconstruction energy resolution, including effects from energy spreading due to Fermi motion, track angular and momentum resolution, and the event type uncertainty, is given in Figure 5.12 and Figure 5.13. The events with energies below 2 GeV predominately were determined with muon range energy in the toroids while those above 2 GeV were determined with momentum fits through the toroids.

5.6. Acceptance and Background

Acceptance for muon events in the detector was determined from the percentage of reconstructed Monte Carlo events which passed all of the criteria imposed on the real data. At each of nine energies .5,.6,.75,1.,1.25,1.5,2.0.3.0 and 5.0 GeV 2000 Monte Carlo events including the natural mixture of the charged current event channels. The values acquired from this determination are plotted in Figure 5.14 as a function of neutrino energy. The acceptances were calculated for incident neutrino energy even though the reconstructed event might have appeared at a lower energy. This represents a problem when attempting to correct the spectra for acceptance as the non-quasi-elastic events are improperly weighted. In order to circumvent this problem when calculating the total event number, three functions were used

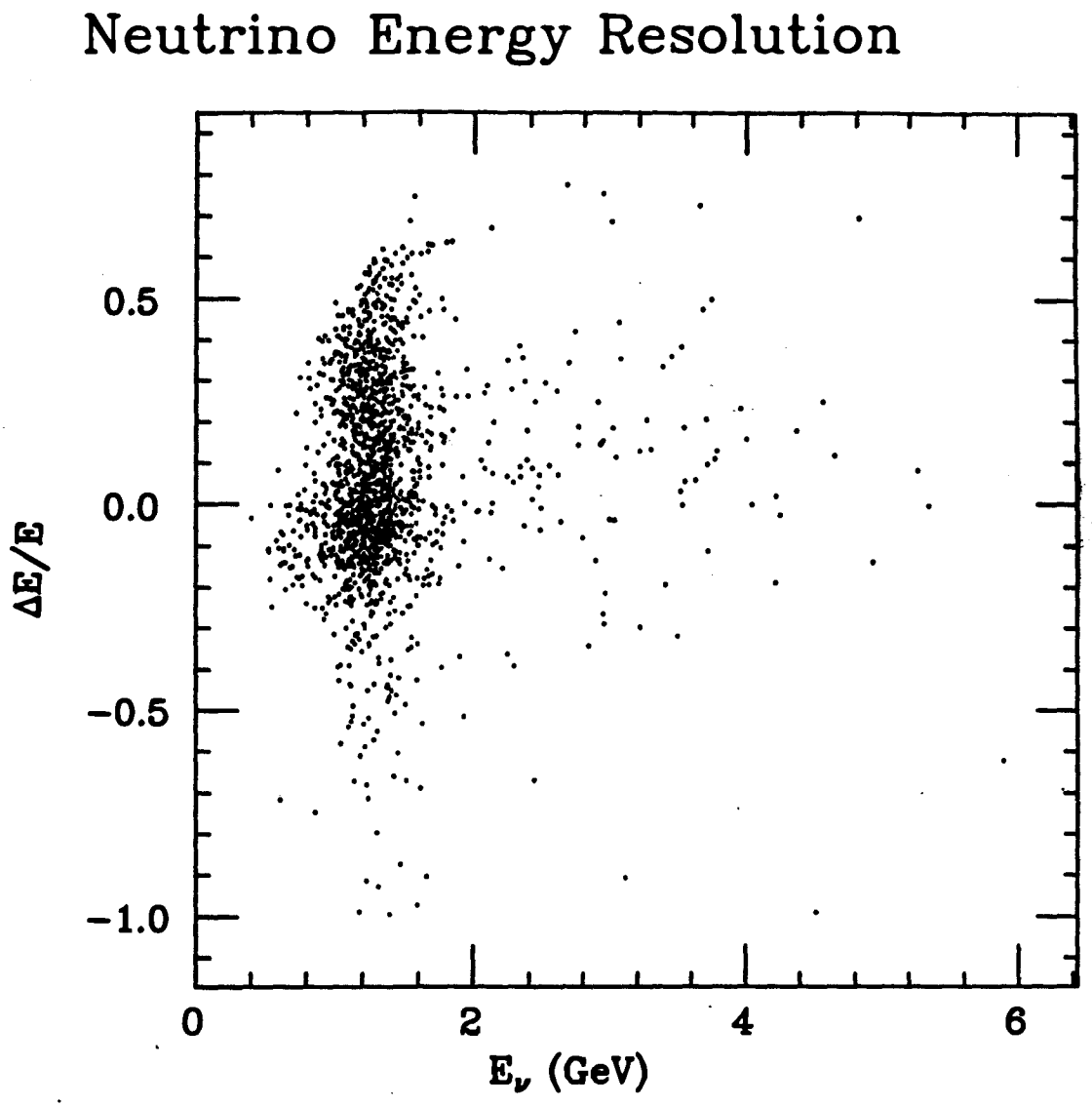

Figure 5.12: Muon neutrino energy resolution as a function of neutrino energy calculated from Monte Carlo events. Distributions are for $(E_{M.C.} - E_{fit}) / E_{M.C.}$.

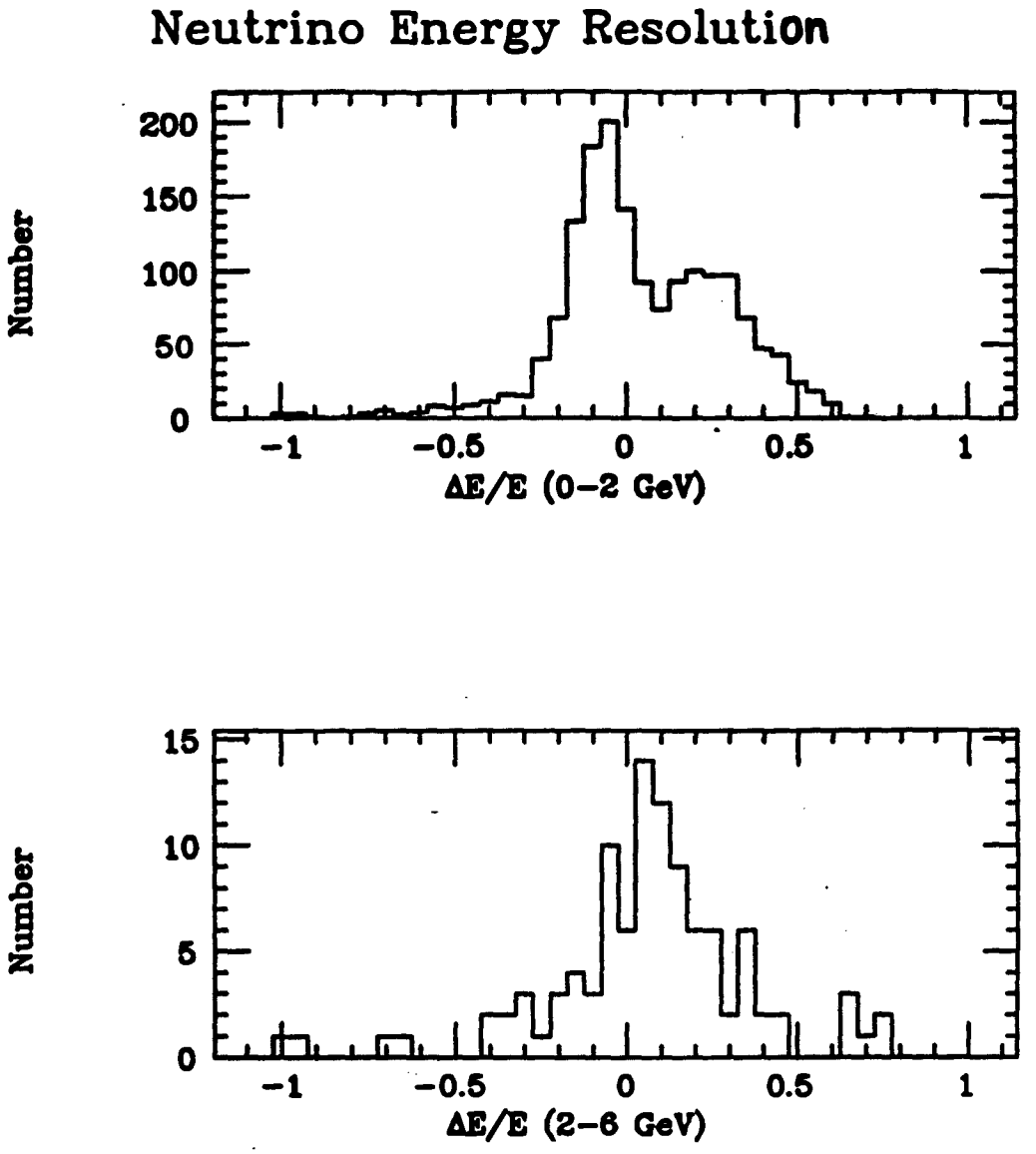

Figure 5.13: Muon neutrino energy resolution for 0–2 GeV and 2–6 GeV neutrinos energy determined from Monte Carlo events. Distributions are for $(E_{M.C.} - E_{fit})/E_{M.C.}$.

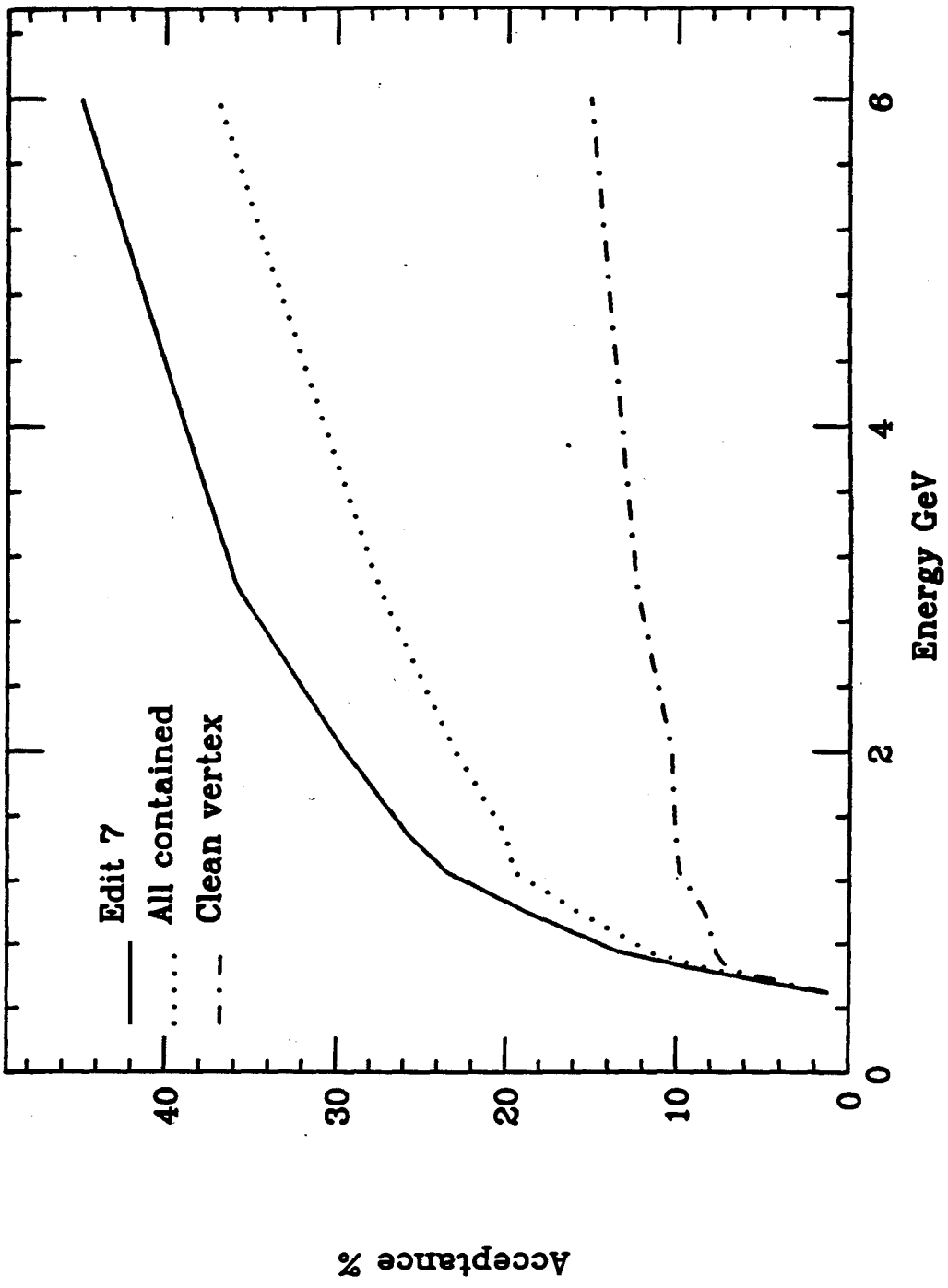

Figure 5.14: Acceptance as a function of neutrino energy for various stages of the analysis.

to calculate weighted acceptance numbers for the two energies of the data. These functions were the acceptance function for all contained events, a linear cross section of $\sigma/E_\nu = .8\times10^{-38}cm^2$, and the calculated beam spectra function. The weighted acceptance numbers which were achieved from this calculation are .185 and .200 for the 240 kA and 280 kA data respectively.

The backgrounds to the muon normalization due to misidentified events can only be estimated at this point. These were events which were counted as muon quasi-elastic or single-pion but were actually of some other topology. There were two problems: (1) a track other than a muon was selected in the event and reconstructed as a muon, and (2) an event type not included in the Monte Carlo (multi-pion) was selected and reconstructed as either a quasi-elastic or single-pion event. The first issue was addressed from acceptance calculations for neutral current Monte Carlo events which, because they never include a muon, demonstrate the frequency that a pion or proton is selected in the reconstruction. The acceptance for neutral current single π events thrown with a 240 kA beam spectrum is less than .8% and the acceptance for neutral current elastic events ($\nu_\mu p \rightarrow \nu_\mu p$) are probably at the 1 to 2 % level. Therefore, since these neutral current events comprise about 20% of the total cross section, the contamination due to them was around .5%. Because Monte Carlo charged pions tended to be greater in length than those expected in the data, as discussed in Chapter 4 (section 4.3) the acceptance for neutral current data events was even lower.

The contamination due to the other source is higher, but difficult to estimate without a more complete Monte Carlo which includes the complex charged current reactions. However, a rough estimate can be made based upon the calculation of the multi-pion rate performed in Chapter 4. The multi-pion event rate might be as high as 20% that of the single pions at 2 GeV; below 2 GeV it is much less. Therefore, assuming the multi-pion events have approximately the same acceptance as the single-pion channels, and that 30% of the beam events are above 2 GeV the percentage of accepted multi pion events is very roughly 6% of the total event sample. Preliminary studies of these event channels indicate that acceptance for

these events is lower than those channels studied and thus their contribution even less than calculated above.

5.7. Data and Monte Carlo Reconstruction

5.7.1. Muon θ_{mu} vs. E_{mu} Distributions

One important aspect of the data is the relationship between the angle of the muon, $\cos\theta_\mu$, and its kinetic energy, E_μ. This relationship is purely kinematical and reflects, to some degree, the quality of the analysis and identification of primary tracks as muons. The $\cos\theta_\mu$ vs. E_μ distributions for the data and the Monte Carlo are shown for the 1.27 and 1.46 Gev beams in Figure 5.15 through Figure 5.18 with the projected histograms for $\cos\theta_\mu$ and E_μ. Because these distributions contain both quasi-elastic and nucleon resonance events, as well as a broad range of neutrino event energies, the distributions are quite wide but the agreement between the general shapes of the data and Monte Carlo is good.

5.7.2. Neutrino Energy Distributions

Verification that the neutrino beam energy distribution was what the beam calculation had predicted was critical. There were three major characteristics of the energy distribution which were under question. First, was the shape of the main peak correct? Second, was there a low energy component in the measured neutrino distribution which could not be understood from the beam calculations? Third, was the high energy tail of the distribution commensurate with the beam calculations? All of these considerations were important to confirm that the beam was well understood.

The general shape of the neutrino energy distribution and the low energy component are closely related. The low energy component was a problem because non-quasi-elastic events were mapped to a lower energy by the reconstruction. Therefore even the neutrino beam spectrum which was calculated appeared to have a low energy component when it passed through the event Monte Carlo and all stages of the analysis. Two approaches were taken to study these two concerns. First, consistency between the shapes of the reconstructed data and Monte Carlo for all contained events (as defined in section 5.3) was examined and are shown in Figure 5.19 for the

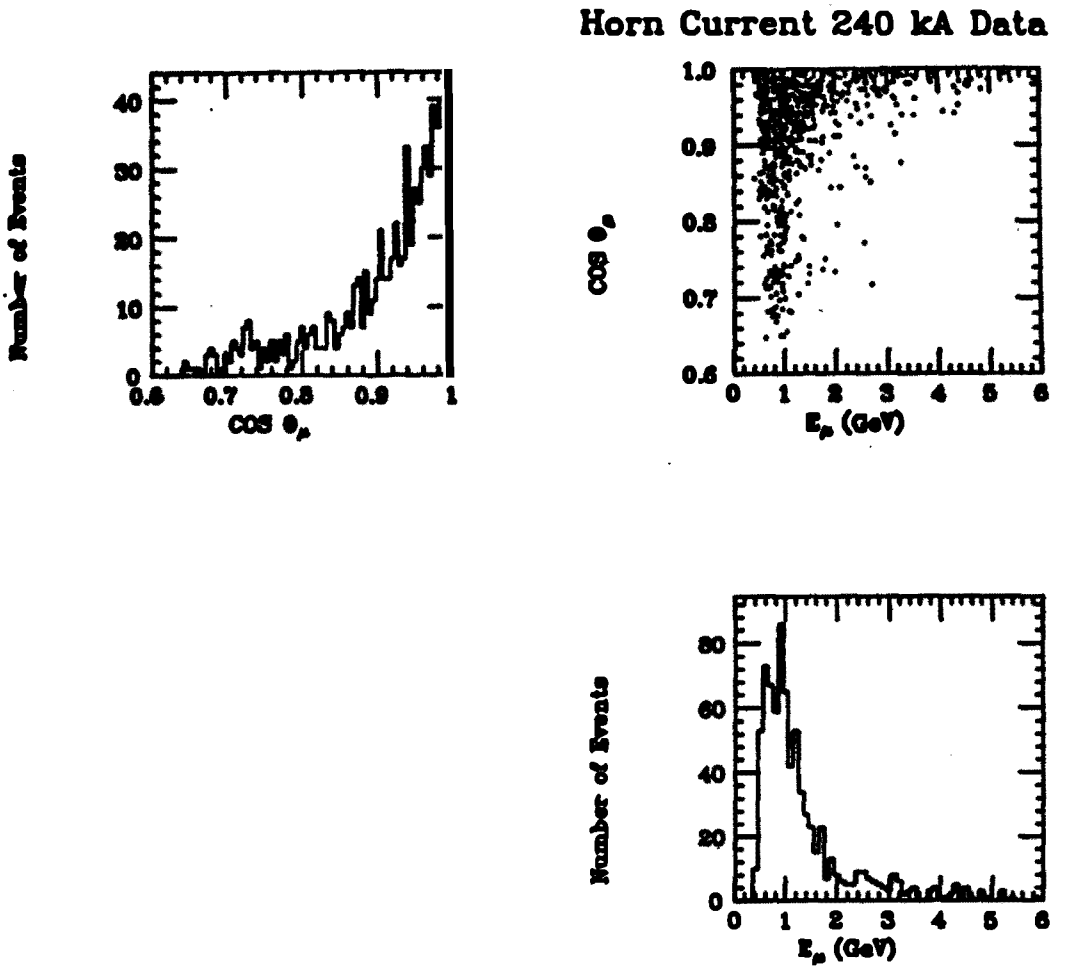

Figure 5.15: Distribution of $\cos\theta_\mu$ vs. E_μ for 1.27 GeV neutrino beam data. Projections of the histogram show the $\cos\theta_\mu$ and E_μ distributions.

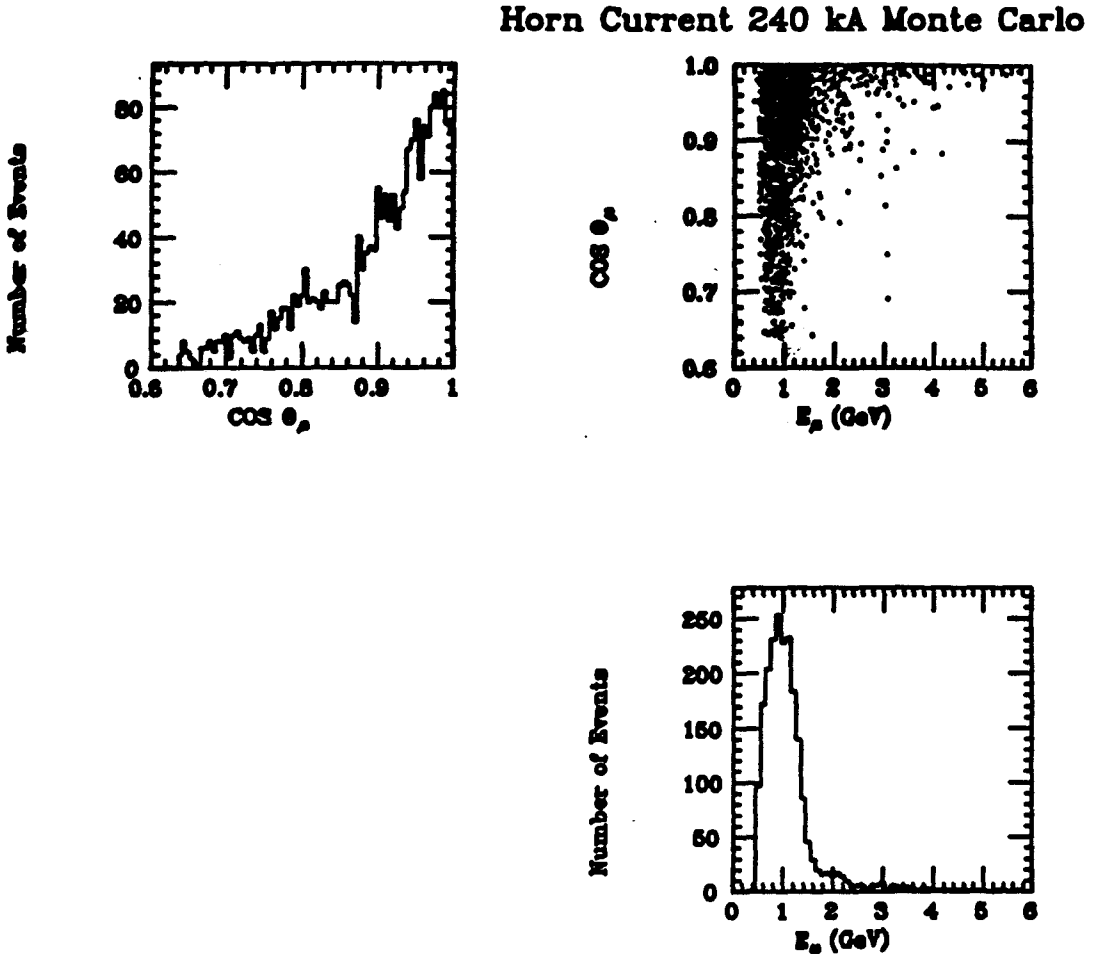

Figure 5.16: Distribution $\cos\theta_\mu$ vs. E_μ for 1.27 GeV neutrino Monte Carlo. Projections of the histogram show the $\cos\theta_\mu$ and E_μ distributions.

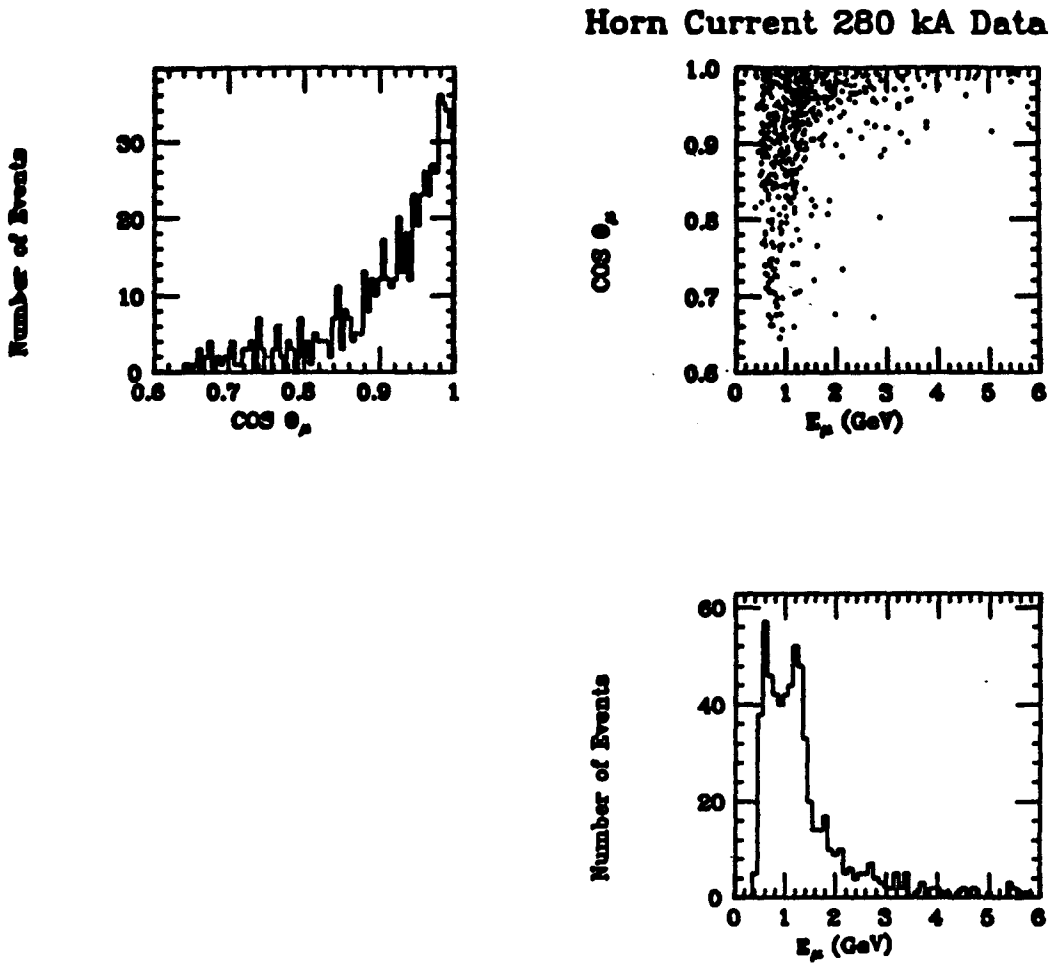

Figure 5.17: Distribution of $\cos\theta_\mu$ vs. E_μ for 1.46 GeV neutrino beam data. Projections of the histogram show the $\cos\theta_\mu$ and E_μ distributions.

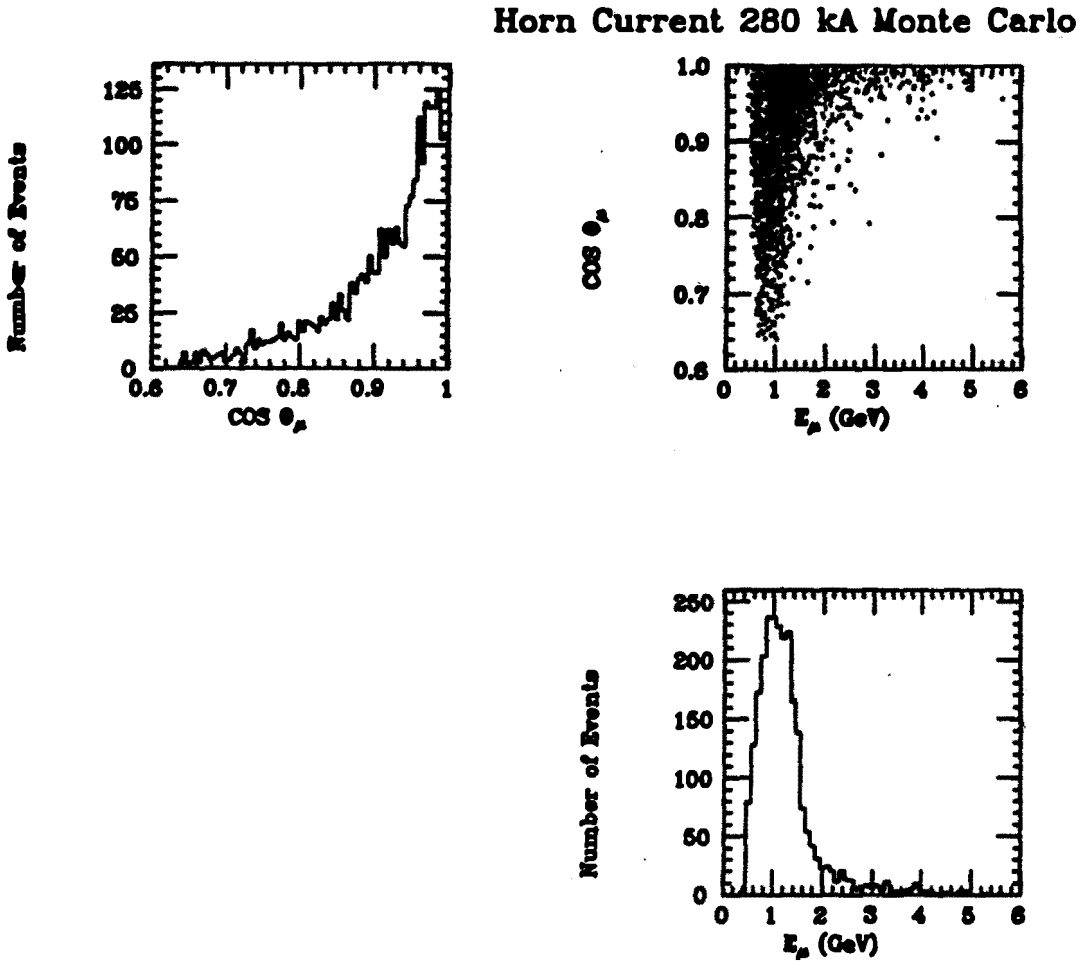

Figure 5.18: Distribution of $\cos\theta_\mu$ vs. E_μ for 1.46 GeV neutrino Monte Carlo. Projections of the histogram show the $\cos\theta_\mu$ and E_μ distributions.

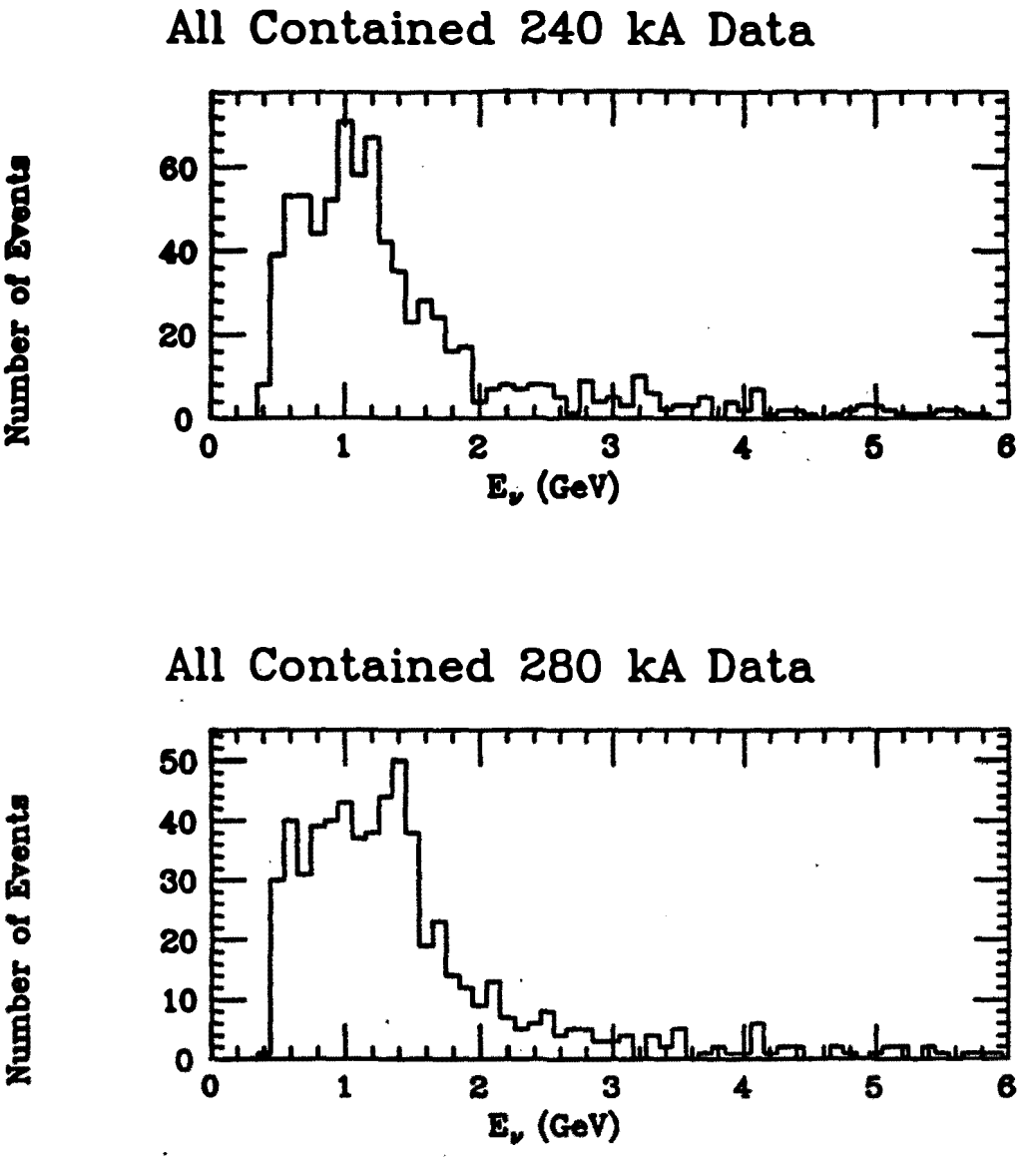

Figure 5.19: Muon neutrino energy distributions for all contained data events at 1.27 GeV (240 kA) and 1.46 GeV (280 kA).

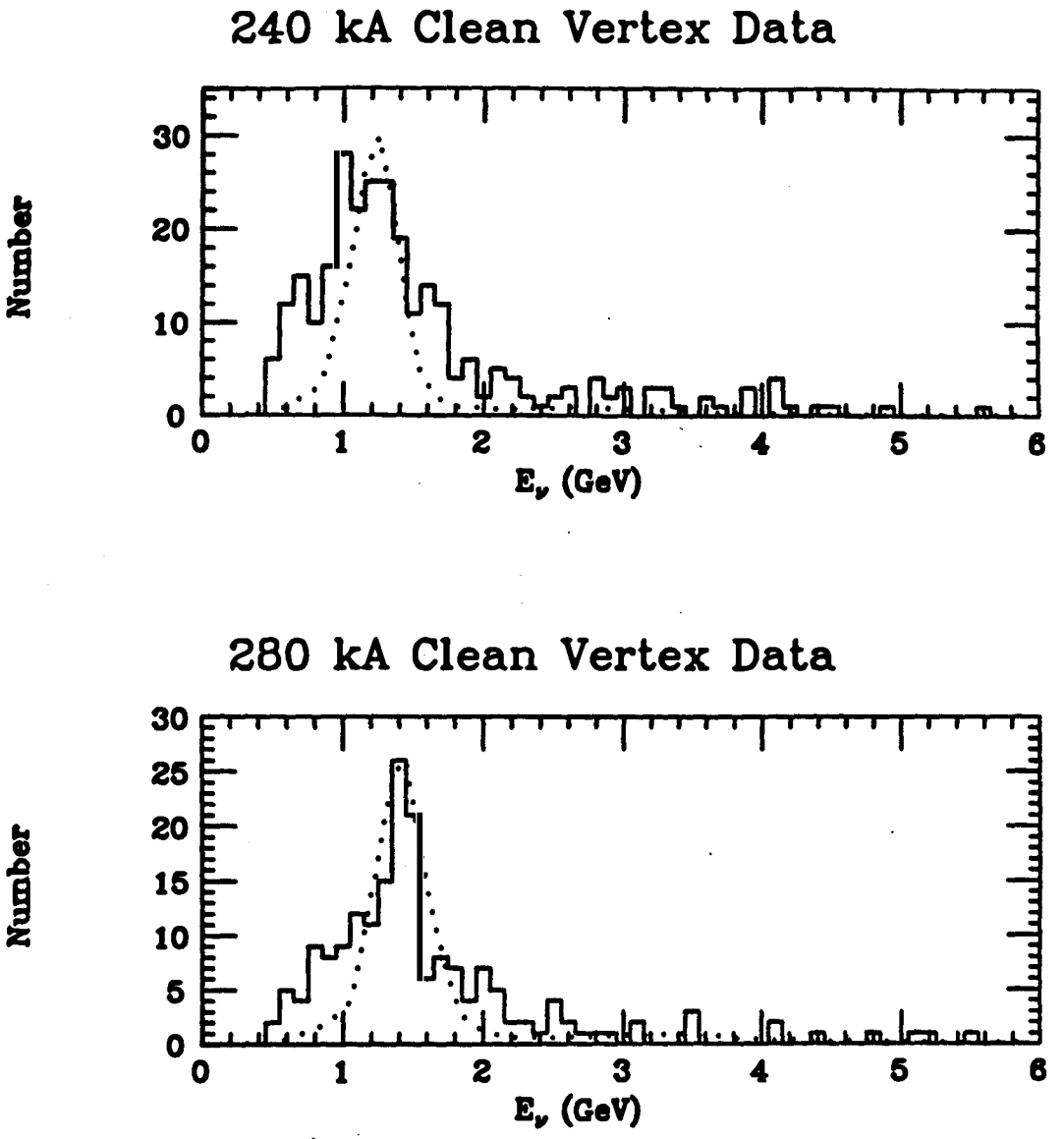

Figure 5.20: Muon neutrino energy distributions for clean vertex events at 1.27 GeV (240 kA) and 1.46 GeV (280 kA). The data is represented by the solid histograms, the dotted curves represent the beam Monte Carlo distributions weighted by cross section and acceptance.

two energy cases. The shapes of the main peaks agree well, and it is believed that the low energy part of the Monte Carlo which appears to be in disagreement with the data can be explained by resonance channels not included in the Monte Carlo. The second approach was to study the neutrino energy distributions of clean vertex events. Since these events represent mostly quasi-elastic events, the reconstruction is much more representative of the actual beam spectrum. The clean vertex energy distributions for the data are shown in Figure 5.20 with the calculated beam distributions corrected for acceptance and cross section. The agreement supports the correctness of the beam calculation.

Because the Monte Carlo was deficient of many of the higher energy event channels, the reconstructed data demonstrates about twice as many events above 2 GeV as the Monte Carlo would indicate. The problem of analysing the high energy tail component in the beam again depended largely on how high energy events fed down to lower energies in the reconstruction. However, an attempt to understand it was made by weighting the calculated beam spectra by the acceptance and by the linear cross section which was measured by Baker et al.. [26] The results show that for the 240 kA and 280 kA data respectively 12.6% and 15.1% of the data should appear above 2 GeV. The data shows about 17% and 19% respectively for the two energies. Thus the data has a higher number of events above 2 GeV then expected by 30%. Clearly this problem is not completely resolved.

5.8. Data Flow and Rate Determination

A complete summary of the data flow is given in Table 5.1. This table traces the data from the number of protons on target, through the Edits, and the muon analysis. The group of events classified "All events" has no criteria placed on vertex type. The cosmic background level in the analysis is about 2% and is composed almost entirely of events which enter the detector from the back through the toroids. A few of these events can be cut by judiciously selecting times that fall within RF bunches of the timing structure of the data. However, the Cerenkov timing in a few runs near the beginning of the Summer 240 kA data was unstable, and several quality events were rejected when the timing criteria was imposed. Therefore, the

		Data sets		
	Reduction step	Summer 240	Fall 240	Fall 280
	General data reduction			
1.	Protons on target $\times 10^{18}$	11.0	8.4	10.1
2.	Neutrino beam spills	1123683	727878	767758
3.	Edit 1	203126	120038	136807
4.	Edit 3	16541	10187	12150
5.	Edit 6	5093	3217	4511
	Muon data analysis reduction			
6.	Edit 7	796	596	988
7.	Toroids functioning	710	596	988
8.	All in time and contained.	428(9)	321(12)	609(12)
9.	Clean vertex	158(6)	93(6)	168(10)
	The number of free trigger events are indicated by ().			

Table 5.1: The data flow for the muon analysis.

only timing criteria which was imposed on the events was that they be within the AGS beam spill.

With the values from the muon analysis, the rates and statistical errors have been calculated and rough estimates of the average cross sections for the beam energy distributions have been made. They are presented in Table 5.2. The values for the total number of events represent those events passing all of the criteria imposed in the analysis corrected for detector acceptance. These acceptance corrected numbers were used to calculate the event rate with the number of protons on target measured by the the U716 current transformer near the interaction target in the neutrino U-line (entry 1 of Table 5.2). The average event rate including all three sets of data was 2.40±.12 interactions per 10^{16} protons on target. The calculation of the cross sections was performed using the values for mass of the detector (section 2.2) and neutrino rate as calculated with the beam Monte Carlo (section 3.2). All of the numbers are normalized to a detector area of 516 cm × 516 cm, which is 88%

Parameter	Summer 85 240 kA	Fall 85 240 kA	Fall 85 280 kA
Number of Protons on target $\times 10^{16}$ (U716).	10.5±.5	8.4±.4	10.1±.5
Total contained events	428	323	609
Free trigger events	9	12	12
Net contained events	419±20	311±18	597±24
Acceptance for beam spectrum	.185	.185	.200
Acceptance corrected	2265±108	1681±97	2985±120
Rate calculation (neutrino interactions per 10^{16} protons on target).	1.89±.14	1.76±.13	2.60±.19
Neutrinos per proton on target from the beam calculation.	$2.77^{+1.11}_{-.28} \times 10^{-5}$	$2.77^{+1.11}_{-.28} \times 10^{-5}$	$3.27^{+1.31}_{-.33} \times 10^{-5}$
Measured neutrino cross section averaged over beam spectrum $\times 10^{-38}$ cm^2.	$1.54^{+.15}_{-.61}$	$1.46^{+.15}_{-.58}$	$1.79^{+.18}_{-.71}$

Cross section per nucleon target calculation:

$$\sigma = N_{Interactions} A_{Detector\ area} / N_{Incident} N_{Targets}$$

Detector fiducial parameters employed:

Mass = 201×10^3 kg.

$N_{Targets} = 1.20 \times 10^{32}$ kg.

Area = 516 cm × 516 cm = 2.66×10^5 cm^2

Table 5.2: Rate calculation and cross section determination for the three data sets.

of the total area. Because the neutrino rate from Table 3.3 is given in neutrinos per interacting proton, these values were corrected by a factor of .6 to reflect the percentage of the total protons on target which interacted in the target. Values for cross section per nucleon weighted with the beam spectra for 240 kA and 280 kA yield values of 1.0 and 1.2 $\times 10^{-38} cm^2$ respectively. The values for the cross sections

which result from the data are higher than these weighted numbers by about 40%. This is within the rather large errors which come primarily from the uncertainty in target production used in the beam calculations.

Chapter 6.
Electron Analysis

Selection and analysis of the electron or "shower" sample proceeded in a similar fashion to that of the muons. As in the muon case, only events passing Edits 1, 3, and 6 were examined. A special screening algorithm, Edit 5, was developed to further reduce the number of shower candidates. A complete description of each of the data edits is given in Appendix D. Events passing the Edit 5 cuts were eye scanned by physicists to select the final electron candidate sample. Several approaches to determine the energy of the electron shower were explored including integrated pulse area, total number of peaks, and number of cells hit. The angle of the electron was determined with a weighted fit to the shower pattern. A simple event classification scheme was used to reduce contamination from gammas and to correlate the data with the Monte Carlo. Finally, the neutrino energy of each electron event was calculated from kinematics.

As in the muon case, detector acceptance and background estimations were performed with the event Monte Carlo and the ν_e rate was calculated for all of the data. The acceptance was determined by passing Monte Carlo events through identical selection and reconstruction procedures as the real data and observing the number of electron events which were retained. The component of the background due to misidentification of non-electron events was determined from the number of these events which were retained in the selection and reconstruction procedure. Employing the number of event candidates, the acceptance and the estimation of the background, a ν_e rate was determined.

6.1. Shower Selection

Selection of the final electron candidates consisted of four stages. The initial phase of the shower selection consisted of the Edit 5 algorithm which examined event pattern development, length, features of the event energy distribution and containment within the detector. This algorithm was designed to provide a high efficiency for shower selection and therefore a large number of non-shower events also passed the Edit 5 cuts. With the shower sample reduced to a more easily

handled level, all of the Edit 5 events were eye scanned by physicists in two stages. The rules employed in the two scans were as follows:

Scan 1. The track must have been 'shower-like' in both views. This required that the track (1) have multiple hits in several planes (2) skipped planes occasionally and (3) contained pulse shapes from the flash encoders which demonstrated a complicated multi-track signature. The vertex was required to have been greater than two wires from the edge and at least 2 planes from the front and 15 planes from the back of the detector.

Scan 2. The length of an electron shower was required to be at least 15 planes in both views. This requirement represented approximately a 700 MeV cut on the energy of an electron. Additional shower-like patterns were classified as π^0s if they contained at least 4 hits in each view.

Finally, a pattern analysis was performed on each surviving event which examined characteristics of the average shower behavior involving energy deposited per plane, number of hits per plane, the transverse size of the shower development, and the number of missing hits within the pattern. These final cuts were designed to significantly reduce the number of background events in the sample. A typical example of a shower event is shown in Figure 6.1 and included in Figure 6.2 are pulse shapes for 10 planes from shower and muon candidate events as recorded with the flash ADCs.

6.2. Electron Reconstruction

6.2.1. Pattern Recognition

To a great extent the determination of the energy, and to a lesser extent of the angle of the electron depended on which hits were included in the shower pattern. At the vertex extra hits could be included in the shower pattern which were actually due to protons or pions from the interaction, or from extraneous noise in the detector. Including these extra hits tended to increase the energy calculated for the electron and alter the angle in an unpredictable manner. Because of the nature of shower events an electron was expected to skip planes occasionally and near the end, as the shower lost most of its energy, it was possible for hits to show up which were difficult to identify with the shower or for energy to exit the detector even though stringent

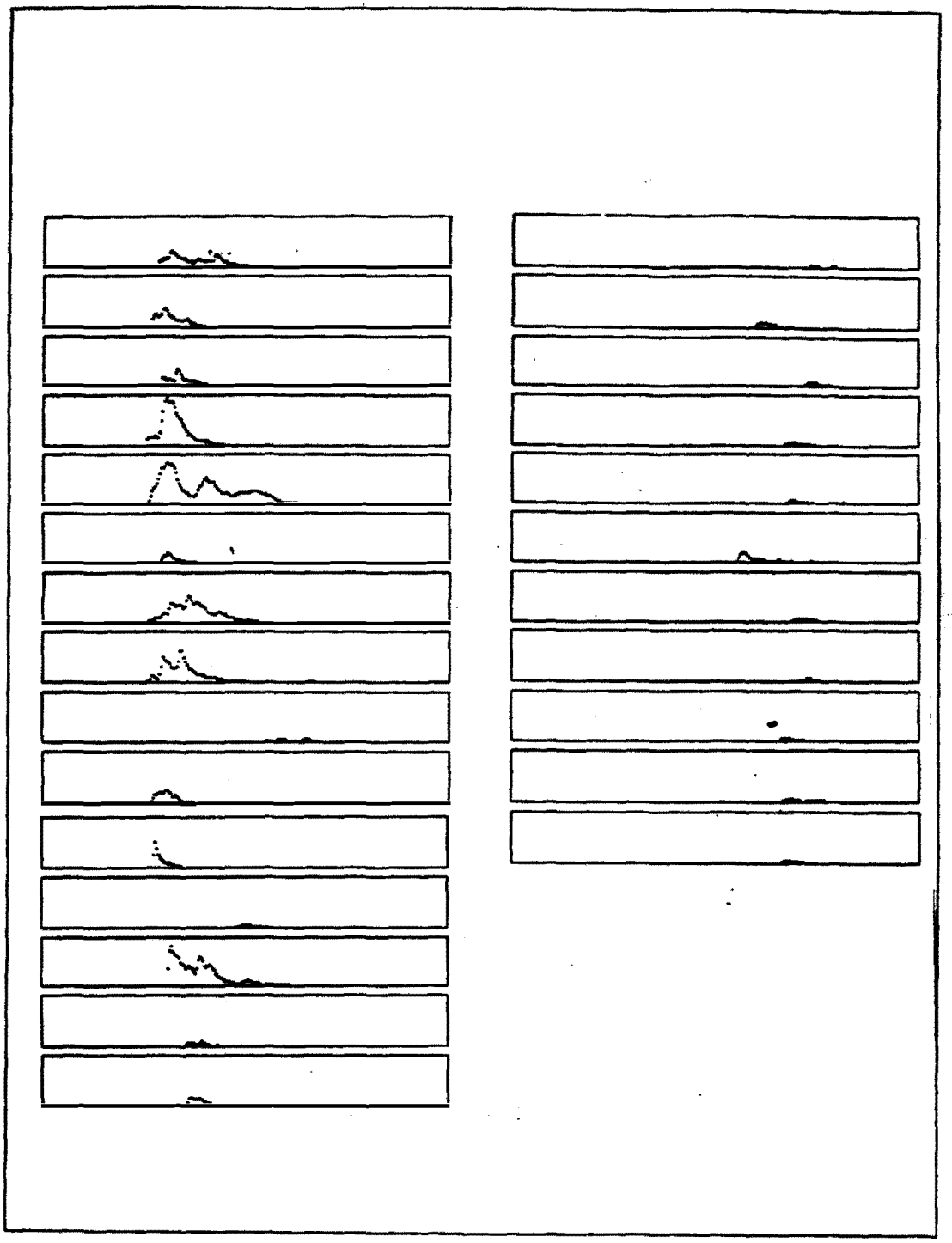

Figure 6.2: Flash encoder pulse shapes for 10 planes of a shower candidate (left) and muon candidate (right).

containment requirements were made on the event. It should be noted that although noise hits were a consideration generally they contained little pulse area and thus represented a small fraction of the total energy for pulse area measurement.

6.2.2. Shower Angle

The angle of the electron in shower events was determined using a weighted fit of the hits in the shower pattern. Assuming that the initial trajectory of the electron was in the direction of the highest energy density of the shower, a straight fit to the hits in the cluster was performed with the hits in each plane weighted by their pulse area. This gave an approximate angular resolution of about $\pm 5^{\circ}$. In events where the vertex was not extremely clean, this angle was affected by adjacent hits which were usually due to other tracks or fragments from the interaction.

6.2.3. Shower Energy

The actual measurement of the shower energy was tried with three different approaches. Integration of the total pulse area of the hits in the shower involved extensive normalization using cosmic ray muons. Several attempts were made to count peaks using the information collected by the flash encoders. The number of PDTs represented a crude measurement of the shower energy; however, the resolution was limited by the large size of the drift tubes.

Pulse area integration was determined to be the method of energy measurement which involved the least amount of systematic error. In order to employ the pulse areas, an extensive effort was required to establish a set of normalization constants for each run. The normalization was necessary due to the large effects on pulse area which were caused by changes in barometric pressure, temperature, gas mixture and small variations in PMT high voltage. These constants were compiled by measuring the average values of pulse area for the cosmic ray muons which were collected between beam triggers at the rate of approximately .6 cosmic rays per trigger. As mentioned in Chapter 2, to assure a sample of cosmic ray muons with angular distributions consistent with the data, the cosmic ray trigger was set up to acquire small angle tracks. Additional cuts were imposed to the cosmic ray data when it was fit in the analysis as follows:

1. Noise hits, i.e. hits unrelated to the track, were not used.

2. In case of a double hit in a plane, neither hit was used as it was suspected that these were an indication for a hard Delta ray which would be misrepresentative of the pulse area of a minimum ionizing particle.
3. Chambers for which the track was determined to have only passed through a corner were eliminated from the area calculation.

The average value for pulse area for each track was multiplied by a factor of $1/\cos\theta_x$ or $1/\cos\theta_y$ for the vertical and horizontal chambers respectively, where θ_x and θ_y represent the angle with respect to the beam axis of the x and y track projections. There were no angular cuts imposed on the data other than those of the cosmic ray trigger. The angular distributions for θ_x extend out to about 30°, and for θ_y out to about 45°. This normalization procedure was performed both for data from the main detector and for similar data obtained with the test detector.

Energy calibration and the resolution achieved with the pulse area measurement were determined with data taken in the A2 test beam. Electron data was taken at energies of .6,.8,1.0,1.5,2.0,3.0 and 4.0 GeV with angles of 0° and 30°. Additional details of the setup in the A2 test beam were discussed in Chapter 2. The pulse area measurements as demonstrated in Figure 6.3 are linear with energy for all energies measured at the 0° orientation. The higher energy points in the 30° data appear to fold over as observed in Figure 6.4, an effect which is believed to have been caused by energy escaping near the narrow central portion of the detector when in the 30° configuration. Assuming this hypothesis is true, the calibration for electron showers can be represented as

$$E\,(GeV) = A/5880 \qquad 6.1$$

with A representing the measured pulse area in arbitrary flash encoder units. The energy resolution for this data is also shown in Figure 6.3. From the slope of the line in these plots, the resolution is determined to be

$$\sigma\,(E) = \frac{20\%}{\sqrt{E}} \qquad 6.2.$$

Although pulse area was the parameter ultimately used for electron energy determination, track counting and hit counting were also examined using test beam data. Track counting was an attempt to utilize the pulse area structure as a function

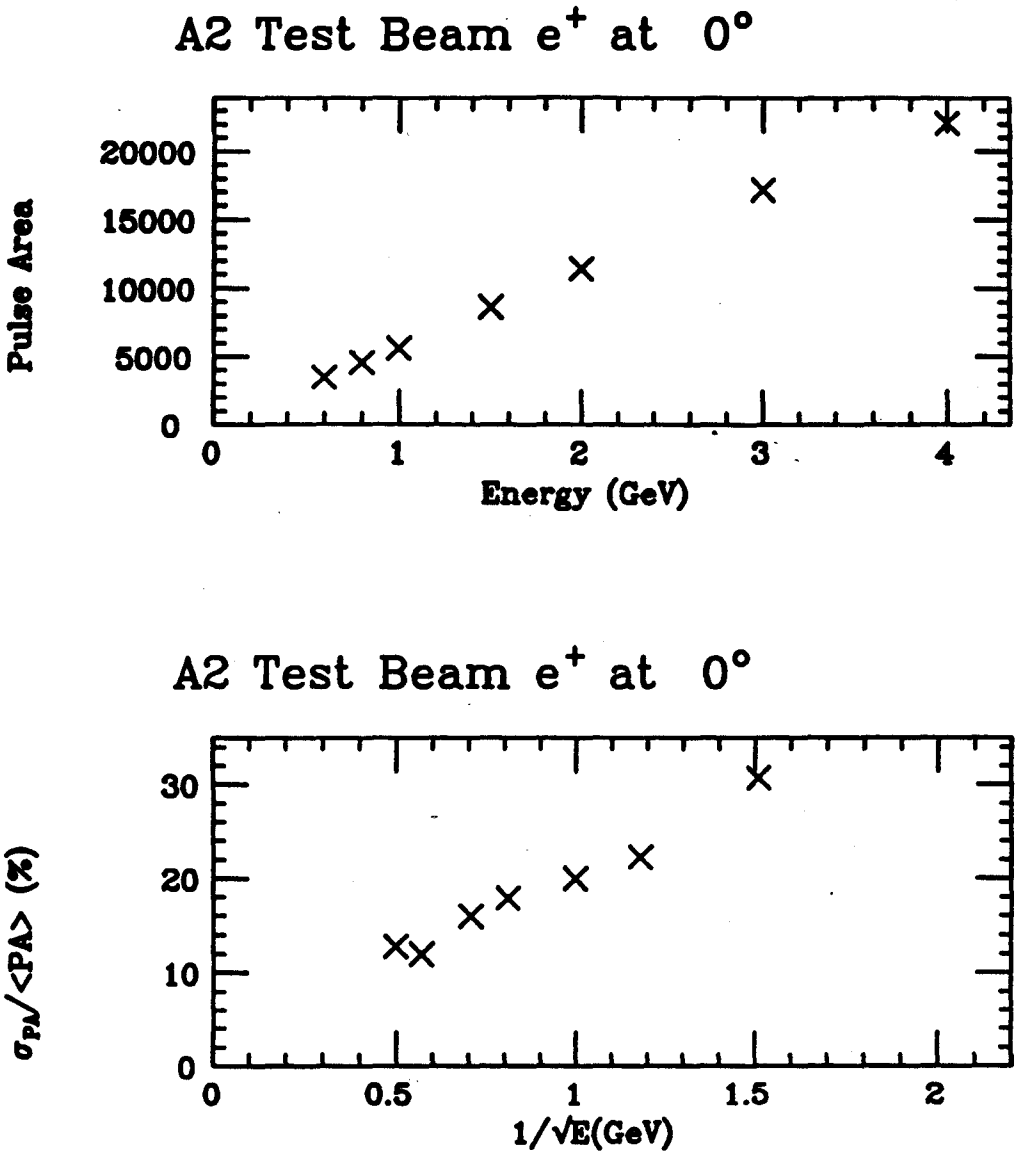

Figure 6.3: Detector pulse area response and energy resolution for 0 degree electrons from calibration data acquired in the BNL A2 test beam.

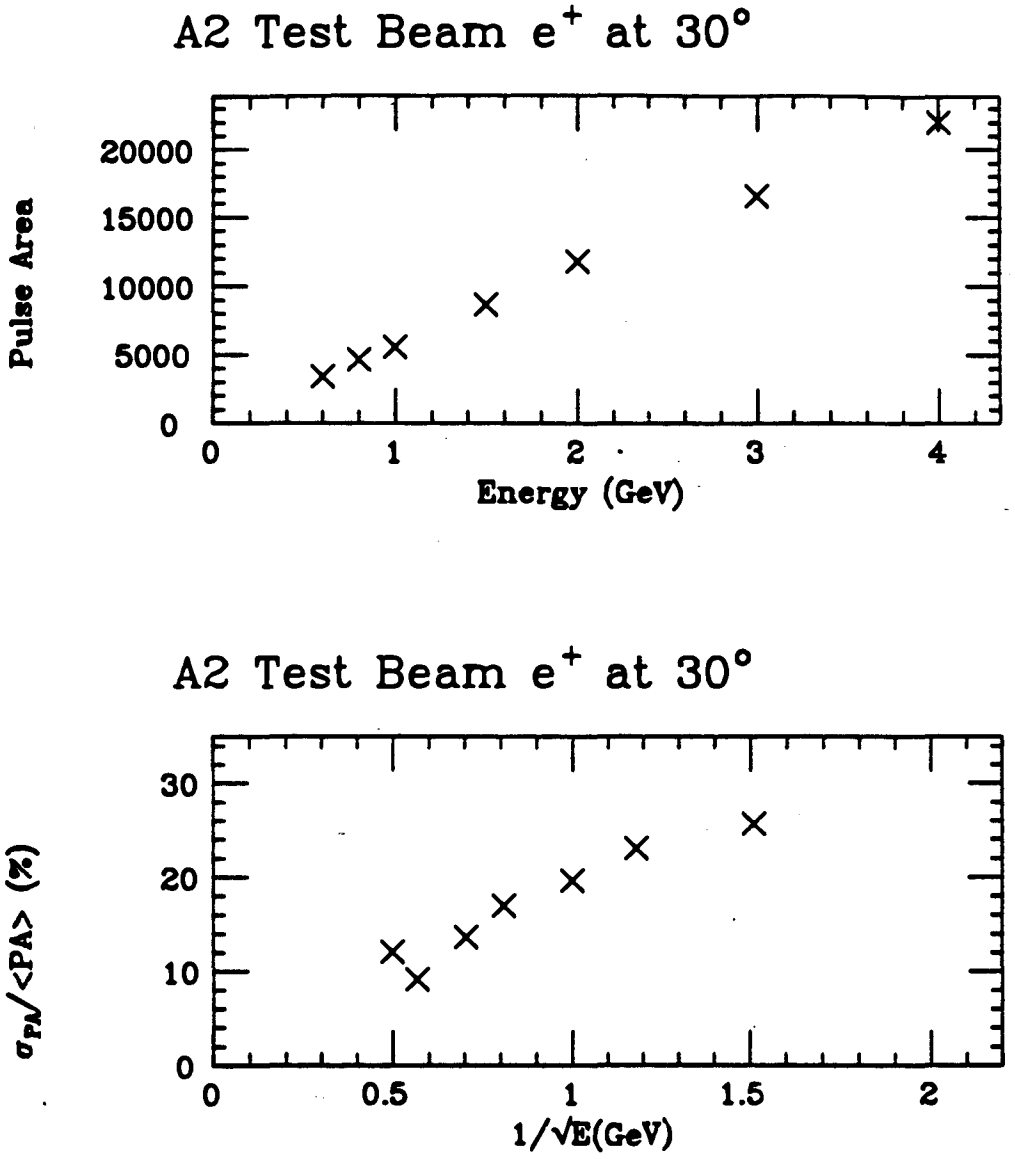

Figure 6.4: Detector pulse area response and energy resolution for 30 degree electrons from calibration data acquired in the BNL A2 test beam.

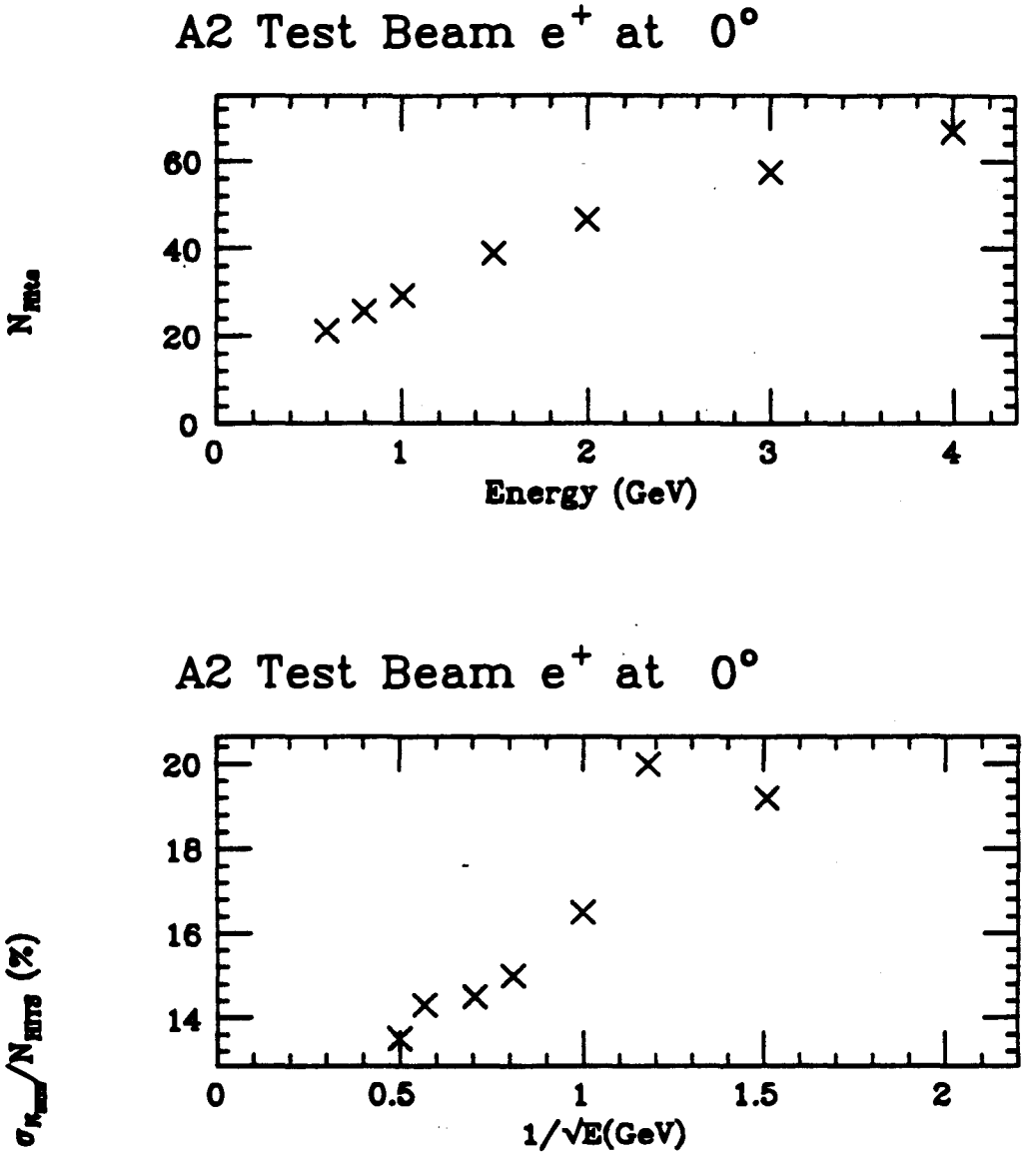

Figure 6.5: Detector number of hits response and energy resolution for 0 degree electrons from calibration data acquired in the BNL A2 test beam.

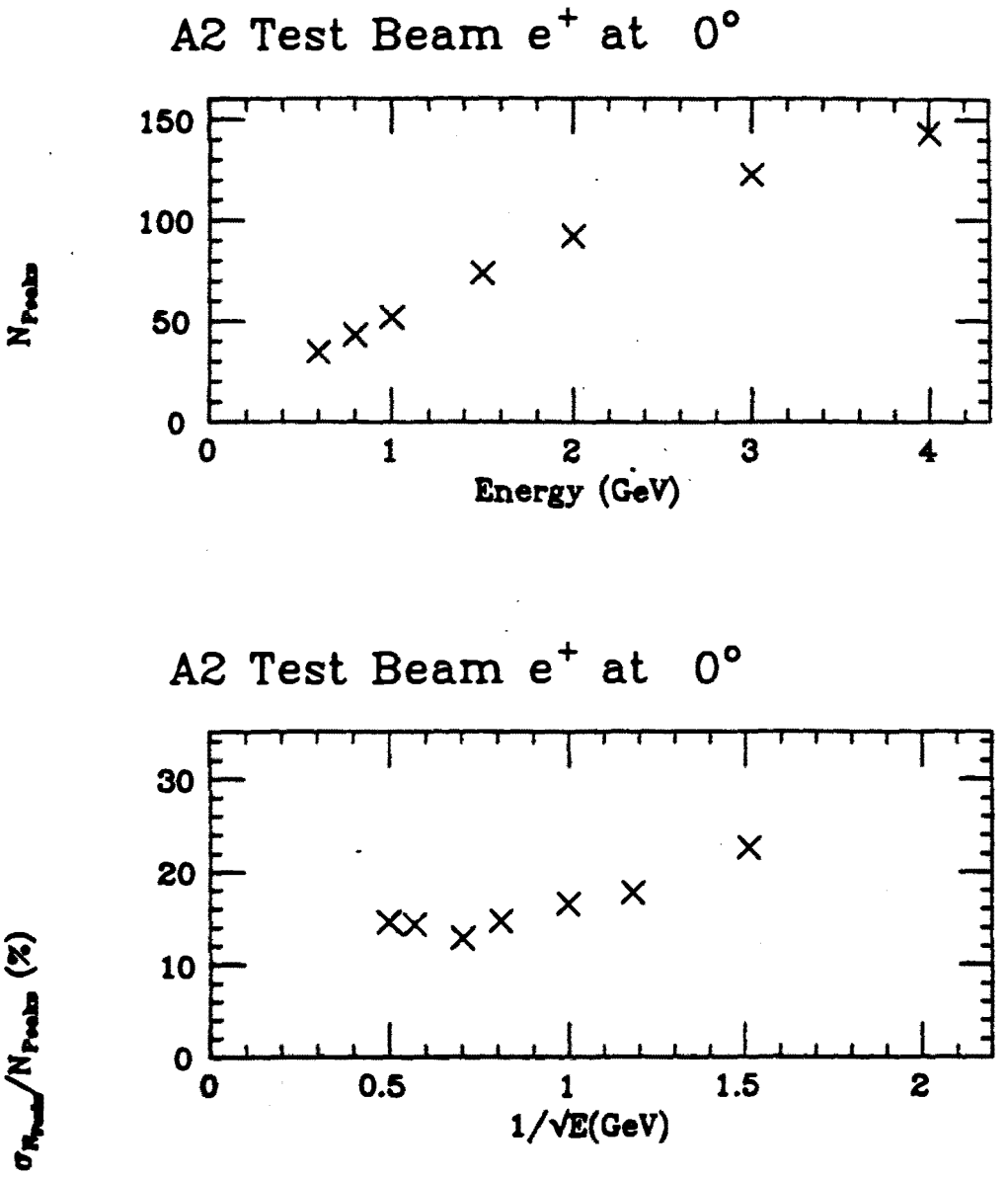

Figure 6.6: Detector number of peaks response and energy resolution for 0 degree electrons from calibration data acquired in the BNL A2 test beam.

of time recorded by the flash encoders to determine the total number of tracks in each cell of the shower. The energy was then determined by assuming that the total number of tracks was proportional to the energy of the shower. A simple algorithm was developed which counted each peak of 3 or more units of pulse height as a track. The calibration and resolution curves for this track counting technique, Figure 6.5, demonstrate that although the resolution seems to be better than pulse area measurement, the calibration is not linear. There are also several systematic errors which require more effort to understand. Hit counting is simply counting the total number of cells which were included in the shower. This technique gives the expected result of even more marked saturation at high energy than track counting with the results shown in Figure 6.6.

6.3. Acceptance and Background

	Analysis Stage Efficiencies (percent)				
Event type	Edit 5	Scan 1	Scan 2	Final stage	
				π^0	electron
Signal					
ν_e events	32.±2.	26.±2.	22.±2.	–	16.±2.
Backgrounds					
$\nu_\mu N \rightarrow \mu^- X\pi^0$	22.±1.0	4.0±.5	2.4±.4	.46±.16	.84±.21
$\nu_\mu N \rightarrow \nu_\mu X\pi^0$	6.7±.7	3.1±.5	2.1±.4	.81±.25	.66±.22

Table 6.1: Measured efficiencies for Monte Carlo events selected as electron candidates from charged and neutral current electron and muon neutrino events thrown with 240 kA neutrino spectrum. The errors are statisiical.

Two important elements involved in the acceptance of shower events were the efficiency of selecting electrons and the acceptance of electron events. The efficiency was studied by observing the number of electron events from A2 test data and the Monte Carlo which survived the edits. Analysis efficiency as a function of shower energy is given in Figure 6.7 for test beam data and Monte Carlo showers at 0 degrees. Acceptance as a function of energy for ν_e was calculated using a flat spectrum

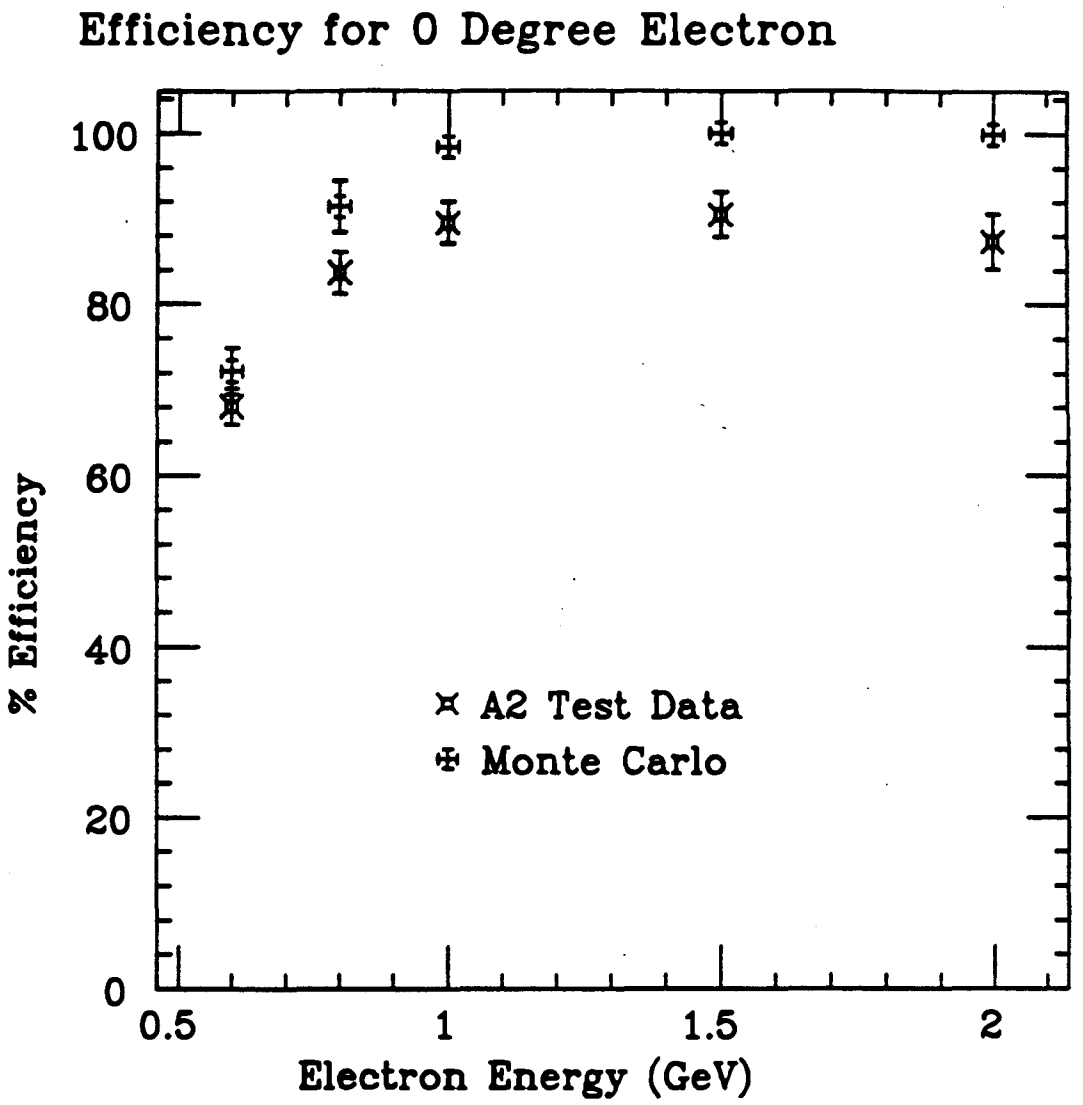

Figure 6.7: Efficiency of electron shower selection for A2 test data and Monte Carlo electrons at 0 degrees.

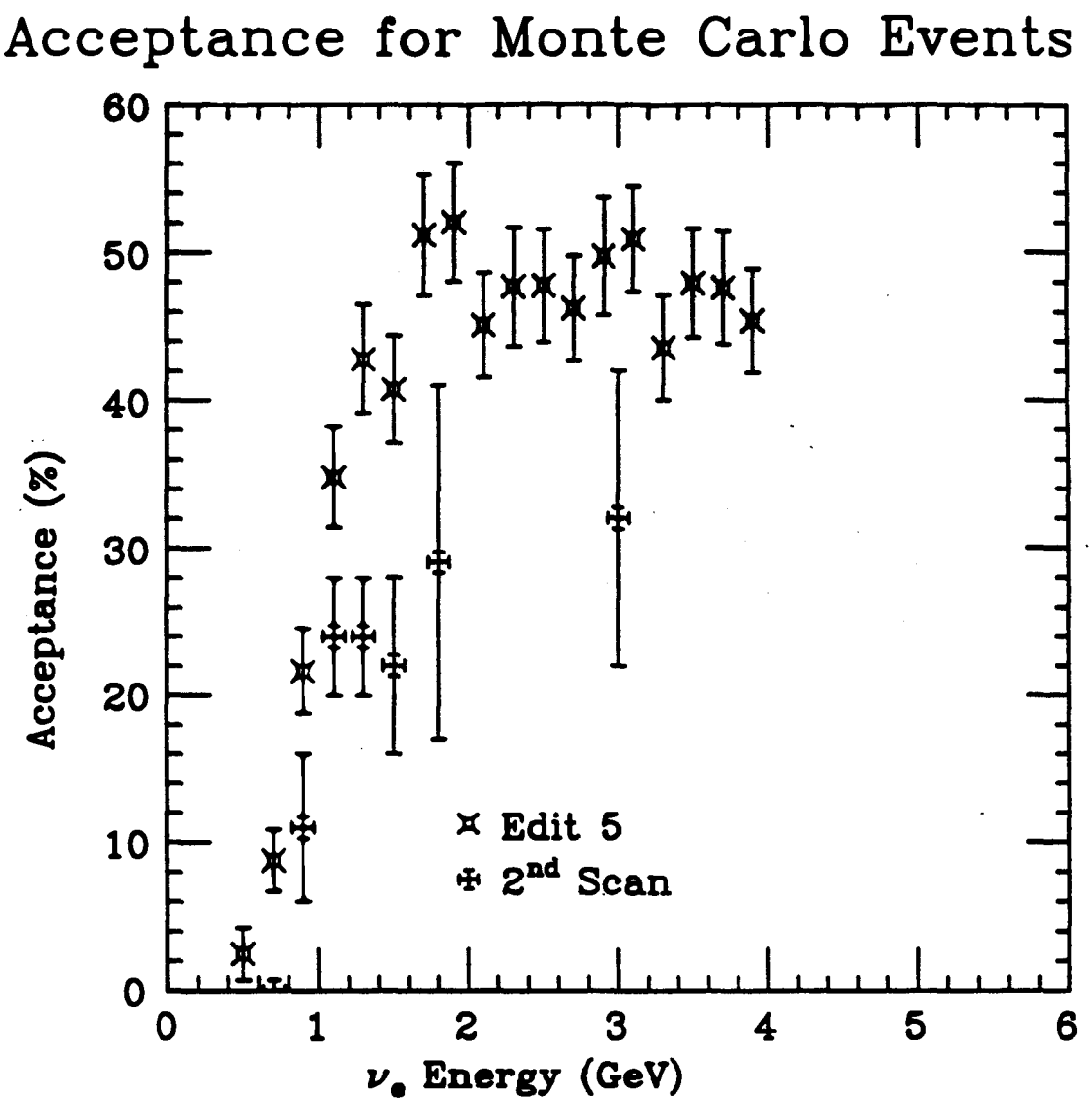

Figure 6.8: Electron neutrino event acceptance as a function of incident neutrino energy.

of ν_e events thrown with the event Monte Carlo. This sample of Monte Carlo electron neutrino events contained the proper mixture of quasi-elastic and single pion event channels. The events were passed through the filtering and reconstruction procedure discussed above. From this, the energy dependant acceptance for the Edit 5 shown in Figure 6.8 was determined. A similar procedure was performed on a smaller sample of Monte Carlo events to determine the acceptance of the second scan, results are also given in Figure 6.8; the errors are statistical. A summary of the acceptance values determined with the Monte Carlo 240 beam spectrum and event generation is given in Table 6.1 for the Edit 5 and each of the scans.

The determination of the backgrounds was performed for the beam-related component, and for the non-beam-related, cosmic ray component. The beam related backgrounds were classified into four general categories: (1) wideband ν_e , (2) neutral current single pion , (3) charged current single pion,and (4) multipion and exotic nucleon resonance decay. Wideband ν_e was calculated using the ν_μ normalization numbers. In the other cases the backgrounds were due to particle misidentification and they were examined using the Monte Carlo, data from the A2 test beam, and the neutrino data. The cosmic ray component was determined from the number of free trigger events which were included in the final electron candidate sample. Summaries of acceptance for the backgrounds due to π^0 neutral and charged current events is presented in Table 6.1.

Problems related to particle misidentification were of two varieties, the background due to charged hadrons and that from π^0s. Because of the manner in which particles interacted in matter, it was possible for hadrons and even muons to appear as showers at certain levels. This was not studied using the Monte Carlo as the version used for this electron analysis did not include nuclear interaction of hadrons. However, contributions of muons, charged pions, and protons appearing as showers was studied from data taken at the A2 test beam and preliminary analysis indicated that the efficiency for selecting each of these sources as showers was less than 1%.

The background due to π^0 events was a significant concern. Because the event channels included in the Monte Carlo were incomplete, a technique was developed to determine the number of π^0 events appearing as electrons by comparing the data

to the Monte Carlo. The analysis procedure outlined in the preceding sections was performed on a combined sample including the data, and 10,000 charged current Monte Carlo ν_μ events, 2000 neutral current Monte Carlo ν_μ events, and 500 Monte Carlo ν_e events. All of the tracks in each of the shower events surviving the Edit 5 and the two scans were classified as one of the following types:

Electron. A shower which originated at the event vertex.

Gamma. A shower which originated at least two planes from the event vertex and had at least four correlated hits in both views. This meant that the gamma would require nearly one radiation length to convert into a shower.

Short-track. A non-shower-like track less than 15 planes which is 1.5 nuclear interaction lengths..

Long-track. A long non-shower-like track greater than 15 planes in length.

From this classification, events determined to have two gammas were assumed to be π^0s. Although the $M^2_{\pi^0}$ was calculated using the energies and opening angles of the showers, no cuts were made based on this. Using this technique, the acceptance for neutral current and charged current π^0 Monte Carlo events identified either correctly as π^0s or misidentified as electrons was determined and their ratio computed. These values are given in Table 6.1 and the ratio for the charged current case is $.84/.46 = 1.8$ and for the neutral current case is $.66/.81 = .81$. The sample of events found in the data which were categorized as gamma + gamma with no other tracks present included four events. Assuming these events comprise the neutral current component of such events in the data, a preliminary number of four misidentifyed electron shower events was assumed.

6.4. Neutrino Energy Calculation and Data Reconstruction

Event energy calculation was performed in a similar manner as that for the muon case. The kinematic equation 5.6 was employed with M_e replacing M_μ. All cases were reconstructed with the proton mass used for M_w. The energy distributions for the reconstruction of the all of the electron candidate events is shown in Figure 6.11 with estimations of the background levels due to π^0s and beam ν_e contamination. Distributions for θ_e versus E_e are shown in Figure 6.10 and Figure 6.9 for the

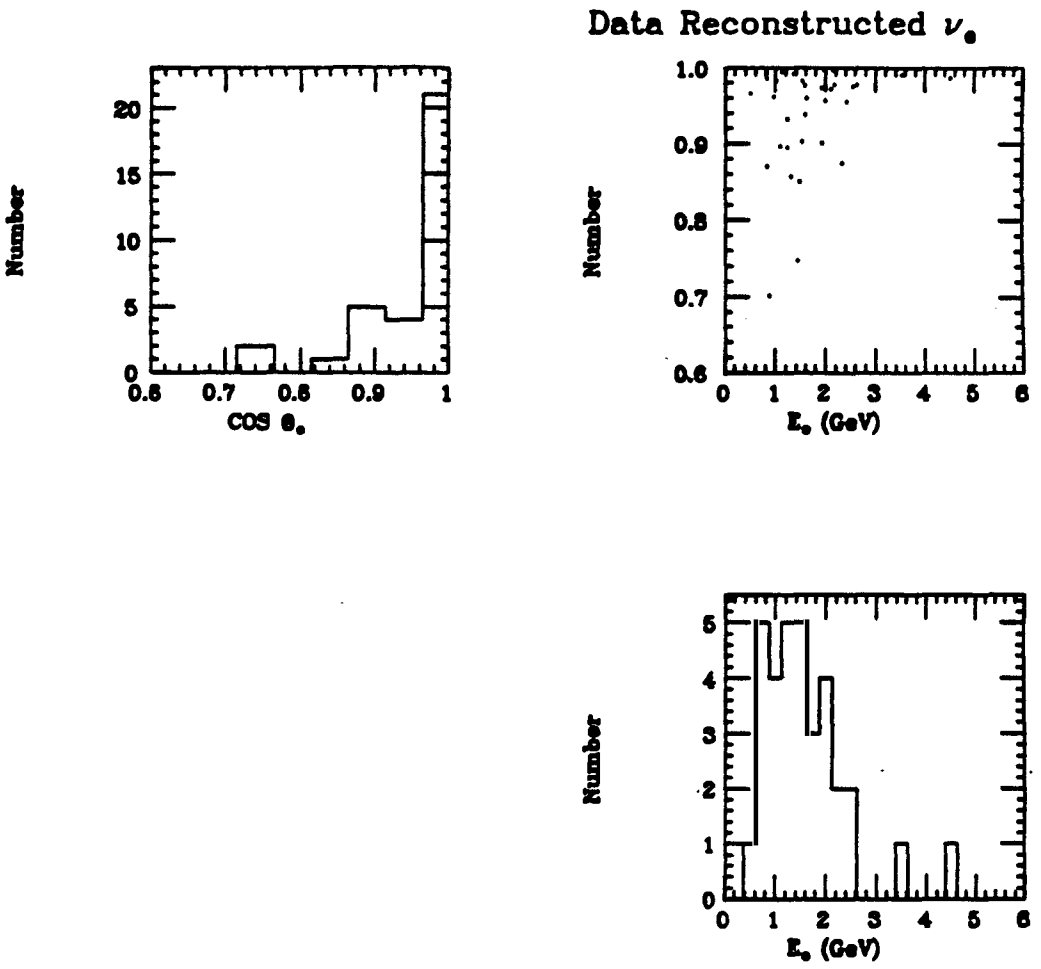

Figure 6.9: Distributions for θ_e versus E_e for the final electron candidates.

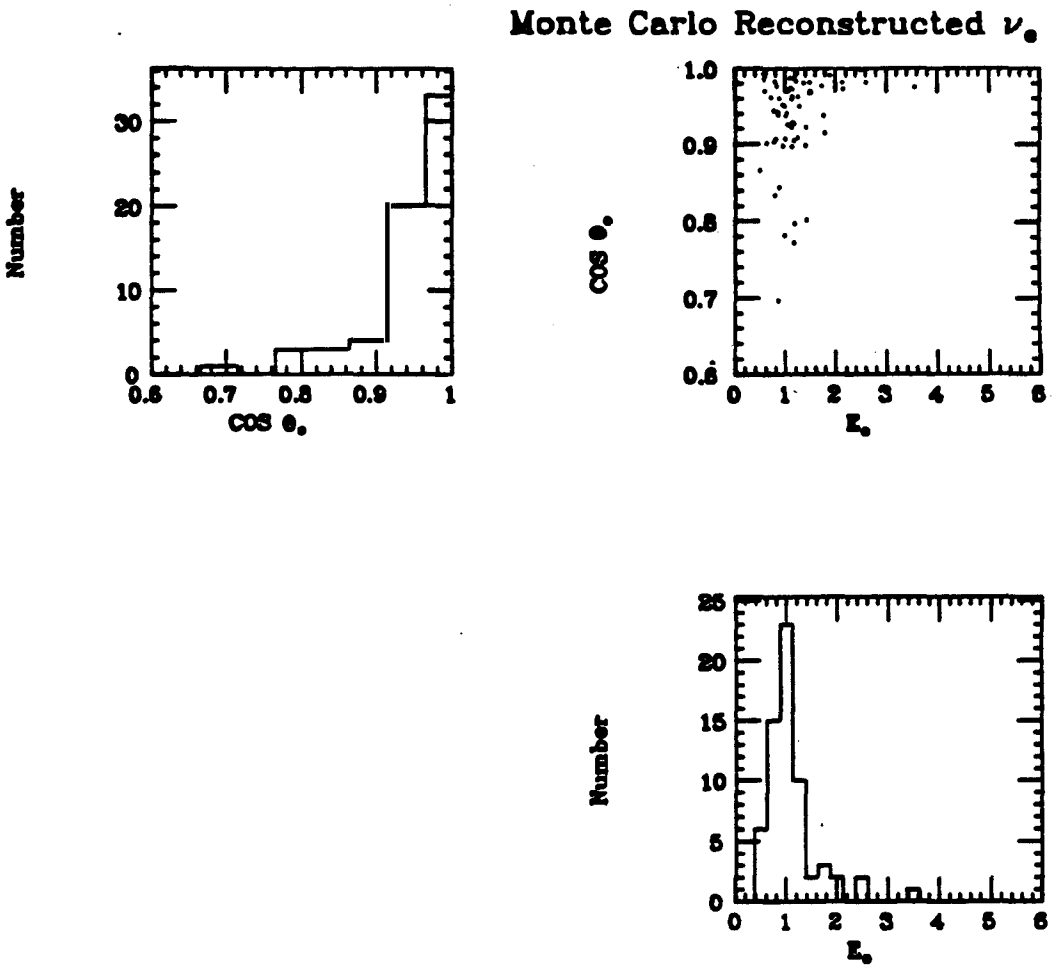

Figure 6.10: Distributions for θ_e versus E_e for the Monte Carlo electrons.

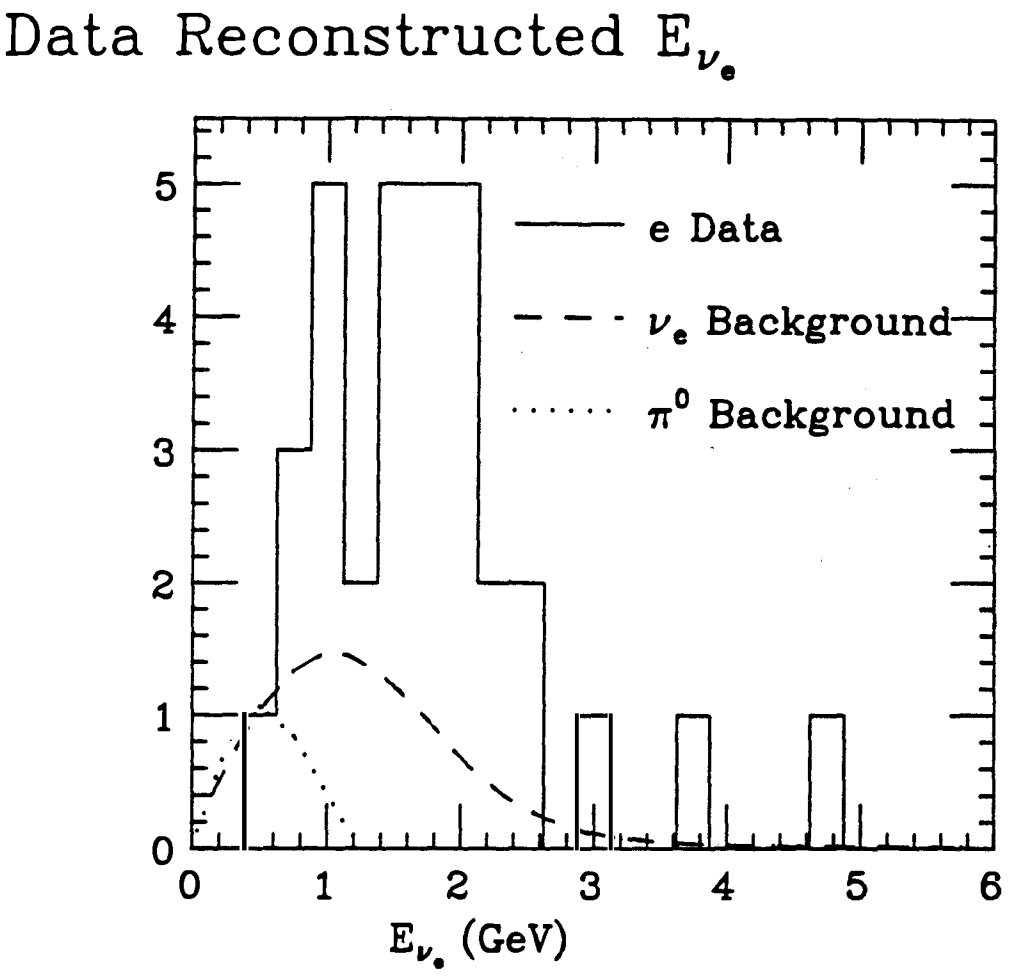

Figure 6.11: Energy distributions for reconstructed data shower events for all three neutrino runs. Estimations of backgrounds from π^0 and beam ν_e are also shown.

Monte Carlo and the combined data sets. The angular distribution of the electron candidates is slightly peaked toward small angles which does not agree well with either the Monte Carlo prediction or the angular distribution of the muons. This anomaly is not yet well understood but may be caused by the angular acceptance of the electron events.

6.5. Data Flow and Rate Determination

		Data sets		
	Reduction step	Summer 240	Fall 240	Fall 280
	General data reduction			
1.	Protons on target $\times 10^{18}$	11.0	8.4	10.1
2.	Neutrino beam spills	1123683	727878	767758
3.	Edit 1	203126	120038	136807
4.	Edit 3	16541	10187	12150
5.	Edit 6	5093	3217	4511
	Electron analysis reduction			
6.	Edit 5	549	368	736
	Eye Scans			
7.	Scan 1	84	55	133
8.	Scan 2	36	31	53
9.	Final pattern cuts for combined data sets			
	Measured as electron		34(1)	
	Measured as π^0		4(0)	
	The number of free trigger events are indicated by ().			

Table 6.2: The data flow for the electron analysis.

A summary of the electron data analysis reduction is given in Table 6.2. This contains the complete history of the data flow as traced from the number of protons on target through the final numbers for observed π^0s and electrons in the sample. These final two numbers were used in conjunction with the results obtained from the Monte Carlo of Table 6.1 to calculate the rate for electrons observed in the data.

Parameter	Combined data sets
Number of protons on target $\times 10^{18}$ (U716).	29.5±1.5
Contained events	34±6
Free trigger cosmic rays	1
Background from π^0s	4
Background from ν_es	10
Acceptance for 240 kA Monte Carlo beam spectrum	.16±.04
Acceptance and background corrected	$119 \pm 30_{stat.} \pm 30_{syst.}$
Rate calculation (neutrino interactions per 10^{16} protons on target).	$4.0 \pm 1._{stat.} \pm 1._{syst.} \times 10^{-2}$

Table 6.3: Rate calculation of electron events for the three data sets combined. The systematic errors are estimated.

To determine the number of electrons expected from the beam calculation, the total number of muon events as calculated in Chapter 5 was used. This number is 59 which when corrected for 16% electron acceptance becomes 10. The steps involved in the rate calculation are contained in Table 6.3. The final number of electrons observed, with the π^0 (4) and beam (10) backgrounds subtracted, was 19 which gave an acceptance corrected rate of $4.0 \pm 1._{stat.} \pm 1._{syst.}$ per 10^{18} protons on target. The systematic errors quoted were estimated and are based mainly upon uncertainties in the electron acceptance and π^0 background; they are not well understood yet.

Chapter 7.
Conclusion

7.1. Data and Analysis Summary

In the preceding chapters, the information necessary to calculate a $\nu_\mu \rightarrow \nu_e$ mixing probability has been presented. In summary, the most important parameters are shown in Figure 7.1 including the beam energy distribution, total interaction cross sections, detector acceptance functions, and measured electron neutrino spectrum with backgrounds. The beam calculation for the muon spectrum agrees qualitatively with that measured, and quantitatively with the ν_μ event rate observed. The number of event channels included in the event Monte Carlo contribute to a total cross section which agrees with previously measured values up to about 1.5 GeV where multi-pion channels become significant. The acceptance functions for muons and electrons demonstrate a very sharp rise near the low energy portion of the beam spectrum which makes it difficult to identify the electron signal unambiguously. Finally, the electron energy spectra of the data is broader than expected but the number of electrons appears to be well above the estimated backgrounds.

The beam calculation for the muon spectrum agreed qualitatively with that measured. It was however, difficult to observe the exact character of the beam due to the inability to precisely identify each event as either quasi-elastic or from a nuclear resonance state. An attempt was made to enhance the quasi-elastic sample by examining events which had little or no energy deposited near their vertexes in addition to the single muon track. The energy distribution of this sample indicates that the observed beam corresponded to that predicted. From the rate of muon events measured in the detector, a calculation of the total cross section was made and was higher than previous bubble chamber measurements by about 50%. It is believed that this inconsistency is within the errors of the target production used in the beam calculation.

Event channels included in the event Monte Carlo produce a total cross section which, up to about 1.5 GeV, agrees with previously measured values. Above this energy multi-pion channels which have not been completely considered become

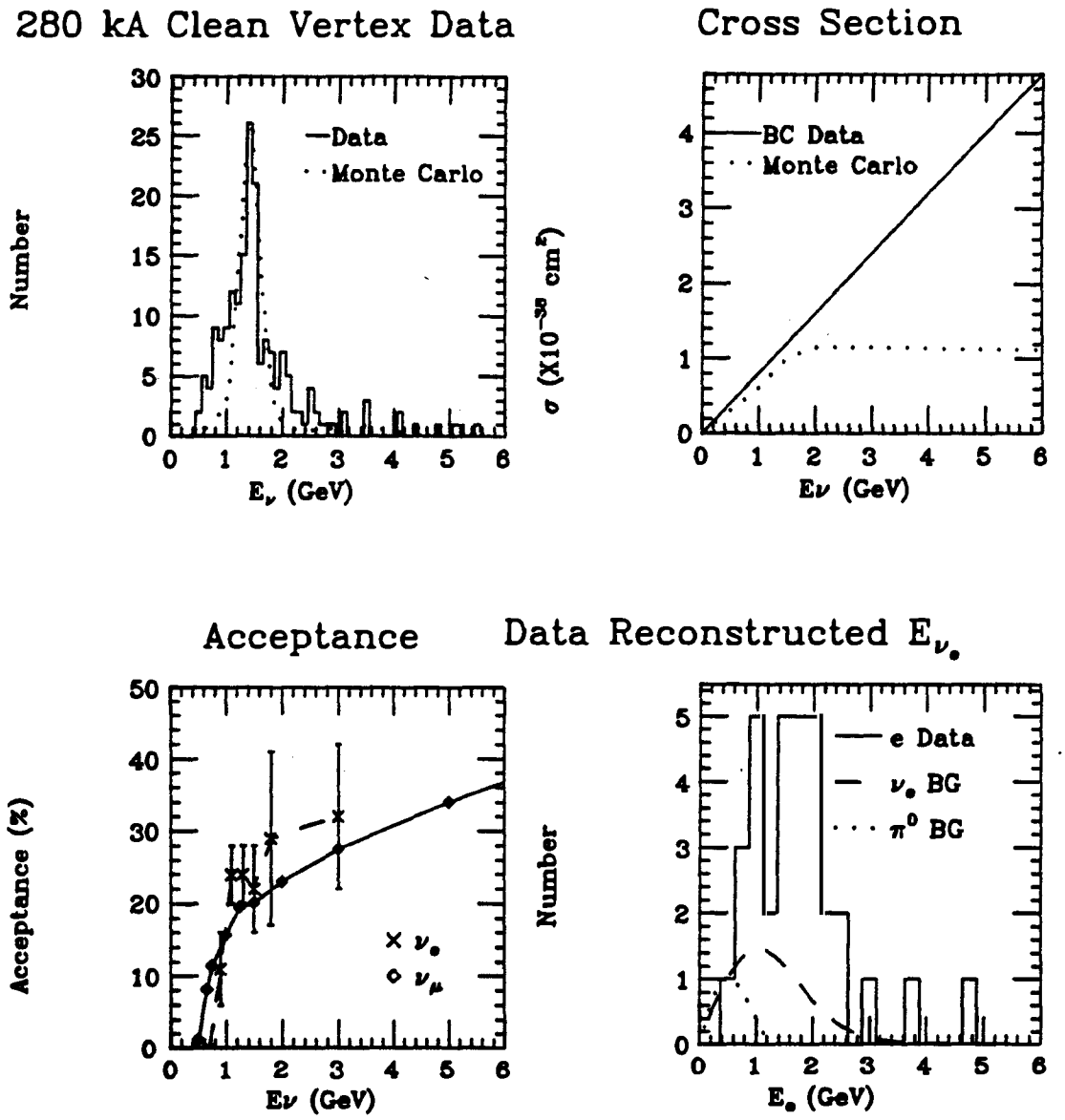

Figure 7.1: Summary plots showing the results of the beam calculation and muon data for 280 kA horn current, total cross section for event channels included in the event Monte Carlo compared to that measured at the BNL 7 foot bubble chamber, acceptance functions for the muon and electron analysis, and the electron spectrum observed with estimates of the backgrounds from the ν_e component in the beam and misidentifyed π^0 events.

significant. The severity of the problem is overstated by the linear cross section of the plot however, as the neutrino flux for energies above 2 GeV is small as a result of the the narrowband beam. It is believed that the calculation of the level of the contamination of the electron sample which was based both on data and on Monte Carlo has been performed correctly but the systematic errors are not yet understood. The fact that the Monte Carlo employed in the electron analysis did not include hadronic particle interaction could cause the estimated backgrounds to be low.

A very sharp rise near the low energy end of the beam energy spectrum was exhibited by the acceptance functions for both muon and electron analysis. This made it difficult to understand the contribution of low energy backgrounds to the muon and electron samples. When averaged over the beam spectra for the two horn currents employed, considering the effect of a linear rise in neutrino cross section, values of about 19% acceptance were calculated for the ν_μ and 16% for the ν_e events. The degree at which event topologies other than those included in the event Monte Carlo entered the data can only be estimated but could be as high as 6% for the muons and perhaps higher for the electrons.

The observed electron spectrum is much broader than that of the muons. It is believed that this is due to the poor energy resolution for low energy electrons. In the electron spectrum are also several unexplained high energy events which tended to be the result of forward showers. The origin of these events may be related to the unexpectedly high number of events observed in the muon data above 2 GeV, however this has not been confirmed. The angular distribution of the electron candidates seem to peak at smaller angles than expected, this is another problem left to pursue. Estimated distributions for the backgrounds are plotted with the electron spectra including that from misidentified π^0s and the ν_e component in the beam in Figure 7.1.

7.2. Calculation of $P(\nu_\mu \rightarrow \nu_e)$ and Comparison with Current World Limits

In order to calculate a value for $P(\nu_\mu \rightarrow \nu_e)$, results from the three sets of data were combined to increase the electron event statistics. As has been calculated in

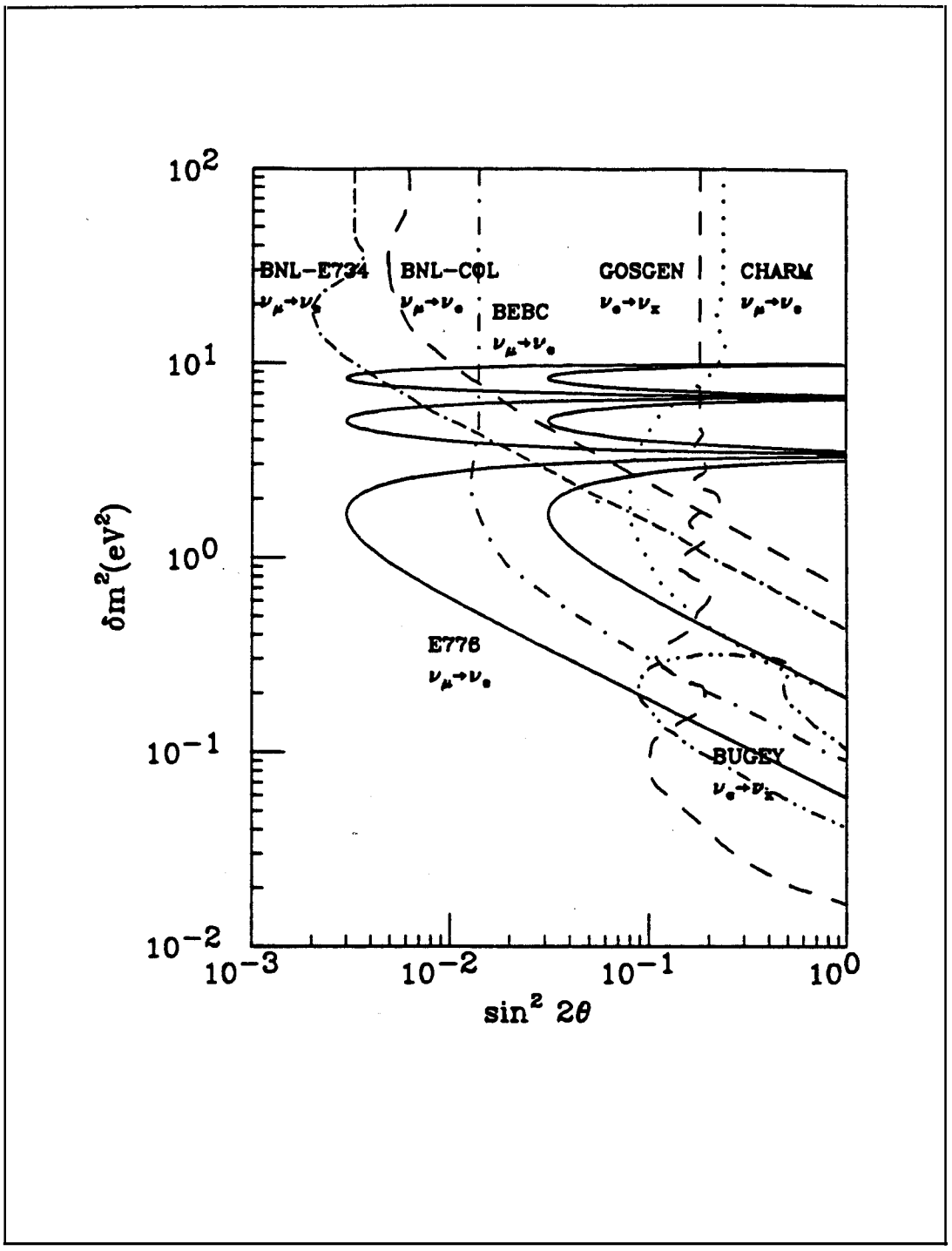

Figure 7.2: Preliminary results for $P(\nu_\mu \rightarrow \nu_e)$ plotted as δm^2 vs. $\sin^2 2\theta$ and compared to current world limits.

Chapter 5, the observed muon neutrino event rate was 2.40±.12 per 10^{16} protons on target. The analysis of Chapter 6 show the measured rate for electron events to be 4.0±1.4 per 10^{18} protons on target with the errors added in quadrature. Therefore, the final number for the mixing is estimated to be

$$\frac{N_{\nu_e}}{N_{\nu_\mu}} = \frac{R_{\nu_e}}{R_{\nu_\mu}} = .017 \pm .007 \ .$$

The comparison of this result to current world experimental limits is presented in a standard plot of δm^2 vs. $\sin^2 2\theta$ in Figure 7.2.

7.3. Major Problems with the Data and Analysis and Possible Solutions

There were many problems related to the analysis which cause the positive oscillation result to require some scepticism. Because the reconstructed muon data has a 30% unexplained excess in the region above 2 GeV, some questions arise concerning the accuracy of the beam calculation and thus the electron neutrino background calculated for the beam. Because of the lack of ability to distinguish certain neutral and charged current $\nu_\mu N \rightarrow X + \pi^0$ events from electron candidates, many questions remain with regard to this category of event. In particular, at what level do the multi-pion event channels which were missing from the event Monte Carlo enter the electron candidate sample. The angular distribution of the electron events was more forward peaked than that of the muons which could indicate that low angle π^0s, from some source, might represent a significant misidentified component. Also, a major concern is how the poor low energy acceptance and electron energy resolution affect the appearance of misidentified π^0 events in the reconstruction. Finally, there were a few other sources of background which have not been considered carefully including coherent π^0 production[27] and other more exotic sources such as resonance decay into ηs.

Solutions to the problems ventured above include more comprehensive calculations of the beam components, more complete Monte Carlo event simulation, better identification of π^0s and ultimately the use of two upgraded detectors at two locations from the neutrino source. In the beam calculation the target production uncertainties require clarification, especially the effect of a relatively thick target and the nuclear interaction of pions and kaons in the horn and collimators. The

event Monte Carlo used in this analysis was lacking detail in several important areas: (1) it produced none of the multi-pion interaction channels, (2) the nuclear interaction of hadrons within the target nucleus and especially while the particles were traversing the detector was incomplete. Further attempts are required to understand differences between signatures of electron and π^0 showers in an effort to better discriminate against the π^0 background events. Finally, to ultimately understand the beam, a second detector should be built between the current one and the target and data from the two detectors compared. If the detector acceptance and energy resolution problems are to be addressed, the current detector should be upgraded and the new detector built appropriately.

Appendix A.
Track Trajectory in a Toroidal Magnetic Field

Due to the toroidal magnetic field, it is most convenient to solve the toroid track trajectory problem in a cylindrical coordinate system. The components of the acceleration are given as

$$a_r = \frac{d^2r}{dt^2} - r\left(\frac{d\theta}{dt}\right)^2, \tag{A.1}$$

$$a_\theta = r\frac{d^2\theta}{dt^2} + 2\frac{dr}{dt}\frac{d\theta}{dt}, \tag{A.2}$$

$$a_z = \frac{d^2z}{dt^2}. \tag{A.3}$$

The force on the particle is given as

$$m\vec{a} = \frac{q}{c}\vec{v}\times\vec{B} = \frac{q}{c}\begin{vmatrix} \hat{r} & \hat{\theta} & \hat{z} \\ \frac{dr}{dt} & r\frac{d\theta}{dt} & \frac{dz}{dt} \\ 0 & B_\theta & 0 \end{vmatrix} \tag{A.4}$$

From this we see that $a_\theta = 0$ and thus

$$\frac{d}{dt}\left(r^2\frac{d\theta}{dt}\right) = 0, \tag{A.5}$$

which implies the conservation of angular momentum

$$L = mr^2\frac{d\theta}{dt} = \text{constant}. \tag{A.6}$$

From A.1 and A.4 we get

$$m\frac{d^2r}{dt^2} - \frac{L^2}{mr^3} = -\frac{q}{c}B_\theta\frac{dz}{dt}, \tag{A.7}$$

and from A.3 and A.4 we get

$$m\frac{d^2r}{dt^2} = \frac{q}{c}B_\theta\frac{dr}{dt}. \tag{A.8}$$

The solution to (A.7) and (A.8) is

$$r_{out} = r_{in} + \left(\frac{dr}{dt}\right)_{in}t + \frac{1}{2}kt^2, \tag{A.9}$$

$$z_{out} = z_{in} + \left(\frac{dz}{dt}\right)_{in} t + \frac{qB_\theta}{2mc}\left(\frac{dr}{dt}\right)_{in} t^2 \qquad (A.10)$$

and

$$mr_{out}^2\left(\frac{d\theta}{dt}\right)_{out} = mr_{in}^2\left(\frac{d\theta}{dt}\right)_{in}. \qquad (A.11)$$

with

$$k = \frac{L^2}{m^2 r_{in}^3} - \frac{qB_\theta}{mc}\left(\frac{dz}{dt}\right)_{in}, \qquad (A.12)$$

and

$$\omega^2 = \frac{3L^2}{m^2 r_{in}^4} + \left(\frac{qB_\theta}{mc}\right)^2. \qquad (A.13)$$

Using equations (A.9), (A.10), and (A.11) the particle was stepped through the toroid steel with dE/dx energy loss and step size of .5 cm. The position of the track was converted from rectangular detector coordinates into cylindrical coordinates as it entered a steel plate, and conversely when it exited the plate. In the rectangular system the calculated track position was compared with the measured hit position.

Appendix B.
Multiple Scattering Error Matrix

As particles pass through the material of the detector, their paths are altered by multiple coulomb scattering. A correlation matrix can be constructed which describes the effect of a displacement at the i^{th} plane on the position measurement at the j^{th} plane.

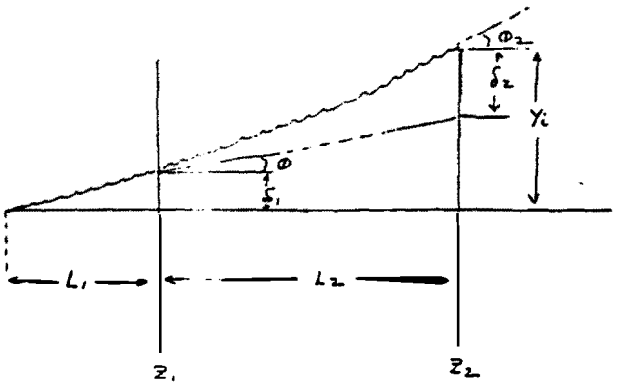

As shown in the figure above, the following parameters are defined which describe the track's position and direction at the i^{th} plane

ϕ_i = net multiple scattering in plane i

δ_i = plane displacement at the end of plane i.

y_i = total displacement at the end of plane i

With these parameters, a fundamental correlation matrix can be produced.

$$\phi_i \phi_j = \sigma_\phi \delta_{ij}$$

$$\delta_i \phi_j = \delta_j \phi_i = \frac{L_i}{2} \sigma_\phi^2 \delta_{ij}$$

$$\delta_i \delta_j = \frac{L_i^2}{3} \sigma_\phi^2 \delta_{ij}$$

where

$$\sigma^2 = \frac{(.015\text{GeV})^2}{(p_i \beta_i)^2} \frac{L_i}{L_{rad}}$$

The displacements from the no multiple scattering case for the 1^{st}, 2^{nd}, 3^{rd},...i^{th} plane are

$$y_1 = \delta_1$$

$$y_2 = y_1 + L_2\phi_1 + \delta_2 = (\delta_1 + \delta_2) + L_2\phi_1$$

$$y_3 = (\delta 1 + \delta_2 + \delta_3) + \phi_2 L_3 + \phi_1 (L_2 + L_3)$$

$$\vdots$$

$$y_i = \sum_{k=1}^{i} \delta_k + \sum_{k=1}^{i-1} \phi_k \sum_{m=k+1}^{i} L_m$$

$$= \sum_{k=1}^{i} \delta_k + \sum_{k=1}^{i-1} \phi_k z_{ki}$$

where $z_{ki} = \sum_{m=k+1}^{i} L_i = z_i - z_k$.

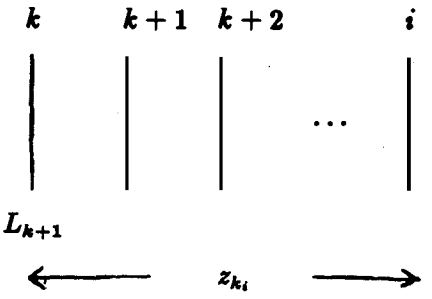

Because $z_{ii} = z_i - z_i = 0$

$$y_i = \sum_{k=1}^{i} (\delta_k + \phi_k z_{ki}) .$$

Then

$$y_i y_j = \sum_{k=1}^{i} \sum_{l=1}^{j\,(i \le j)} (\delta_k + \phi_k z_{ki}) (\delta_l + \phi_l z_{lj})$$

and with this we get

$$\sigma_{ij}^2 = y_i y_j = \sum_{k=1}^{i(i \le j)} \sigma_k \left[\frac{L_k^2}{3} + \frac{L_k}{2} (z_{kj} + z_{ki}) + z_{ki} z_{kj} \right] .$$

This represents the multiple scattering component $\sigma_{(ms)}$. The complete correlation matrix also includes the measurement error

$$\sigma_{ij}^2 = \sigma_{ij(ms)}^2 + \sigma_{ij(meas)}^2 \delta_{ij} .$$

From this, the error matrix is calculated

$$S = \sigma^{-1} .$$

With this error matrix, the χ^2 is defined as

$$\chi^2 = \sum_{ij} (y_i - y(z_i)) S_{ij} (y_j - y(z_j)) .$$

Appendix C.
Toroid Field Measurement

Toroid field measurements were performed to determine their values for the 5 iron planes by members of the AGS magnet group. [28] In order to make the measurements, 5 search coils were wound into each toroid at the locations indicated in Figure C.1. These coils consisted of 10 turns of wire wound perpendicular to the magnetic field through small holes penetrating the steel. The cross sectional area of the coils was 193.55 cm^2 for the 12.7 cm plates and 280.58 cm^2 for the 17.6 cm plates. By ramping up the current through the main toroid windings (thereby increasing the magnetic field) and integrating the *EMF* from the search coils, the magnetic field can be measured as follows.

$$V = EMF = -\frac{d\phi}{dt}$$

and thus

$$B = \frac{\int_{t=0}^{t} V\,dt}{\text{Area}}.$$

The units of this are

$$B(\text{KGauss}) = \frac{10^2 \int_{t=0}^{t} V\,dt(\text{mVSec})}{\text{Area}\,(\text{cm}^2)}.$$

Figure C.2 shows the field measurements taken for the 5 toroid magnets with a ramping period of 10 sec and an voltage integrating period of 20 sec. One anomalous point in toroid 4 is believed to be due to an error in the number of turns which were included in the search coil.

In order to verify that the iron was saturated by the field, measurements were taken ramping up to two current levels (12KA and 15KA) at a high rate (1 Sec). These studies indicate, though not conclusively, that the field was beginning to saturate at the higher currents as shown in Figure C.3. This is especially true for the region near the center of the toroids.

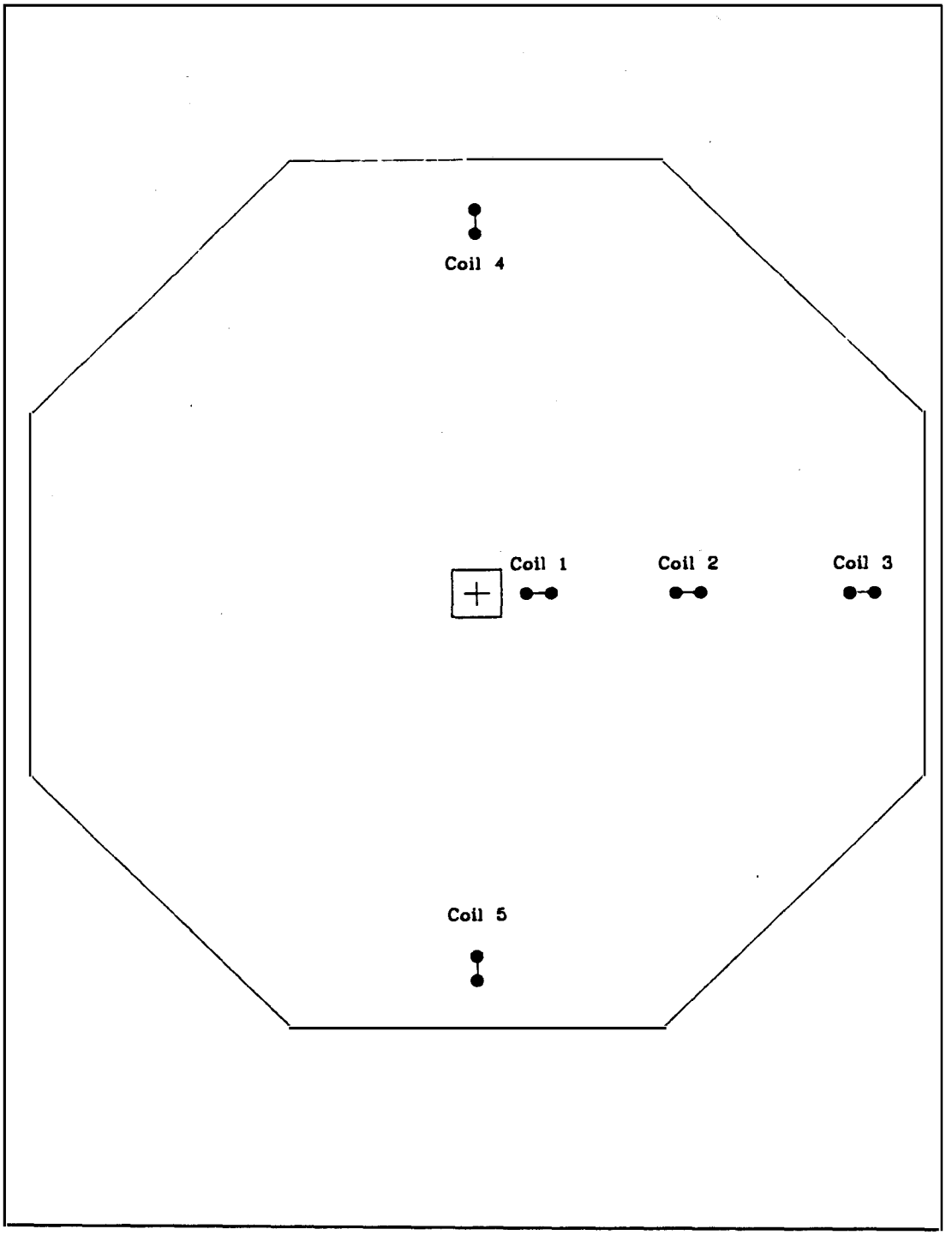

Figure C.1: Locations of the coils on the toroid steel used to measure the magnetic field.

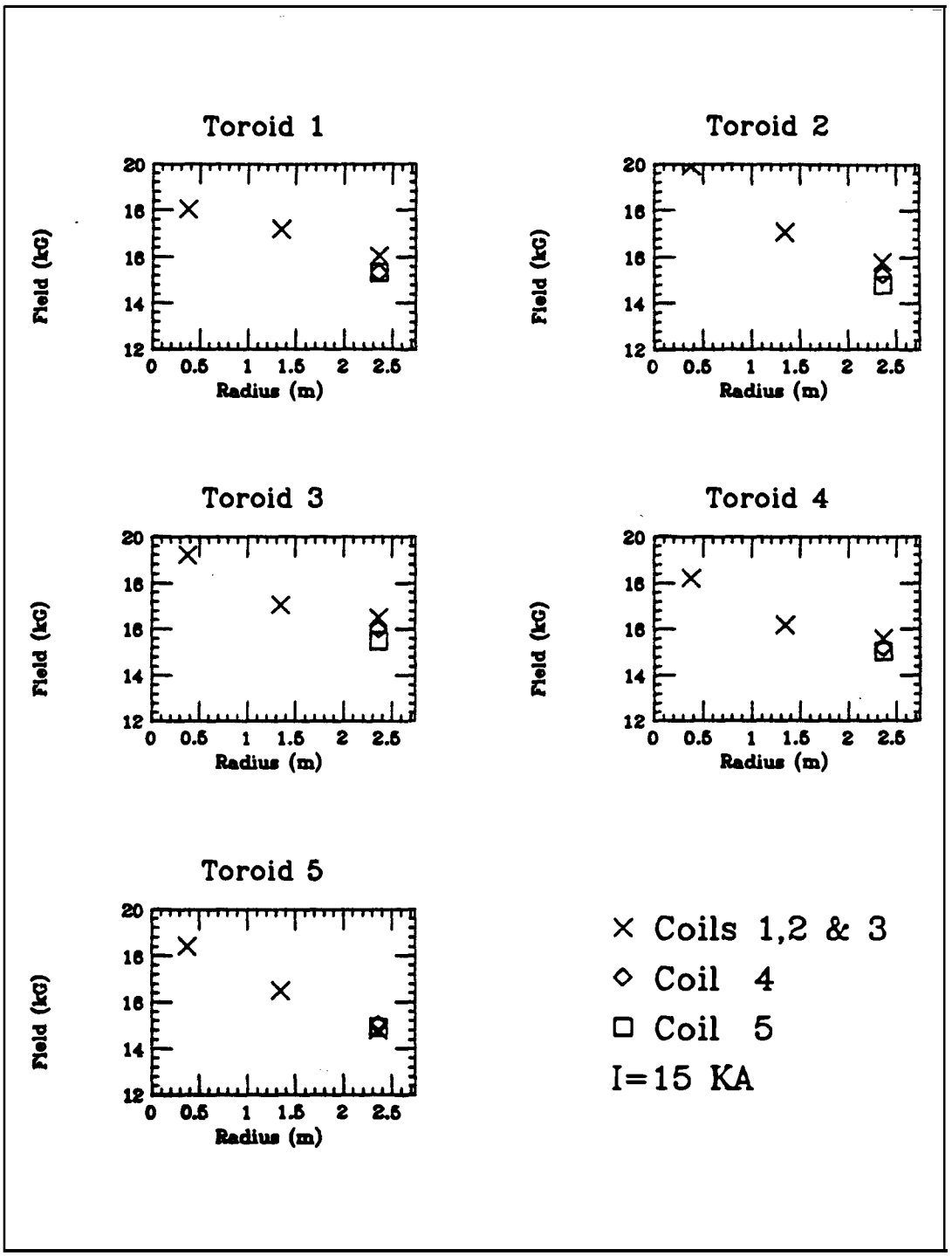

Figure C.2: Field measurements for each of the toroid steel plates as a function of radius of the measurement coil from the center of the toroid

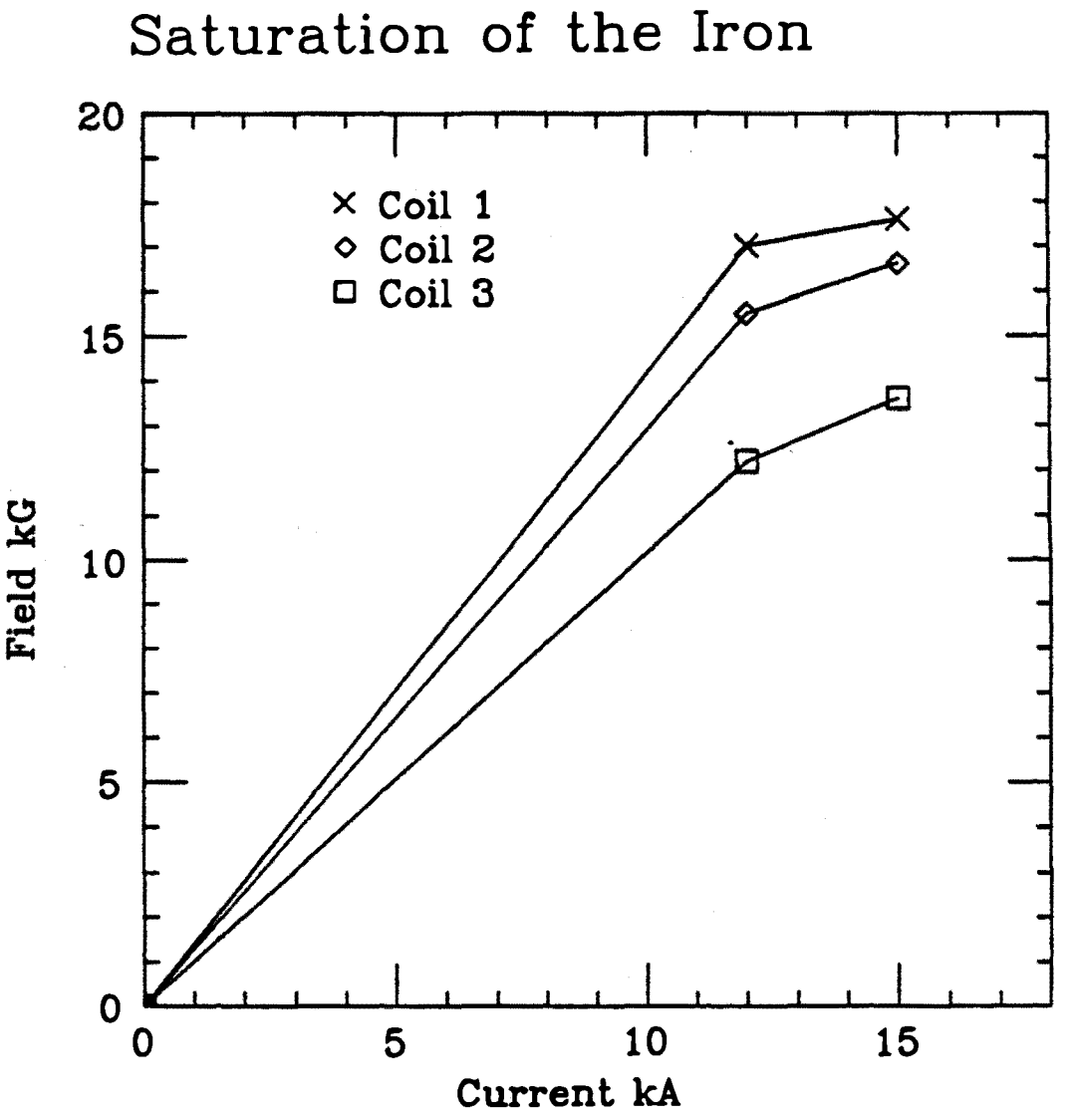

Figure C.3: Field measurements which indicate that the steel was saturated by the magnetic field

Appendix D.
The Data Edits

In order to reduce the raw data sample, a series of edits was performed which kept only potentially interesting events. In the following descriptions of the edits, the upstream end of the detector is referred to as the 'front', or 'beginning', and the downstream end is called the 'back' or 'end'. The portion of the detector constructed with concrete and aluminum absorber is called the 'electron' detector and the toroidal portion of the detector is referred to as the 'toroids'.

D.1. Edit 1

The first edit was designed to eliminate empty events or events consisting of scattered single hits. The total number of drift tubes firing was required to be greater than or equal to ten. A cleanup was performed in which only hits with at least one additional hit 'nearby' were considered. Nearby hits were defined as being within an area defined by the "x"s in the following table with the "o" representing the hit under consideration.

hit wire	-3	-2	-1	0	+1	+2	+3
hit plane-4	x	x	x	x	x	x	x
hit plane-2		x	x	x	x	x	
hit plane			x	o	x		
hit plane+2		x	x	x	x	x	
hit plane+4	x	x	x	x	x	x	x

With the hits retained by this filtering process at least three consecutive planes in each view were required for the event to be saved.

D.2. Edit 3

This edit was designed to further reduce the number of event candidates for muons and showers. Again, the number of drift tubes was required to be greater than or equal to 10. As in Edit 1 an additional cleanup was done this time requiring at least two hits 'nearby' (as defined in D.1). With these hits, at least 4 consecutive

planes were required in each view. The track was reconstructed with a track finding algorithm and the following requirements were imposed on it.

1. If the reconstruction failed, the event was retained unless (a)the number of PDT's was greater than 250, (b)the number of phototubes was greater than 80, or (c)the number of toroid hits was greater than 10.
2. At least one track in either view must have met the following criteria: (a)The number of PDT hits was greater than or equal to four, (b) it was at least three planes in length, (c) its beginning was within the fiducial volume defined as four planes from the front of the detector, and at least two wires from the edge.
3. If there were tracks in both X and Y views then the difference between the upstream-most planes in the two views was required to have been less than or equal to 10 planes.

D.3. Edit 6–The Contained Edit

An attempt was made with this edit to further reduce the sample of events to those for which the main track or shower was contained within the detector. Each event was reconstructed by the pattern recognition routine (PATTREC) in which a "track" had the following attributes:(a)the number of hits was greater than or equal to 4, (b)the length was at least three planes and (c)for at least one track in each view the positions of the beginnings must match to within ten planes. An identification was made of muons and showers by measuring the pulse area deposited in each plane of the track. This pulse area was that of the hit in the track plus any hits adjacent to it in the plane. With these areas muons and showers were defined and examined as follows:

1. Muons had an average pulse area per plane of less than 200 and and an average pulse length per plane of less than 50 time ticks (22.4 nS per tick).
2. Showers were further augmented by searching near tracks not identified as muons to pick up additional hits which may have been excluded by the pattern recognition algorithm.

Muon events were retained based on the following criteria:

1. Multi-prong events which formed 'v's or 'stars' were all retained.

2. The position of the track's beginning matched within 3 planes and the position of the track's end matched within 5 planes. In each view, the track was required to be greater than 6 planes in length.
3. The total length in both views was required to be greater than 15 planes for tracks contained in the electron detector, and greater than 10 planes for tracks which entered the toroids.
4. The slope of the track in both x and y projections was less than 1.1. Slope was defined as the x or y distance over the z distance traveled by the track.
5. All single tracks which met the muon criteria were either contained or passed through the back plane of the electron detector (i.e they entered the toroids). Containment required that the projection of the track onto the next or previous plane was greater than one wire from the edge on all four sides of the detector the detector. Also, the hits at the beginning and ends of the track were required to be at least one wire from the edge of the detector. None of the hits in the track were allowed to occur in the front four planes of the electron detector.

Tracks identified as showers were retained with the following shower rules.

1. Total pulse area was required to be greater than 4000 units. This represented a cut on kinetic energy of about 300 MeV.
2. Tracks which loosely matched in both x and y views were required to have total pulse areas of greater than 2000 units either view . If the event seemed to enter the toroids this was lowered to 1000 units.
3. The length was required to be greater than 8 planes.

For shower events no fiducial cuts were imposed in this edit. Most of the events which passed this edit as showers were rather poor candidates.

D.4. Edit 7–The Muon Edit

Edit 7 was designed specifically to enhance the clean muon sample. It was identical to Edit 6 except more stringent track length cuts were imposed. If the track stopped in the main detector, a minimum of 23 planes were required, which is about 450 MeV kinetic energy for a muon. For tracks which entered the toroids, a minimum of 18 planes was required.

D.5. Edit 5–The Shower Edit

A routine was developed which selected showers by examining hits and assigning them to groupings based on location, pulse area, and timing criteria. The algorithm proceeded as follows:

1. Each track found by the pattern recognition routine (PATTREC) was defined as either a shower or a single particle. For showers, the average pulse area of the track (excluding the end points) was required to be greater than 220 units.
2. Additional hits near each track were assigned to it if they were within ± 1 wire of the track for single particles, and ± 2 wires for showers.
3. The tracks defined in steps 1 and 2 were then matched in the X and Y views. The requirements for matching tracks were that the end (downstream) plane differ by less than 5 planes, and the beginning (upstream) plane differ by less than 3 planes, in the two views. The timing for the tracks was required to be close (within 1 μsec) for the two views.
4. Beginning with the longest track, all of the tracks found were then grouped together based on timing. If the match was sufficiently good for the longest track in each view, then a vertex location was calculated for the group. If the match was not good, then an attempt was made to match different length tracks. This was done by searching at the ends of all of the tracks for hits which might have been related to the tracks but were separated by several skipped planes. If the track was near the edge of the flash encoder timing window then an extended search was conducted allowing 6 skipped planes in a ± 3 wire radius of the track trajectory. After these attempts were made the matching was again attempted.
5. All unused hits which remained at this point were assigned to nearby tracks.

With nearly all of the hits for the event now assigned to tracks, and these tracks assigned to groups, showers were required to meet the following criteria.

1. The length of the shower was greater than 14 planes.
2. The slope of the shower in both X and Y projections was less than 1.1. Slope was defined as the X or Y distance over the z distance traveled by the track.

3. If any of the tracks in any of the groups was not contained within the fiducial volume of the detector, that group was excluded from the decision to keep the event. The fiducial volume was here defined as 17 planes from the back, 2 planes from the front, and two wires from the edge of the detector.
4. Any track which was not matched in both views was subjected to criteria 2 and 3 above.

Appendix E.
AGS and Decay Tunnel Signals

Several numbers were supplied to us from the AGS computer via a Datacon serial link to our parallel CAMAC crate. The information which was supplied for the duration of the data taking period included in this report are included in the following table.

Number	Name	Description
1.	PULSE NUMBER	AGS pulse number mod 1000
2.	TOTAL RADIATION LOSSES	U-line ionization loss monitors
3.	BEAM MOMENTUM	Beam momentum in MeV/c
4.	AGS REP RATE	Time between spills in Milliseconds
5.	H5 MONITOR	Radiation monitor at H5 extraction magnet
6.	TIME	Time of day
7.	DATE	Date of the year
8.	TRANSPORT EFFICIENCY	U-line intensity / ring intensity
9.	BEAM RADIUS	Radius of beam in AGS (mm)
10.	SHAVING LOSSES	Amount of beam lost in AGS due to shaving
11.	EXTRACTION TIME	Time of extraction in units of beam revolutions (2.69 μsec)/revolution
12.	H5 TRIG-EXAU4	Not used
13.	EXAU1	Trigger for detector, horn current and pion monitor
14.	EXAU2	Not used
15.	EXAU3	Trigger for horn power supply

Number	Name	Description
16.	UXCBM	Circulating beam intensity monitor
17.	UX15	Intensity transformer located at U-15
18.	UX716	Intensity transformer located at U-716
19.	UP698	Vertical beam targeting dipole
20.	UD700	Horizontal beam targeting dipole
21.	UD400	Horizontal dipole at U-400
22.	Not used	
23-42.	U-LINE LOSS MONITORS	Ionization loss monitors
43.	CHARGE TIME	Horn charge time in Milliseconds
44.	HORN CURRENT PEAK 1	Horn current peak from coil on load
45.	HORN CURRENT PEAK 2	Horn current peak from coil on load
46.	TARGET THERMOCOUPLE	Tempurature of target
47.	TARGET TELESCOPE	Scintillation counter located upstream of target
48.	SWIC 1	Multi-wire ionization chamber to measure beam position
49.	SWIC 1 MOMENT	Spacial width of charge distribution from SWIC
50.	SWIC 2	
51.	SWIC 2 MOMENT	
52.	SWIC 3	
53.	SWIC 3 MOMENT	
54-64.		Reference numbers

Twenty RG62 coaxial cables were supplied by the AGS and were patched from the "B" trailer to our experimental area. Signal assignments to these cables follow.

Number	Signal name	Description
1.	CERENKOV #1	Located in the decay tunnel near the iron shield
2.	CERENKOV #2	Located in the decay tunnel on pion monitor base
3.	CERENKOV #3	Located in the decay tunnel on pion monitor base
4.	Spare	Connected through to horn trailer
5.	XCBM pulse train	Internal beam intensity monitor
6.	N/A	Poor signal cable
7.	Horizontal U718 SWIC	SWIC oscilloscope display
8.	Vertical U718 SWIC	SWIC oscilloscope display
9.	N/A	Bad signal cable
10.	X-mit to MCR	Serial line to MCR monitor terminal
11.	Recv from MCR	Serial line to MCR monitor terminal
12.	N/A	Bad signal cable
13	AGS INFO LINE	Datacon serial data
14.	AGS 1KC CLOCK	AGS clock for predet
15.	AGS 100KC CLOCK	AGS clock for predet
16.	AGS FRAME NUMBER	Pulse train with AGS frame number mod 1000
17.	AGS SPARE	Spare signal cable
18.	AGS SPARE	Spare through multiplexer
19.	AGS EXAU1	Experiment autodet, trigger for detector readout
20.	AGS H5 start	AGS beam extraction time

References

1. B. Pontecorvo, JETP 34,247 (1958).
2. G. Marx, Acta Phys. Ac. Sci. Hung.,3,55(1953).
3. R. Davis, Jr., Phys. Rev. 97,766(1955).
4. B. Pontecorvo Zh. Eksp. Teor. Fiz. 53, 1717 (1967)[Sov. Phys. JETP 26,984 (1968)]V. Gribov and B.Pontecorvo, Phys. Lett. ,28B,493 (1969)S.M. Bilenky and B. Pontecorvo, Phys. Reports 41,225 (1978).
5. V. Flaminio and B. Saitta ,Neutrino Oscillation Experiments, Istituto Nazionale di Fisica Nucleare, INFN PI/AE 85/86 (1985); question, "Neutrino Masses: Theory and Experiment", Comments on Nuclear Particle Physics, Vol. 9, No. 5, pp. 169-182, (1981); C.W. Kim and Hiroyuki Nishiura, "Effects of the Third Generation on the Neutrino Oscillations",JHU-HET 8506 (1985); Boris Kayser,"On the Quantum Mechanics of Neutrino Oscillation", Phys. Rev. D, 24 110, (1981).
6. op. cite. V. Flaminio, "Neutrino Oscillation Experiments".
7. Richard S. Wolf,"Measurement of Gas Constants for Various Proportional-Counter Gas Mixtures", NIM, 115, 461-463, (1974); see also A. L. Ward, Phys Rev. 112, 1852 (1958)& Journal of Appl. Phys. **33**, 2789 (1962); M. W. Charles, Journal of Physics **E5** 95 (1972).
8. Particle Data Group,"Review of Particle Properties", Phys. Lett. 170B p.38 (1986).
9. F. Sauli, CERN 77-09,p.2,(1977).
10. D. H. Perkins, *Introduction to High Energy Physics* p. 38 (1972)Addison-Wesley Publishing Company, Inc.
11. J. R. Sanford, C. L. Wang, "Empirical Formulas for Particle Production in p-Be Collision Between 10 and 35 BeV/c",Parts I and II, Accelerator Department, AGS internal report, BNL report number 11479 (1967).
12. H. Grote, R. Hagedorn, J. Ranft,"Atlas of Particle Production Spectra", CERN report,(1970).

13. E. D. Commins and P. H. Bucksbaum, *Weak Interactions of Leptons and Quarks*, (Cambridge University Press, Cambridge, 1983), p. 290.

14. op. cite. E. D. Commins and P. H. Bucksbaum *Weak Interactions of Leptons and Quarks.*

15. D. Rein and L. M. Sehgal,"Neutrino-Excitation of Baryon Resonances and Single Pion Production", Annals of Physics **133**, pp. 79-153 (1981).

16. The values included in Table 4.1 were taken from tables on pp. 86 and 117 and from the plot on p. 118 of the previous reference.

17. T. Gaisser, M. Nowakowski, and E. A. Paschos, Phys. Rev. D 33 1233 (1986); see also S. Adler, S. Nussinov & E. A. Paschos, Phys. Rev. D9 2125 (1974).

18. A. Le Yaouanc, L. Oliver, O. Pene, J. C. Raynal & C. Longuemare ,Phys. Rev. D 15 2447 (1977).

19. Richard L. Ford and Walter R. Nelson, *The EGS Code System*, SLAC-210,1978; see also D. W. O. Rogers, "Low Energy Electron Transport with EGS", NIM, **227**,pp. 535-548 (1984).

20. G. Z. Molier, Z. Naturforsch, **3a** p.78 (1949).

21. R. M. Sternheimer and R. F. Paierls, Phys. Rev. B3(1971)3681.

22. A. Grant, "A Monte Carlo Calculation of High Energy Hadronic Cascade in Matter", NIM 131 pp.167-172 (1975).

23. J. Ranft,Particle Accelerators, Vol.3,pp. 129-161 (1972).

24. T. Kitagaki et al. ,Phys. Rev. D 9 2554 (1986).

25. Op. Cite. Sternheimer (1971).

26. N. J. Baker et al.,Phys. Rev. D,25 617 (1982)

27. D. Rein and L. M. Sehgal,"Coherent π^0 Production in Neutrino Reactions", Nuclear Physics B223 29,(1983)..

28. Memo from A.S.Carroll reporting the measurements performed by J. Weisenbloom and R. Stoehr of the AGS magnet group

Vita

Lee Harold Lueking was born in Oxford, Nebraska on April 16, 1957. He attended Oxford public schools and graduated in May of 1975. In the fall of that same year he enrolled at Hastings College, Hastings, Nebraska majoring in Physics and Mathematics. During the summer of his junior year he participated in an undergraduate research program at Iowa State University working in a low temperature solid state lab. He received his B.A. from Hastings in the spring of 1979. After entering The Johns Hopkins University, Baltimore, Maryland, he received a Master of Arts Degree in 1982. His Doctoral research was conducted in collaboration with physicists from Columbia University Nevis Labs, The Johns Hopkins University, and The University of Illinois, Urbana, investigating muon neutrino to electron neutrino oscillation at Brookhaven National Laboratory. He spent three and a half years at BNL helping construct the neutrino detector, acquiring data, performing analysis, and completing his Ph.D. dissertation.